Thermohydraulics and Suppression of Nucleate Boiling in Upward Two-Phase Annular Flow: Probing Multiscale Physics by Innovative Diagnostics

By

Guanyu Su

B.Sci., Power Engineering, Chongqing University, 2008
M.Sci., Nuclear Science and Engineering, Shanghai Jiao Tong University, 2011
M.Sci., Nuclear Science and Engineering, Massachusetts Institute of Technology, 2015

SUBMITTED TO THE DEPARTMENT OF NUCLEAR SCIENCE AND ENGINEERING IN PARTIAL FULFILLMENT OF THE REQUIREMENTS FOR THE DEGREE OF

DOCTOR OF PHILOSOPHY IN NUCLEAR SCIENCE AND ENGINEERING

AT THE

MASSACHUSETTS INSTITUTE OF TECHNOLOGY

JUNE, 2018

Signature of author: _____
Guanyu Su
Department of Nuclear Science and Engineering
June, 2018

Certified by: _____
Jacopo Buongiorno
Professor of Nuclear Science and Engineering
Thesis Supervisor

Certified by: _____
Eissa Al-Safran
Associate Professor of Petroleum Engineering, Kuwait University
Thesis Reader

Certified by: _____
Emilio Baglietto
Associate Professor of Nuclear Science and Engineering
Thesis Reader

Certified by: _____
Bren Phillips
Research Scientist, Nuclear Science and Engineering
Thesis Reader

Accepted by: _____
Ju Li
Battelle Energy Alliance Professor of Nuclear Science and Engineering
Chair, Department Committee on Graduate Students

Thermohydraulics and Suppression of Nucleate Boiling in Upward Two-Phase Annular Flow: Probing Multiscale Physics by Innovative Diagnostics

By

Guanyu Su

Submitted to the Department of Nuclear Science and Engineering on May 25, 2018 in Partial Fulfillment of the Requirements for the Degree of

Doctor of Philosophy in Nuclear Science and Engineering

Abstract

In the fuel assemblies of a boiling water reactor (BWR) the steam quality increases along the assembly's length as heat is transferred from the fuel rods to the water coolant. Nucleate boiling is the dominant heat transfer mechanism at low and intermediate steam qualities (typical of the bubbly and slug/churn flow regimes), while forced convective evaporation dominates at higher steam quality in the annular flow regime. The transition of the heat transfer mechanism, also called suppression of nucleate boiling (SNB), affects the local heat transfer coefficient (HTC), the stability of the liquid film, and the entrainment dynamics. To support the efficient design and safe operation of future BWRs with higher power density, a thorough understanding of the thermohydraulic mechanisms and an accurate prediction of the transition conditions for SNB in annular flow is quite desirable.

An innovative diagnostic technique combining synchronized infrared thermography and an electrical conductance-based liquid film thickness sensor was utilized here to investigate the details of the SNB phenomena with high spatial and temporal resolutions. The main control parameters of the tests included: the mass flux from 700 to 1400 $kg \cdot m^{-2} \cdot s^{-1}$, steam quality from 0.01 to 0.08, and heat flux from 100 to 2000 $kW \cdot m^{-2}$. The system pressure was held close to atmospheric pressure. At each set of conditions, the local distributions of the 2D surface temperature, 2D heat flux, and quasi-2D liquid film thickness were measured. From the measured data, the SNB heat flux, the SNB wall superheat, and the hydrodynamic properties of the disturbance waves were extracted. The experimental observations show for the first time the multiscale interaction of the extremely thin film and small nucleation cavities (on the scale of 10 micron), with the large disturbance waves and their associated temperature oscillations (with

wavelengths of ~10 cm). A first of a kind 1D mechanistic model was developed to accurately capture this unique transient effect of the disturbance waves on the local heat transfer. The experimental results also suggest a strong dependency of the SNB heat flux and wall superheat on steam quality, with a second-order, weaker dependency on total mass flux. The same dependency is also found for the disturbance wave properties. A complete set semi-empirical correlations was proposed for predicting the time-averaged film thickness and SNB thermal conditions. Good agreement is found between the semi-empirical correlations and the experimental results. The database generated in this project can be further used for development and validation of CFD models of SNB and two-phase heat transfer in annular flow.

THESIS SUPERVISOR: Jacopo Buongiorno, Ph.D.
TITLE: Professor of Nuclear Science and Engineering

Fate whispers to the warrior: “You cannot withstand the storm.”

The warrior whispers back: “I am the storm.”

---- Anonymous

Acknowledgements – Forging My Sword

Forging a sword is easy, but forging an Excalibur is hard. It requires not only the perseverance of Sisyphus, the creativity of Lu Ban (鲁班), and the accuracy required to detect gravitational waves, but most importantly, it is a life-long march. I see doing research as forging a sword. I hope the sword I am forging will eventually become another legendary sword, like Excalibur, someday.

If asked the crucial thing to forge a legendary sword, what would be your answer? The material, the design, the magic decoration, or the swordsmith? In my opinion, it is the soul of the sword. With soul, the sword becomes the history itself, witnessing the legend of success. Prof. Buongiorno is the person who gave the soul to my sword. Your impressive words are still like from yesterday: "Guanyu, nothing is TOO difficult at MIT". Whenever I hesitated when confronted with a hard problem, this sentence jumped out in my mind like a magic spell that pushed me forward: "Well, well, if I don't overcome this issue, how can I go further?" Just like that, I magically believed your magic spell. The hardest part of my PhD was the indefatigable attempts to challenge you with my eye-opening but sometimes too naïve ideas and theories. You easily defeated me with a piece of paper, a randomly grabbed pen, your erudite knowledge, and usually ended with a mysterious smile as if to say: "Boy, good job, but try it harder next time." I guess your stress-free responses gave me impetus to continue challenging you tirelessly and fearlessly. There were for sure countless times that you put your unconditional trust in me: "Guanyu, I think you can do it in ten minutes/two hours/one day/...". I think I was too young to sense time the way you did. At the beginning of my PhD, I terribly doubted the speed of my clock. Amazingly here I am, I indeed made it in your time scale. I swear I read this sentence from some serious book: "when you get close to the speed of light, you start to see things differently." You never minded if you had to slow down in order to help me accelerate. Professor, when I look up to you, I see the soul of lion and the heart of ocean. I believe that is also what you carved into my sword.

With no doubt, the body material is the foundation of a sword. Choosing the most appropriate one is beset with difficulties. Stumbling into the nuclear field, and stepping into the topmost palace of technology with such respect and awe, I was overwhelmed and bewildered without any expectation of future achievements. As I was deeply doubting myself, Dr. McKrell showed up and led me through the dense fog like a sage. He encouraged me: "I can tell what kind

of student can be successful." I grabbed this silver lining in a wink, not even caring if it was shining for me. I do not remember how many times he supported my blue-sky thoughts with realizable solutions, how many times he halted me right before the failure with one simple sentence: "Do things in the proper way." From Dr. McKrell, I experienced the power of pursuing accuracy and precision. I sometimes imagined that Lu Ban could have been reborn with blonde hair. He did not simply pick a popular material for my sword, like Damascus steel. He believed that I could do better than those popular ones. Instead, he passed down the approach for selecting the material to me, and allowed me to make decisions. Dr. McKrell left us in a hurry. I hope he would smile and rub his hands excitedly if he could see the work I have accomplished.

Dr. Phillips is the other person who lay down another foundation with me, the hilt of my sword. We worked closely in the lab every day, building and testing my experimental loop, just as the hand grabs the hilt. His new ideas always inspired me to make modifications that lead to more convenient operation of my loop and equipment. His optimism has deeply influenced me, and my laughter has become more and more like his. Thank you for the hilt. It makes my sword more comfortable to use.

Prof. Al-Safran sharpened the edge of my sword with his fresh "outsider's" mindset and valuable thoughts. He showed me the splendid world outside of my area. He is like a large treasure-house, and continuously shared his knowledge from a different point of view. Every time I read out the Ali-Baba magic spell, Prof. Al-Safran gave me ten correlations. His generosity prevented me from being biased by only one idea.

I also would like to express my appreciation for Prof. Prasser and Dr. D'Aleo, who provided one of the most important pieces of equipment for my investigation. I cannot imagine how much they struggled and how much effort they expended. In the end, the rare elements were added and the sword was strengthened.

There was a time I never thought things could go not as fluidly as I planned. When Prof. Baglietto asked me if I had any backup plan one and a half year ago, I was not able to give him an answer because of my overconfidence. Now I am very grateful for his question. It was the cross-guard that he introduced, which prepared me for an unexpected situation.

I would like to thank KAPL for sponsoring my work. Without their support, I could not have afforded any of the equipment. Without their patience, I could have just remained trapped in the middle of thorns, achieving nothing.

An anonym closely watched my progress. Whenever I was blocked, he showed up and helped forge my sword with his Mjölnir without asking. Prof. Bucci, I saw you under your cloak. The discussions with you were very helpful and supportive. I still recall the fantastic iteration of "disagree with the disagreement to my disagreement."

I appreciate the brilliant talks with Andrew, who also taught me a lot about American culture. I appreciate Carolyn's help with the FTIR. I appreciate Artyom for making me several pieces of my test channel. I appreciate all my colleagues who had helped and spent valuable time with me, Melanie, Chi…

And last but not least, I would like to give my heart to my wife Jing Yang. You are the scabbard of my sword, who always protects me at my most vulnerable moment. I may foolishly over-expose my sharpness without your covering. You are a much wiser person than I am. My sword would be rusted without your care.

My appreciation also flies far back to China, to my hometown, and to my beloved parents. You unselfishly sent me far away to pursue the art of sword- forging in technology. I hope I have made you prouder.

At the end of these acknowledgements, with tears running in my eyes, I do not know how much nonsense I have written down. I look up again to the motto of MIT: Mens et Manus, which always reminds me of a similar wisdom from a Chinese philosopher back in the Ming dynasty: Integration of knowledge and action (知行合一). It is time to start my new journey again with my mind and hands.

Table of Contents

List of Figures

List of Tables

Nomenclature

Notation	Description	Unit
A	Total flow area	[m^2]
A_{pixel}	IR camera pixel area	[μm^2]
A_{TS}	Test section cross section area	[m^2]
α	Void fraction	[-]
α_l	Liquid thermal diffusivity	[$m^2 \cdot s^{-1}$]
α_s	Sapphire thermal diffusivity	[$m^2 \cdot s^{-1}$]
Bo	Boiling number $\frac{q''}{h_{lg}G}$	[-]
Bo_*	Modified boiling number $Bo^{-1}\left[1+x\left(\frac{\rho_l}{\rho_g}-1\right)\right]$	[-]
Co	Convection number defined at Eq. 2-10	[-]
Cp_l	Liquid specific heat	[$J \cdot kg^{-1} \cdot {}^oC^{-1}$]
Cp_s	Sapphire specific heat	[$J \cdot kg^{-1} \cdot {}^oC^{-1}$]
c	Molar concentration	[$mol \cdot L^{-1}$]
D_h	Hydraulic diameter	[m]
D_h^*	D_h/L	[-]
dt_{int}	IR camera integration time	[ms]
Δp_{ET}	Measured total pressure drop from the entrance channel inlet to the test assembly outlet	[bar]
$\Delta T_{le_{sat}}$	Local equivalent superheat, $T_{le}-T_{sat}$	[^oC]
ΔT_{sat}	Wall superheat, T_w-T_{sat}	[^oC]
ΔT_{sub}	Subcooling	[^oC]
δ	Liquid film thickness	[m]
E	Liquid entrainment rate	[-]
E_{ITO}	Emitted photon flux equivalent counts from ITO	[-]
E_{max}	Maximum achievable liquid entrainment rate defined at Eq. 2-16, 28, 29	[-]
e	Protonic charge	[-]
ε	Permittivity of the solution	[$F \cdot m^{-1}$]
ε_H	Eddy diffusivity of heat	[$m^2 \cdot s^{-1}$]
ε_M	Eddy diffusivity of momentum	[$m^2 \cdot s^{-1}$]
f_i	Interfacial friction coefficient	[-]
f_l	Liquid friction coefficient based on mean liquid velocity	[-]
f_m	Two-phase mixture friction coefficient	[-]

f_{sg}	Gas friction coefficient based on gas superficial velocity	[-]
G	Total mass flux	[kg·m^{-2}·s^{-1}]
G_g	Gas phase mass flux	[kg·m^{-2}·s^{-1}]
G_l	Liquid phase mass flux	[kg·m^{-2}·s^{-1}]
g	Gravitational acceleration	[m·s^{-2}]
h	General heat transfer coefficient	[W·m^{-2}· ^{o}C^{-1}]
h_{ce}	Convective evaporation heat transfer coefficient	[W·m^{-2}· ^{o}C^{-1}]
h_{in}	Liquid specific enthalpy at test assembly inlet	[J·kg^{-1}]
h_l	Saturated liquid specific enthalpy	[J·kg^{-1}]
h_{lg}	Specific latent heat	[J·kg^{-1}]
I_{amb}	Incoming photon flux equivalent counts from ambient	[-]
I_{lens}	Incoming photon flux equivalent counts from lens	[-]
j_g	Superficial gas velocity	[m·s^{-1}]
$j_{g_{cr}}$	Critical superficial gas velocity defined at Eq. 2-19	[m·s^{-1}]
j_g^*	Dimensionless gas superficial velocity defined at Eq. 4-2	[-]
j_l	Superficial liquid velocity	[m·s^{-1}]
K_e	Exit form loss coefficients of the test assembly	[-]
K_i	Inlet form loss coefficients of the test assembly	[-]
k_B	Boltzmann's constant	[J·K^{-1}]
k_g	Gas conductivity	[W·m^{-1}· ^{o}C^{-1}]
k_l	Liquid conductivity	[W·m^{-1}· ^{o}C^{-1}]
k_s	Sapphire conductivity	[W·m^{-1}· ^{o}C^{-1}]
L	Length	[m]
L_{ET}	Length from the entrance channel inlet to the test assembly outlet	[m]
L_{TS}	Length from the center of the test section to test assembly outlet	[m]
Λ	Equivalent conductivity defined at Eq. 4-4	[Ω^{-1}·cm^2·N^{-1}]
Λ_0	Infinite-dilute equivalent conductivity	[Ω^{-1}·cm^2·N^{-1}]
$\dot{m}$	Total mass flow rate	[kg·s^{-1}]
$\dot{m}_l$	Liquid phase mass flow rate	[kg·s^{-1}]
$\dot{m}_{lf}$	Liquid film mass flow rate	[kg·s^{-1}]
$\dot{m}_{lf_{cr}}$	Critical liquid film mass flow rate	[kg·s^{-1}]
μ_g	Gas phase viscosity	[Pa·s]
μ_l	Liquid phase viscosity	[Pa·s]

N	Normality of a solution, equivalent mass per liter	[N]
N_{bb}	Spectral integrated photon flux corresponding to the blackbody radiation (Planck's Law) from the ambient at room temperature	[$m^{-2} \cdot s^{-1}$]
N_{CB}	Convective boiling number defined at Eq. 2-11	[-]
Nu_{lc}	Nusselt number based on cavity radius, $\frac{hr_c}{k_l}$	[-]
$N_{\mu l}$	Liquid viscosity number defined at Eq. 2-18	[-]
N_{pch}	Phase-change number defined at Eq. 4-9	[-]
N_{sub}	Subcooling number defined at Eq. 4-8	[-]
n_f	Focal number of the lens	[-]
nc_{ew}	Camera counts corresponding to empty well	[-]
nc_{fw}	Camera counts corresponding to full well	[-]
O_{center}	Total outgoing photon flux equivalent counts from center ITO	[-]
O_{outer}	Total outgoing photon flux equivalent counts from outer ITO	[-]
p	General pressure	[bar]
Pr_l	Liquid Prandtl number	[-]
Pr_t	Turbulent Prandtl number defined at Eq. 7-31	[-]
P_w	Wetted perimeter	[m]
p_g	Gas phase pressure	[bar]
p_l	Liquid phase pressure	[bar]
p_{out}	Measured test section outlet pressure	[bar]
p_{sat}	Interpolated saturation pressure at specific elevation of test section	[bar]
ϕ_g^2	Two-phase pressure drop multiplier	[-]
π	Ratio of a circle's circumference to its diameter, 3.14159…	[-]
π_{Pallev}	Pi group defined at Eq. 2-14	[-]
π_{Wallis}	Pi group defined at Eq. 2-15	[-]
Q_{mes}	Volumetric flow rate measured from flow meter	[$m^3 \cdot s^{-1}$]
$\dot{q}$	Power	[W]
$\dot{q}_{loss}$	Total heat loss through test assembly	[W]
$\dot{q}_{tot}$	Total power input at tube-bundle boiler	[W]
q''	General heat flux	[$W \cdot m^{-2}$]
q''_w	Heating wall heat flux	[$W \cdot m^{-2}$]
Re_g, Re_{sg}	Gas phase Reynolds number $\frac{GxD_h}{\mu_l}$	[-]

RI_{amb}	Reflected incoming photon flux equivalent counts from ambient	[-]
RI_{lens}	Reflected incoming photon flux equivalent counts from lens	[-]
Re_l, Re_{sl}	Liquid phase Reynolds number defined on $\frac{G(1-x)D_h}{\mu_l}$	[-]
Re_{lf}	Liquid film Reynolds number $\frac{4\dot{m}_{lf}}{\pi D_h \mu_l}$	[-]
r_b	Minimum bubble radius that is determined by wettability of heating surface and size of cavity during the bubble growth	[m]
r_c	Nucleation cavity radius	[m]
ρ_g	Gas phase density	[kg·m^{-3}]
ρ_{gold}	Gold reflectivity	[-]
ρ_l	Liquid phase density	[kg·m^{-3}]
ρ_s	Sapphire density	[kg·m^{-3}]
$\bar{\rho}$	Mixture density of the gas core taking into account the entrained droplets	[kg·m^{-3}]
σ	Liquid-steam surface tension coefficient, or conductivity, referring to specific paragraph	[N·m^{-1}], [μS·cm^{-1}]
σ_{x_i}	Uncertainty of directly measured quantity	
σ_y	Total propagated uncertainty	
T	General temperature	[K]
T_{bulk}, T_b	Bulk liquid temperature	[^{o}C]
T_l	Liquid temperature	[^{o}C]
T_{le}	Local equivalent saturation temperature from Young-Laplace equation	[^{o}C]
T_{mes}	Local temperature measurement from RTD	[^{o}C]
T_{ml}	Temperature at the outer edge of momentum laminar boundary layer	[^{o}C]
T_{tl}	Temperature at the outer edge of thermal laminar boundary layer	[^{o}C]
T_s	Sapphire temperature	[^{o}C]
T_{sat}	Saturation temperature	[^{o}C]
T_w	Wall temperature	[^{o}C]
T^+	Dimensionless temperature defined at Eq. 2-7	[-]
t	Time	[s]
τ_i	Interfacial shear stress at liquid-steam interface	[Pa]
τ_w	Wall shear stress	[Pa]
u^*	Wall shear velocity defined at Eq. 2-8	[m·s^{-1}]
v_g	Mean gas core velocity	[m·s^{-1}]

v_l	Mean liquid core velocity	[m·s^{-1}]
v_{lg}	Specific volume difference between saturated liquid and vapor	[m^3·kg^{-1}]
v_{sg}	Superficial gas velocity	[m·s^{-1}]
v_{sl}	Superficial liquid velocity	[m·s^{-1}]
We	Weber number $\frac{\rho_g j_g^2 D_h}{\sigma}\left(\frac{\rho_l-\rho_g}{\rho_g}\right)^{1/3}$	[-]
We_{cr}	Critical Weber number defined at Eq. 2-17	[-]
W_e	Total number of the electron well for each pixel of IR camera	[-]
X_{tt}	Lockhart–Martinelli number $\left(\frac{1-x}{x}\right)^{0.9}\left(\frac{\rho_g}{\rho_l}\right)^{0.5}$	[-]
x	General steam quality, or axis name, referring to specific paragraph	[-], [m]
x_e	Equilibrium steam quality	[-]
y	Wall normal distance	[m]
y_{top}	Location at the bubble apex	[m]
y^+	Dimensionless wall normal distance defined at Eq. 2-9	[-]
z	Valency of the ion in Section 4.4.5, otherwise flow direction	[-],[m]

1. Introduction

1.1. Motivation

In a BWR, heat is transferred from the fuel rod to the coolant, leading to phase change in the subchannels of the assembly. As steam quality increases, the coolant flow eventually transitions to the two-phase annular regime before exiting the fuel assembly [1] as illustrated in Figure 1-1. At low and intermediate steam qualities, typical of bubbly and slug/churn flow regimes, nucleate boiling is the dominant heat transfer mechanism. After the flow regime transitions to annular flow at higher steam qualities, nucleate boiling may be suppressed and replaced by forced convective evaporation. This transition process, also called suppression of nucleate boiling (SNB) (its reverse process is called onset of nucleate boiling), affects the local heat transfer coefficient, the stability of the liquid film, as well as the entrainment dynamics [2]. Thorough understanding of the thermohydraulic mechanisms and an accurate prediction of the corresponding transition conditions for SNB in annular two-phase flow are required to advance the BWR performance towards higher power density and enhanced safety.

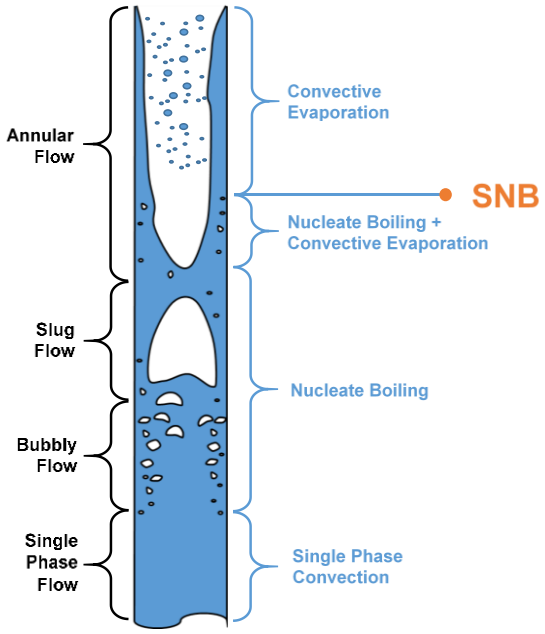

Figure 1-1: *Flow regimes and corresponding heat transfer modes in a typical boiling channel. Nucleate boiling is the dominant heat transfer mode in bubbly flow and slug/churn flow regimes. Convective evaporation dominates in annular flow. The condition under which nucleate boiling is entirely suppressed in the transition region is SNB.*

Independently, boiling heat transfer and annular two-phase flow dynamics have received extensive attention and been widely studied for decades: numerous mechanistic models and empirical correlations have been developed to predict the thermal behavior under various flow conditions [3]. However, the combined process of nucleate boiling in annular flow is scarcely studied, due to the difficulties of establishing stable steam-water annular flow, while simultaneously generating nucleate boiling at such condition. Moreover, the measurement techniques for this unique thermohydraulic process are also lagging behind. The limited knowledge of the local characteristics, e.g. liquid film thickness, interfacial wave properties and local distribution of thermal parameters, leads to large uncertainties in prediction of heat and mass transfer in two-phase annular flow, which further prevents a solid understanding of the SNB transition in annular flow. Nevertheless, it is exactly the big gap in such area that makes this topic intriguing and the present study valuable.

1.2. Objectives

The objective of this work is to conduct a first of a kind local investigation of the SNB conditions in steam-water upward two-phase annular flow. The experimental database can help to generate insightful knowledge of the heat transfer processes and flow dynamics in annular flow. The novel experimental observations may also inspire more comprehensive mechanistic models for annular flow associated phenomena.

An innovative diagnostics combining synchronized infrared thermography and an electrical conductance-based liquid film thickness sensor was developed to investigate the close-up details of the SNB phenomena, as well as heat and mass transfer in annular flow. The experimental tests were conducted at atmospheric pressure with the main control parameters of mass flux from 700 to 1400 $kg \cdot m^{-2} \cdot s^{-1}$, steam quality from 0.01 to 0.08, and heat flux from 100 to 2000 $kW \cdot m^{-2}$. At each set of conditions, the local distributions of 2D surface temperature, 2D heat flux, and quasi-2D liquid film thickness were measured, from which the SNB heat flux and wall superheat were extracted, as well as the hydrodynamic properties of the disturbance waves. A first of a kind 1D mechanistic model was developed for accurately capturing the unique transient effect of the disturbance waves on SNB conditions and local heat transfer. Also, a complete set of semi-empirical correlations was proposed for predicting the time-averaged values of film thickness and SNB conditions in nuclear reactor system codes such as RELAP.

2. Background and Previous Research

In this chapter, an introduction of previous studies on flow patterns, suppression of nucleate boiling in annular flow, liquid film thickness measuring methods and correlations, and liquid entrainment rate predictions, is presented.

2.1. Flow Patterns (Flow Regimes)

In multiphase flow, the specific geometry or topology of each phase are often referred to as flow patterns or flow regimes. In the situation of interest in nuclear reactors, such topology refers to the liquid and steam phases. The two-way coupling of the global topology of multiphase and the local thermo-hydrodynamics of each phase component determines the appearance or the disappearance of specific phenomena. Consider the upward flow of subcooled water entering a typical subchannel in a BWR, where water is heated by the surrounding fuel rods, similar to a uniformly heated tube shown in Figure 1-1. Due to the heat addition, the flow regime experiences successively single phase flow, bubbly flow, slug/churn flow and annular flow in the flow direction, as steam quality increases. In annular flow, the steam phase merges completely into a continuous steam core in the center of the channel while the liquid phase still exists as a continuous annulus along the fuel rod surface. The steam core may contain droplets entrained from the liquid film.

A flow regime map, which is typically illustrated on a superficial liquid velocity j_l versus superficial gas velocity j_g diagram, is commonly used to identify the various flow regimes. Different correlations of $j_l = f(j_g)$ were proposed for defining the boundary between two adjacent regions on the flow regime map [1]. The most widely used criteria for annular flow in nuclear system, featuring relatively small subchannel diameters, were developed by Wallis (based on flow reversal mechanism, Equation 2-1) [4] and Taitel et. al. (based on droplet suspending mechanism, Equation 2-2) [5] respectively:

$$j_g > 0.9\left[\frac{g(\rho_l - \rho_g)D_h}{\rho_g}\right]^{0.5} \tag{2-1}$$

$$j_g > 3.1 \frac{\left[g\sigma(\rho_l - \rho_g)D_h\right]^{0.25}}{\rho_g^{0.5}} \tag{2-2}$$

where $\rho_l, \rho_g, \sigma, D_h, g$ are liquid density, steam density, liquid-steam surface tension coefficient, channel hydraulic diameter, and gravitational acceleration, respectively. Based on Taitel et. al.'s work, Barnea proposed a stricter criterion by considering the following two possible blockage mechanisms of liquid in steam core: a) instability of the liquid film due to localized partial downward flow; b) transient large supply of liquid in the film (equivalent to very tall surface wave) [6]. Ansari et. al. further modified Barnea's criteria by taking into account the effect of entrainment as j_g increases [7]. Due to the complexity and the implicit nature of Barnea-Ansari et. al.'s criteria, the set of equations and solving procedure are not presented here. The expected test range is plotted on the following flow map together with various authors' criteria for annular flow. As shown in Figure 2-1, even with the strictest criterion, most of the expected test range for our experiments still falls into the annular region. The plot also suggests that the lowest steam quality (x_e) to ensure annular flow is around 0.016.

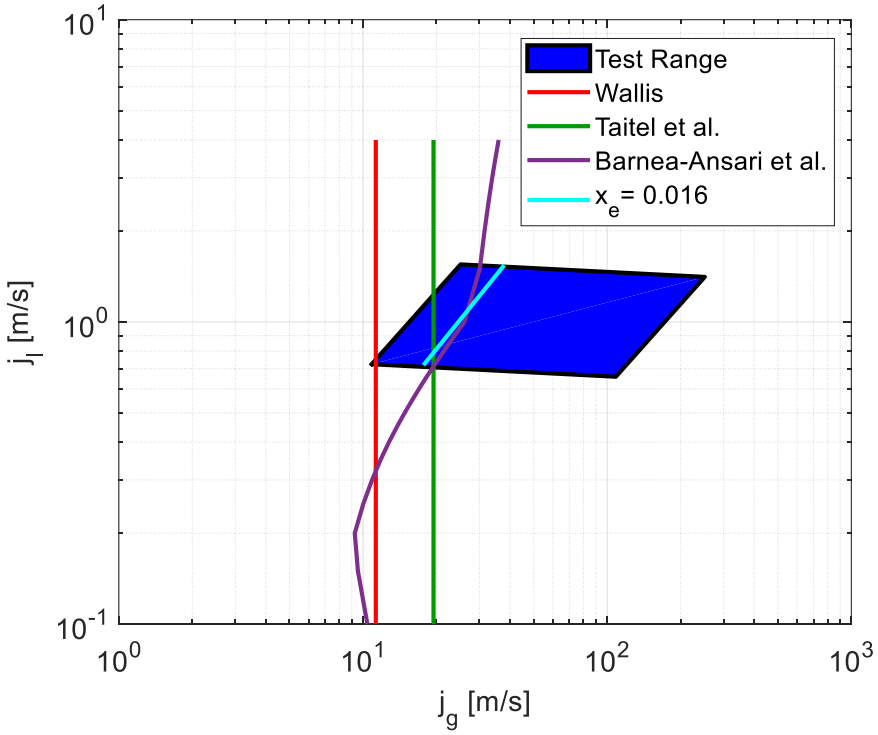

***Figure 2-1**: The expected test range in comparison with various authors' criteria for annular flow. Most of the expected test range falls into the annular region, while a small section is located in the slug-annular transition region.*

2.2. Suppression of Nucleate Boiling in Annular Flow

As the liquid film thins quickly in annular flow, ranging from millimeter to micron scale, the thermal resistance across the liquid film decreases accordingly, and therefore forced convective evaporation enhances the heat transfer in the thin liquid film. At a specific film thickness, forced convective evaporation can be so efficient that the wall superheat becomes too low to support nucleate boiling on the heated surface. However, if the heat flux increases or the mass flux decreases due to abnormal or accident conditions, e.g. reactor transients or loss of flow accidents, the wall temperature may rise sufficiently to again trigger bubble nucleation. After the reappearance of the bubble nucleation, the heat transfer coefficient may be enhanced, while the interaction between bubbles and the thin liquid film may lead to higher droplet entrainment because of bubbles bursting through the film or the breaking up of the liquid thin film. The conditions for SNB in annular flow are the focus of present study. [1] [3] [8]

As discussed above, two basic mechanisms are involved in the SNB process. On one hand, we have the requirements for occurrence of bubble nucleation. On the other hand, we have the forced convective heat transfer across the liquid film, and the evaporation process at the film surface, which determine the temperature distribution and the heat flux transported. The conditions at which SNB occurs result from the combined effects of the above mentioned mechanisms. Eventually, the SNB problem breaks down into the interrogation and quantification of those two mechanisms.

In heterogeneous boiling, bubbles are usually generated from cavities existing on the heating surface. One of the most widely used models to estimate the thermal requirements for bubble nucleation in heterogeneous condition is the so-called Hsu's model [9]. Hsu's model postulates that the bubble can grow out of the nucleation site if the saturation temperature corresponding to the internal pressure of the incipient bubble (or steam embryo) is reached or exceeded all over its surface (normally limited by the top of the bubble):

$$T_l(y_{top}) \geq T_{le}(y_{top}) \tag{2-3}$$

where T is the temperature profile; y is the distance away from the heating surface. Subscript l denotes liquid; le denotes local equivalent saturation condition; top denotes the bubble apex; sat denotes the saturation condition. The Hsu's model is shown diagrammatically in Figure 2-2.

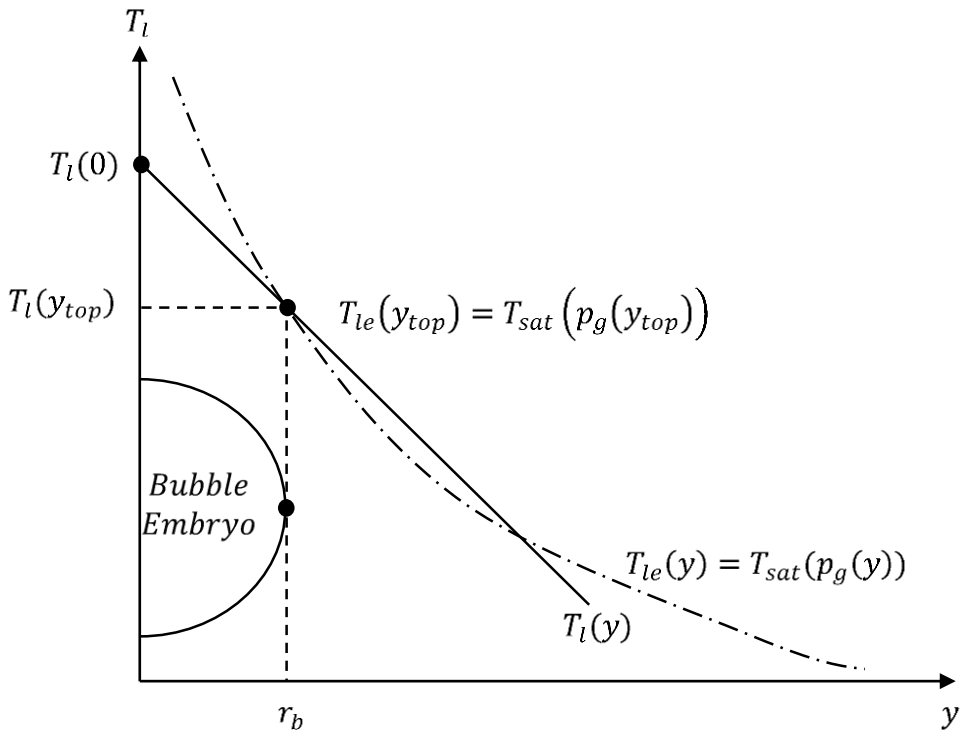

***Figure 2-2**: Hsu's criterion for bubble nucleation. The liquid temperature at the top of the bubble embryo $T_l(y_{top})$ needs to equal to or exceed the local saturation temperature $T_{le}(y_{top})$ that is determined by the internal gas pressure p_g.*

The nucleation at a certain cavity, with radius r_c, occurs when the actual liquid temperature profile $T_l(y)$ has the first intersection point with the local equivalent saturation temperature profile. The local saturation temperature profile can be obtained by the combination of Young-Laplace equation and linearized Clausius-Clapeyron equation [3] (more accurately either the integration of Clausius-Clapeyron equation, or a steam table):

$$\begin{cases} p_g - p_l = \dfrac{2\sigma}{r_b} \\ \dfrac{p_g - p_l}{T_{le} - T_{sat}} = \dfrac{h_{lg}\rho_g}{T_{sat}} \end{cases} \quad \rightarrow \quad T_{le}(y) = T_{sat}(p_l)\left(1 + \frac{2\sigma}{h_{lg} r_b \rho_g}\right) \tag{2-4}$$

where r_b is the minimum bubble radius that is determined by wettability of heating surface and size of cavity during the bubble growth; σ is the surface tension of liquid; h_{lg} is the latent heat; T_{sat} is the saturation temperature based on liquid pressure p_l. Only the cavities that are capable of trapping steam can potentially be nucleation sites on a heating surface. The capability for a cavity to trap steam depends on the geometry of the cavity and the wettability of the liquid on the heating

surface. In general, the advancing front of the liquid needs to touch all sides of the cavity before it wets the bottom of the cavity (refer to [3] for more detailed description). r_b can be related to y or r_c according to the surface condition. On a hydrophilic surface, such as metal fuel cladding and the indium tin oxide (ITO) heater used in present study, r_b equals to r_c.

The application of Hsu's model requires the temperature profile $T_l(y)$ in water, which is determined by the forced convective evaporation heat transfer between the heated wall (T_w) and bulk water flow (T_{bulk}). In analogy with single-phase convective heat transfer, force convective evaporation is also expressed by Newton's law of cooling with an equivalent heat transfer coefficient (h_{ce}):

$$q'' = h_{ce}(T_w - T_{bulk}) \tag{2-5}$$

In the present proposed study, heat flux will be controlled during the experiments, hence the temperature difference will vary with the heat transfer coefficient. As introduced in Section 1.2, the heated wall temperature will be measured by IR thermography, the bulk temperature, which should ideally be the saturation temperature, will be measured by inserted TC or RTD. Eventually, the heat transfer coefficient can be calculated by Newton's law of cooling. With the heat flux, the heated wall temperature, the bulk temperature and the liquid film thickness measured by LFS as boundary-condition inputs, the temperature distribution within the liquid film can be calculated by models. One of the approaches uses the analogy of heat transfer with the turbulent momentum transfer [1]:

$$1 = \left(\frac{1}{Pr_l} + \frac{\varepsilon_H}{\mu_l/\rho_l}\right)\frac{dT^+}{dy^+} \tag{2-6}$$

where

$$T^+ = \frac{Cp_l\rho_l u^*}{q''}\left[T_w - T(y)\right] \tag{2-7}$$

$$u^* = \sqrt{\frac{\tau_w}{\rho_l}} \tag{2-8}$$

$$y^+ = \frac{u^* y \rho_l}{\mu_l} \tag{2-9}$$

where Cp is the specific heat, τ_w is the wall shear stress, ε_H is the eddy diffusivity of heat. Equation 2-6 can be integrated from $T^+ = 0\ at\ y^+ = 0$ to $T^+ = T^+(\delta)\ at\ y^+ = y^+(\delta)$, assuming

that the heat and momentum eddy diffusivities are equal and applying an appropriate expression of ε as a function of y^+.

The above approach is only applicable when the thermohydraulic steady state is reached in both the liquid film and the heater. If the passage of the disturbance waves impacts the local heat transfer significantly, the time-dependent local temperature profile may be such that the bubble nucleation criterion is satisfied and thus intermittent bursts of bubbles occur, which makes the prediction of SNB very challenging.

There is currently no specific research available on the SNB in annular flow. Only a few papers on convective boiling had some discussion of it.

In 1980s, Kandlikar [10][11] developed a simple correlation for predicting saturated flow boiling heat transfer coefficients of water in both horizontal and vertical tubes based on a database of 1100 data points covering the range: pressure 1.1-64.2 bar, mass flux 67-8179 $kg \cdot m^{-2} \cdot s^{-1}$, vapor quality 0.001-0.699, channel diameters 5-32 mm and heat flux 4.7-2280 $kW \cdot m^{-2}$. The simple correlation was later extended to ten different fluids based on 5246 data points. A dimensionless "convection number" (see Equation 2-10) was proposed for the identification of the transition from nucleate boiling dominated heat transfer to forced convective evaporation dominated heat transfer, which could be tenuously interpreted as a criterion for the SNB in annular two-phase flow. SNB is expected to occur in water when the convection number reaches a critical value of 0.65. Kandlikar was interested in developing a heat transfer correlation, not specifically identifying the conditions for complete suppression of nucleate boiling.

$$Co = \left(\frac{1-x}{x}\right)^{0.8} \left(\frac{\rho_g}{\rho_l}\right)^{0.5} \tag{2-10}$$

Similarly, Klimenko [12] suggested a generalized correlation for two-phase forced flow heat transfer in both vertical and horizontal channel flow, based on the experimental data of nine different fluids (including water) at a wide range of flow parameters: pressure 0.61-30.4 bar, mass flux 50-2690 $kg \cdot m^{-2} \cdot s^{-1}$, vapor quality 0.017-1, channel diameters 1.63-41.3 mm. The transition from nucleate boiling to forced convective evaporation is expected to happen when the mass flux is sufficiently high and the film thickness is sufficiently small. Based on this assumption, a dimensionless "convective boiling number" (different from the "convection number" by

Kandlikar) was recommended to determine the transition (see Equation 2-11), where G is mass flux, g is gravitational acceleration, q'' is heat flux, and h_{lg} is latent heat). The convective boiling number was derived from the conventional boiling number for identifying the two-phase flow heat transfer regime. A critical value of 1.6×10^4 was suggested for the transition to forced convective evaporation heat transfer regime. The same caveat for Kandlikar's criterion applies here. The suggested critical convective boiling number was not determined from direct measurement of SNB, but rather a central value of a fairly broad transition region between forced convective evaporation and nucleate boiling.

$$N_{CB} = Bo_* \left(\frac{\rho_g}{\rho_l}\right)^{1/3} \tag{2-11}$$

Where $Bo_* = Bo^{-1}\left[1 + x\left(\frac{\rho_l}{\rho_g} - 1\right)\right]$, $Bo = \frac{q''}{h_{lg}G}$.

More recently in 2002, Barbosa et al. [13] conducted forced convective boiling experiments of water in an annulus test section with equivalent diameter of 12.9 mm. The purpose of the investigation was to study the forced convective boiling heat transfer coefficients in annular flow. The test conditions varied over a test matrix of pressure 1.28-1.56 bar, mass flux 23.6-43.3 $kg{\cdot}m^{-2}{\cdot}s^{-1}$, inlet quality 0.48-0.79 and heat flux 9.3-326.9 $kW{\cdot}m^{-2}$. High speed video was utilized to interrogate the topology of the liquid film, the occurrence of nucleate boiling in the liquid film, and the droplet entrainment and deposition. The occurrence of nucleate boiling was observed at sufficiently high heat fluxes. Correspondingly, the heat transfer coefficient increased slightly. No criterion for nucleate boiling suppression was proposed.

In summary, there is a lack of specific studies on the local heat transfer and flow conditions, which lead to SNB in annular two-phase flow. The existing empirical models are insufficient to provide accurate local prediction. The present study is devoted to the first of a kind rigorous identification of SNB along with local measurement of annular flow parameters, such as 2D heated surface temperature profile, quasi-2D film thickness profile and surface wave propagation. With the new database, interrogation of the local and global heat transfer mechanisms and flow dynamics related to SNB will be possible.

2.3. Liquid Film Thickness

In annular flow, the liquid film thickness is a key boundary condition for the instantaneous temperature distribution across the liquid film and hence the heat flux transferred, which eventually determines the SNB. In addition, the surface wave propagation may also create oscillations of the heating wall temperature, as well as entrainment of liquid droplets, thus affecting the time-dependent variation of the heat transfer coefficient.

2.3.1. Measuring Techniques

Much effort has been made for measuring the film thickness in the past decades. Various techniques were developed based on different working principles: some are intrusive, some are non-intrusive.

The most widely used and most mature intrusive technique for measuring film thickness and two-phase flow cross section morphology is the wire-mesh sensor. The idea of using arrays of wire-mesh to measure the volumetric fraction of water in crude oil pipeline was first introduced by Johnson [14]. Many researchers tried to apply this concept in later investigations of two-phase flow. The most successful configuration was developed by Prasser as shown in Figure 2-3 [15]. One array of parallel wires behaves as transmitter electrodes, while the other array of parallel wires behaves as receiver electrodes in the direction perpendicular to the transmitting wires. When an exciting voltage pulse is applied to the transmitter wire, the receiver wires will receive a current at the crossing point from the transmitter wire. The received current depends on the media passing through the crossing point, e.g. low current for a gas and high current for a liquid. This configuration can measure the 2D phase distribution across the flow, and hence the liquid film thickness at the wall with sampling rate up to 10,000 Hz. The biggest drawbacks of this method are the disruption to the liquid film and the limited spatial resolution in the film thickness direction (3 mm resolution at 16×16 wire-mesh) [16][17]. Prasser's sensor design was motivated by the desire to measure the phase distribution in relatively large tubes (larger than 4 cm in diameter), for which that resolution is sufficient. However, the wire-mesh sensor approach is not suitable for the present study (or any reactor core subchannel application) since the estimated film thickness is much less than 3 mm.

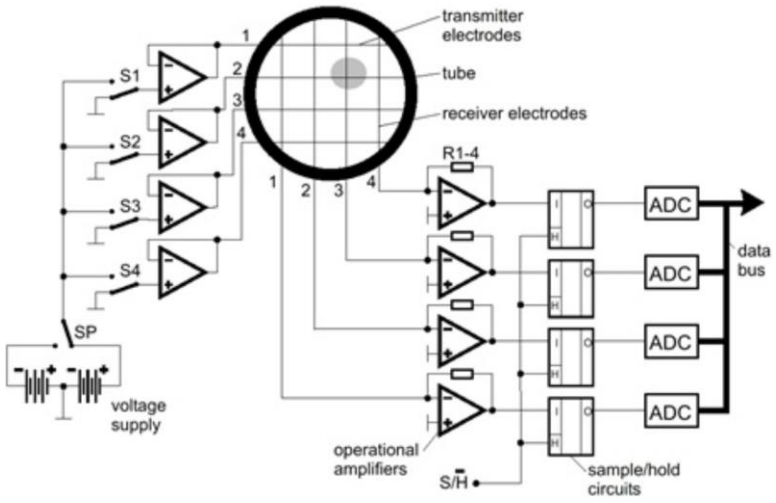

***Figure 2-3**: Block diagram illustrating the working principle of a 4×4 wire-mesh system. Plus/minus voltage pulses are imposed to transmitter wires. Currents are received at receiver wires through the crossing points with the transmitter [15].*

Among the non-intrusive techniques, the optical methods are the most common. Researchers had tried various illumination systems coupled with video cameras, in order to look inside the water thin film. Schubring [18] used Planar Laser Induced Fluorescence to visualize a specific lateral cross section of the liquid film, as shown in Figure 2-4 left. The liquid film was identified by the spectrally filtered contrast image recorded by a CCD camera. Pan [19] applied a similar method using LED light shadowgraphy with high speed camera, as shown in Figure 2-4 right. These two optical methods are ideal for the measurement of a smooth liquid-gas interface, due to the relatively easy setup and post-processing. However, they are of limited value when the interface is the wavy and highly disturbed, as is always the case in annular flow, especially when a wave trough blocks the light path between the measuring point and camera, as shown in Figure 2-5. As a result, these two methods could underestimate the actual film thickness. Besides this blocking effect, the viewing distortion is another significant drawback when the optical path traverses multiple curved liquid-steam interfaces. An illustrative example of image distortion caused by curved interfaces is shown in this video [20], in which a right-pointing arrow can appear as a left-pointing arrow, and a forward slash can become a backward slash.

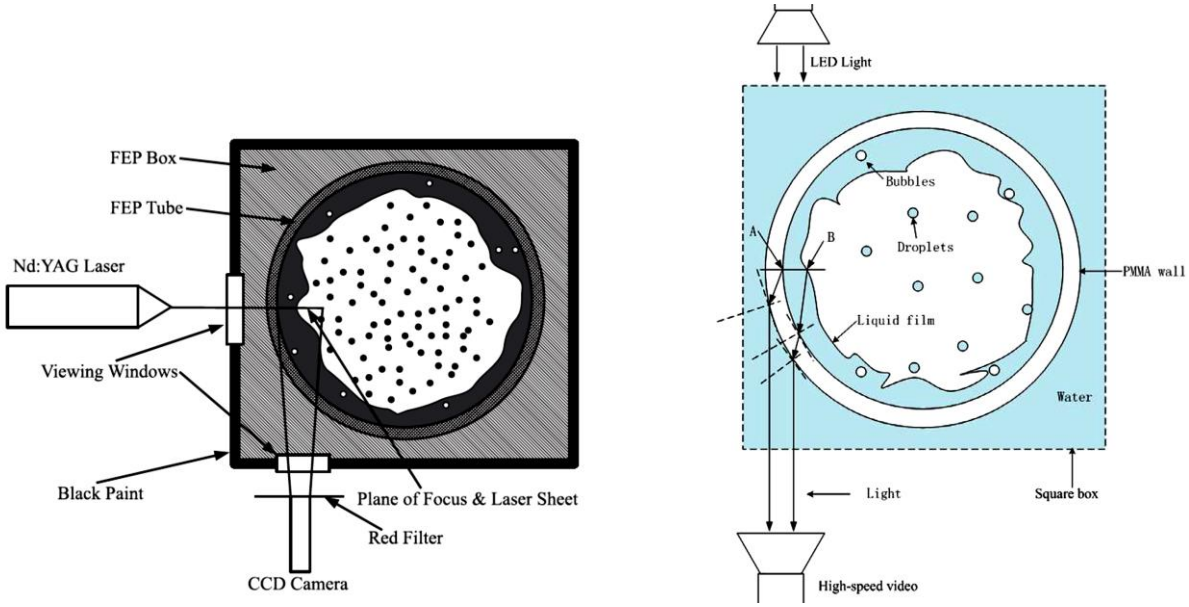

***Figure 2-4**: Schubring's PLIF method (left) [18] versus Pan's shadowgraphy (right) [19].*

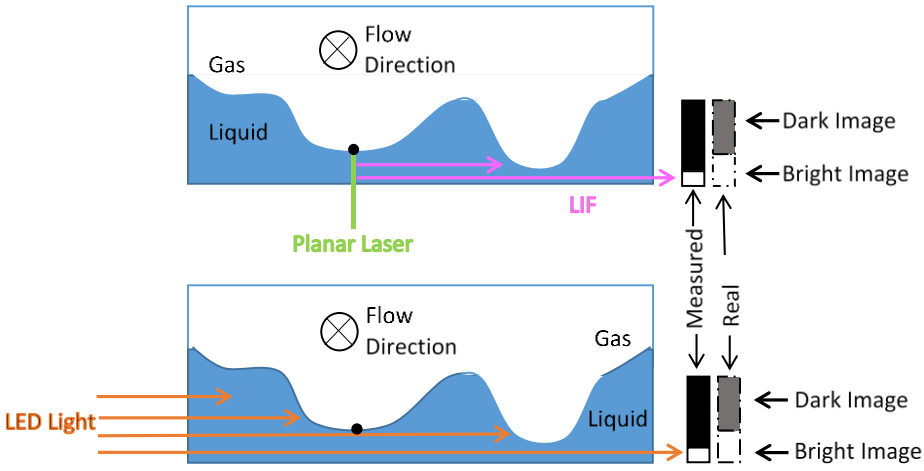

***Figure 2-5**: Illustration of the drawbacks of the typical optical methods. The wave trough between the measuring point and the camera distorts the contrast image.*

With the development of printed circuit board and surface engineering, novel surface-mounted electric conductance-based sensors have been developed in Prasser's group at ETH Zurich [21]. These sensors have unique strengths, as they allow for non-intrusive measurement of liquid film thickness ranging from a few microns up to several millimeters with ~10 kHz sampling rate, which covers the expected liquid film thickness, and is sufficient for detecting the propagation of the surface waves [22][23][24]. The spacing between two neighboring

sensors can be as small as 0.2 mm, which enables a high spatial resolution 2D mapping of the liquid film. An example configuration of the surface-mounted sensor is shown in Figure 2-6 [24].

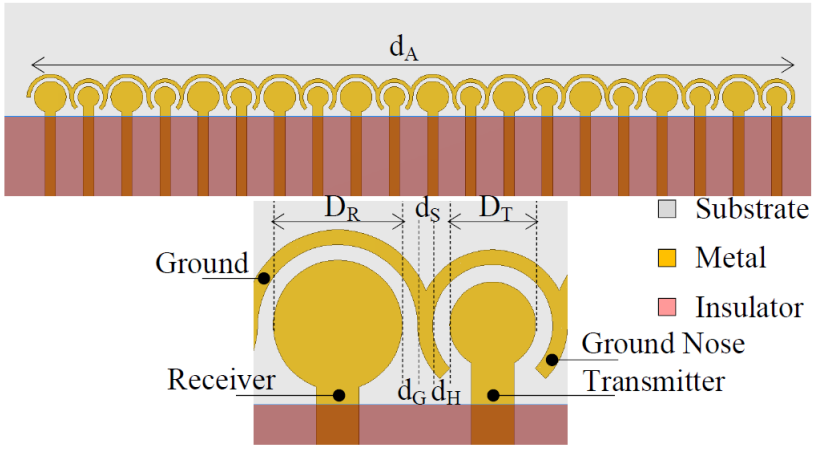

***Figure 2-6**: An example configuration of the surface-mounted sensor. The top picture shows an array of 10 sensor pairs providing 10 measuring points. The bottom picture shows the enlarged view of a sensor pair. d_A=5 mm, D_R=0.15 mm, d_G=0.045 mm, d_S=0.035 mm, d_H=0.025 mm, D_T=0.1 mm. [24]*

Given the attractive features of these novel surface-mounted sensors over earlier techniques, we decided to collaborate with Prasser's group at ETH Zurich to jointly develop a special liquid film sensor (LFS), which would fit best the conditions of the present study.

2.3.2. Hydrodynamic Mechanisms and Prediction Models

The topic of liquid film thickness in annular flow has been intensively studied for decades both experimentally and analytically. Many empirical correlations have been proposed based on the existing data sets. Unfortunately, almost all the experiments were conducted with air-water two-phase system at room temperature [19][25][26][27][28], which is neither typical for the steam-water system in BWRs (normal or accident conditions), nor for the present study. At elevated temperature with the existence of phase change, the characteristics of the liquid film may differ from those achieved from air-water system, due to the differences in fluid properties and phase interaction. Despite the discrepancies, previous models can still be used for understanding the physics and providing a bounding value of the liquid film thickness under the expected range of the present study. Since different researchers carried out studies under different ranges of boundary conditions, some overlap with the expected test range of present study while others do

not, only the more mechanistic approaches that can be reasonably extrapolated are of interest to the present review.

In early investigations (1970), a simple estimation of the liquid film thickness was to assume no liquid entrainment in the vapor, so that the film thickness was related to the void fraction by the following approximate equation [2]:

$$\delta P_w \approx (1-\alpha)A \tag{2-12}$$

Where α is the void fraction, δ is the film thickness and A is the total flow area, and P_w is wetted perimeter. Using D_h of a flow channel, the above equation can be reorganized as:

$$\delta \approx \frac{(1-\alpha)D_h}{4} \tag{2-13}$$

With an appropriate estimation of void fraction, e.g. Lockhart-Martinelli or Dix correlations [3], the film thickness can be evaluated. Many researchers also tried to fit empirical correlations to their experimental databases [29][30][31][32][33]. Normally, the film thickness was correlated with the Reynolds numbers or/and Froude numbers which were defined in terms of the mass fluxes of liquid (G_l) or/and gas (G_g). The predictions of film thickness in the expected range of our test matrix (mass flux 750-1500 kg·m^{-2}·s^{-1}, inlet quality 0.01-0.1) by several relevant correlations are plotted in Figure 2-7. In the plot, the abbreviations represent the names of the authors: LM-Lockhart-Martinelli, Dix-Dix, Hori-Hori, Hens-Henstock, Fuka-Fukano, Mac-MacGillivray, Bern-Berna. As we can see, the predicted film thickness at our test conditions generally ranges between 2 mm and tens of microns.

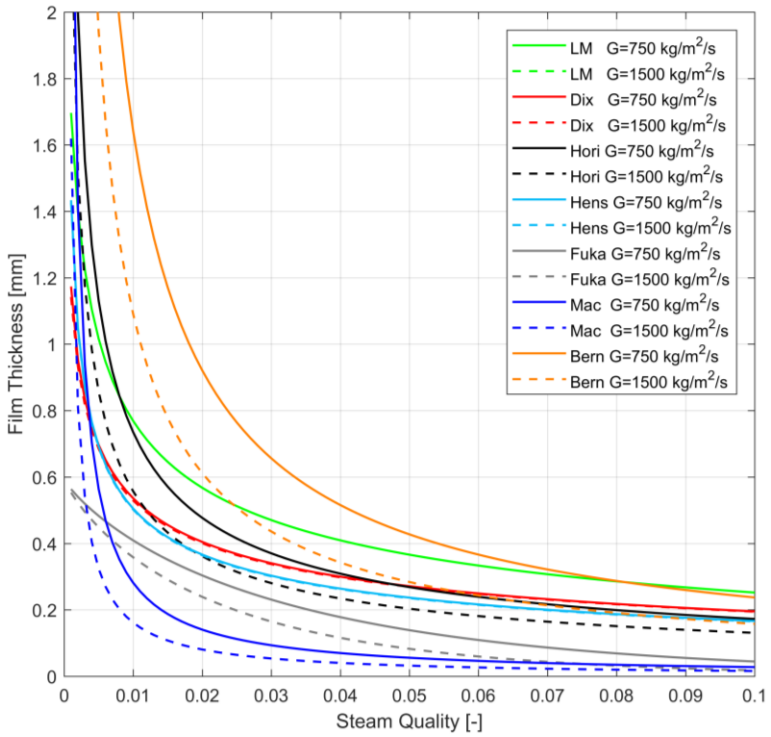

***Figure 2-7**: Film thickness predicted by multi-authors' correlations at mass flux 750 and 1500 kg·m^{-2}·s^{-1}, inlet quality below 0.1*

All the predictions of film thickness shown in Figure 2-7 represent the time-averaged film thickness. However, the liquid film in annular flow is not stationary, and in fact it presents surface waves with amplitudes that significantly deviate from the average film thickness. Such temporal variation of the film thickness could change the temperature profile in the liquid film, hence the SNB conditions would be affected as well.

In general, there are two types of waves in annular flow. One is called "ripple waves", which are low amplitude waves (order of the mean film thickness) at the interface; this is the only type that exists at low flow rates. At higher flow rates, there is another type, the "disturbance waves", which have a large amplitude (several times the mean film thickness). For example, Hewitt found that disturbance wave amplitudes were always ~5 times the mean film thickness in his experiments [34]. At the high mass flux conditions typical of nuclear reactors, the effect of disturbance waves is more pronounced than that of the ripple waves.

Several parameters are often used to characterize a disturbance wave, i.e., the wave amplitude, the wave width, the wave frequency and the wave velocity. The absolute amplitude of

disturbance waves decreases with increasing gas superficial velocity and so does the film thickness. Sawant (2008) [35] performed experiments measuring film thickness, including disturbance waves, in channel with hydraulic diameter of 9.8 mm (similar to our expected channel). An example plot is shown in Figure 2-8. Zhao (2013) et. al [36] showed that disturbance waves become more pronounced as annular flow reaches its fully developed state. Their measurements showed that disturbance wave magnitudes varied between 2-4 times of the mean film thickness. However, their measurements were likely biased low due to averaging of the film thickness over the probes measurement area. Han et. al (2006) [37] measured several wave characteristics including wave width in a 9.525 mm diameter tube. They found that the wave height decreased with both increasing gas and liquid velocities. Over their narrow range of mass fluxes (G_l=100-200 kg·m^{-2}·s^{-1}, G_g =18−47 kg·m^{-2}·s^{-1}) the wave widths were found (full width at wave minimum) to range from 10-50 mm (see Figure 2-9). In summary, the disturbance wave heights are ~4 times the film thickness and have a width of 10-50 mm. The wave speed is estimated between 2 and 10 m.s^{-1} with a frequency in the range from 15 to 50 Hz.

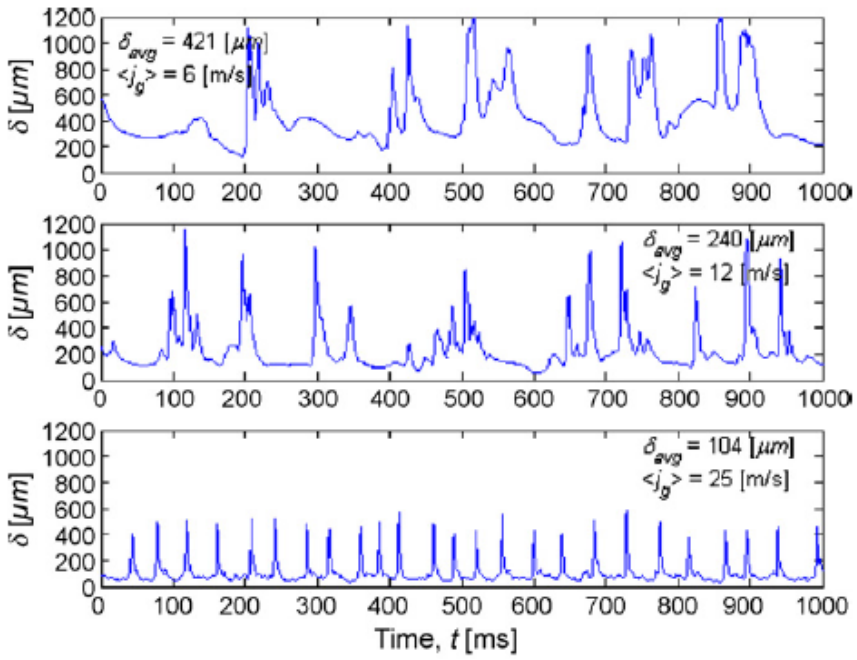

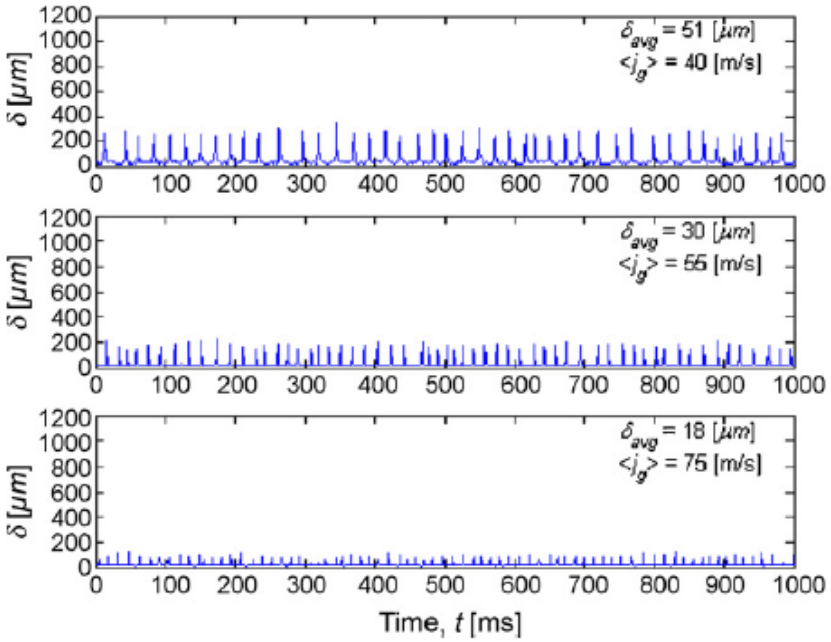

***Figure 2-8**: Disturbance wave magnitudes from [35] for Re_l =950, and P =1.2 bar. Both the average film thickness and the disturbance wave amplitude decrease with increasing gas superficial velocity.*

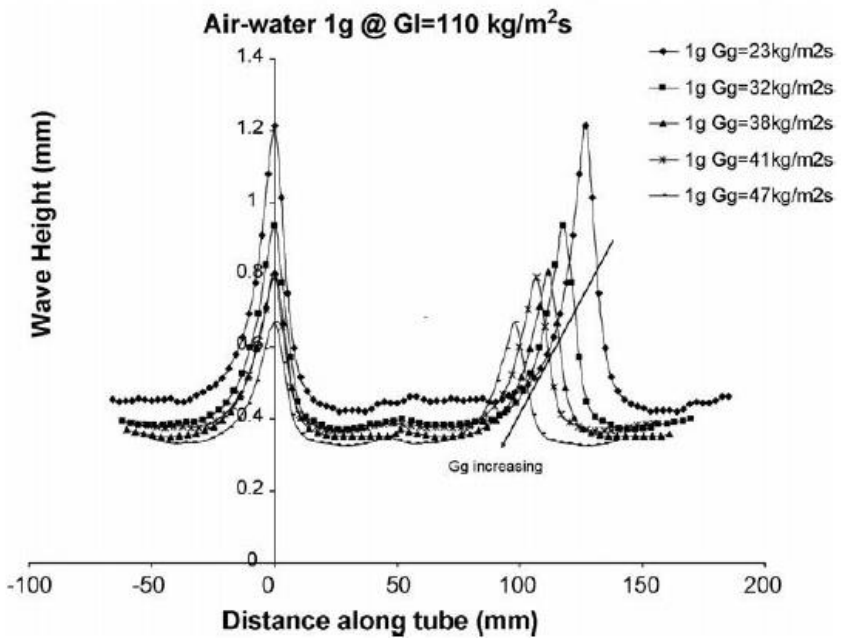

***Figure 2-9**: The typical disturbance wave shape (amplitude, width) versus gas mass flux from [37]. Both the amplitude and the width of the disturbance wave decrease with the increasing gas mass flux.*

The wave velocity for the conditions of interest to our experiments was estimated based on the correlation by Pearce [38]. The wave frequency is bound to nearly a single order of magnitude between 3 and 30 Hz [38][39]. A typical value of 15 Hz was used to estimate the magnitude of the wavelength. Figure 2-10 shows the wavelength and wave velocity.

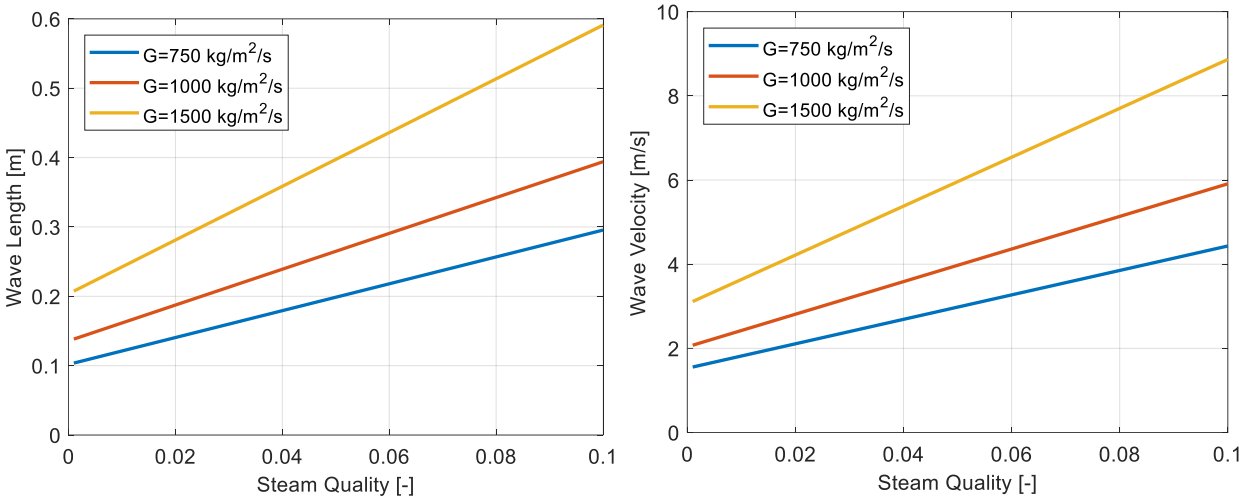

***Figure 2-10**: The estimated wavelength (left) and wave velocity (right) by Pearce's correlation. Both wavelength and wave velocity increases with increasing steam quality and total mass flux.*

2.4. Liquid Entrainment

Liquid entrainment is a unique phenomenon in annular flow, which is caused by the velocity difference between the gas core and the liquid film. When the velocity difference is small, a smooth interface can be formed. As the velocity difference increases, the gas phase creates a shear stress/drag which may accumulate liquid, thus generating surface waves traveling faster than the bulk of the liquid film. Since a balance is still maintained among momentum flow, drag/shear force, surface tension and gravity, the liquid phase can remain continuous. However, at sufficiently high velocity difference, the deformation of the liquid film is so severe (typically tall disturbance waves) that droplets are torn off from the liquid film. The process of the gas core tearing liquid droplets off the liquid film is one major mechanism of liquid entrainment in annular flow [40]. It is obvious that the liquid entrainment process directly impacts the characteristics of the liquid film and thus SNB, since the gas core transports momentum to the surface waves, tears off mass from the liquid film, and limits the height of the surface waves. The correct understanding of the

entrainment mechanisms and an accurate estimate of the entrainment rate are of crucial importance.

In concurrent annular flow, there are generally four types of entrainment mechanisms as shown in Figure 2-11 [2][33][40]: A) roll wave, B) wave undercut, C) bubble bursting, and D) liquid impingement. According to the experimental observation from Hall-Taylor et al [41], and Woodmansee [42], the dominant mechanism of liquid entrainment for low viscosity liquid (such as water) is roll wave. The entrained droplets are teared off from the tip of the large amplitude roll waves (also known as disturbance wave) by the gas core [43].

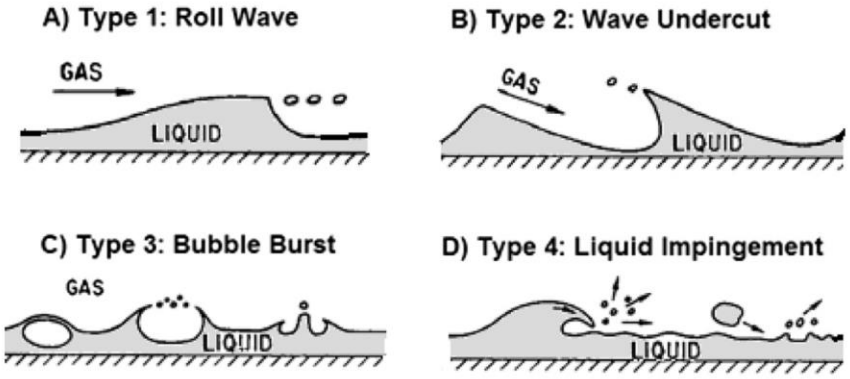

***Figure 2-11**: Liquid entrainment mechanisms in concurrent flow. Roll wave is found to be the dominant mechanism for low viscosity liquid, like water. [2]*

Based on the widely accepted entrainment mechanism introduced above, many models and correlations have been proposed for predicting the entrainment rate. Only the models or correlations generated from water experiments are reviewed here, since water is the coolant in BWRs and thus the working fluid in present study.

Pallev and Filippovich published one of the earliest correlation for entrainment rate in 1966 [44], which is based on the dimensionless group below:

$$\pi_{Pallev} = \frac{\bar{\rho}}{\rho_l}\left(\frac{\mu_l v_g}{\sigma}\right)^2 \tag{2-14}$$

where v_g is the mean velocity of gas core, and $\bar{\rho}$ is the mixture density of the gas core taking into account the entrained droplets. Later in 1968, Wallis published a short discussion on Pallev's

correlation and pointed out that the dimensionless group should be replaced with the following one, which correlated better with the experimental results [4][45].

$$\pi_{Wallis} = \left(\frac{\rho_g}{\rho_l}\right)^{0.5} \frac{\mu_g v_g}{\sigma} \tag{2-15}$$

Wallis presented a plot with measured entrainment rate versus the π_{Wallis}, but he did not propose a new correlation based on his dimensionless group. Other researchers summarized a correlation based on the plot that Wallis published [46].

$$E = 1 - \exp\left\{-0.125\left[10^4 \frac{j_g \mu_g}{\sigma_l}\left(\frac{\rho_g}{\rho_l}\right)^{0.5} - 1.5\right]\right\} \tag{2-16}$$

In 1975, Ishii and Grolmes published a set of well-known criteria for judging the initiation of liquid entrainment in annular flow [40]. They proposed that the gas Weber number needed to exceed a critical value (We_{cr}) in order to induce liquid entrainment. The set of criteria correlated the critical gas superficial velocity (j_{gcr}) with the liquid viscosity number ($N_{\mu l}$) at different ranges of liquid film Reynolds number (Re_{lf}). At the initiation of entrainment, the liquid film Reynolds number equals the normal Reynolds number based on liquid superficial velocity ($Re_{lf} = Re_{ls}$), since all the liquid still remains in the liquid film. Ishii and Grolmes' critical gas superficial velocity was later reformulated as critical Weber number by Sawant [50].

$$We_{cr} = \frac{\rho_g j_{gcr}^2 D_h}{\sigma}\left(\frac{\rho_l - \rho_g}{\rho_g}\right)^{0.25} \tag{2-17}$$

$$N_{\mu l} = \frac{\mu_l}{\left\{\rho_l \sigma\left[\frac{\sigma}{g\left(\rho_l - \rho_g\right)}\right]^{0.5}\right\}^{0.5}} \tag{2-18}$$

$$Re_{lf} = \frac{4\dot{m}_{lf}}{\pi D_h \mu_l} = Re_{ls}, at\ entrainment\ initiation$$

$$Initiation\ Criteria\begin{cases} \dfrac{\mu_l j_{g_{cr}}}{\sigma}\sqrt{\dfrac{\rho_g}{\rho_l}} \geq N_{\mu l}^{0.8}, Re_{lf} > 1635 \\ \dfrac{\mu_l j_{g_{cr}}}{\sigma}\sqrt{\dfrac{\rho_g}{\rho_l}} \geq 11.78 N_{\mu l}^{0.8} Re_{lf}^{-\frac{1}{3}}, \ 160 < Re_{lf} < 1635 \\ No\ Entrainment\ All\ Range, \quad Re_{lf} < 160 \end{cases} \tag{2-19}$$

In 1986, Oliemans [47] adopted an oversimplified way to correlate the entrainment rate. The proposed correlation is basically a multiplication of all the related parameters with each of them raised to a specific power. This approach achieved some good agreement in a specific data range, but the accuracy is questionable in a wider range due to purely empirical nature of the correlation. In addition, the correlation does not considered the entrainment initiation, which can be included by replacing $j_g\ with\ (j_g - j_{g_{cr}})$, using Ishii's criteria.

$$\frac{E}{1-E} = 10^{\beta_0}\rho_l^{\beta_1}\rho_g^{\beta_2}\mu_l^{\beta_3}\mu_g^{\beta_4}\sigma^{\beta_5}D^{\beta_6}j_l^{\beta_7}j_g^{\beta_8}g^{\beta_9} \tag{2-20}$$

In 1989, Ishii and Mishima [48] developed a correlation for predicting entrainment rate at fully developed condition, i.e., entrainment rate equals to deposition rate. The interesting aspect is that such correlation does not consider the entrainment initiation criteria Ishii and Grolmes published before [40]. The predicted entrainment rate goes to zero, when the superficial gas flow rate goes to zero instead of the critical value at the initiation of entrainment. The entrainment initiation criterion can be taken into account by manually replacing $j_g\ with\ (j_g - j_{g_{cr}})$. The original equation is presented below.

$$E = \tanh(7.25 \times 10^{-7} We^{1.25} Re_l^{0.25}) \tag{2-21}$$

where $We = \frac{\rho_g j_g^2 D_h}{\sigma}\left(\frac{\rho_l - \rho_g}{\rho_g}\right)^{1/3}$

Pan and Hanratty developed a correlation considering the suppression of disturbance wave at high entrainment rate [49]. With such suppression, they found there was a maximum achievable entrainment rate limit (E_{max}) at each specific liquid flow rate. They correlated the E_{max} with a critical liquid film mass flow rate ($\dot{m}_{lf_{cr}}$). Unfortunately, they did not develop a correlation to estimate the critical liquid film flow rate, but simply applied an experimentally measured value from a very specific condition.

$$\frac{E/E_{max}}{1 - E/E_{max}} = 6 \times 10^{-5}\frac{\left(j_g - j_{g_{cr}}\right)^2\left(\rho_g\rho_l\right)^{0.5}D}{\sigma} \tag{2-25}$$

where

$$E_{max} = 1 - \frac{\dot{m}_{lf_{cr}}}{\dot{m}_l} \tag{2-26}$$

$$\frac{D^{0.5} j_{g_{cr}} \left(\rho_l \rho_g\right)^{0.25}}{\sigma^{0.5}} \cong 40 \tag{2-27}$$

In 2009, Sawant confirmed Pan's finding that the increase of entrainment rate will reach a maximum plateau (E_{max}) as the gas flow rate increases after the entrainment initiation, at a specific liquid flow rate. Sawant attributed the maximum entrainment rate limit to the fact that the liquid film flow rate eventually dropped below the critical value as the film kept losing mass. Therefore, liquid could not be further teared off from the film even at higher gas velocity [49]. For the entrainment initiation, Sawant kept using the critical Weber number from Ishii and Grolmes [40].

$$E = E_{max} \times tanh[a(We - We_{cr})^{1.25}] \tag{2-28}$$

where

$$E_{max} = 1 - \frac{13 N_{\mu l}^{-0.5} + 0.3\left(Re_l - 13 N_{\mu l}^{-0.5}\right)^{0.95}}{Re_l} \tag{2-29}$$

$$a = 2.31 \times 10^{-4} Re_l^{-0.35} \tag{2-30}$$

In 2012, Al-Sarkhi successfully simplified Sawant's expression for the E_{max}, and found his modified E_{max} fitted better to Sawant's data [51].

$$E_{max} = 1 - \exp\left[-\left(\frac{Re_l}{1400}\right)^{0.6}\right] \tag{2-31}$$

The above-mentioned correlations for predicting entrainment rate are compared in Figure 2-12. For each correlation, three constant entrainment rates, i.e., from left to right: 0, 0.25 and 0.75, are plotted on the $j_l \; vs. \; j_g$ coordinate.

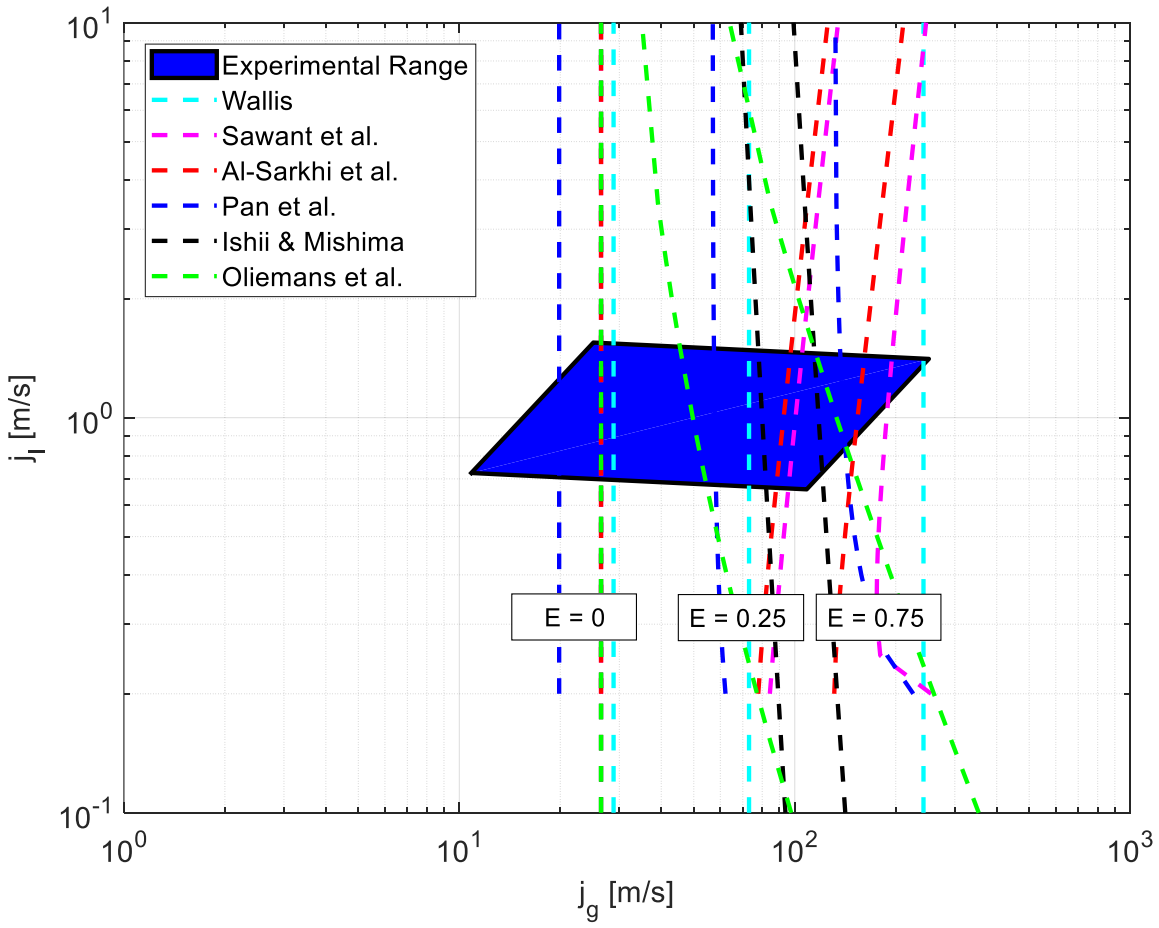

***Figure 2-12**: Comparison of various author's correlation for predicting liquid entrainment rate, together with the experimental range of present study. The latter plot of the series adds one more curve on top of the previous one. There is generally no agreement among different correlations especially at high entrainment rate.*

As shown in Figure 2-12, there is qualitative agreement (entrainment increases with increasing j_g), but no quantitative agreement among the different correlations. Because of the overlap of its experimental data with the conditions of interest in present study, the Al-Sarkhi's modified Sawant correlation is selected for the calculation of entrainment rate in the present study. (Sawant's experiments used a 0.95 cm pipe inner diameter, air-water flow, atmospheric pressure and vertical upward co-current flow.)

3. Scope of the Work

The main purpose of the present work is to provide direct measurement of SNB in annular upward two-phase flow with innovative diagnostics, in order to investigate the SNB mechanisms. Meanwhile, the accurately measured local parameters can be used to enhance the understanding of the annular flow thermohydraulic phenomena.

From a Computational Fluid Dynamics (CFD) point of view, accommodating the local information obtained from these new boiling experiments should enable development of a more accurate heat partitioning approach for the representation of the flow boiling mechanisms. Classic heat partitioning models are specifically developed for subcooled flow boiling, in which the total heat flux is decomposed into various partitioned components according to the involved heat transfer mechanisms [52]. With the direct measurement and the enhanced understanding of the annular flow thermohydraulic phenomena, an "extended" heat partitioning model (EHPM) would extend the applicability outside the classic subcooled regime all the way into the annular flow from either modifying the partitioned components or replacing some of them.

The expected thermohydraulic conditions for this study are listed in Table 1. The range of the parameters are generally chosen to be representative of the normal operating conditions in BWR-5 [3] to the extent possible in our facility, and to span a sufficiently broad range of values to observe meaningful trends.

***Table 3-1**: Expected thermohydraulic conditions compared with BWR-5.*

Parameter	Units	BWR-5	Current Work
Two-phase Components	[-]	Steam-Water	Steam-Water
Mass Flux (G)	[$kg \cdot m^{-2} \cdot s^{-1}$]	1584	700-1400
Heat Flux (q'')	[$kW \cdot m^{-2}$]	~500	100-2000
Steam Quality (x_e)	[-]	0-0.14 (inlet to outlet)	0.01-0.08 (inlet)
Bo $= \frac{q''}{h_{lg}\dot{m}}$	[-]	1.910	0-6.349
Bulk Temperature (T_{bulk})	[°C]	278.3-286.1	100-105 (outlet) /limited by equipment/
Pressure (P)	[MPa]	7.14	0.101-0.12 (outlet) /limited by equipment/
Hydraulic Diameter (D_h)	[mm]	12.3 (subchannel)	10
$Re_l = \frac{G(1-x)D_h}{\mu_l}$	[-] × 10^5	2.08-1.79 (inlet to outlet)	0.0797-0.526 (inlet) /limited by equipment/
$Re_g = \frac{GxD_h}{\mu_g}$	[-] × 10^5	0-1.42 (inlet to outlet)	0.0203-0.889 (inlet)
ρ_l/ρ_g	[-]	37.34	1483
μ_l/μ_g	[-]	4.775	22.75

As shown in Table 3-1, good match/coverage is achieved between current work and BWR-5 conditions for two-phase components, mass flux, heat flux, steam quality, and boiling number (Bo). The notable exception is pressure, which indirectly produces the distortion in the density and viscosity ratios. In the specified range of the experimental conditions, the expected annular flow parameters can be explored with the diagnostic methods listed in Table 3-2.

***Table 3-2**: Expected annular flow parameters to be measured and corresponding diagnostic methods.*

Parameter	Measurement Method
2D Temperature Distribution on Heated Surface	IRC
Location of Nucleate Boiling	IRC
Bubble Departure Base Diameter	IRC
Bubble Departure Frequency	IRC
Heat Flux	PI+EB
Heat Transfer Coefficient	IRC+ PI+EB
Film Thickness	LFS
Inlet Equilibrium Quality	EB, FM
Inlet Temperature	RTD, TC
Outlet Temperature	RTD, TC
Inlet Flow Rate, Mass Flux, Reynolds Number	FM
System Pressure	PT, PG

***Table 3-3**: List of abbreviations in Table 3-2.*

Abbreviation	Full Name
EB	Energy Balance
FM	Flow Meter
LFS	Liquid Film Sensor
IRC	Infrared Camera
PI	Power Input
PG	Pressure Gauge
PT	Pressure Transducer
RTD	Resistance Temperature Detector
TC	Thermocouple

The highlight in Table 3-2 is the application of two synchronized innovative imaging techniques, i.e., IR thermography with LFS. Such close-up imaging techniques provide the multiscale interaction of the extremely thin film and small nucleation cavities (in the scale of 10 micron), with the large disturbance waves and the associated temperature oscillations (in the scale of 10 cm). SNB is an important outcome from this multiscale interaction.

A detailed test matrix to be carried out is listed below. Equilibrium steam quality (x_e) and total mass flux (G) are the two main control parameters for the flow. At each combination of flow parameters, heat flux is first ramped up until vigorous boiling appears, and then gradually reduced below SNB.

***Table 3-4**: Test matrix for the main flow control parameters.*

Nominal Steam Quality [-]	**Nominal Total Mass Flux [kg·m^{-2}·s^{-1}]**		
	750	**1050**	**1350**
0.016	X	X	X
0.030	X	X	X
0.050	X	X	X
0.070	X	X	X

4. Design and Construction of Two-Phase Annular Flow Facility

In this chapter, the design and construction of the flow loop, the test assembly and the test section are presented. The instrumentations for monitoring the flow loop conditions are introduced, together with their measuring uncertainty. A flow loop shakedown was conducted to eliminate the possibility of two-phase flow instability at elevated steam quality condition.

4.1. The Flow Loop

In the present study, the flow loop (built for and used in a previous project) has undergone major modifications in order to accommodate a new test section mounted at the top end of the new test assembly. The schematic of the new flow loop and an actual picture of the completed test facility are shown in Figure 4-1 and Figure 4-2, respectively.

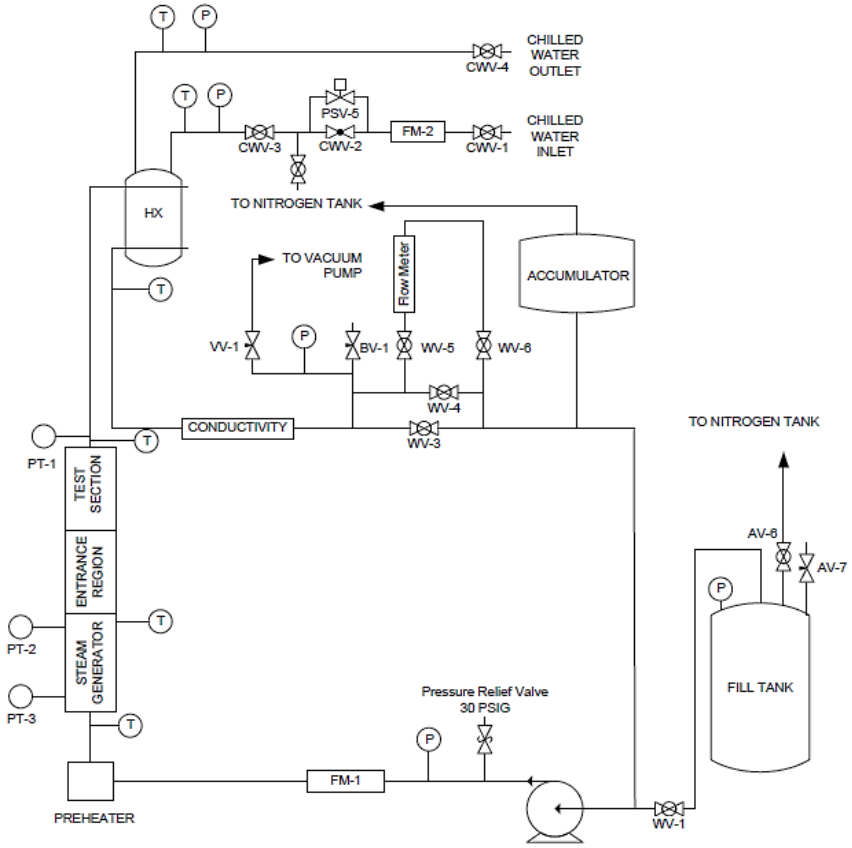

***Figure 4-1**: Schematic drawing of the new flow loop. Many modifications have been done for accommodating the tall test assembly that generates, develops, and measures the annular flow and SNB.*

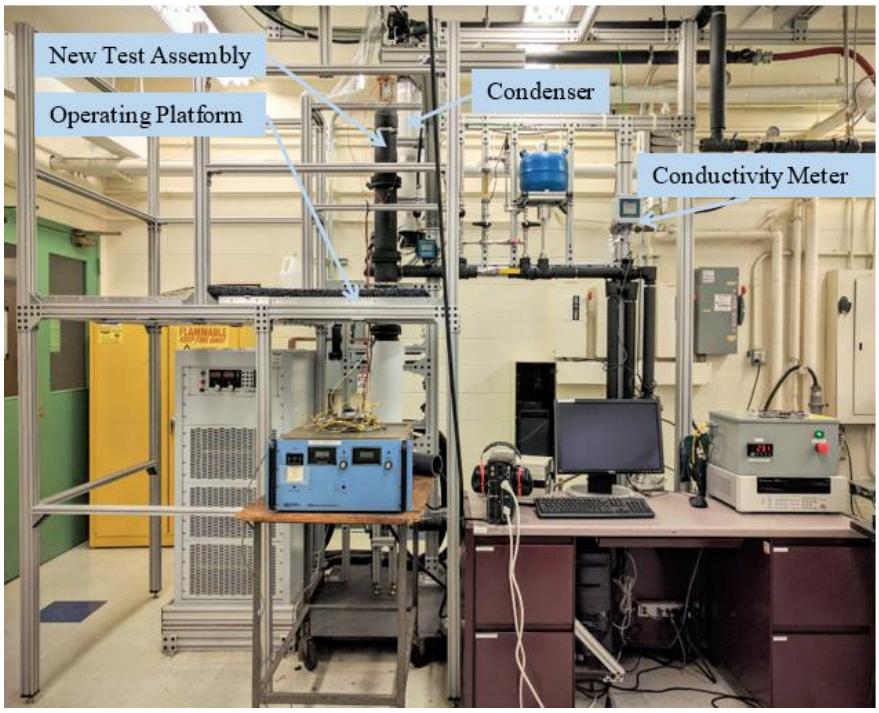

***Figure 4-2**: The real picture of the completed test facility.*

The new test assembly was built on the left side of the flow loop. The condenser was relocated right after the exit of the test section with the purpose of reducing the two-phase flow section in the loop, and hence increasing the flow stability. A new conductivity sensor was installed after the condenser, to measure the conductivity of water at single-phase condition. A new operating platform surrounding the test assembly was constructed out of aluminum T-slotted frames. The platform provides a safe and stable elevated working surface for the operator and other local measuring techniques such as IRC and LFS, since the test section is located at the tallest point of the test assembly. The reconstructed flow loop is the first steam-water annular flow loop in NSE, MIT for the direct measurement of the local thermohydraulic parameters of the annular flow associated phenomena.

4.2. Test Assembly

The test assembly is 2.066 m tall and consists of 5 main components: inlet diffuser, tube-bundle boiler, outlet nozzle, entrance channel and test section, as shown in Figure 4-3. The test assembly is made of 316 stainless steel in order to resist corrosion especially with steam-water mixtures at elevated temperature condition.

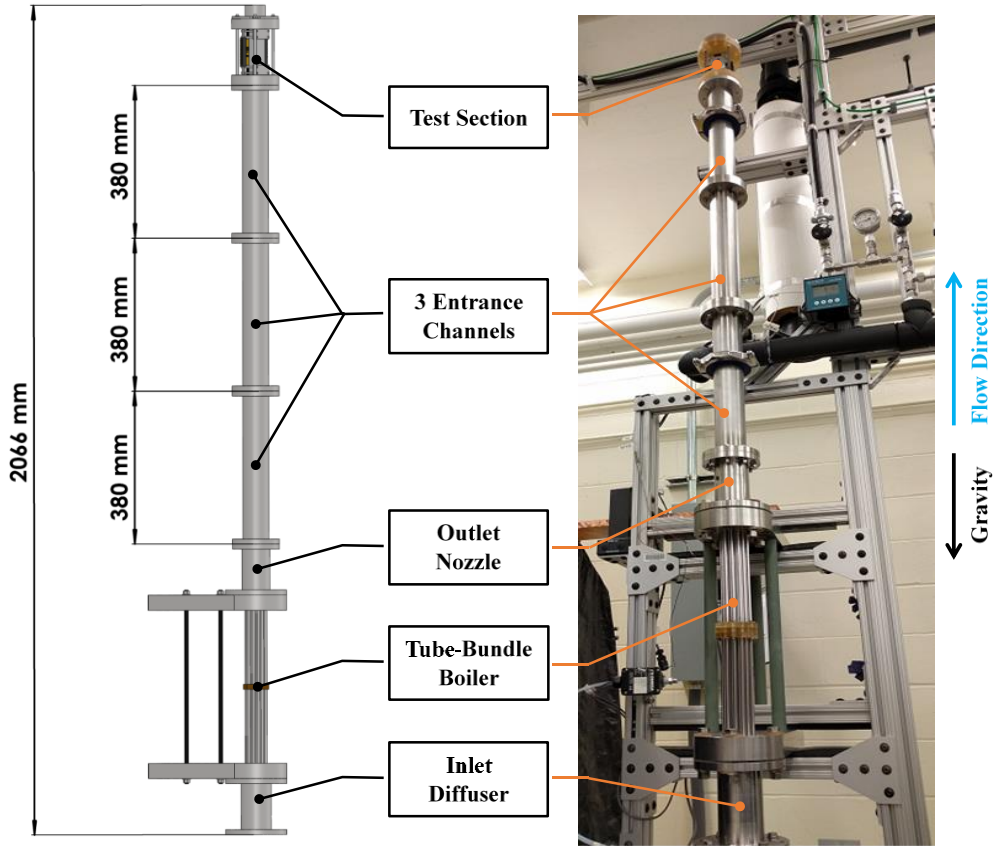

***Figure 4-3**: The test assembly for annular flow. It comprises 5 components: Inlet diffuser, Tube-bundle boiler, Outlet diffuser, 3 entrance channels, and Test section. The fluid flows from the bottom to the top.*

Water enters the test assembly from the inlet diffuser at the bottom, and then flows upwards. The inlet diffuser distributes the flow into 19 tubes of the tube-bundle boiler. In the tube-bundle boiler, water is heated up to generate the desired steam quality. The tube-bundle is energized by a DC power supply, and thus the heat is generated by Joule heating. The maximum power of the boiler is 50 kW, which is capable to produce more than 10% equilibrium steam quality (x_e= 0.1) at the highest expected mass flux of 1400 kg·m^{-2}·s^{-1}, while keeping the heat flux well below the CHF limit, i.e., the operating heat flux is only 350 kW·m^{-2}. After the boiler, the two-phase mixture flows into the entrance channel through the outlet nozzle that provides a gradual change of the flow cross section.

The entrance channel consists of three identical modules that have a rectangular cross section of 1cm by 1cm, i.e., the same geometry of the test section. The entrance channel needs to be sufficiently long, in order to let the two-phase mixture reach fully developed annular flow

condition before it flows out. A widely used criterion is given by Ishii and Mishima [48] which correlates the length over diameter ratio (L/D_h) with the dimensionless gas superficial velocity (j_g^*), and the total liquid Reynolds number (Re_l):

$$\frac{L}{D_h} \geq 600 \left(\frac{j_g^*}{Re_l} \right)^{0.5} \tag{4-1}$$

where Re_l holds the same definition as in previous chapter, and

$$j_g^* = j_g / \left\{ \frac{\sigma g (\rho_l - \rho_g)}{\rho_g^2} \left[\frac{\rho_g}{(\rho_l - \rho_g)} \right]^{\frac{2}{3}} \right\}^{\frac{1}{4}} \tag{4-2}$$

This criterion actually turns out to be a proportional function of steam quality since mass flux cancels out. Thus, the longest required developing length occurs at the highest steam quality. At the steam quality of 0.08, which is the highest expected steam quality in present study, the fully developed annular flow requirement is $L/D_h > 27$. To safely ensure the fully developed annular flow, a conservative factor of 4 is multiplied to the criterion. The total length of the present entrance channel is $L/D_h = 114$, which is sufficient to reach fully-developed annular flow. More discussion and a proposed future work to validate the fully-developed annular flow condition are presented in Section 8.3.

After the entrance channel, the flow enters the actual test section, which features the instrumented heater on one side of the rectangular cross section. The heater is designed to generate a heat flux sufficient to initiate nucleate boiling even at the highest imposed mass flux. The 2D temperature profile of the heater, all the relevant boiling parameters and the liquid film thickness will be measured in the test section.

4.3. Test Section

The test section design that could be applied for this study should take into account several considerations: a) optical path to access to the ITO heater by the IR camera; b) circulation/measurement of electrical power; c) resistance to elevated working temperature (around 100 ^{o}C); d) durability to multiple thermal cycle; e) alignment of different parts in the flow

direction; f) ease of fabrication and cost. The test section was originally designed by Dr. Bren Phillips [53] and later modified by the author. The finalized design is shown in Figure 4-4.

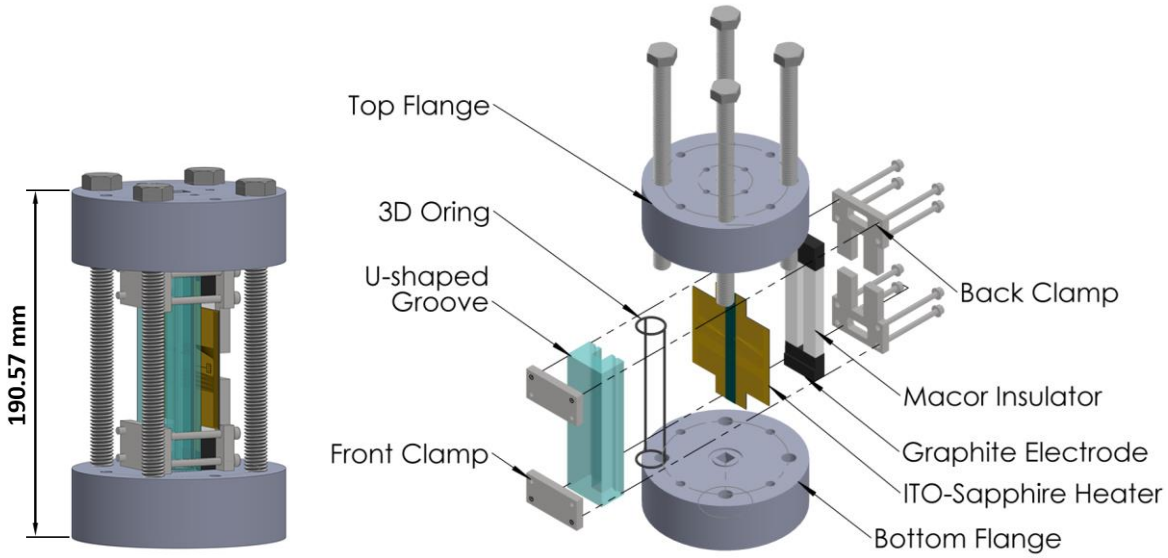

***Figure 4-4**: 3D Design of the test section: the assembled view (left), the exploded view (right)*

The test section is composed of a test channel and two flanges. The test channel is made of a U-shaped ceramic piece with 1cm by 1cm cross section, mated to the ITO-Sapphire heater and with a 3D o-ring sealing the surfaces in between. These parts are held together by two pairs of stainless steel clamps. The test channel is then sandwiched between two 38.1 mm thick flanges that have the same rectangular shape through hole as the test channel. The interfaces between the flanges and the test channel are also sealed by the 3D o-ring. The whole test section is held together by 4 threaded rods sized ¼”-20. The total length of the designed test section is 190.57 mm while the heated length is 94.56 mm. The ITO-Sapphire heater is designed to generate a heat flux sufficient to initiate nucleate boiling even at the highest imposed mass flux and steam quality. The 2D temperature profile of the heater and the liquid film thickness are measured in the test section. The fabricated and assembled test section is shown in Figure 4-5.

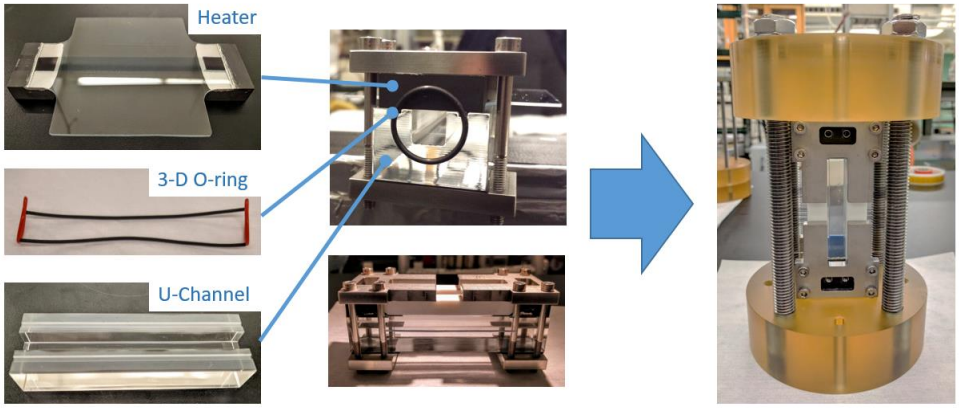

***Figure 4-5**: Real picture of the parts and assembled test section. The assembling process is illustrated from left to right*

The cruciform ITO-Sapphire heater is epoxied to a pair of ultra-fine-grain graphite electrodes via silver conductive epoxy before assembled to test channel, as shown on the top left picture in Figure 4-5. The electrical resistance through the silver epoxy and graphite electrodes can be neglected due to the relatively low resistivity, small thickness, and large contact area (estimated 0.000046 Ω for silver epoxy and 0.0095 Ω for graphite electrodes). A pair of threaded holes with threaded inserts are fabricated on the backside of the graphite electrodes for power supply and voltage measurement separately, as shown in Figure 4-6. It can also be seen that the stainless steel clamps together with the Macor insulators form a 1.2 cm by 74.4 cm viewing window for the IR measurement of the ITO strip heater.

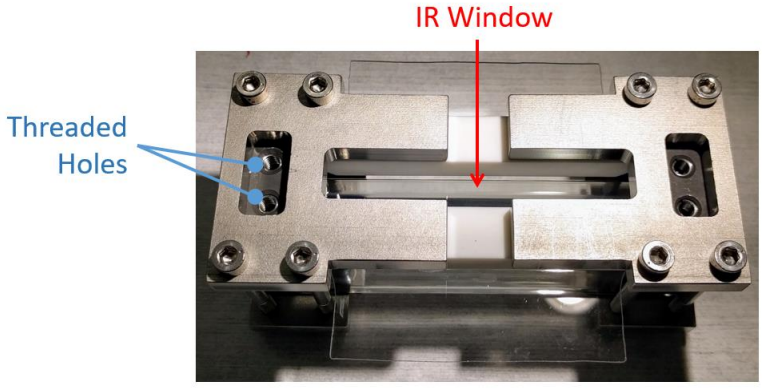

***Figure 4-6**: Backside of the assembled test channel. Two threaded holes for electrical connection and measurement separately. One opening window sized 1.2 cm by 74.4 cm for IR measurement of the ITO strip heater.*

All the materials used for fabricating the test section have been selected in consideration of their resistance to elevated temperature up to 110 ^{o}C, especially those containing polymers. The silver epoxy has a maximum manufacturer rated temperature of 121 ^{o}C [55]. The flanges are made of polysulfone, which retains its mechanical properties up to 150 ^{o}C [55]. The 3D o-ring is made of high temperature silicone that withstand temperature up to 232 ^{o}C [57].

Material's resistance to thermal cycle is another concern of the design, since the whole test assembly heats up to at least 100 ^{o}C for maintaining steam-water annular flow during the tests, and then cools back down to room temperature after the tests. Such thermal cycle can cause crack and eventually damage to the ceramic U-shaped piece. The originally U-shaped was made of quartz for the purpose of visible inspection, which experienced cracking damage after alignment pinholes were manufactured. It was later replaced with Macor, since Macor has more than 2 times fracture toughness of quartz [58].

The alignment between the test channel and the flange is an important aspect of the assembling process, as well as the alignment between the test section and other parts of the test assembly. A misalignment of the order of 100 μm during assembling may still be considered acceptable in a single-phase experiment with channel diameter of the order of 1 cm, because the boundary layer is relatively thick and thus the bulk is insensitive to the small misalignment. However, with the smallest liquid film thickness of a few tens of microns in annular flow, the 100 μm misaligning step is already a large obstacle to the liquid film. The alignment pin-pinhole coupling was designed and fabricated to enhance the alignment accuracy. The alignment pin-pinhole couplings for flange-flange junction and test channel-flange junction are illustrated in Figure 4-7. The alignment accuracy was quantified by a DSLR camera and LED backlighting, the resolution of which was 7 μm per pixel. With improved alignment, the average step at test channel-flange junction and flange-flange junction were 10 μm and 30 μm separately. The test channel-flange junction before and after applying alignment pin-pinhole coupling is shown in Figure 4-8.

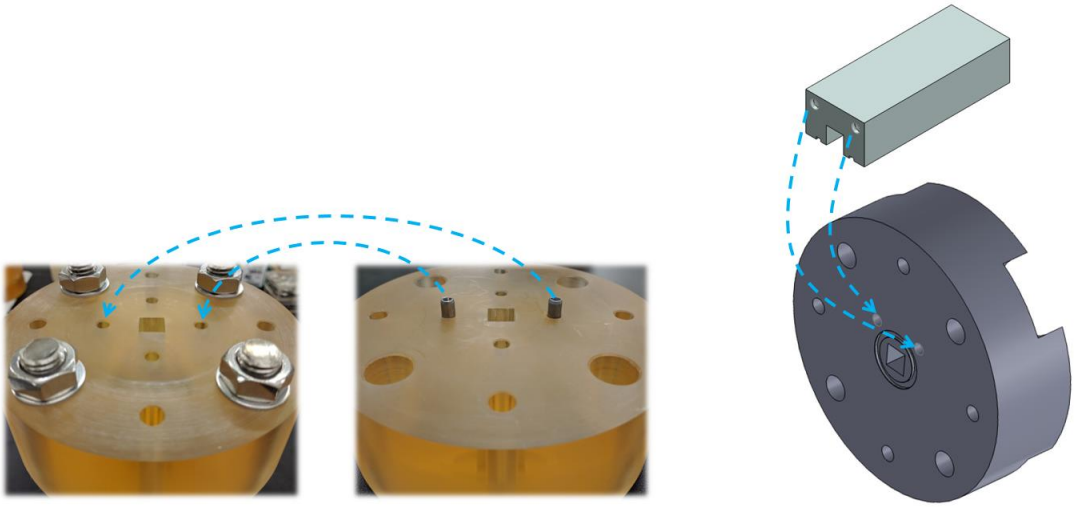

***Figure 4-7**: Illustration of pin-pinhole coupling for enhancing the alignment accuracy: flange-flange alignment(left), test channel-flange alignment (right).*

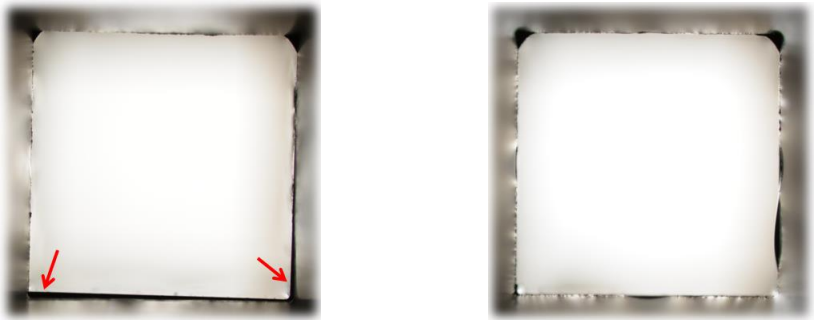

***Figure 4-8**: The test channel-flange junction before (left) and after (right) applying alignment pin-pinhole coupling. The "steps" marked by the red arrows are larger than 100 µm in the left picture. The "steps" in the right picture is either one pixel or less, ~10 µm (note the black shadows are lubricant droplets, not misalignment steps).*

4.4. Instrumentation for the Flow Loop

The deployment of the instrumentations for monitoring the flow loop condition is shown in Figure 4-1, in which T is RTD temperature probe, PT is pressure transducer, FM is flow meter, and Conductivity is conductivity probe.

4.4.1. Flow Measurement

An accurate flow measurement is of crucial importance in present study, since it directly affects the total mass flow rate and the equilibrium steam quality, which further impact thin film

flow hydrodynamics and local heat transfer. Normally, the flow meter outputs the volumetric flow rate (Q_{mes}). In order to achieve the mass flow rate, a local liquid density is required from the local temperature measurement (T_{mes}).

$$\dot{m} = Q_{mes} * \rho_l(T_{mes}) \tag{4-3}$$

The mass flux in the test assembly, and thus the test section, is simply the mass flow rate divided by the cross section.

An Omega FV-102-SS vortex flow meter, with measuring range 0.756×10^{-4} to 7.56×10^{-4} $m^3\cdot s^{-1}$, is used to measure the volumetric flow rate. The flow meter was calibrated in the lab by Forrest (a previous PhD student) [54]. The uncertainties in slope and intercept of fitted calibration curve are 3.58×10^{-4} $m^3\cdot s^{-1}\cdot A^{-1}$ and 4.28×10^{-6} $m^3\cdot s^{-1}$ respectively. The overall uncertainties over the present test range are ± 45 $kg\cdot m^{-2}\cdot s^{-1}$ (6%) at 750 $kg\cdot m^{-2}\cdot s^{-1}$, and ± 48 $kg\cdot m^{-2}\cdot s^{-1}$ (3.4%) at 1400 $kg\cdot m^{-2}\cdot s^{-1}$.

4.4.2. Pressure Measurement

Pressure is measured at various locations of the flow loop by either pressure transducers or pressure gauge. The two important measuring points are located at the inlet of the entrance channel and at the outlet of the test section, to verify that the temperature is at saturation before and after the test section.

Omega PX329-050A5V pressure transducers, with measuring range 0 to 3.4 bar, were used to measure the absolute pressure at the two crucial locations. The manufacturer stated uncertainty was 0.25% of full scale, equivalent to ± 0.0085 bar.

4.4.3. Temperature Measurement

Accurate temperature measurement is essential to determining the important parameters in current work, such as the equilibrium steam quality and the saturation temperature. The IR thermography calibration before each test also relies on the classically measured temperature. Given the high precision and high accuracy of four-wire resistance temperature detector (RTD), RTDs were applied at the three most important locations of the test assembly, i.e., the inlet of tube-bundle boiling, the inlet of entrance channel, and the outlet of test section.

Omega PR-11-3-100-1/8-6-E four-wire RTDs, with measuring rage -200 ^{o}C to 600 ^{o}C, were used in the present study. The manufacturer's stated accuracy is ± 0.15 ^{o}C.

4.4.4. Tube-Bundle Boiler Voltage and Current Measurement

The boiler generates heat from Joule heating by directly energizing the tube-bundle, and thus evaporates liquid water into steam. The input power of the boiler is an important parameter to calculating the equilibrium steam quality. The voltage and current across the boiler are measured to determine the electrical power delivered to the tube-bundle.

The voltage range of the present DC power supply is less than 16 V, thus the voltage can be directly measured by the data acquisition system (DAS). The measuring uncertainty of the DAS is ± 0.005% of the reading. Two wire taps are spot welded to each pole of the boiler for measuring the imposed voltage. The taps are located as close to the root of the tube-bundle as possible to minimize the potential drop along the conductor plate.

The estimated current applied in the tests is of the order of 1000 A, due to the small resistance of the tube-bundle and the high power required for generating steam. Using a traditional current shunt is not practical for such high current range. Instead, a non-contact transducer based on the Hall effect is installed around the positive busbar, as shown in Figure 4-9 [54]. The LEM HAZ 6000 current transducer has a measuring range of ± 6000A, with a manufacturer stated uncertainty of ± 60 A.

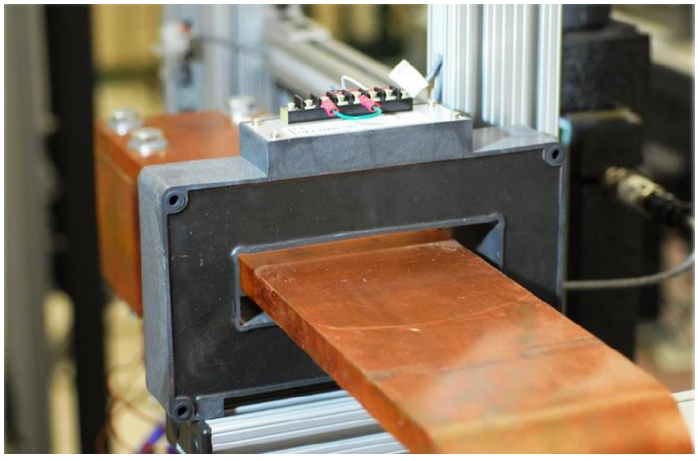

***Figure 4-9**: Hall-effect current transducer installed around the positive busbar.*

4.4.5. Conductivity Measurement

The LFS relies on electric conduction through water to measure the liquid film thickness. Thus, the conductivity of the water used in the experiments has to be measured. An aqueous solution of KNO_3 with an expected conductivity of 100-400 $\mu S \cdot cm^{-1}$ was used as the working fluid instead of DI water, since the conductivity of DI water was too low for the LFS measurement. The conductivity of aqueous solutions (as well as that of pure water itself) has a strong dependency on temperature. Hence, it was important to monitor the conductivity of the circulating fluid online, in order to perform an accurate measurement of the liquid film thickness. A Yokogawa™ conductivity measuring system was used: it consists of a FLXA21 multi-purpose meter and a SC4A two-wire conductivity probe with cell constant of 0.1 cm^{-1} thus measuring range 0.2-2,000 $\mu S \cdot cm^{-1}$.

Since the manufacturer did not provide the measuring uncertainty versus temperature, the ability of the probe to measure conductivity at elevated temperature was evaluated by comparing the measurement to the predictions of a theoretical Debye-Hückel-Onsager model [59][60]. For a compound with cations and anions having the same valency (e.g. NaCl, KNO_3), this model gives the following equations:

$$\Lambda = \Lambda_0 - (B_1\Lambda_0 + B_2)\sqrt{c} \tag{4-4}$$

$$B_1 = \frac{e^2 z^2 \left(2-\sqrt{2}\right)}{6\varepsilon k_B T}\left(\frac{8\pi N e^2 z^2}{\varepsilon k_B T}\right)^{\frac{1}{2}}\left(\frac{N}{1000}\right)^{\frac{1}{2}} \tag{4-5}$$

$$B_2 = \frac{F^2 z}{3\pi\mu_l N}\left(\frac{8\pi N e^2 z^2}{\varepsilon k_B T}\right)^{\frac{1}{2}}\left(\frac{N}{1000}\right)^{\frac{1}{2}} \tag{4-6}$$

where Λ is the equivalent conductivity; Λ_0 is the infinite-dilute equivalent conductivity; c is the molar concentration; e is the protonic charge; z is the valency of the ion; N is the normality of the solution; ε is the permittivity of the solution; k_B is Boltzmann's constant; T is the absolute temperature. The specific conductivity ($\mu S \cdot cm^{-1}$) then can be calculated from the equivalent conductivity:

$$\sigma = \Lambda\left(\frac{N}{1000}\right) \tag{4-7}$$

The measured data were obtained with KNO_3 solution (at 307 ppm and 438 ppm) prepared by mixing KNO_3 powder and DI water, separately weighed using a scale with the accuracy of 0.01 g. Temperature ascending and descending tests were conducted up to 60 °C. The agreement with Debye-Hückel-Onsager model is good with an overall uncertainty of less than 1%.

4.5. Flow Loop Shakedown and Flow Instability

The present investigation required the flow loop to work at relatively high steam quality. The presence of considerable amount of steam raised the possibility of two-phase flow instabilities, especially in the form of density wave oscillations (DWO). Such flow instability leads to the intense oscillation of the system pressure and the mass flow rate. Local burnout could happen at the boiler, should the flow rate be not sufficient. Calculations and experiments were conducted to predict, confirm, and exclude the possible occurrence of the flow instability.

Prior to the tests, two separate calculations were carried out with RELAP and the non-dimensional group method, to predict the conditions for DWO in our test assembly for the expected test matrix.

RELAP calculations were first carried out with the help of Dr. Phillips [61], in the range of the expected mass fluxes and steam qualities ($x_e \leq 0.1$). Typical results are shown in Figure 4-10. The predicted average velocities for the liquid and vapor phases at the boiler and at the entrance channel are stable. The RELAP calculations suggested that no flow instability would appear across the whole test matrix.

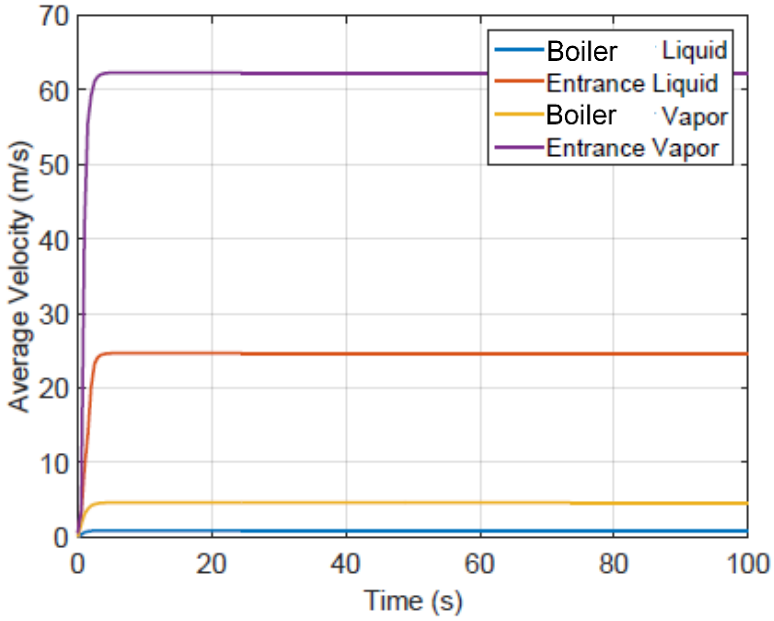

***Figure 4-10**: Stable flow predicted by RELAP at x_e=0.1 and G=1500 kg·m^{-2}·s^{-1}*

An analytical approach based on the non-dimensional group method was also used, to strengthen the conclusions of the RELAP analysis. In this method, a stability map is generated using the non-dimensional subcooling number (N_{sub}) and the phase-change number (N_{pch}) [3]:

$$N_{sub} = \left(\frac{h_l - h_{in}}{h_{lg}}\right)\left(\frac{\rho_l - \rho_g}{\rho_g}\right) \tag{4-8}$$

$$N_{pch} = \left(\frac{\dot{q}}{h_{lg}\dot{m}}\right)\left(\frac{\rho_l - \rho_g}{\rho_g}\right) = (x_e + \frac{C_p \Delta T_{sub}}{h_{lg}})\rho_l v_{lg} \tag{4-9}$$

where $h, \rho, \dot{m}, \dot{q}, C_p, \Delta T_{sub}, x_e$ are specific enthalpy, density, specific volume, mass flow rate, total power, specific heat, and subcooling, respectively; subscripts l, lg and in represent saturated liquid, difference between saturated gas and saturated liquid, and inlet condition, respectively. The stability criterion is then given by the following equation, which is plotted in the stability map of Figure 4-11.

$$N_{pch} \leq N_{sub} + \frac{2(K_i + f_m/2D_h^* + K_e)}{1 + 0.5(f_m/2D_h^* + K_e)} \tag{4-10}$$

where K_i, K_e are the inlet and exit form loss coefficients of the test assembly, respectively; f_m is the two-phase mixture friction coefficient; D_h is the hydraulic diameter; L is the length of the heated section; D_h^* is D_h/L.

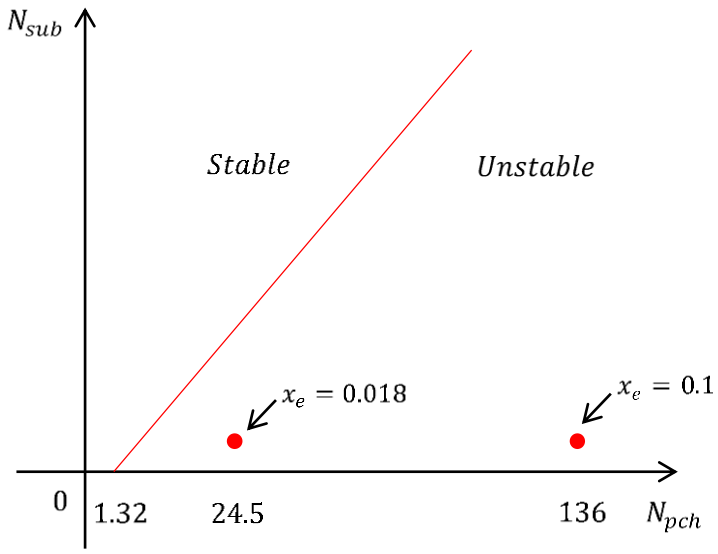

***Figure 4-11**: Stability map for density wave oscillations in the test assembly. Red points show two bounding steam quality conditions at 1500 kg·m^{-2}·s^{-1}(not to scale), both of which falls in the unstable zone.*

Figure 4-11 shows that high N_{sub} values and low N_{pch} values are preferred to prevent DWO. In the expected test matrix conditions, $N_{sub} \to 0$ because the test assembly inlet condition is very close to saturation, while $N_{pch} = 13.6\sim136$. Basically, the stability is determined by N_{pch}. Therefore, in contrast with the results of RELAP, the non-dimensional analysis suggested that the whole test matrix would fall in the unstable zone with the original flow loop configuration shown in Figure 4-1.

To resolve the discrepancy between the RELAP calculations and the non-dimensional group analysis, a test run was conducted at mass flux of 1500 kg·m^{-2}·s^{-1} and vapor quality of $0.01 - 0.02$. DWOs were unfortunately observed. During the oscillations, the following cycle of flow patterns repeated itself approximately every 10 to 15 seconds: flow stagnation/reverse → annular flow → bubbly flow → annular flow → flow stagnation/reverse, and so on. The oscillating flow parameters recorded by the DAS at a sampling rate of 1 Hz are listed in Table 1. Therefore, it

seems that in our case the non-dimensional analysis is more reliable at predicting the DWOs than RELAP.

***Table 4-1**: Mean and oscillating parameters during a test with DWOs.*

Parameter	Mean Value w/Oscillation
Mass flux [$kg \cdot m^{-2} \cdot s^{-1}$]	1500 w/±500
Equilibrium steam quality	~0.018
Boiler P_{in} [bar]	1.5 w/±0.15
Test section P_{out} [bar]	1.32 w/±0.13
Boiler T_{in} [℃]	92
Boiler max power [kW]	11.5
Boiler max heat flux [$kW \cdot m^{-2}$]	89
Test assembly transit time [s]	1.33 (at ~1.5 $m \cdot s^{-1}$)

A practical way to enhance the stability of two-phase flows is to increase the inlet form loss of the test assembly, as suggested by Equation 4-10. A ½ in flow restriction valve was installed at the inlet of the test assembly as shown in Figure 4-12. The orifice diameter of the valve is 6.35 mm (¼ in), which gives a form loss coefficient $K_i \approx 104$ at all-open condition according to the manufacturer. The form loss coefficient can be further increased by closing the valve. With the form loss coefficient at all-open condition, the stability map is replotted in Figure 4-13. The expected upper bound value of N_{pch} for our test matrix now falls in the stable zone, hence all other operating points should be in the stable zone. The additional inlet form loss added 3.35 m to the loop head loss at G=1500 $kg \cdot m^{-2} \cdot s^{-1}$, which could still be overcome by pump head.

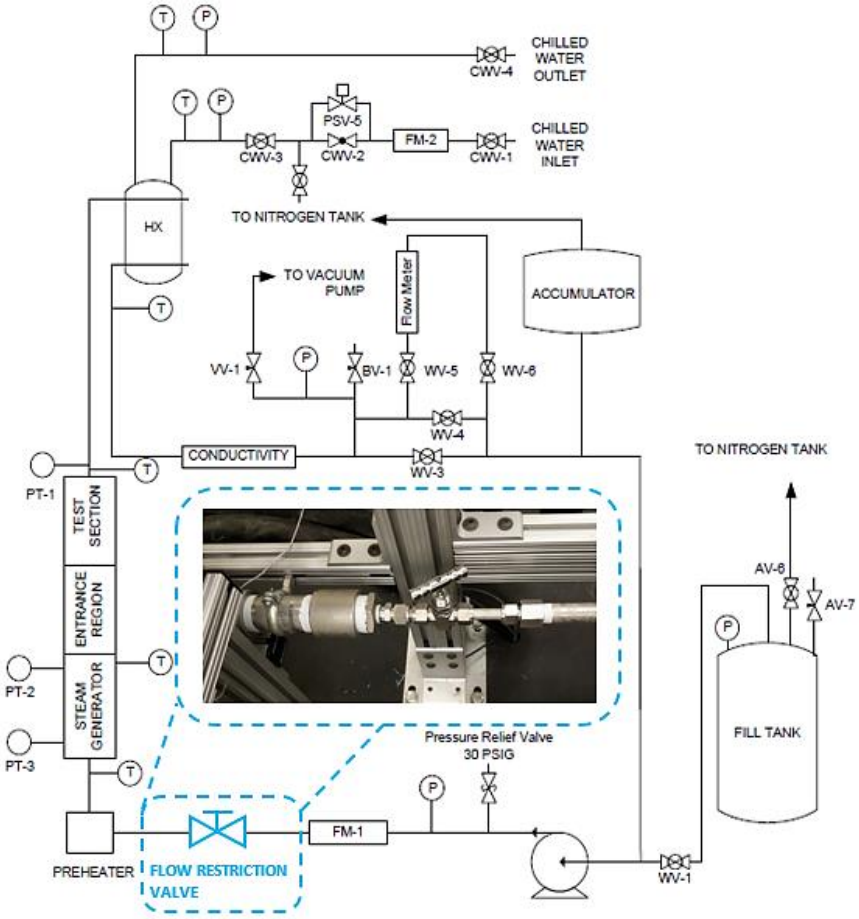

***Figure 4-12**: Modified flow loop configuration with the stabilizing flow restriction valve. The valve is located right before the test assembly and after the pump.*

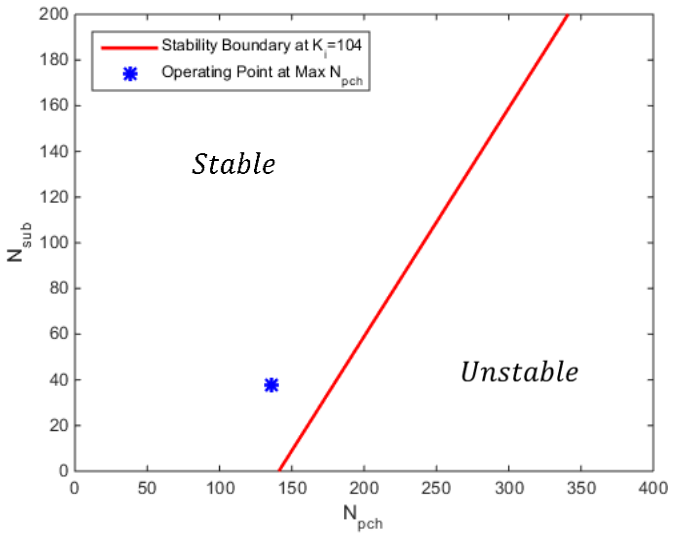

***Figure 4-13**: Stability map of the test assembly with inlet K_i=104 from the flow restriction valve. The upper bound value of the test matrix falls in the stable zone.*

Additional tests were conducted with the flow restriction valve installed, at mass flux up to 1450 $kg \cdot m^{-2} \cdot s^{-1}$ and steam quality up to 0.05. The flow stability was achieved and sustained at all conditions, which confirmed the correctness of the stability map analysis.

At mass flux of 790 $kg \cdot m^{-2} \cdot s^{-1}$ and steam quality of 0.015, the test assembly inlet pressure, outlet pressure and mass flux were acquired simultaneously with a second data acquisition system (DAS) at 100 Hz while the main control DAS was running. (Note the main DAS cannot run faster than 1 Hz under the present LabView configuration with many I/O and control signals). The purpose of employing a faster secondary DAS was to check if any significant oscillation in the loop could disturb the liquid film in the frequency range <100 Hz (the typical range of disturbance wave frequency).

The data acquired by the second DAS were first validated against the main DAS at single-phase conditions, which confirmed the correctness of the output. Then, the acquired data at annular flow conditions was examined with the Fast Fourier transform (FFT) to check if there was any dominant oscillating frequency.

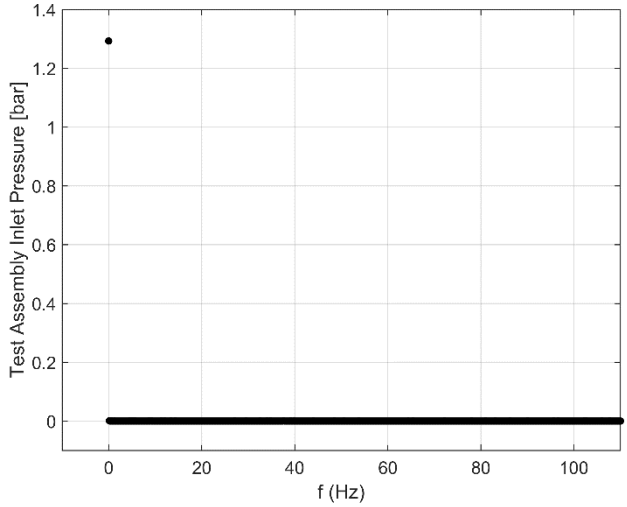
Test Assembly Inlet Pressure [bar]
f (Hz)

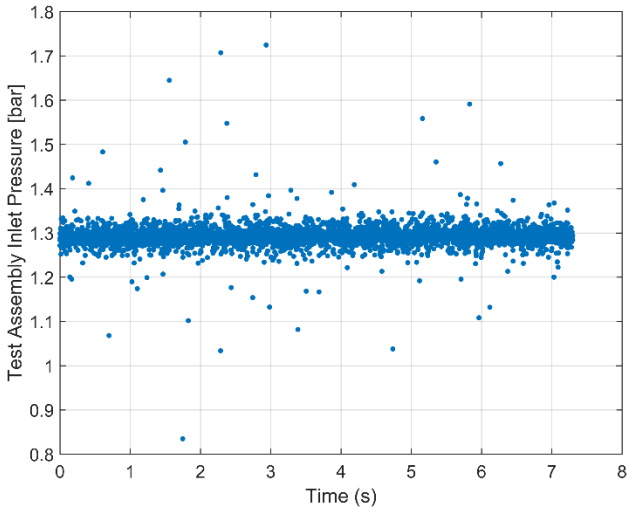
Test Assembly Inlet Pressure [bar]
Time (s)

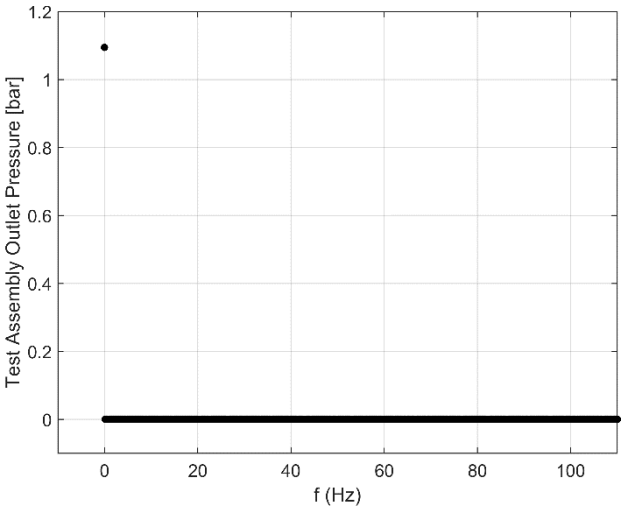
Test Assembly Outlet Pressure [bar]
f (Hz)

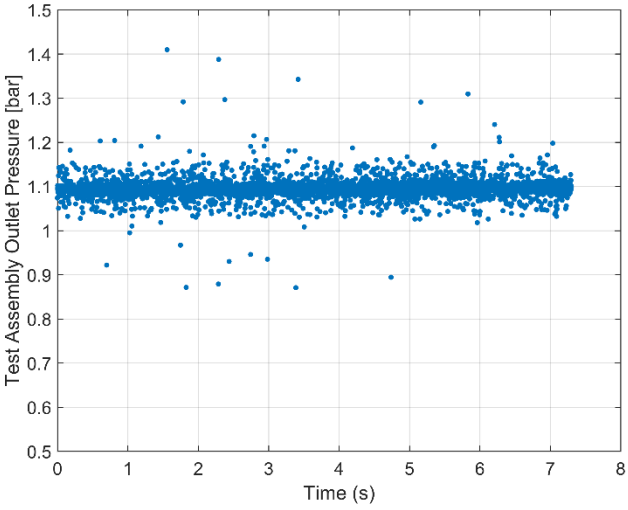
Test Assembly Outlet Pressure [bar]
Time (s)

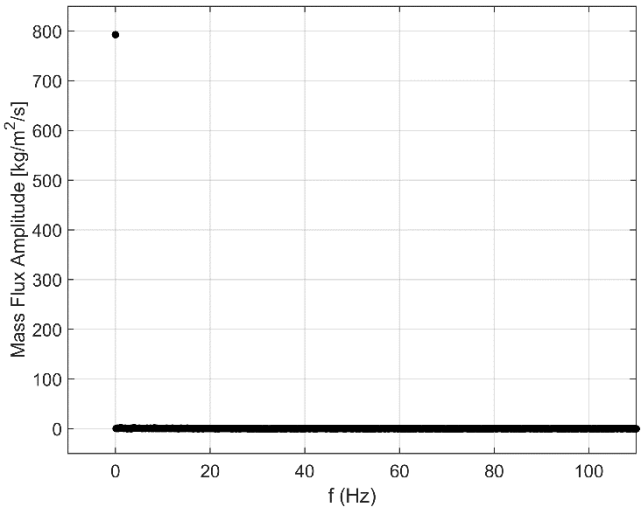
Mass Flux Amplitude [kg/m2/s]
f (Hz)

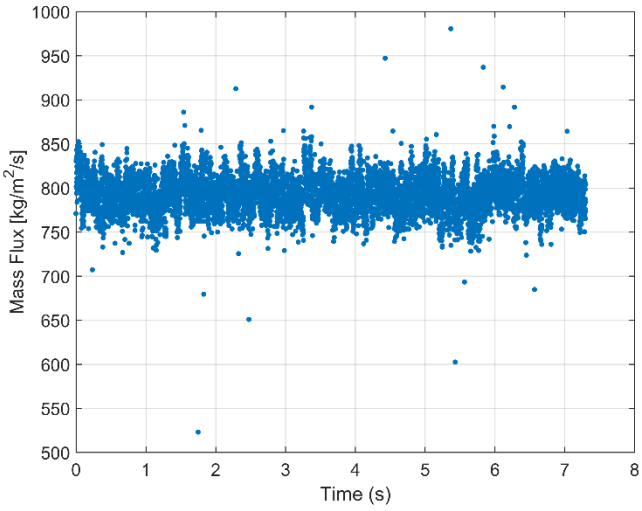
Mass Flux [kg/m2/s]
Time (s)

***Figure 4-14**: Sample results of test assembly inlet pressure (top), outlet pressure (middle) and mass flux (bottom). Left column: frequency domain; right column: time domain. Only 0 Hz peaks emerge, which correspond to the mean values.*

As shown in the left column of Figure 4-14, there is only one peak in the frequency domain on each plot, i.e., 0 Hz frequency. The mean value and standard deviation calculated in time domain for inlet pressure, outlet pressure and mass flux are: 1.29±0.021 bar, 1.09±0.018 bar and 793±21 $kg \cdot m^{-2} \cdot s^{-1}$. They are all within the manufacturer stated accuracy.

5. Innovative Diagnostics

In this chapter, the diagnostics used to explore the SNB in annular flow are presented. The general configuration of the apparatus, the basic measuring principles, and the validation and calibration process are introduced.

5.1. IR Thermography

5.1.1. Basic Principles and Apparatus

According to Planck's law, the thermal radiation (photon flux and spectrum) emitted by a surface is a strong function of the surface temperature [62]. Based on this fact, a non-intrusive temperature measurement is feasible by properly recording the thermal radiation from an emitting object, and this is the theoretical basis of infrared thermography [63]. Specifically, under boiling conditions at ambient pressure, in the temperature range of interests (~100 to 150 ℃), Mid-IR infrared radiation is commonly used, since it gives relatively strong radiation intensity at the temperatures of interest for this work and also the highest sensitivity of radiation intensity with respect to temperature, which ensures a high signal to noise ratio. In order to practically realize this technique, a radiating surface needs to be used, together with an IR detector.

Inherited from the work in our group [64], the heater for the present study comprises a sapphire substrate (1 mm thick), with indium-tin oxide (ITO) film as heating element (700 nm thick, 94.56 mm length, 9 mm width) and IR emitter (opaque in the mid-IR range). The ITO film is wrapped from the top of the heater (in contact with water) to the bottom of the heater (in contact with air). The configuration of the heater is shown in Figure 5-1. The special cruciform shaped substrate is designed to allow for the surface-mounted electrical leads of the LFS to protrude from the two sides, as will be discussed in the next section. With such configuration, electrical wires can be epoxied to the air side of the heater which avoids electrode exposure to water as well as disturbance to the fluid. When energized with electric current, the ITO film heats up by Joule-heating. Because the ITO heater is so thin, the temperature drop across the ITO is negligible, and thus the 2D temperature distribution of the boiling surface can be effectively measured.

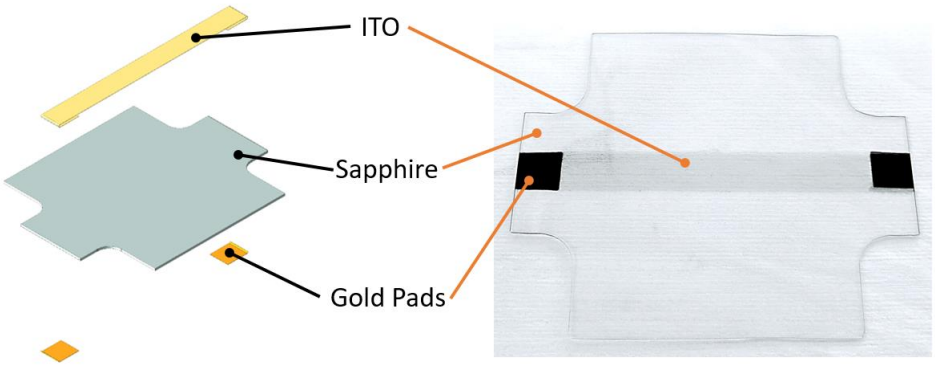

***Figure 5-1**: ITO heater configuration: design (left), real heater (right). A 700 nm wrap-around ITO layer is deposited on top of a 1mm thick sapphire substrate. A pair of gold pads are deposited on each end of the ITO layer*

An IRC-800HS high-speed infrared camera with an InSb photon detector will be used to record the IR emission from the ITO heater, as shown in Figure 5-2. The sensor of the IR camera captures mid-IR (in the 3-5μm wavelength range) radiation. Each pixel of the InSb sensor has a well of 7 million electrons. Every time a photon hits the pixel, one electron is moved from the valence to the conduction band and creates a voltage difference, which is the signal measured as camera counts. To finally achieve the temperature of the radiating surface, the simplest way is to correlate the camera counts with the temperature using a calibration curve, as shown in Figure 5-3. However, if there is a non-fully-transparent medium between the radiating surface and the infrared camera such as the sapphire substrate underneath the ITO (sapphire slightly emits between 4.5 μm and 5 μm), and/or there is a time-dependent temperature distribution on the surface, the simple calibration curve approach is no longer applicable. In this situation, a coupled conduction-radiation model is required to accurately estimate the surface temperature (see Figure 5-4). For the details of the conduction-radiation model, please refer to reference [65].

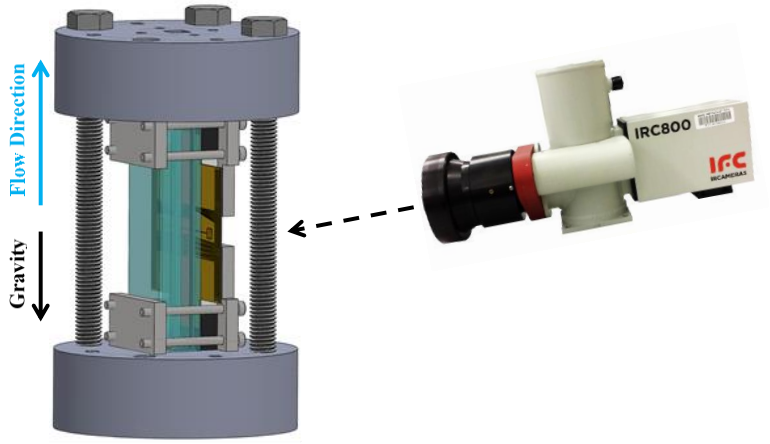

***Figure 5-2**: Test section with the IRC setup. Note: one threaded rod is hidden for clearer view of the channel.*

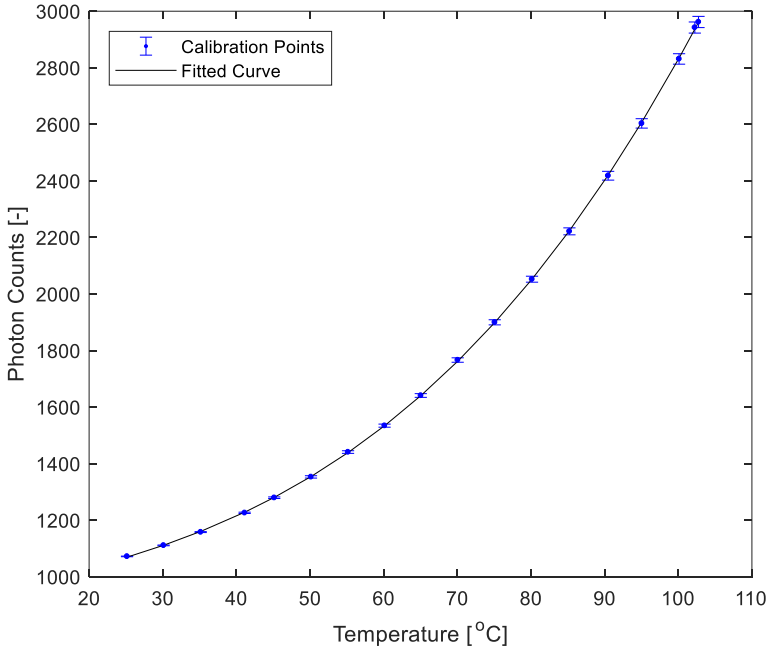

***Figure 5-3**: Example of calibration curve for the photon counts versus temperature. The calibration curve is accurate only at steady state and with a fully transparent substrate.*

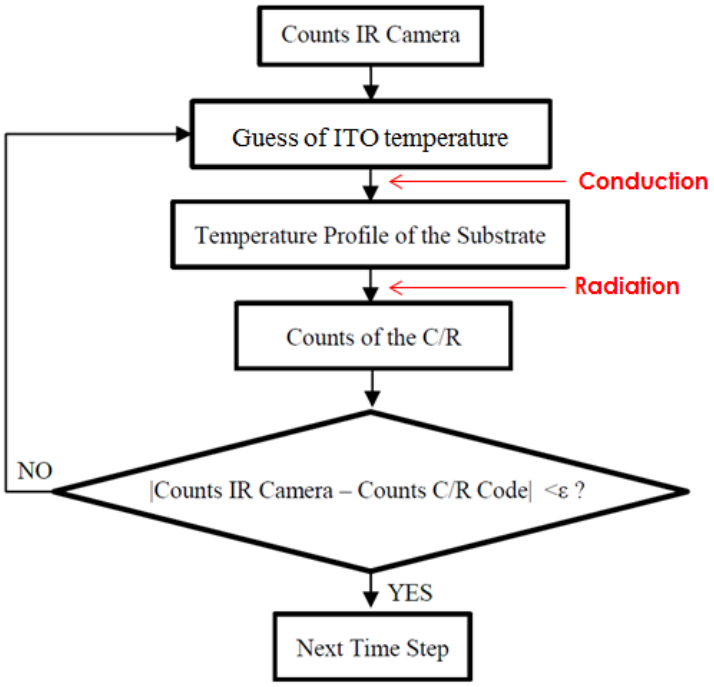

***Figure 5-4**: Flow chart of the coupled conduction-radiation model. An iterative process is required to solve the inverse problem for the temperature profile.*

The IRC-800 camera used in this study has a maximum 2D image resolution of 640 × 512 pixels. Using a proper lens, e.g. 100 mm germanium lens (f/2.3) with a 19 mm extension ring, a spatial resolution of approximately 100 microns can be achieved. Under a windowed-down condition, the camera can record at a frequency as high as 4000 Hz. As a compromise between viewing the whole ITO surface and keeping a sufficiently high frame rate, a window size of 640 × 112 pixels at 2000 Hz frame rate was selected for the actual SNB tests. With such high spatial and temporal resolution, the IRC-800 camera will be capable of identifying the local bubble nucleation events as well as the associated boiling properties on the heated surface by the temperature foot print of the bubble (see Figure 5-5). In general, IR thermography coupled with the specialized heater discussed previously, has the advantage of simultaneously measuring the locations where boiling happens and the corresponding local temperature, whereas the traditional optical camera/TC/RTD based method lacks the spatial and temporal resolution to do so.

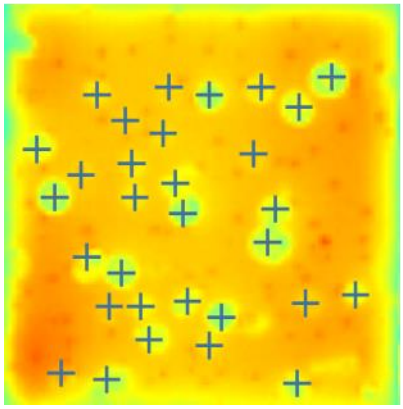

***Figure 5-5**: Example of nucleation site identification from the bubble footprint. The bubble footprint is a characteristic "cold" mark created by a bubble on the heating surface. The crosses denote the locations of the nucleation sites.*

5.1.2. Correction of the Non-Uniformity from Reflection

Due to the use of a large aspect ratio ITO-Sapphire heater (9 mm by 94.56 mm) in the present study, a new challenge of non-uniform IR radiation emission (halo effect) arises, which was not observed in previous studies using smaller (10 mm by 10 mm) heaters, as shown qualitatively in Figure 5-6. The halo effect is different from the normal vignetting effect that tends to create an opposite gradient. The impact of vignetting effect is excluded from carrying out the two-point non-uniformity correction when preconditioning the IR camera.

In Figure 5-6, the IR images were taken at adiabatic condition in which a uniform temperature and thus uniform IR radiation emission are expected. However, the IR image shows a halo effect (Figure 5-6 (a)): "colder" in the center, "hotter" toward the ends. The difference between the IR camera counts at each pixel and the coldest pixel is found to be almost the same at low temperature (room temperature) or high temperature (saturated water conditions), which points to reflected radiation as the possible cause of the non-uniformity. When the lower part of the heater was covered with an IR-black diffusive surface as shown in Figure 5-6 (b), the halo effect disappeared from that region, but persisted in the bare region. A third test was conducted using a lens with twice as large diameter as shown in Figure 5-6 (c). It is clearly seen that the larger lens results in a weaker halo effect.

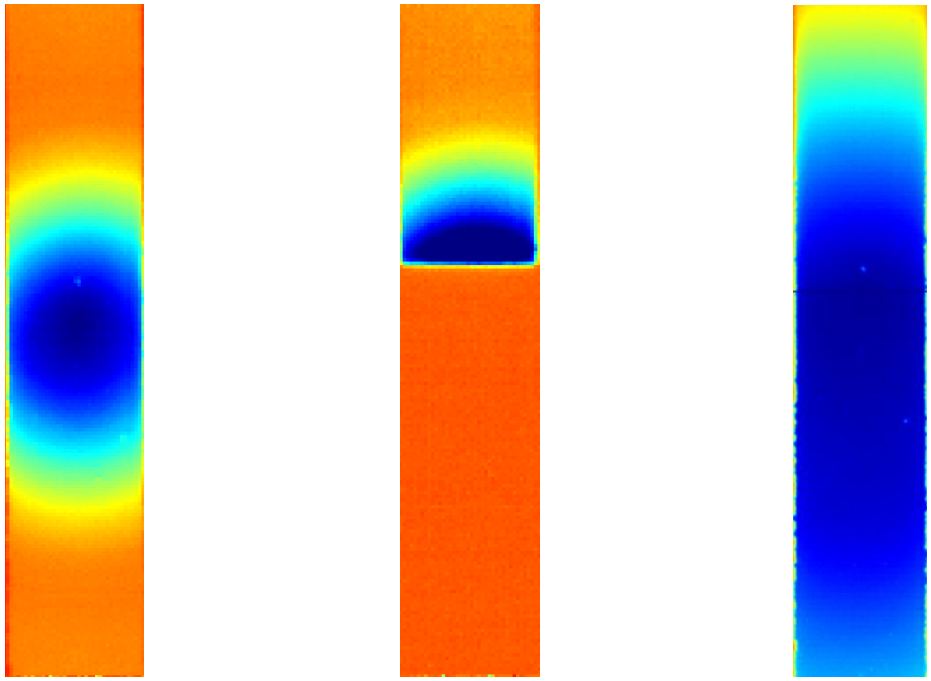

(a) 50 mm lens (b) 50 mm lens half-covered (c) 100 mm lens

***Figure 5-6**: Non-uniform IR image from the surface of the heater. The heater is not energized, thus its temperature is uniform and equal to the saturation temperature of the water. (a) refers to the test with 50 mm lens. (b) refers to the test with 50 mm lens, while heater half-covered by a diffusive IR-black surface. (c) refers to the test with 100 mm lens.*

Based on these observations, a reflection-based mechanism is proposed to explain the halo effect, as illustrated in Figure 5-7. In this figure, the same line color denotes the same source of radiation: ambient is orange, lens is dark blue, ITO is light blue. The dash line denotes radiation incoming to the ITO heater, while the solid line denotes the outgoing radiation from the ITO heater. We distinguish two areas in the discussion: the center area that appears cooler; the outer area that appears hotter.

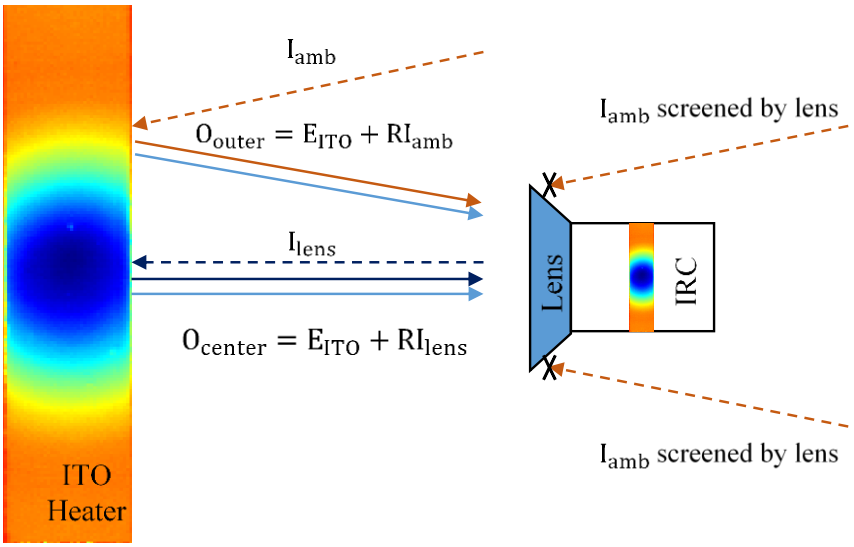

***Figure 5-7**: Schematic drawing for the mechanism of reflection causing the halo effect. "I", "O", "E", "RI" stands for incoming, outgoing, emission and reflected incoming, separately.*

In the center area, the ITO mainly reflects the incoming radiation from the lens (I_{lens}) back to the lens, which is very small since the camera is held at low temperature. The incoming radiation from the ambient is either screened by the lens, or impinge at a steep angle on the ITO, thus its reflection is not captured by the camera. As a result, the outgoing radiation from ITO to the lens in the center region (O_{center}) is a combination of ITO emission (E_{ITO} light blue) and reflected lens radiation (RI_{lens}).

In the outer area, the ITO mainly reflects the incoming radiation from the ambient (I_{amb}) with a low angle close to the surface normal. As a result, the outgoing radiation from ITO to the lens (O_{outer}) is a combination of ITO emission (E_{ITO}) and reflected ambient radiation (RI_{amb}). Since the radiation from the ambient is basically a blackbody radiation, it enhances the radiation signal significantly and hence makes the outer area looks hotter.

The reflection mechanism also explains why a larger lens results in a larger uniform area (Figure 5-6 (c)), since more area is screened from the ambient radiation by the lens. Hence, a larger lens is preferred. The mechanism also suggests that the further away is the lens from the heater, the stronger the halo effect in the center area.

The proposed mechanism is then quantitatively described by a theoretical model and validated against experimental measurement, as reported next. As mentioned before, the difference

between the camera counts (total counts recorded in 300 μs integration time) at the hottest and coldest spots is nearly constant, independent of temperature, i.e., 515 counts at 25 °C; 575 counts at 104 °C):

$$O_{outer} - O_{center} = RI_{amb} - RI_{lens} \cong 515{\sim}575 \tag{5-1}$$

The camera counts corresponding to the reflected ambient radiation are estimated as follows [65]:

$$RI_{amb} = f\left(\rho_{ITO} * N_{bb}(@23\,℃)\right) = 1144 \tag{5-2}$$

Where $\rho_{ITO} \approx 0.76$ is the reflectance of the ITO-Sapphire interface; N_{bb}(@23 °C) is the spectral integrated photon flux corresponding to the blackbody radiation (Planck's Law) from the ambient at room temperature; the function *f* is the conversion from the photon flux to the camera counts.

$$N_{bb}(T = 23\,°C) = \int_{3\mu m}^{5\mu m} \frac{2\pi c}{\lambda^4 (e^{\left(\frac{c_2}{\lambda T}\right)} - 1)} d\lambda = 1.1376 \times 10^{20}\ \ m^{-2}.s^{-1} \tag{5-3}$$

$$f(x) = \left(\frac{x}{4n_f^2}\right) dt_{int} A_{pixel} \frac{(nc_{fw} - nc_{ew})}{W_e} \tau_{os}\, QE + (nc_{ew} + \dot{n}c_{\mathrm{dc}} \cdot dt_{int}) \tag{5-4}$$

Where $n_f = 2.3$ is the focal number of the lens; $\tau_{os}\, QE = 0.7$ represents the combined effect of the loss through the lens to the filter to the camera sensor; $dt_{int} = 0.3\, ms$ is the integration time of the camera; $A_{pixel} = 20\mu m \times 20\mu m$ is the pixel area; $W_e = 7 \times 10^6$ is the total number of the electron well for each pixel; $nc_{fw} = 16000$ and $nc_{ew} = 375$ are the camera counts corresponding to full well and empty well, respectively.

The radiation/photon flux coming from the camera is a bit complex to estimate analytically, since it involves an intermittent lens-filter-sensor system emitting at different temperatures. Instead, a measurement aided method was conducted by covering the lens with a gold mirror which has a reflectivity $\rho_{gold} > 0.99$. The measured counts are 650. With this measurement, the counts corresponding to the reflected radiation from the camera are calculated as:

$$\begin{cases} 650 = \left(\dfrac{0.99N_{cam}}{4n_f^2}\right) dt_{int} A_{pixel} \dfrac{(nc_{fw} - nc_{ew})}{W_e} \tau_{os}\, QE + (nc_{ew} + \dot{n}c_{\mathrm{dc}} \cdot dt_{int}) \\ RI_{lens} = \left(\dfrac{0.76N_{cam}}{4n_f^2}\right) dt_{int} A_{pixel} \dfrac{(nc_{fw} - nc_{ew})}{W_e} \tau_{os}\, QE + (nc_{ew} + \dot{n}c_{\mathrm{dc}} \cdot dt_{int}) \end{cases} \quad (5\text{-}5)$$

$$\rightarrow RI_{lens} = 584 \quad (5\text{-}6)$$

$$\rightarrow RI_{amb} - RI_{lens} = 560 \quad (5\text{-}7)$$

Comparing Equation (5-7) with Equation (5-1), the reflection-based estimation is consistent with the measurement. The result confirms the correctness of the proposed mechanism.

Now that the cause of the halo effect is known, we can correct for it: i.e.,, the raw IR counts acquired at each pixel are reduced by the calculated counts due to additional reflected radiation from the ambient, which is essentially the deviation between every pixel and the coldest pixel at adiabatic condition.

A test using a larger lens was conducted at mass flux 821 kg·m^{-2}·s^{-1}, steam quality 0.011. The IR images were post-processed with the method described above. The results show that the combination of the modified optics and the post-processing method produces data that are physically correct and of high quality, as shown in Figure 5-8.

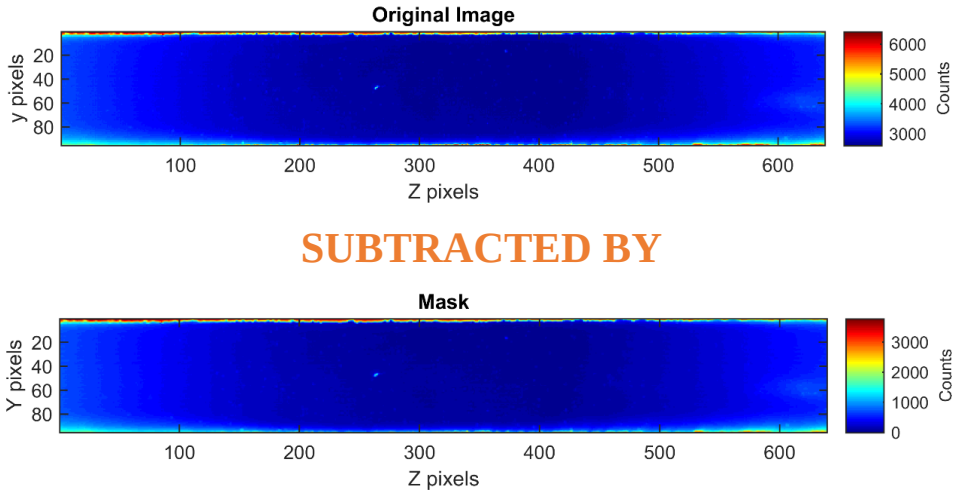

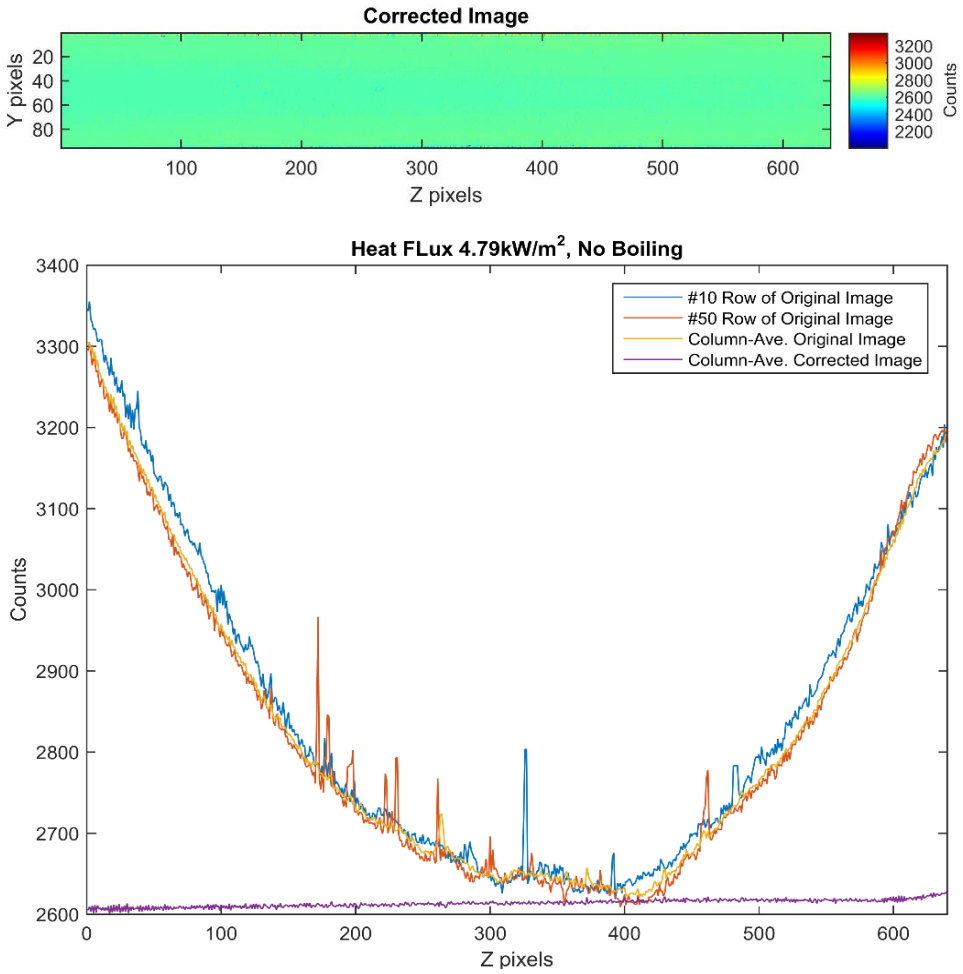

***Figure 5-8**: Elimination of the halo effect from the IR image. The purple line represents the counts after correction.*

In the plots of Figure 5-8, the blue curve represents the counts profile of the original IR image at the 10th row along the flow direction Z (the horizontal row at the10th Y pixel location); the red curve represents the profile of the original IR image at the 50th row; the orange curve represents the column-average (averaged over all the rows at each column) profile of the original IR image; the purple curve represents the column-average profile of the IR image after correction. The three curves from the original image overlap with each other rather well, which suggests that the counts gradient in the Y direction is small compared to the one in the Z direction. The curves from the original image only intersect the curve from the corrected image at the point with the lowest counts. The result confirms the correctness of the post-processing.

5.2. Liquid Film Sensor (LFS)

5.2.1. Basic Principles and Apparatus

The concept of the surface-mounted LFS used in this study was developed by Prof. Michael Prasser at ETH Zurich. The sensor is based on the electrical conductance measurement between a pair of custom-shaped electrodes, exposed to the flow and flush mounted on a substrate that constitutes the mechanical support, as illustrated in Figure 5-9. One of these electrodes, identified as the transmitter (Tx), delivers a short bipolar square voltage pulse. The amplitude of the bipolar voltage pulse (±3 V) is below the threshold of the water electrolysis and the duration is kept short (6 μs), to prevent liquid ionization. If the two electrodes are connected by a conductive liquid layer, the signal received by the complementary electrode, the receiver (Rx), will be proportional, within a specific range, to the liquid height. The feasibility study has shown that the linear range is strongly influenced by the distance between the electrodes and their shape. To extend the usable thickness range of the sensors, a third grounded electrode is placed close to the middle point between the receiver and the transmitter (see Figure 5-10). Therefore, a significant fraction of the electrical current will be diverted to the ground electrode, which inevitably decreases the amplitude of the received signal somewhat, however the linear dependency between the transmitter-receiver signal and liquid film thickness will benefit from a larger liquid thickness range. Compared to the wire-mesh sensor [15][16], which is widely used for phasic measurement (film thickness, void fraction, phasic velocity), Prasser's new film sensor concept [21] has the advantages of being non-intrusive and having higher sensitivity.

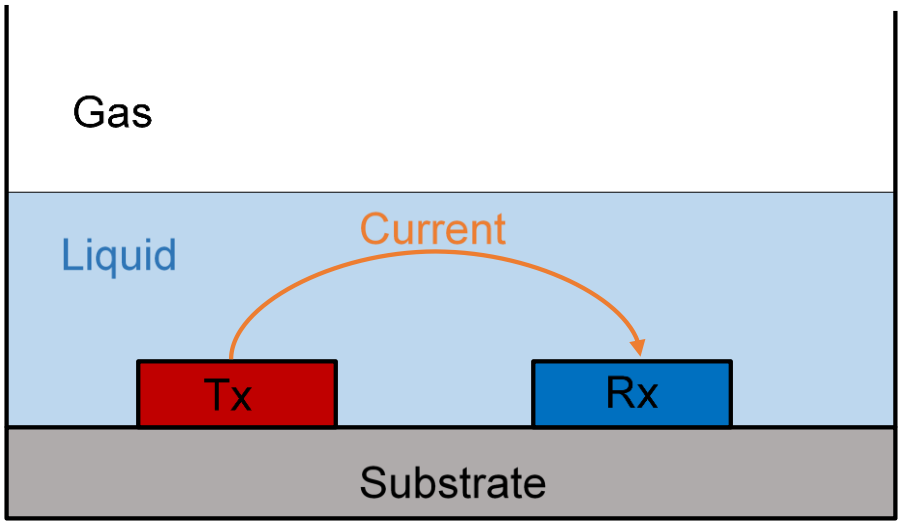

***Figure 5-9**: Schematic of the working principle of LFS (not to the scale). The red block represents the voltage transmitter (Tx), while the blue block represents the current receiver (Rx).*

In the current study, MIT collaborates with ETH Zurich (Prasser's group) to develop a special surface-mounted LFS that can most accurately measure the expected liquid film thickness in the range of 0 to 2.8 mm. For achieving a quasi-2D profile of film thickness, the sensor comprises arrays of electrodes creating a multipoint measurement over the surface, as shown in Figure 5-10. For designing the shape and the relative distance at which the electrodes are placed, a simulation was carried by ETH Zurich out with an in-house numerical solver for the potential field equation. By varying the liquid film thickness, the response of the sensor was simulated. According to the simulation, a triangular geometry was found to provide a desirably high sensitivity. The configuration allows to connect more receivers, simplifying the layout, and at the same time providing electrical separation between neighboring electrodes.

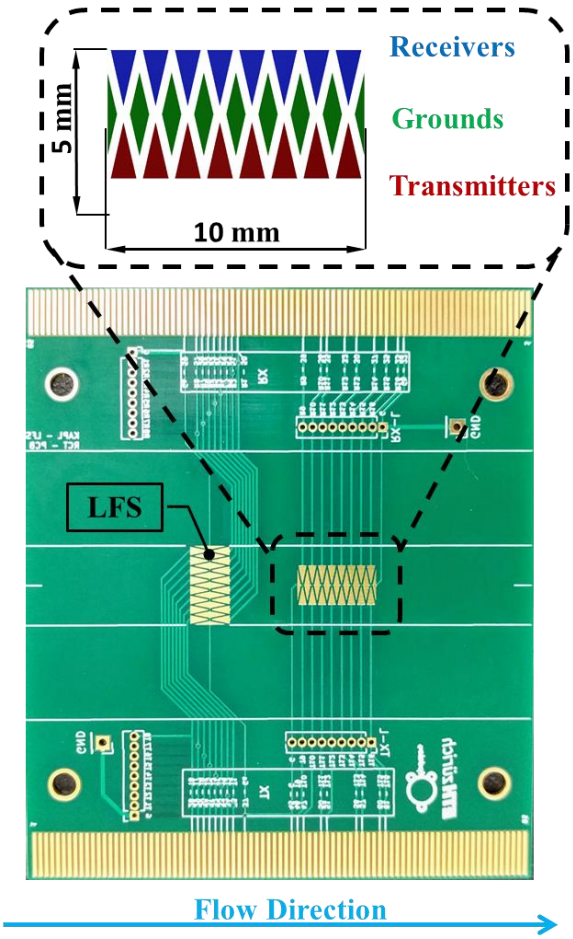

***Figure 5-10**: Schematic configuration (top) and photo of LFS (bottom). Each LFS element consists of a transmitter (blue), a receiver (red) and a pair of grounds (green). Arrays of LFS elements were fabricated along the flow direction.*

The first prototype of LFS consists of one longitudinal unit in the flow direction, and one transversal unit in the lateral direction, i.e., at 90^{o} with respect to the flow, as shown in Figure 5-10. Each unit consists of 8 LFS elements which provide liquid film thickness measurements at 8 spatial locations with a distance of 1.25 mm between two neighboring LFS elements. During operation, the transmitters are activated sequentially, whereas the receiver signals are sampled in parallel. The maximum achievable sampling frequency is 10 kHz, which is more than sufficient to capture the frequency of the disturbance wave (less than 50 Hz).

5.2.2. Integrated Configuration and Stand-alone Configuration

The ultimate goal of our diagnostics for annular flow is to achieve the synchronized and collocated measurement of the liquid film thickness, the heating wall temperature and heat flux.

With such synchronized and collocated measurement, we will be able to directly observe and evaluate the instantaneous interaction between the large-scale liquid film thickness oscillation and the heating wall temperature variation, both of which are expected to be caused by the passage of the disturbance wave. The design of the integrated configuration requires the deposition of the LFS on top of the ITO heater, with a thin (~ 1 μm) thermally conductive and electrically isolating layer located in between, as shown in Figure 5-11. Only one test section is needed for installing the integrated LFS-ITO heater.

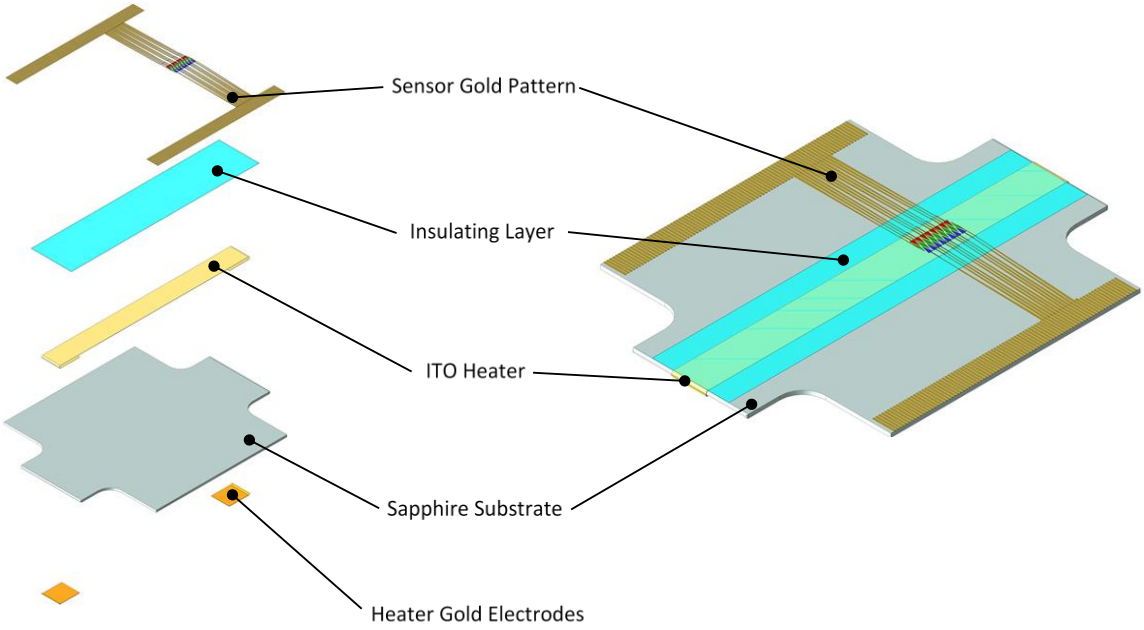

***Figure 5-11**: The integrated configuration of LFS and ITO-Sapphire heater. A thin thermally conductive and electrically isolating layer (light blue) separates the ITO-Sapphire heater with the LFS.*

Several prototype integrated LFS-Heaters were successfully made as shown in Figure 5-12. However, they did not exhibit acceptable durability when exposed to annular flow; as such, none of them could work long enough to reach the SNB conditions.

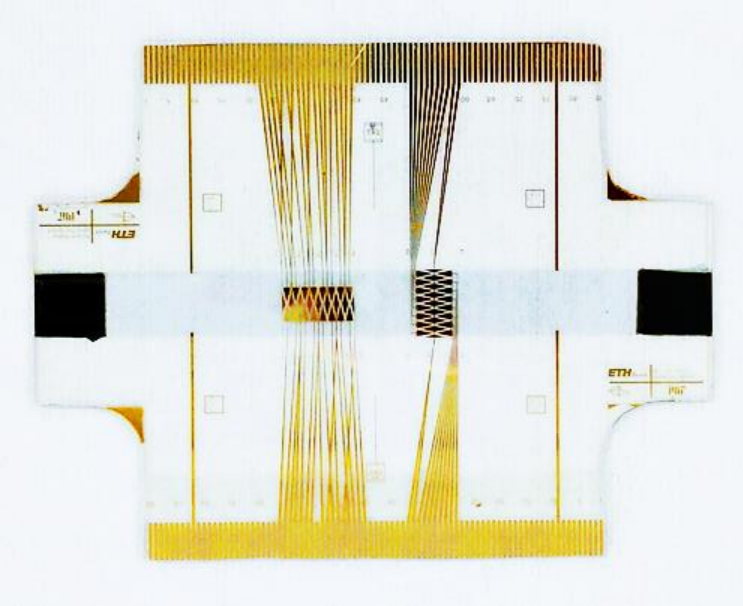

***Figure 5-12**: Prototype integrated LFS-ITO Heater. This prototype suffered from low durability of the SU-8 insulating layer when exposed to annular flow.*

A backup stand-alone configuration was designed and adopted for the experimental measurements in the current study, while work continues on the development of the integrated sensor. Instead of the collocated measurements, the stand-alone configuration separates the locations for the liquid film thickness measurement and the IR thermography measurement into two test sections respectively, as shown in Figure 5-13. The upstream test section accommodates the ITO heater shown in Figure 5-1 (IR thermography), while the downstream test section houses the stand-alone LFS shown in Figure 5-10. Synchronized acquisition of the IR camera and LFS data was still carried out, so that the relation between the temperature distribution on the ITO and the variation of the liquid film thickness could be inferred later by their time-correlation. When the integrated LFS-ITO heater becomes available in the future, several test conditions will be revisited with the integrated configuration, and compared to the results from the stand-alone configuration.

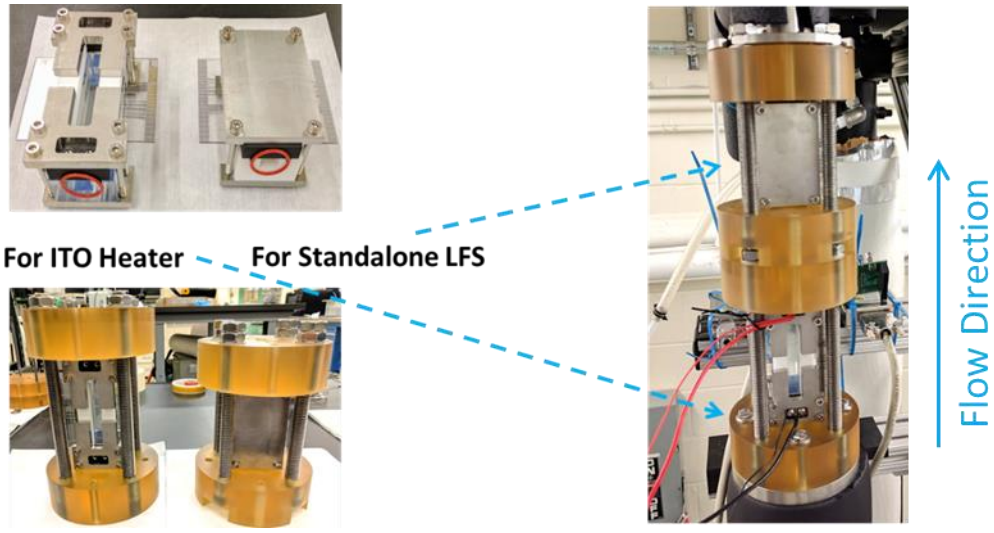

***Figure 5-13**: Images of the stand-alone test section configuration. The ITO heater is installed at upstream, while the LFS is installed downstream.*

5.2.3. LFS Calibration

The LFS was calibrated off-line in a small apparatus at ETH Zurich, as shown in Figure 5-14. The calibration apparatus consists of a step motor, a micrometer screw, a micro-stage, and a controlled plane. During the calibration, the step motor drives the micrometer screw, and thus gradually moves the micro-stage downwards. The minimum step movement of the micrometer screw is 1.25 μm. The micro-stage is mounted with a controlled plane that is parallel to the LFS. A well-controlled liquid film thickness is formed between the controlled plane and the LFS, as the controlled plane gradually pushes down. At each liquid film thickness, the output signal from the LFS is calibrated against the reading from the micrometer-step motor system, thus a calibration curve can be achieved for converting the LFS signal to the thickness value.

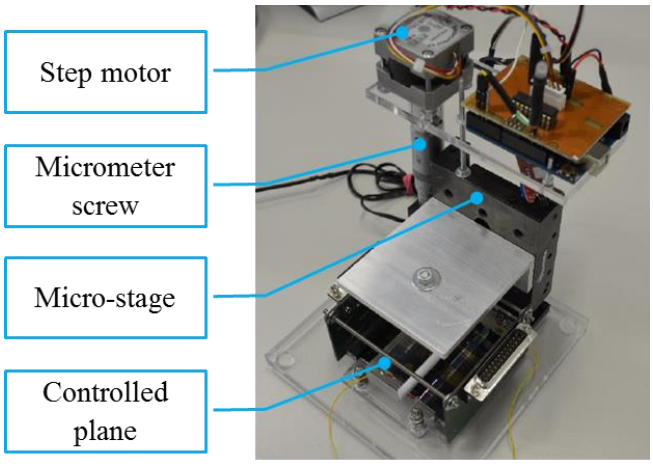

***Figure 5-14**: Image of the calibration apparatus.*

For an accurate and representative calibration, it is important to consider also the correct boundary condition. Since the actual test channel is made of dielectric ceramics (Macor), the boundary condition for the electric field of the LFS should be seen as zero-gradient boundary. To simulate such boundary, a plastic dummy channel was used for the dielectric zero-gradient boundary in the calibration, as shown in Figure 5-15. A plastic piston was connected to the controlled plane to form the liquid film with the LFS inside the dummy channel.

***Figure 5-15**: The plastic dummy channel used in calibration, for simulating the dielectric boundary of the actual flow channel. A plastic piston is used instead of the controlled plan.*

An example of the calibration curve is plotted in Figure 5-16, together with the results from the direct simulation of the electrical potential field. Both the measured and the simulated LFS signals are normalized by the maximum values respectively. As shown, the simulation result

agrees fairly well with the measured calibration curve. Since the calibration apparatus may have mechanical issues when the film thickness is approaching zero, the simulated calibration curve is used given its smooth transition to zero thickness. The LFS was calibrated with a precision of 2.5 μm. The overall uncertainty taken into account the electrical noise is ±13 μm. The calibrated LFS is capable of measuring up to a 2.5 mm thickness of water film. Since each LFS has its own characteristic depending on the neighboring condition, the LFSs locating in the center of the transversal or longitudinal unit have a slightly extended sensitivity up to 2.8 mm compared to the one shown in Figure 5-16.

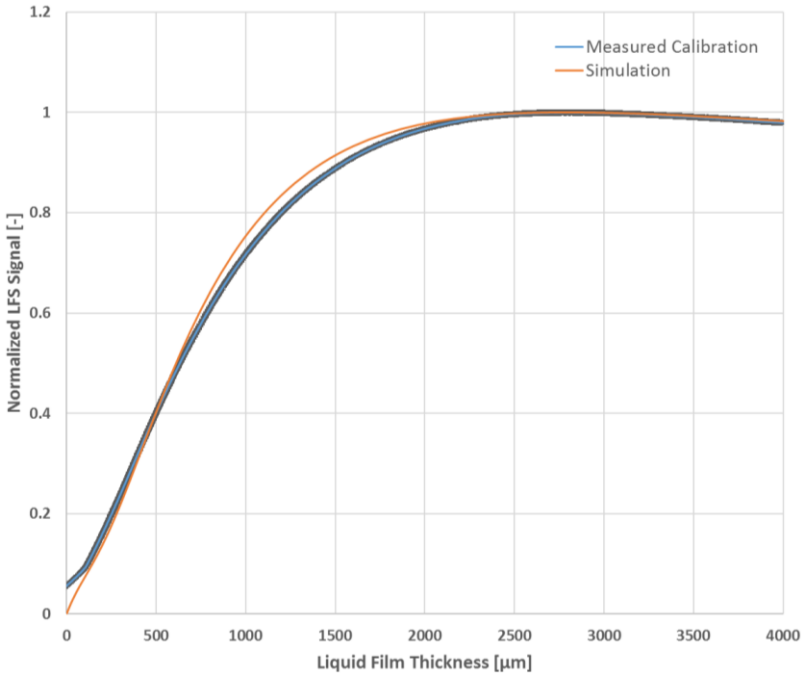

***Figure 5-16**: Comparison between measured calibration curve and simulation. Good agreement has been achieved. The simulation curve shows a better characteristic when thickness approaches zero.*

5.3. Experimental Procedure

For each combination of mass flux and steam quality in the test matrix (see Table 3-4), a steady state condition was first reached. Before ITO heater was energized, the LFS acquired data for a 100 s duration at 10 kHz at adiabatic condition, in order to provide sufficient data points for a statistically robust analysis of the disturbance waves, as well as an accurate inlet condition to the ITO heater. Then, the imposed heat flux was first ramped up until sustained boiling was observed with the IR camera. The heat flux was then gradually decreased with a minimum step of 10 $kW \cdot m^{-2}$,

until boiling completely disappeared. At each heat flux step, after steady state was reached, the synchronized acquisition of the IR camera and LFS data was carried out, so that the relation between the temperature distribution on the ITO and the variation of the liquid film thickness could be inferred by their time-correlation. The IR video was recorded for 3 s at a frame rate of 2 kHz, while the LFS acquired data for 6 s at a sampling rate of 10 kHz.

6. LFS Results: Liquid Film Thickness and Disturbance Waves

In this chapter, the measured liquid film thickness and its statistical profile are presented. A bandwidth criterion is proposed for recognizing the disturbance waves from the other waves with lower amplitude. The disturbance wave properties such as wave velocity, wave amplitude, and wave frequency were extracted using a Skew-Gaussian decomposition algorithm. A mechanism-based correlation was developed for accurate prediction of the mean liquid film thickness.

The liquid film thickness analysis in this section is based on the adiabatic (zero heat flux) measurements with an extended duration of 100 s (1 million data points), which is statistically significant for the characterization of the wavy liquid film behavior.

6.1. Measured Flow Conditions

In the experimental tests, great efforts were made to achieve the steady state flow condition as close to the nominal test matrix conditions as possible. However, due to the strong coupling nature of the total mass flux and the steam quality in steam-water annular flow, it was quite difficult to control both parameters very precisely. The measured flow conditions are listed in Table 6-1, in which the listed uncertainty represents the total uncertainty (total propagated uncertainty if a quantity is not measured directly). Given the non-negligible pressure drop along the flow by friction, the saturation pressure in the test section (p_{sat}) is linearly interpolated from the outlet pressure of the test assembly as follows:

$$p_{sat} = p_{out} + \Delta p_{ET}\left(\frac{L_{TS}}{L_{ET}}\right) \tag{6-1}$$

where p_{out} is the (measured) pressure at the test assembly outlet; Δp_{ET} is the total (measured) pressure drop from the entrance channel inlet to the test assembly outlet; L_{TS} is the length from the center of the test section to test assembly outlet; L_{ET} is the length from the entrance channel inlet to the test assembly outlet. The form pressure loss at entrance and outlet are neglected since the change of flow geometry is fairly gradual.

***Table 6-1**: The measured flow conditions at each test.*

Test #	***G* [kg·m^{-2}·s^{-1}]**	***x_e* [-]**	***P_{sat}* [bar]**
1	772 ±47	0.016±0.001	1.10±0.01
2	1061±47	0.016±0.001	1.15±0.01
3	1352±46	0.015±0.001	1.11±0.01
4	760 ±48	0.030±0.002	1.16±0.01
5	1055±48	0.031±0.001	1.17±0.01
6	1345±46	0.030±0.001	1.22±0.01
7	751 ±49	0.052±0.003	1.22±0.01
8	1030±50	0.051±0.002	1.25±0.01
9	1336±49	0.050±0.002	1.34±0.02
10	737 ±50	0.074±0.005	1.26±0.01
11	1028±54	0.073±0.004	1.37±0.02
12	1318±54	0.070±0.003	1.44±0.03

6.2. Liquid Film Thickness

The raw signal output of the LFS carries a non-negligible level of noise. A commonly-used low pass filtering algorithm, called Kaiser Window finite impulse response (FIR) filter, was applied to suppress the noise in the frequency spectrum, which is different from a moving average or a Savitzky-Golay filter approach, which are applied in the time domain. The Kaiser Window filter is supposed to be more selective in the frequency spectrum, so that the impact on the passband components is minimized. A generous cutoff frequency of 240 Hz was picked, with the purpose of keeping as much raw information as possible. As the cutoff frequency became smaller, the characteristics of the large surface waves were affected more and more. The details of the Kaiser Window filter are discussed in Appendix A.

The time-averaged liquid film thickness for a representative case are plotted in Figure 6-1. As shown, the time-averaged liquid film thickness exhibits a concave shape profile in the transversal direction, i.e., thinner towards the center of the channel and thicker towards the corners of the channel, for all tests conducted. Such profile becomes thinner and more conformal to the

channel geometry (square shape), as mass flux and steam quality increase (see Figure 6-2), as expected. Note that the two outermost points in the transversal unit usually “saturate” since they are facing the films on the adjacent walls. In the longitudinal unit, the time-averaged liquid film thickness profile is always thin and flat, also expected given the symmetry at the center of the channel. The full database of time-averaged liquid film thickness is reported in Appendix B.

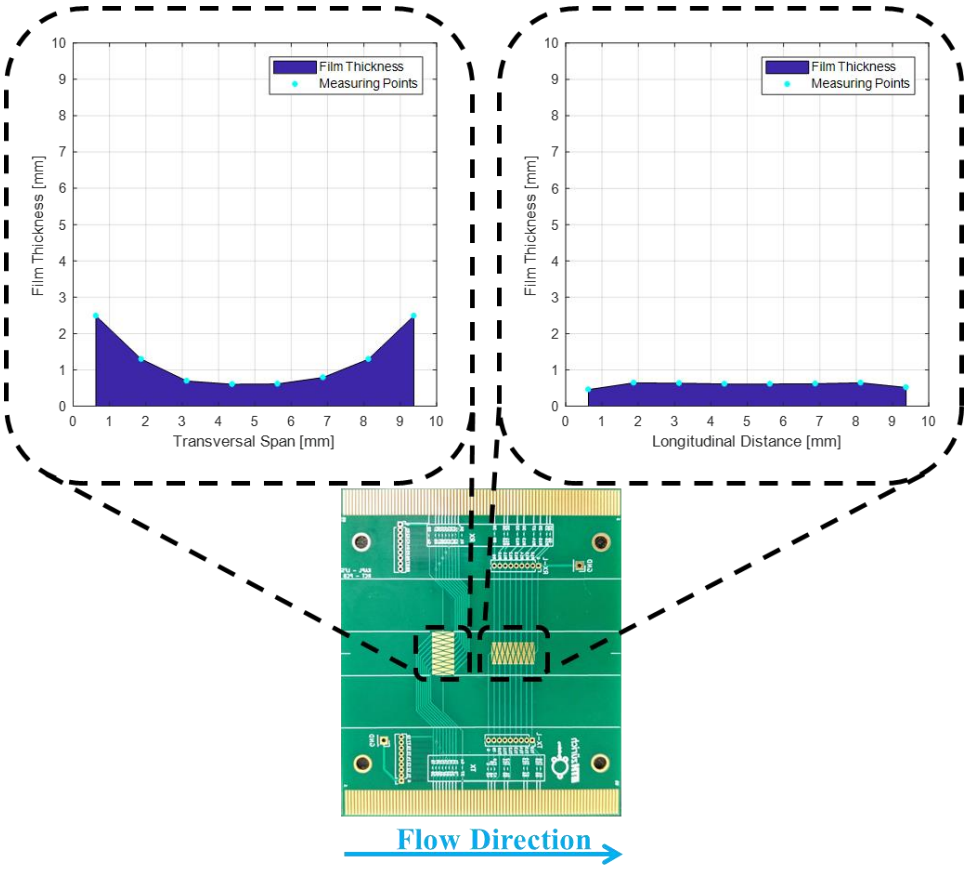

***Figure 6-1**: Time-averaged liquid film thickness measurement from the transversal unit (left) and the longitudinal unit (right), at nominal $G=750\ kg \cdot m^{-2} \cdot s^{-1}$, $x_e = 0.016$. The thickness shows concave profile at transversal direction, while flat profile at longitudinal direction.*

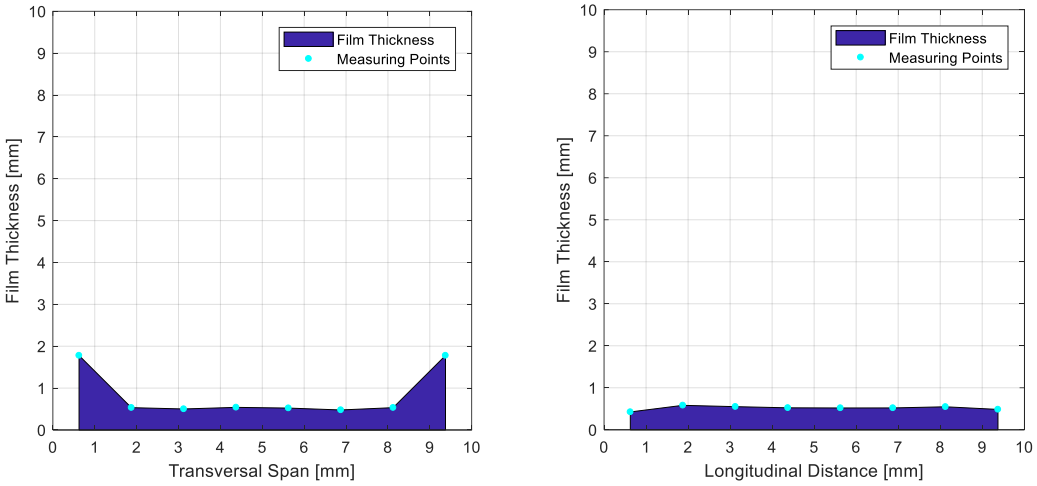

***Figure 6-2**: Time-averaged liquid film thickness measurement at nominal $G=1350\ kg{\cdot}m^{-2}{\cdot}s^{-1}$, $x_e=0.030$. The liquid film becomes thinner and the profile becomes more conformal to the channel geometry.*

The time history of the liquid film thickness measured by the transversal unit is plotted in Figure 6-3 over a duration of 1 s, which gives a clear overview of the periodic rise and fall of the liquid film over time. Note the outer most two measuring points are dropped from the plot due to the saturation issue. In annular two-phase flow, there are disturbance waves that propagate in the flow direction. The crests of the film thickness indicate the arrival of a disturbance wave, while the troughs indicate the departure of a disturbance wave.

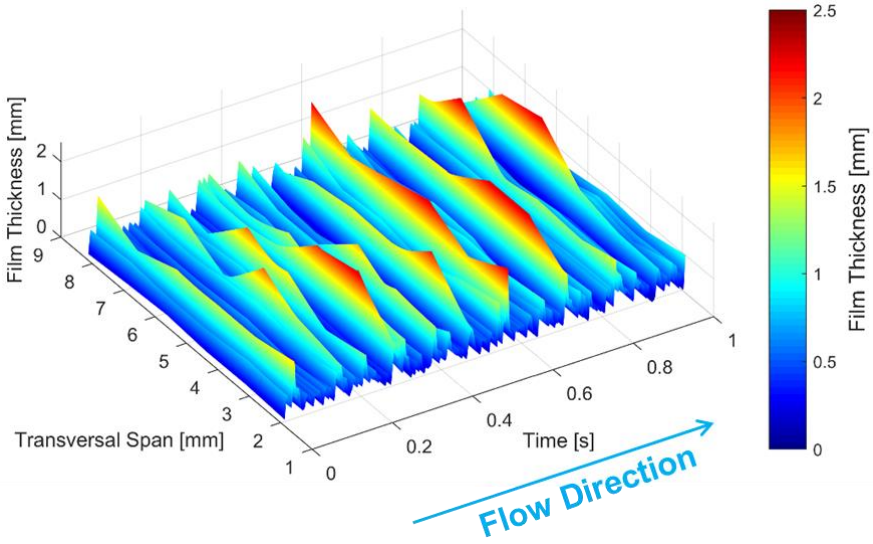

***Figure 6-3**: Time history of liquid film thickness measured at transversal unit at nominal $G=1350\ kg{\cdot}m^{-2}{\cdot}s^{-1}$, $x_e=0.030$. The red peaks indicate the crests of the disturbance waves.*

The typical time history of a single sensor element from the longitudinal unit, which is located at the center of the channel wall (equivalent to 5 mm transversal location in Figure 6-3) is plotted for a duration of 2 s in Figure 6-4. Inspired by the statistical analysis of thin film flow from previous publications [66][67][68], the probability density function (PDF) of the whole 100 s measurement is also plotted to the right of the time history. Figure 6-4 clearly shows the periodic variation of liquid film thickness from a few tens of microns up to approximately 2.5 to 2.8 mm depending on the location of the sensor. The PDF shows a clear peak at medium thickness, and a skewed distribution toward the large thickness. The single bar spike at 2.8 mm indicates the heights of some large disturbance waves exceed the measuring range of the LFS, and represent the remaining tail of the PDF above 2.8 mm. The full database of time history and PDF of single sensor element from the longitudinal unit at each test condition is reported in Appendix C.

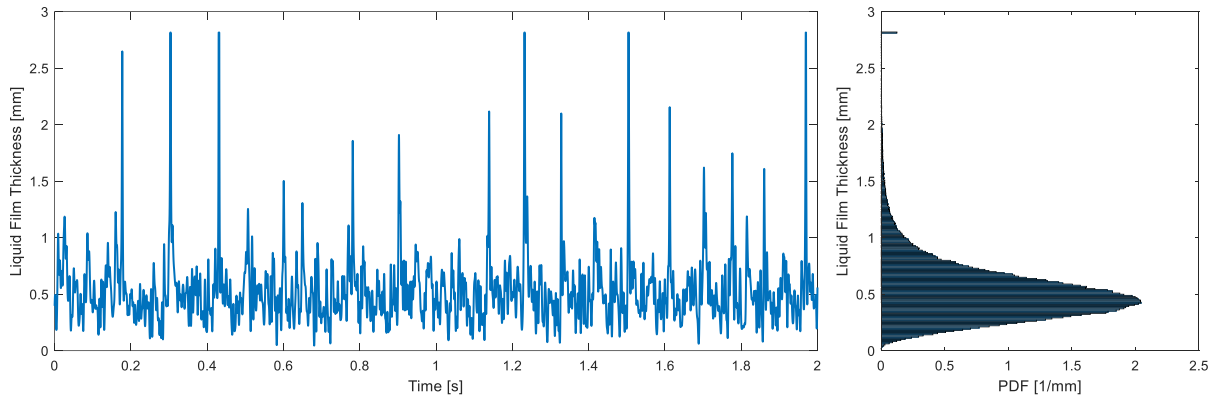

***Figure 6-4**: Time history (left) and PDF (right) of the liquid film thickness measured at a single sensor element from the longitudinal unit, at nominal $G = 1350\ kg \cdot m^{-2} \cdot s^{-1}$, $x_e = 0.030$. The spikes in time history indicate the disturbance wave. The PDF shows a skewed distribution of the liquid film thickness.*

Given the PDF in Figure 6-4, i.e., a profile skewed to the large thickness, the deviations above and below the mean film thickness were calculated separately by the RMS deviation. In the present circumstance, the mean, the plus deviation, and the minus deviation of the film thickness represent different physical processes. The mean film thickness is the embodiment of the mass conservation and the force balance. Thus, the mean film thickness is a fundamental parameter for the prediction of SNB and other heat transfer phenomena. The plus deviation of the film thickness represents the average height of the surface waves above the base film, including both the ripple

waves and the disturbance waves. The minus deviation of the film thickness is the consequence of the accelerated flow following the passage of a large wave.

The 100 s signal were chopped into many statistically significant time slices (5 s each), each of which was treated as an individual test. The mean values of the above three quantities were calculated respectively from each time slice, then the standard deviations of the mean values were evaluated. The results are listed in the Table 6-2 below, where δ, $+\sigma$, $-\sigma$ represent mean, plus deviation and minus deviation of the film thickness respectively. The nominal value (*Nom.*) of the mass flux and steam quality are used to identify the test condition, the measured value of which can be found in Table 6-1 according to Test #. The listed uncertainty represents the total uncertainty (total propagated uncertainty if a quantity is not measured directly).

***Table 6-2**: The mean and standard deviation of the mean, plus deviation and minus deviation of the film thickness.*

Test #	***G* [kg·m^{-2}·s^{-1}]**	**x_e [-]**	**δ [mm]**	**$+\sigma$ [mm]**	**$-\sigma$ [mm]**
1	750	0.016	0.623±0.020	1.038±0.042	0.392±0.017
2	1050	0.016	0.780±0.020	0.931±0.044	0.454±0.021
3	1350	0.016	0.835±0.015	0.381±0.018	0.294±0.015
4	750	0.030	0.487±0.016	0.503±0.033	0.220±0.014
5	1050	0.030	0.492±0.014	0.473±0.021	0.209±0.013
6	1350	0.030	0.528±0.013	0.368±0.022	0.194±0.013
7	750	0.050	0.342±0.014	0.278±0.022	0.152±0.013
8	1050	0.050	0.349±0.014	0.270±0.019	0.145±0.013
9	1350	0.050	0.386±0.014	0.294±0.028	0.146±0.013
10	750	0.070	0.270±0.013	0.189±0.015	0.115±0.013
11	1050	0.070	0.280±0.013	0.192±0.014	0.112±0.013
12	1350	0.070	0.311±0.013	0.227±0.016	0.117±0.013

The mean, plus deviation and minus deviation of the film thickness are plotted against total mass flux at various steam qualities in Figure 6-5. The median of the film thickness is also plotted to give a slightly different point of view from the central value of the skewed distribution. As shown, the plotted parameters barely change with the total mass flux, at the same nominal steam

quality. The mean, median, and plus deviation of the film thickness at norminal G= 750 kg·m^{-2}·s^{-1}, x_e= 0.016 may suffer from the saturation of the LFS signal, which leads to an underestimation of the film thickness. The disturbance waves are normally taller than 2.5 mm at this condition. On the other hand, it is clearly shown that all the parameters decrease appreciably with the increasing steam quality, at the same nominal mass flux.

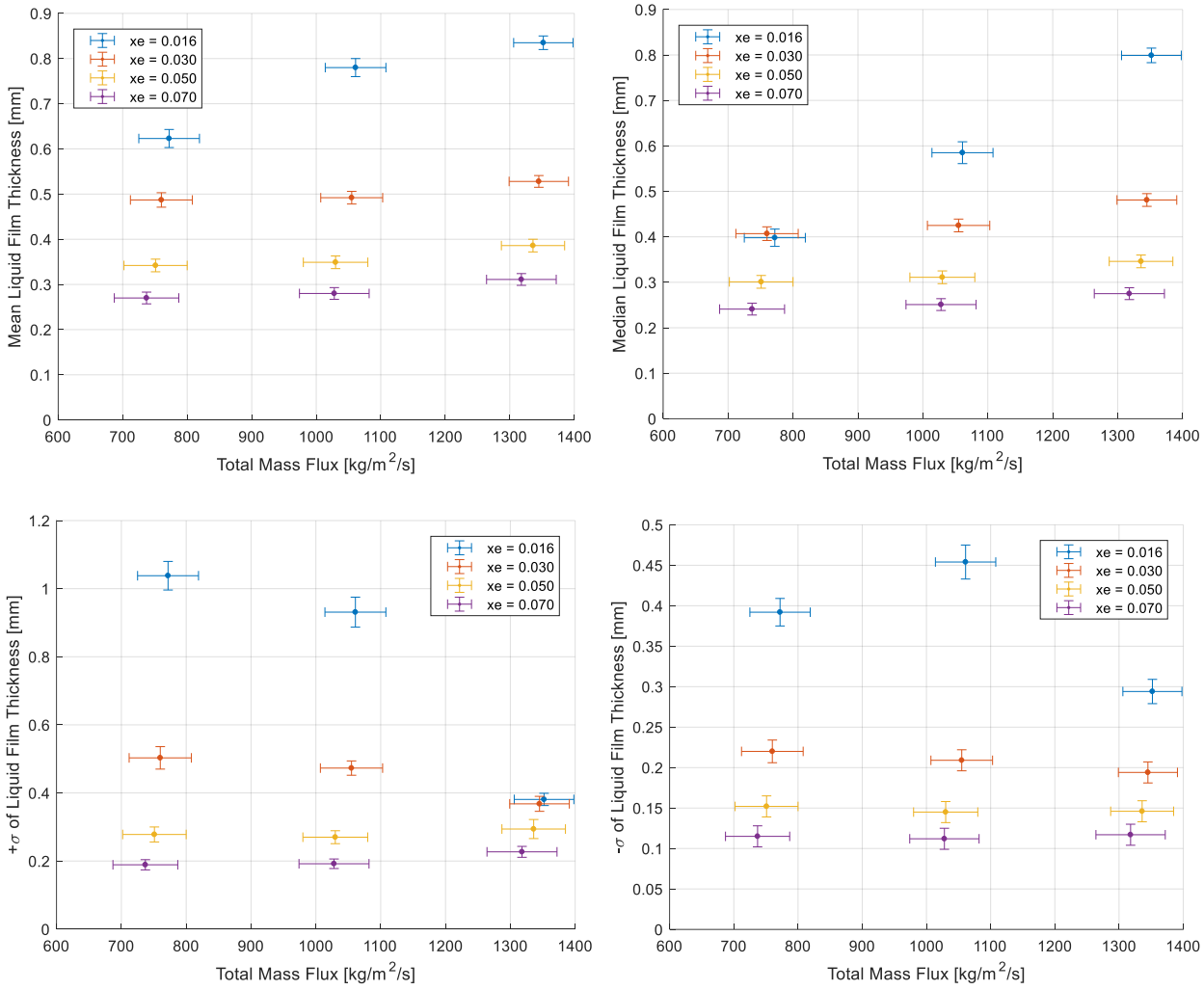

***Figure 6-5**: The mean (upper left), median (upper right), plus deviation (lower left), and minus deviation (lower right) of the film thickness versus mass flux at different steam qualities. The dependency on mass flux is weak (except at x_e=0.016), while the dependency on steam quality is strong at all mass fluxes.*

Given the strong dependency on steam quality, the mean, median, plus deviation and minus deviation of the film thickness are re-plotted versus steam qualities in Figure 6-6. The interesting finding is that the dependency of the plotted parameters on total mass flux is still clear at the lowest

steam quality (nominal 0.016). However, as the steam quality increases, the trends at different total mass fluxes quickly converge.

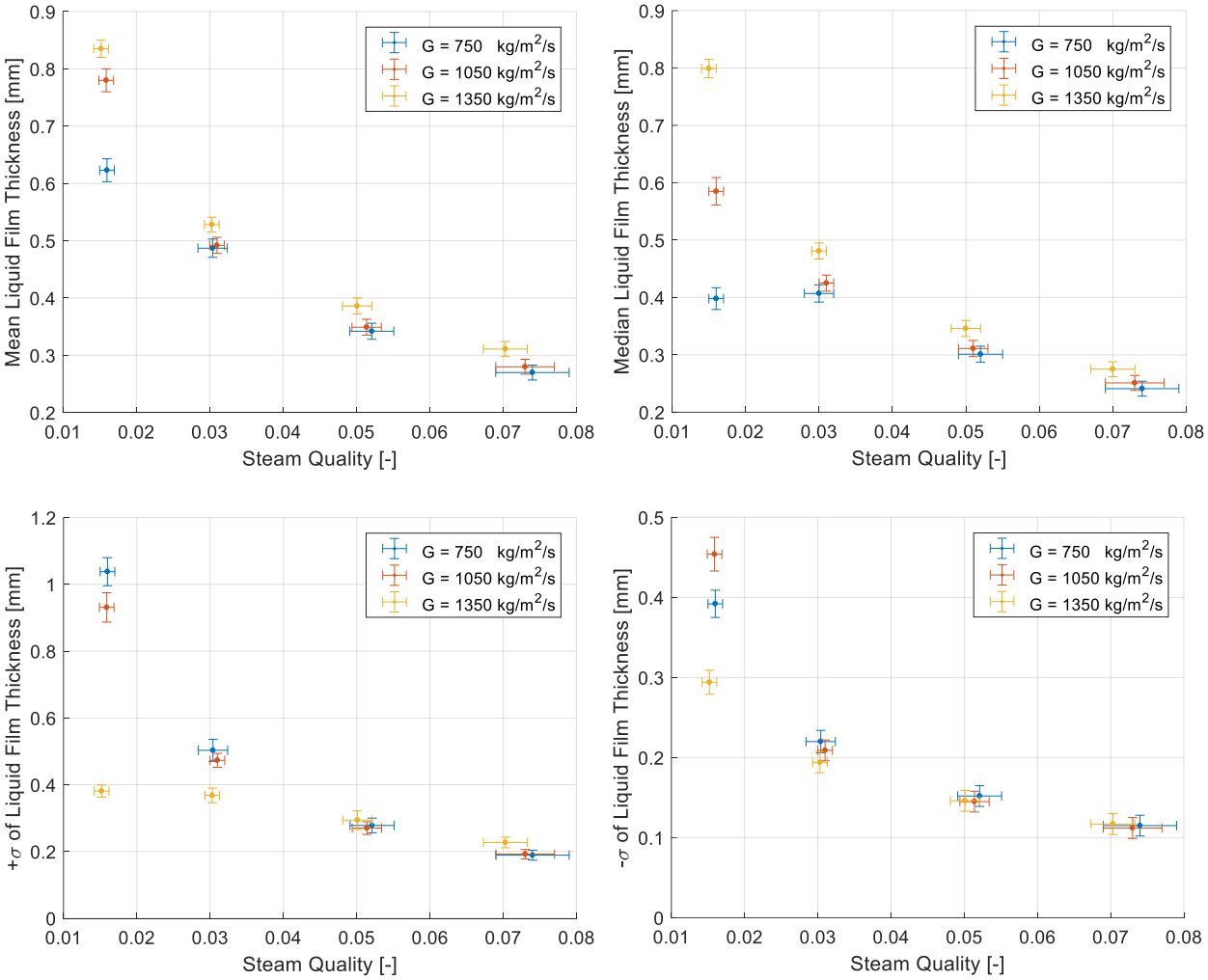

***Figure 6-6**: The mean (upper left), median (upper right), plus deviation (lower left), and minus deviation (lower right) of the film thickness versus steam quality at different mass fluxes.*

The converging trends shown in Figure 6-6 can be explained with the liquid entrainment mechanism introduced in Section 2-4. Three regions are identified according to different stages of liquid-steam interactions and thus the liquid entrainment, as shown in Figure 6-7 using the plot of plus deviation of film thickness. The liquid entrainment rates predicted by Al-Sarkhi's modified Sawant correlation [51] (Eq. 2-31) at each test condition is also shown next to the data points with the same color code.

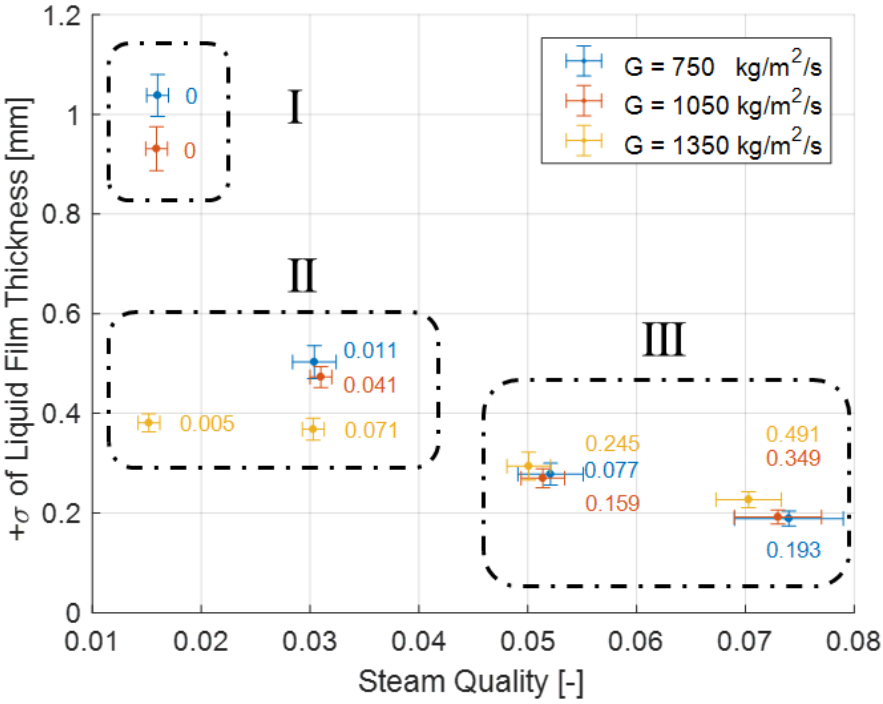

***Figure 6-7**: Three regions of different liquid film behaviors identified by the liquid-steam interaction and the liquid entrainment. The number next to each data point with the same color code is the predicted entrainment rate.*

In region I, the flow condition has not yet fulfilled the initiation of entrainment requirement, thus all the liquid remains in liquid film. The steam core gently pushes, rolls and accumulates the liquid in front of it. Tall disturbance waves are formed. Such process can be illustrated by the beetles analogy (or Sisyphus) shown below.

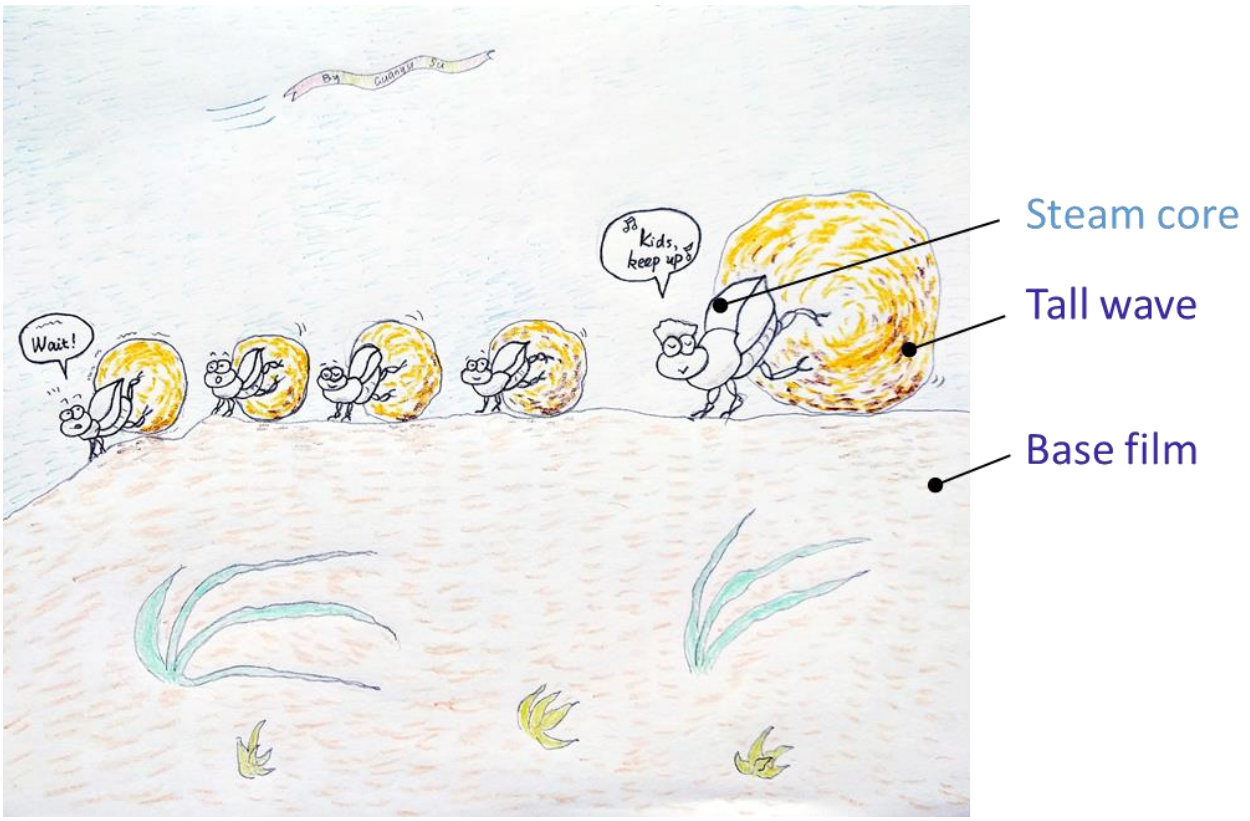

***Figure 6-8**: Beetles analogy of the hydrodynamic mechanism in region I.*

In region II, the liquid entrainment is initiated and gradually increasing at medium steam velocity. The steam core starts entrainment from tearing off the tips of the tall waves, and gradually proceeds toward the main body of the film. The height of the surface waves is reduced, and so does the dependency on the mass flux. Such process can be illustrated by the hollow cutter analogy shown below.

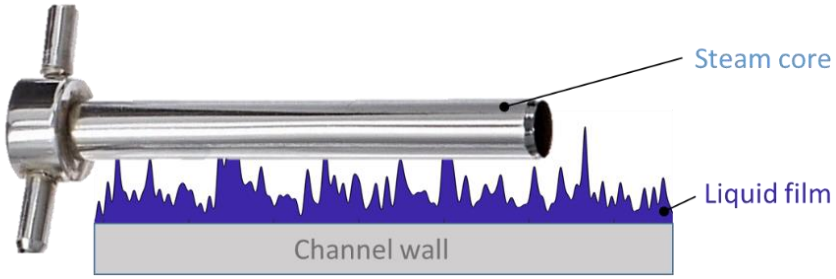

***Figure 6-9**: Hollow cutter analogy of the hydrodynamic mechanism in region II.*

In region III, the high steam velocity results in high liquid entrainment. The steam core erodes into the base of the liquid film, which suppresses the mean height of the surface waves. The

dominance of the liquid entrainment eliminates the dependency on mass flux. Such process can be illustrated by the analogy with a larger and stronger hollow cutter as shown below.

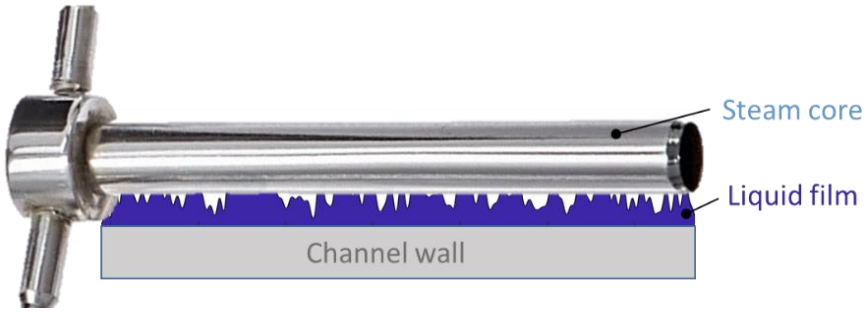

***Figure 6-10**: Hollow cutter analogy of the hydrodynamic mechanism in region III.*

The understanding of the hydrodynamic behavior of the liquid film will be used in a later section for the development of a mechanism-based correlation for mean film thickness.

6.3. Disturbance Wave Properties

6.3.1. Disturbance Wave Recognition

As reviewed in Section 2.3, the disturbance wave in annular flow is often referred to as large amplitude surface wave. Different from the small amplitude ripple that is from surface tension-gravity interaction, the disturbance wave is mostly caused by gas dragging liquid film and thus resulting in tall waves from film accumulation.

In previous investigations, case-by-case tweaked constant film thickness thresholds were used for identifying the disturbance wave [70]. Such a method is practically straight forward, but may suffer from bias, due to the arbitrary selection of the threshold values. In addition, it may also generate error outputs, when ripples are riding on disturbance waves and oscillating around the single constant threshold.

A new robust bandwidth recognition criterion was developed in the current work. Such criterion assumes the large disturbance waves and the small ripple waves are clearly distinguished into two amplitude groups. As a result, the plus deviation ($+\sigma$), and the minus deviation ($-\sigma$) of the film thickness can be used to separate the two groups since they represent the mean crests and troughs of all surface waves. Thus, the mean, plus deviation, and minus deviation of the film thickness are applied to generate the criterion bandwidth, as shown in Figure 6-11. The film

thickness oscillation needs to traverse the whole bandwidth, in order to be recognized as a disturbance wave, which is illustrated between the black vertical bars in Figure 6-11.

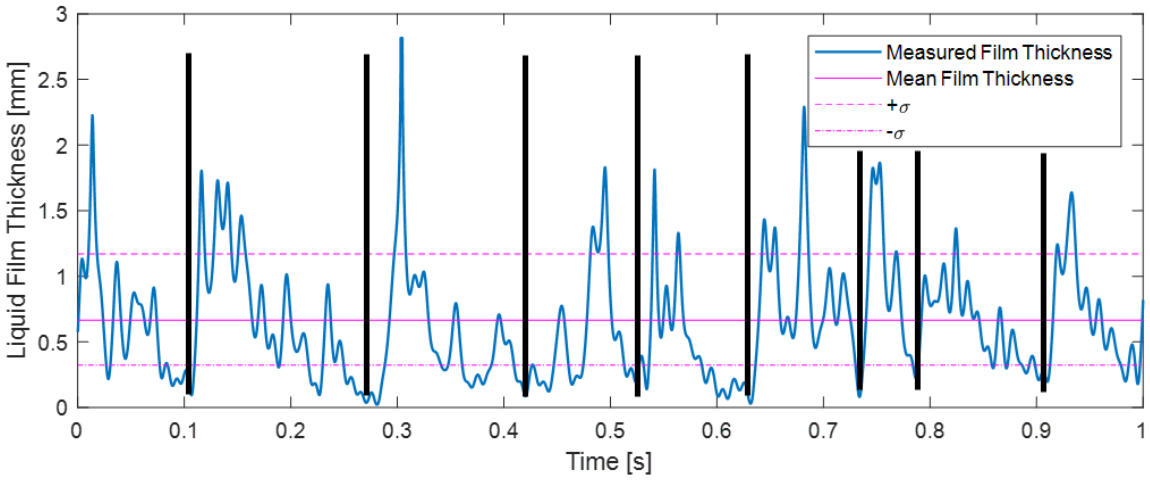

***Figure 6-11**: The bandwidth criterion for the disturbance wave recognition. The black vertical bars identify the disturbance waves recognized by the bandwidth criterion.*

After the recognition process, the oscillation amplitude, the time range and the counts of the disturbance waves were recorded for further estimates of the disturbance wave velocity, amplitude and frequency. The disturbance wave amplitude was calculated as the film thickness difference between the crest and the trough of the wave.

6.3.2. Skewed Gaussian Decomposition for Wave Velocity

With the clearly recognized disturbance waves and a series of LFS along the flow direction it is feasible to extract the propagating velocity of each individual disturbance wave. A well-defined morphology of the disturbance wave is necessary as input to the wave velocity calculation, in order to minimize the uncertainty of the displacement of the wave. Unfortunately, lots of small ripples superimpose on the disturbance waves, and tend to smear out the profile of the latter. As a result, an analytical waveform has to be fitted to each disturbance wave, in order to reconstruct its most probable morphology.

The quality of the fit highly depends on the wave form selected. Three different elementary wave forms are compared in Figure 6-12, together with their PDF. The PDF of the sinusoidal wave shows two peaks at highest and lowest thicknesses respectively. The PDF of the triangle wave is

simply flat. Only the Gaussian train shows a similar PDF profile as the measured thickness (see Figure 6-4), that is peaking at small thickness while skewed toward large thickness. The other finding from the film thickness measurement is that the disturbance wave profile is skewed in the time domain, so that Skewed Gaussians should be used for the fitting instead of the normal ones.

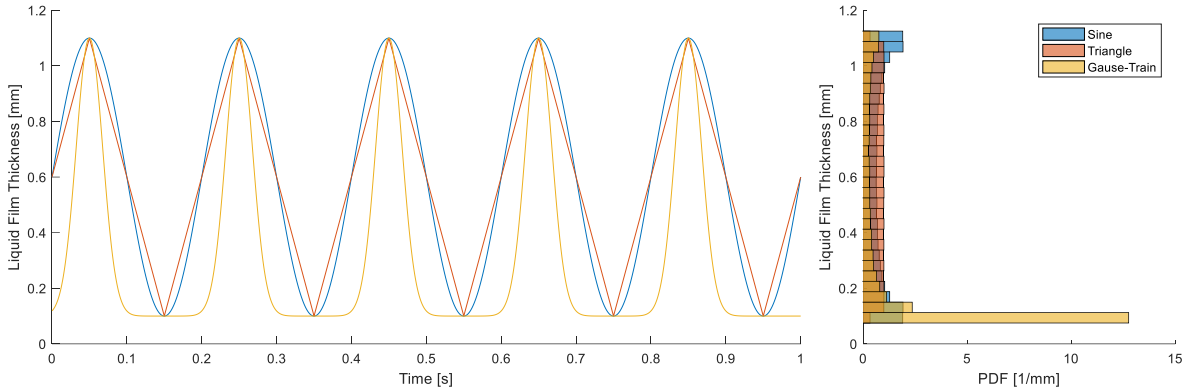

***Figure 6-12**: Comparison of different elementary waveforms. The Gaussian-Train shows the closest PDF to the measured film thickness.*

Inspired by Rychlik's work [71] and Damsohn's work [72], an in-house Skewed Gaussian decomposition algorithm was developed for calculating wave velocity. The thickness signal is decomposed into a series of Skewed Gaussians as given by Eq. 6-2 [73], representing the most probable shape and position of each individual disturbance wave, where t is time; a_i, b_i, c_i, d_i are fitting coefficients for each wave; and *erfc* is the complementary error function providing the necessary skewness. An example of the decomposed wave is compared with the measurement in Figure 6-13, which shows good agreement with the underlying behavior of the waves.

$$\delta(t) = \sum_{i=1}^{n} a_i \, e^{-\left(\frac{t-b_i}{c_i}\right)^2} \, erfc\left(-d_i\left(\frac{t-b_i}{c_i}\right)\right) \tag{6-2}$$

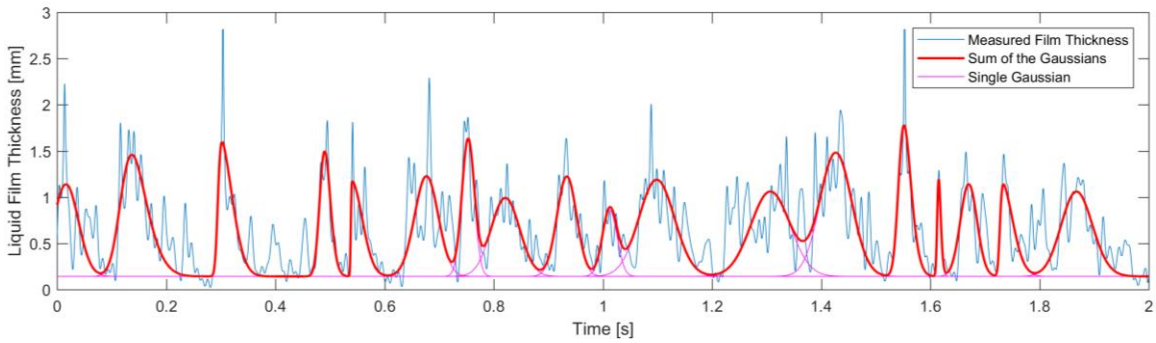

***Figure 6-13**: Skewed Gaussian decomposed disturbance waves compared with the measurement. The single Gaussian captures the individual disturbance wave fairly well, while the sum of the Gaussians reproduces accurately the time history.*

The decomposed Skewed Gaussians from two distanced away sensor-pairs in the flow direction are used to calculate time cross-correlations as illustrated in Figure 6-14; such calculation yields the most probable time delay between each pair of related Gaussians, as shown in Figure 6-15. Given the relatively high wave speed, the further away the two sensor pairs are, the more accurate will be the time delay of the related Gaussians. According to the LFS layout in Figure 5-10, the thickness measurements from the sensor pair at the center of the transversal unit and the one at the furthest end of the longitudinal unit were used. Finally, the velocity of each disturbance wave is calculated by taking the ratio of the spatial distance between the two sensor-pairs and the most probable time delay.

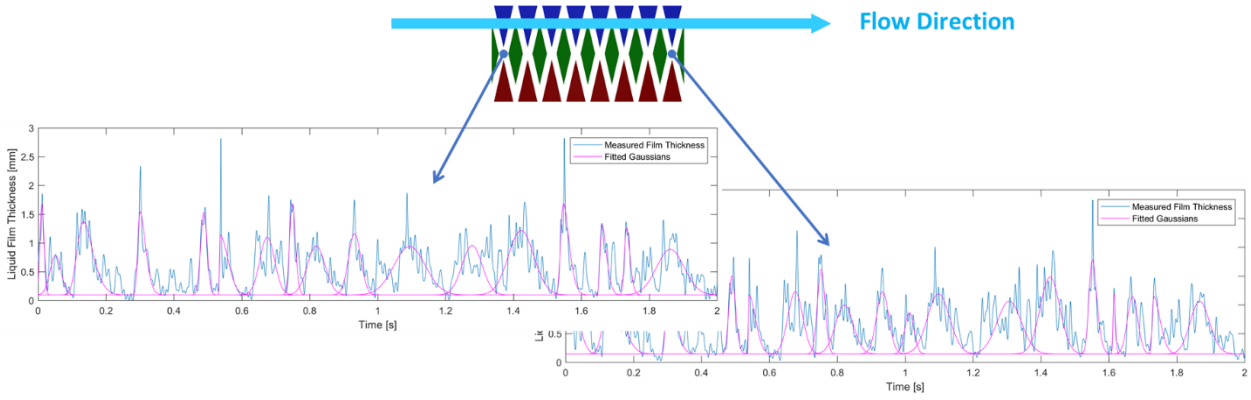

***Figure 6-14**: Illustration of time delay between pairs of Skewed Gaussians.*

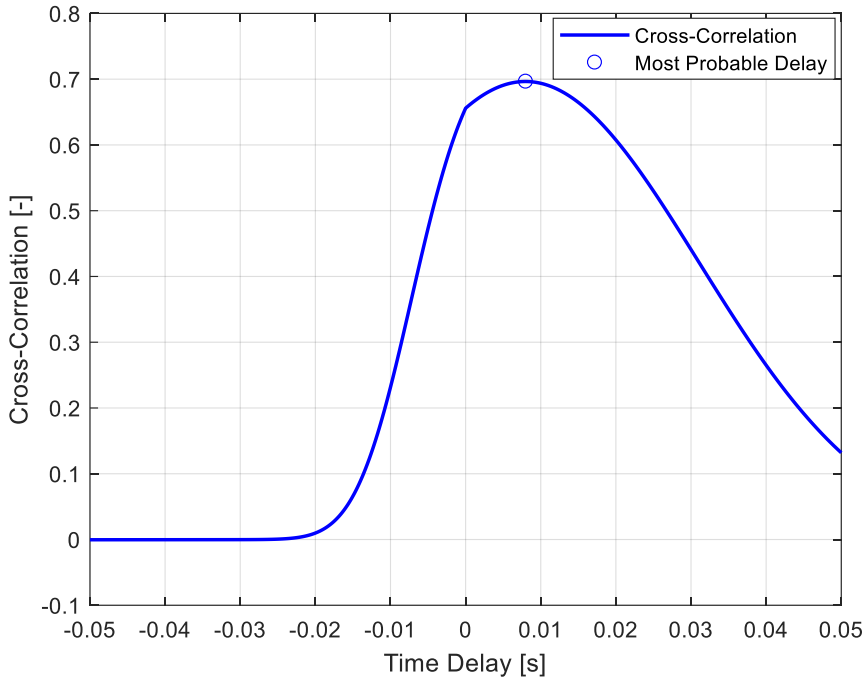

***Figure 6-15**: An example of the cross-correlation between two correlated Gaussians at various time delays. The most probable time delay corresponds to the peak of the curve.*

A typical result of the achieved disturbance wave velocity is shown in Figure 6-16. In the plot, it can be seen that the velocities of few disturbance waves are mistakenly identified as slightly minus value, due to the change of the wave morphology or the propagation path. One example is that a long wave hovers around two sensors, while keeps changing its peak position before it leaves the LFS. Another example is a wave observed at one sensor but missed by the other sensor, since it propagates sideways but not strictly along flow direction. The occasional failure of the cross correlation algorithm suggests there exists a conflict between the wave velocity calculation and the disturbance wave identification. That is, more well spaced-out pairs of LFS can enhance the accuracy of calculating the time delay (thus more accurate velocity), but the disturbance wave itself may change over the long distance travelled between the LFS pair. For a simple evaluation of the calculation quality, a quantity called “wave velocity quality ratio” is defined scaling from 0 to 1, which is the ratio of the number of the velocities larger than zero over the total number of the identified disturbance waves. Overall, the algorithm provided a quality ratio from 0.71 to 0.86 depending on the flow conditions. The Skewed Gaussian decomposition algorithm was validated with the measurement from LFS and the measurement from high speed video (HSV) separately, the details of which are reported in Appendix D.

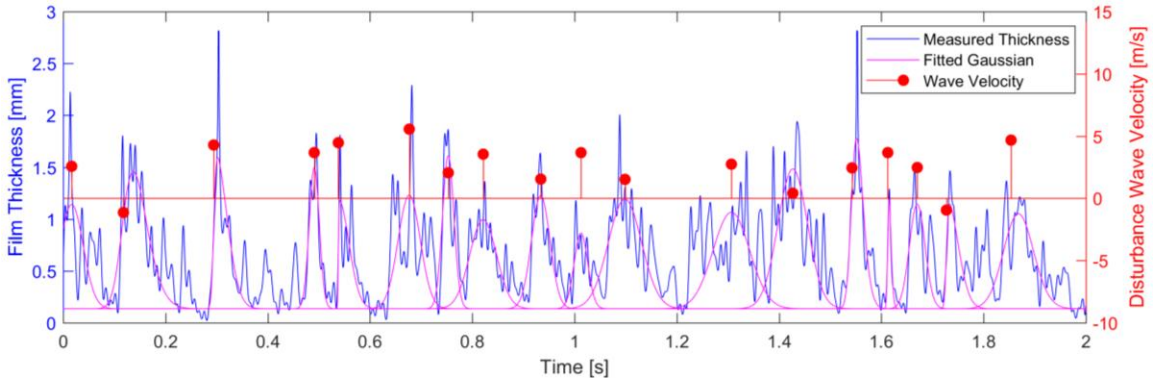

***Figure 6-16**: Sample result of the wave velocity calculated by the Skewed Gaussian decomposition algorithm. The velocity is shown as a dot at the peak position of each Gaussian.*

6.3.3. Results of the Disturbance Wave Properties

The disturbance wave velocity, wave amplitude and wave frequency extracted from the algorithm described above are plotted against the total mass flux at various steam qualities in Figure 6-17. The wave velocity monotonically increases with the increasing mass flux, at constant nominal steam quality. The trend is the same for constant nominal mass flux and increasing steam quality. The dependency of wave velocity on steam quality is also more pronounced than on mass flux. The wave amplitude decreases with the increasing steam quality at constant nominal mass flux. The amplitude of the film thickness at nominal G= 750 kg·m^{-2}·s^{-1}, x_e= 0.016 may be affected by the saturation effect of the LFS signal, which leads to underestimated values. The disturbance waves are normally taller than 2.8 mm at this condition. The wave frequency increases with the increasing steam quality at constant nominal mass flux, except for an outlier point at nominal G= 1350 kg·m^{-2}·s^{-1}, x_e= 0.016. The outlier point will be later (in Section 7.2) shown to be a real physical phenomenon not a measuring error. The outlier frequency may be related to the transition around initiation of entrainment, which could introduce additional disturbance to the liquid film. As shown in Figure 6-7, the predicted entrainment rate is barely above the initiation of entrainment at nominal G= 1350 kg·m^{-2}·s^{-1}, x_e= 0.016.

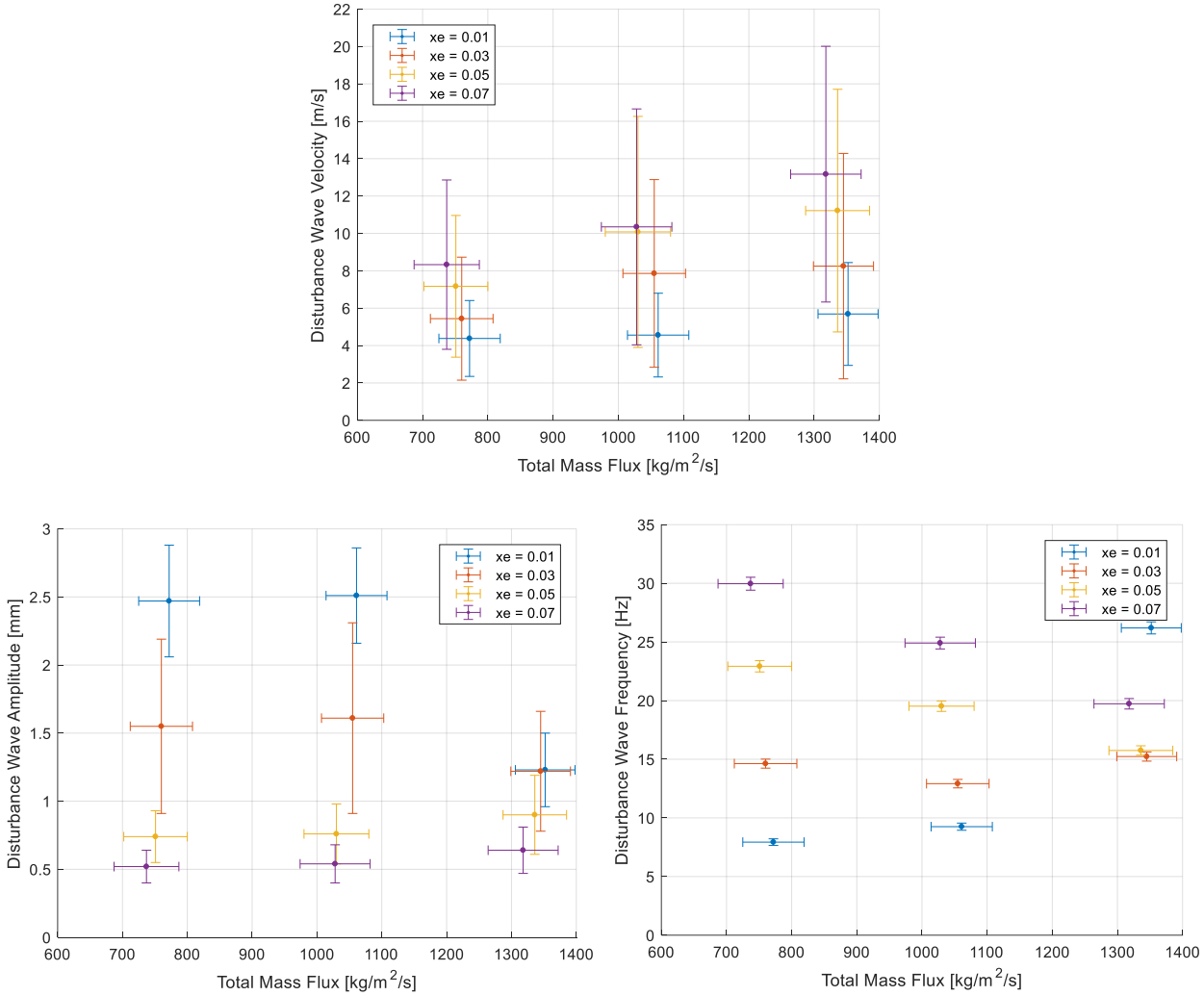

***Figure 6-17**: The disturbance wave velocity (top), amplitude (lower left) and frequency (lower right) versus mass flux at different steam qualities.*

Given the strong dependency on steam quality, the disturbance wave velocity, wave amplitude and wave frequency are re-plotted versus steam qualities in Figure 6-18. The dependency of wave velocity and wave frequency on mass flux have not totally disappeared as steam quality increases. The dependency of the wave amplitude on the total mass flux is visible at the lowest steam quality (nominal 0.016). However, as the steam quality increases, the trends at different total mass fluxes quickly converge, which is exactly the same trend for the plus deviation of the film thickness shown in Figure 6-6.

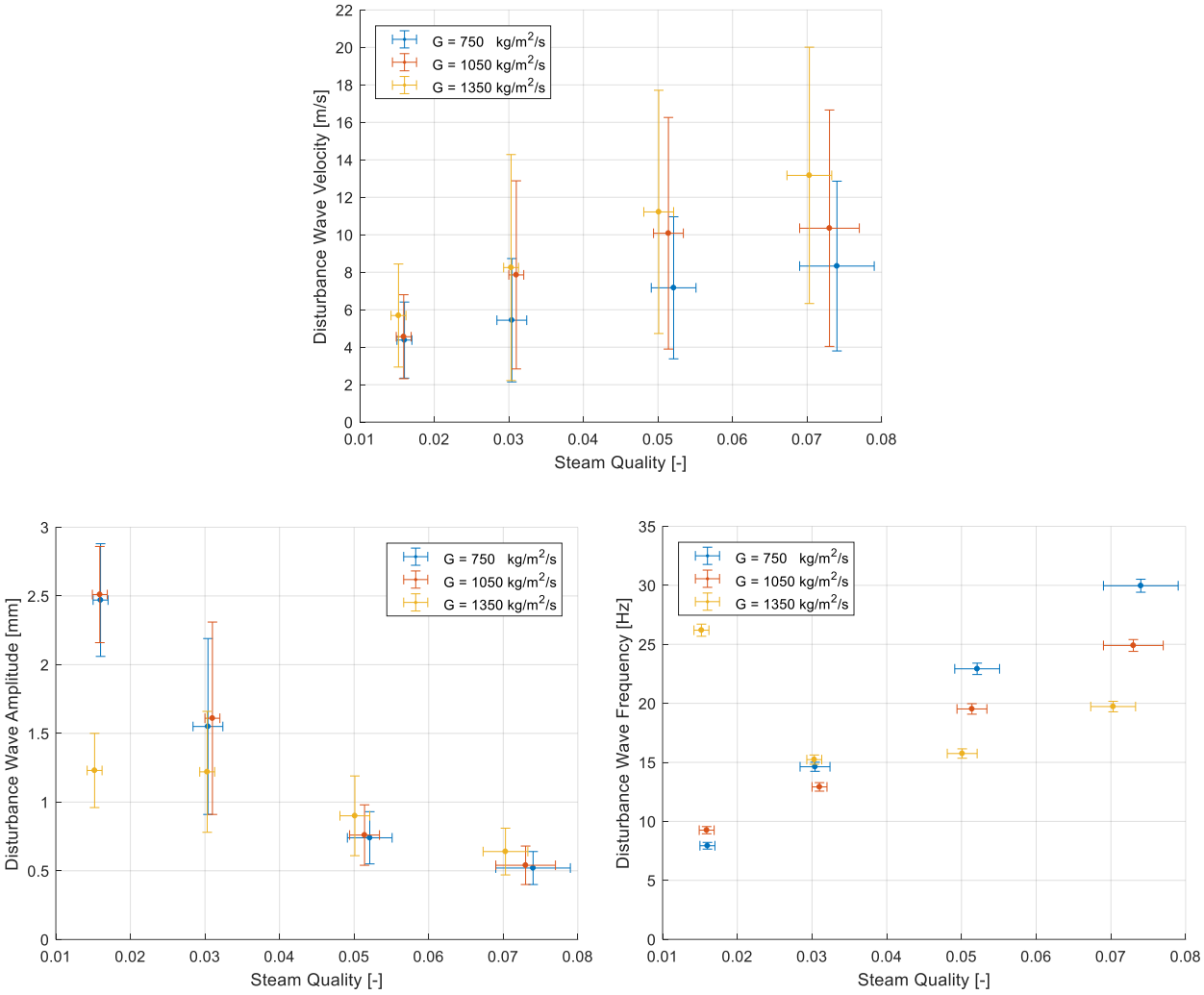

***Figure 6-18**: The disturbance wave velocity (top), amplitude (lower left) and frequency (lower right) versus steam quality at different mass fluxes.*

The wave frequency data were cast in dimensionless form using the Strouhal number ($St_g = fD_h/v_{sg}$), as shown in Figure 6-19. The Strouhal number seems to plateau after a sufficiently high critical steam quality. Generally, the larger is the mass flux, the higher is the critical steam quality.

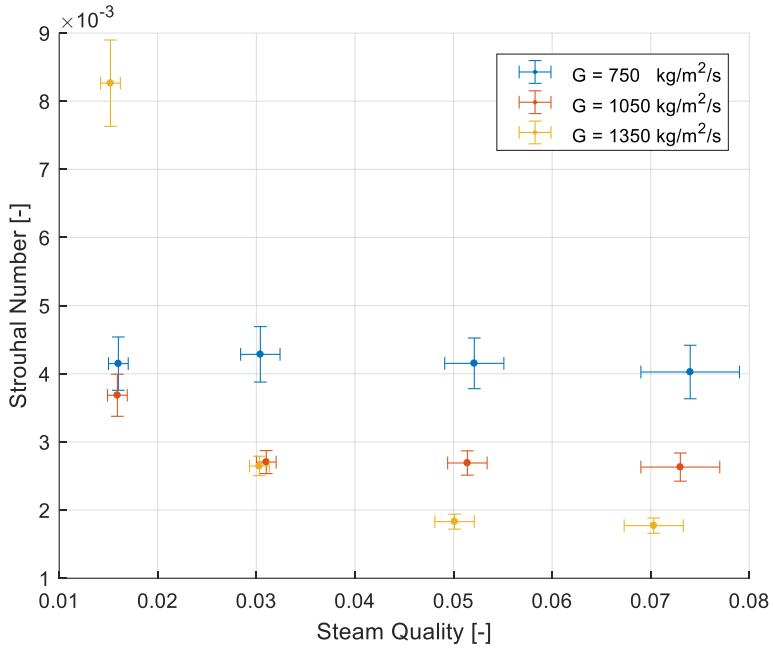

***Figure 6-19**: Dimensionless wave frequency (Strouhal number) versus steam quality at various mass fluxes. Trends seems to plateau at each mass flux as steam quality increases.*

Another interesting finding from Figure 6-17 and Figure 6-18 is that the standard deviations for disturbance wave velocity and frequency are quite large, which indicates broad distributions. Such broad distribution may relate to different sub-categories of the disturbance waves. In the present study, only small ripples and large disturbance waves were considered. No attempt was made to analyze possible sub-categories of the disturbance waves. Examples of the statistical profiles of the disturbance wave velocity and amplitude are shown in Figure 6-9. In general, there is only one mode (i.e., only one maximum in the PDF or probability) for the wave velocity and wave amplitude respectively. However, at low steam quality condition, a second mode could appear at the largest wave amplitude, due to the upper limit of the LFS measurement. As a result, all the disturbance waves with amplitude larger than the LFS limit are concentrated into the last two bins at the largest amplitude end. A full list of the probability profiles of the disturbance wave velocity and amplitude at each test condition are shown in Appendix E.

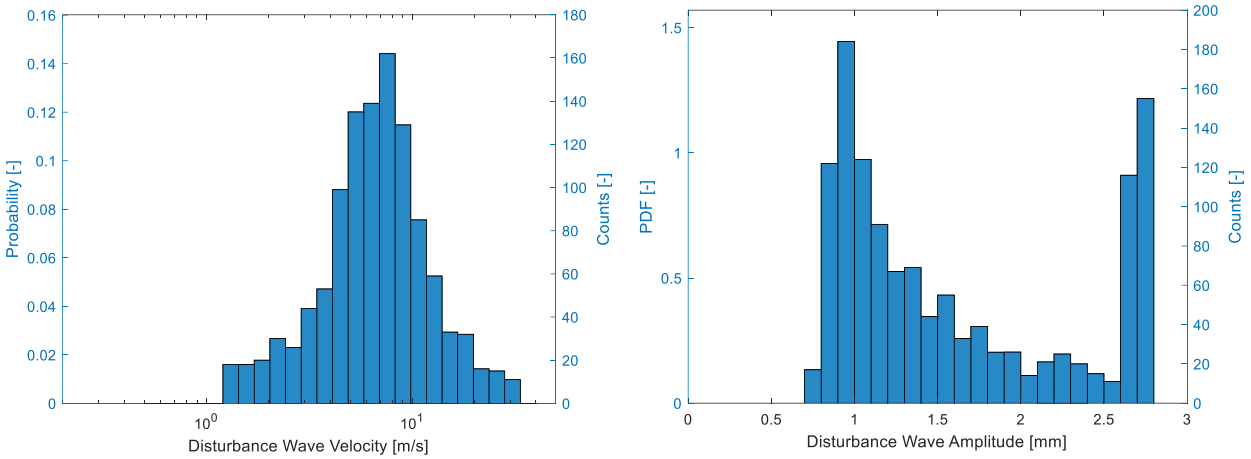

***Figure 6-20**: Sample statistical profiles of disturbance wave velocity and amplitude at G= 1050 kg·m^{-2}·s^{-1}, x_e= 0.030. The mode at the largest amplitude end on the wave amplitude plot is caused by the measuring limit of the LFS.*

6.4. Modeling Liquid Thin Film

In this section the mean liquid film thickness is modeled, as it is the most important boundary condition for the heat transfer model (described in Section 7.4.1) and thus the determination of the SNB conditions. The modeling of the other disturbance wave properties is left to future work.

The liquid film thickness is the outcome of the mass conservation and the force balance on the liquid film at each combination of flow conditions. The film thickness value is strongly related to the pressure gradient, and shear stresses on both sides of the film (liquid-steam interface and channel wall). Pressure is assumed the same in the liquid and vapor phases at a given axial location x. The liquid thin film can be represented two dimensionally, as shown in Figure 6-21 with y and x being the wall normal direction and flow direction, respectively. In Figure 6-21 and Eq. 6-3 to 6-5, g is the gravitational acceleration. δ is the liquid film thickness. $\bar{v}$ and T are the velocity in the flow direction and temperature in the wall normal direction, respectively. With the fully-developed steady-state assumption, the momentum equation can be simplified as follows:

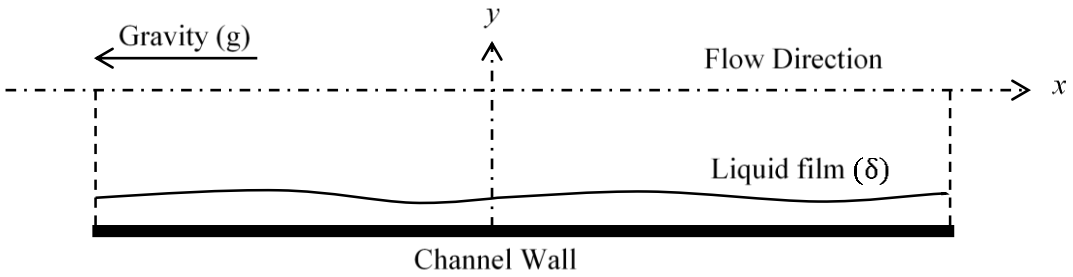

***Figure 6-21**: Simplified 2D geometry of the annular flow.*

$$0 = -g - \frac{1}{\rho_l}\frac{\partial \bar{p}}{\partial x} + \frac{1}{\rho_l}\frac{\partial \tau}{\partial y} \tag{6-3}$$

Integrating the shear stress in the above equation over the film thickness gives:

$$-\rho_l g - \frac{d\bar{p}}{dx} = \frac{\tau_w}{\delta} - \frac{\tau_i}{\delta} \tag{6-4}$$

Replacing the pressure gradient in the liquid film with the two-phase pressure gradient:

$$-\rho_l g - \left(\frac{d\bar{p}}{dx}\right)_{2\phi} = \frac{\tau_w}{\delta} - \frac{\tau_i}{\delta} \tag{6-5}$$

The two-phase pressure gradient can be further expressed by friction and gravity components:

$$-\rho_l g + \rho_m g + \left(\frac{d\bar{p}}{dx}\right)_{2\phi-fric} = \frac{\tau_w}{\delta} - \frac{\tau_i}{\delta} \tag{6-5}$$

The two-phase friction pressure drop was estimated with Friedel correlation [3] in the current test range, which was found to be 3 to 15 times larger than the gravity term depending on the flow conditions. The gravity term is thus neglected to simplify the equation. The two-phase friction pressure drop can be expressed by all gas friction pressure drop and a multiplier.

$$\left(\frac{d\bar{p}}{dx}\right)_{g-fric} \phi_g^2 = \frac{\tau_w}{\delta} - \frac{\tau_i}{\delta} \tag{6-6}$$

Where $\phi_g^2 = 1 + 20X_{tt} + X_{tt}^2$, and $X_{tt} = \left(\frac{1-x}{x}\right)^{0.9}\left(\frac{\rho_g}{\rho_l}\right)^{0.5}$.

All the terms in Eq. 6-6 can be further expressed by velocity and Darcy friction factor:

$$\frac{f_{sg}G^2x^2}{2D_h\rho_g}\,\phi_g^2 = \frac{1}{\delta}\left(\frac{f_l\rho_l\overline{v_l}^2}{8} - \frac{f_i\rho_g\overline{v_g}^2}{8}\right) \tag{6-7}$$

Where f_{sg}, f_l, f_i are friction factor defined on superficial gas velocity v_{sg}, liquid velocity $\bar{v}_l$, and interfacial condition, respectively. Since $\overline{v_g} \gg \bar{v}_l$, the velocity difference between gas and liquid $\overline{v_g} - \bar{v}_l \cong \overline{v_g}$.

Reorganizing the above equation gives:

$$\frac{\delta}{D_h}\,\phi_g^2 = \frac{1}{4}\left(\frac{f_l\rho_l\overline{v_l}^2}{f_{sg}\rho_g v_{sg}^2} - \frac{f_i\rho_g\overline{v_g}^2}{f_{sg}\rho_g v_{sg}^2}\right) \tag{6-8}$$

Applying the mass conservation and the geometry relation below, the average liquid and gas velocity can be converted into superficial liquid and gas velocity. E is the entrainment ratio calculated by Al-Sarkhi's simplified Sawant correlation [51].

$$\bar{v}_l \cong \frac{D_h}{4\delta}v_{sl}(1-E) \tag{6-9}$$

$$\bar{v}_g \cong v_{sg}\frac{\frac{D_h}{4\delta}}{\frac{D_h}{4\delta}-1} \tag{6-10}$$

$$\frac{\delta}{D_h}\,\phi_g^2 = \frac{1}{4}\left(\frac{f_l\rho_l\overline{v_l}^2}{f_{sg}\rho_g v_{sg}^2} - \frac{f_i\rho_g\overline{v_g}^2}{f_{sg}\rho_g v_{sg}^2}\right) \tag{6-11}$$

The friction factors can be expressed in terms of the Reynolds numbers via Blasius relation [3].

$$f_l = C_l Re_{sl}^{-0.25}(1-E)^{-0.25}\left(\frac{D_h}{4\delta}\right)^{-0.25} \tag{6-12}$$

$$f_{sg} = C_g Re_{sg}^{-0.25} \tag{6-13}$$

$$f_i = C_{ig} f_{sg} \tag{6-14}$$

Substituting Eqs. 6-12, 6-13, 6-14 into Eq. 6-11 gives:

$$\frac{\delta}{D_h}\ \phi_g^2 = \frac{1}{4}\left(\frac{C_l}{C_g}\frac{Re_{sg}^{0.25}}{Re_{sl}^{0.25}}\frac{(1-E)^2\ \left(\frac{D_h}{4\delta}\right)^2}{(1-E)^{0.25}\ \left(\frac{D_h}{4\delta}\right)^{0.25}}\frac{\rho_g}{\rho_l}\frac{\mu_l^2}{\mu_g^2}\frac{Re_{sl}^2}{Re_{sg}^2} - C_{ig}\frac{\left(\frac{D_h}{4\delta}\right)^2}{\left(\frac{D_h}{4\delta}-1\right)^2}\right) \tag{6-15}$$

Reorganizing the terms gives:

$$\left(\frac{\delta}{D_h}\right)^3\ \phi_g^2 = \frac{1}{64}\left(\frac{C_l}{C_g}\frac{(1-E)^{1.75}}{\left(\frac{D_h}{4\delta}\right)^{0.25}}\frac{\rho_g}{\rho_l}\frac{\mu_l^2}{\mu_g^2}\frac{Re_{sl}^{1.75}}{Re_{sg}^{1.75}} - C_{ig}\frac{1}{\left(\frac{D_h}{4\delta}-1\right)^2}\right) \tag{6-16}$$

Given the fact that $D_h \gg \delta$ and the larger exponent of the second term on the right hand side of the above equation, the second term is neglected to focus on the main dependencies, and thus simplify the equation. The final functional form is provided as below. Since the system pressure was not appreciably varied in the present study, the exponents for the density ratio and viscosity ratio are fixed according to the derivation.

$$\frac{\delta}{D_h} \propto a_1 Re_{sl}^{a_2} Re_{sg}^{-a_2}(1-E)^{a_4}\left(\frac{\rho_g}{\rho_l}\right)^{0.333}\left(\frac{\mu_l}{\mu_g}\right)^{0.667} \tag{6-17}$$

The coefficients a_i ($a_i > 0$) were varied to achieve the best fit of the data sets as below:

$$\frac{\delta}{D_h} = 0.0146 Re_{sl}^{0.78} Re_{sg}^{-0.65}(1-E)^{0.1}\left(\frac{\rho_g}{\rho_l}\right)^{0.333}\left(\frac{\mu_l}{\mu_g}\right)^{0.667} \tag{6-18}$$

The comparison of the measured δ/D_h and the predicted values by the above correlation is plotted in Figure 6-22, which shows a close agreement within ±5% discrepancy. Note that the data point at G= 750 kg·m^{-2}·s^{-1}, x_e= 0.016 is excluded from comparison due to two reasons. First, the flow condition is still in the transition region between slug/churn flow and annular flow. Second, the LFS measurement was heavily affected by signal saturation for this data point.

The proposed correlation (Eq. 6-18) is also compared with other authors' correlations introduced in Section 2.3.2. As shown in Figure 6-23, Eq. 6-18 obviously gives the best prediction of the present experimental data, since it was fitted to it. The discrepancy of other correlations may come from two aspects: a) the difference in two-phase system, i.e., air-water versus steam-water (present study); b) the difference in superficial liquid velocity, i.e., low j_l versus high j_l (present study). Eq. 6-18 will be the input for modeling the SNB conditions in the following sections.

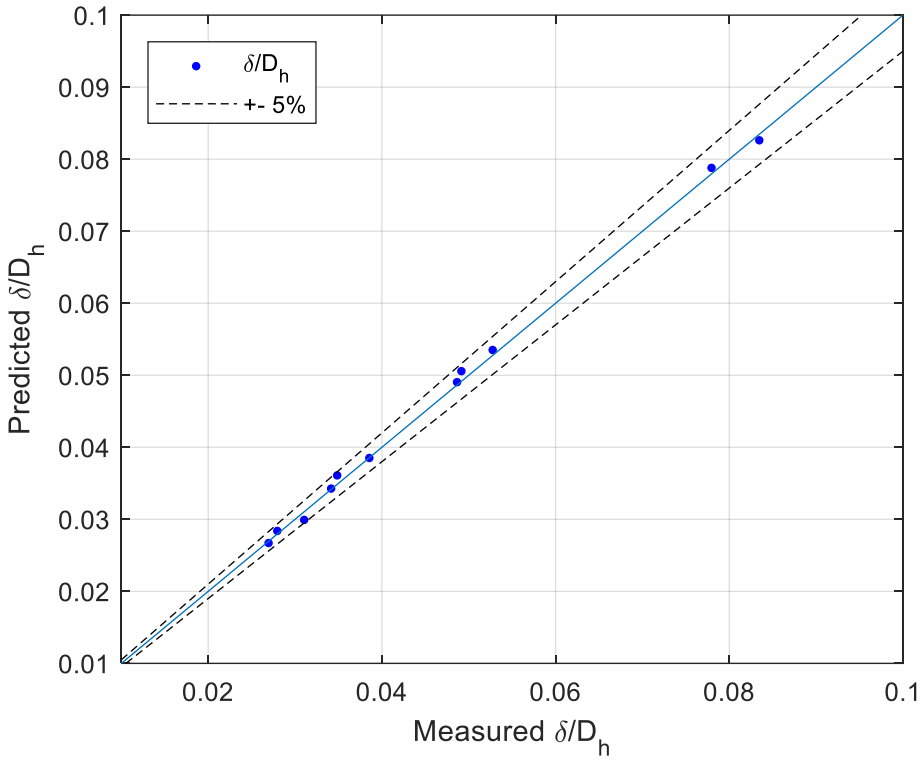

***Figure 6-22**: Comparison between measured and predicted dimensionless film thickness δ/D_h of the proposed correlation. Close agreement within ±5% discrepancy has been achieved.*

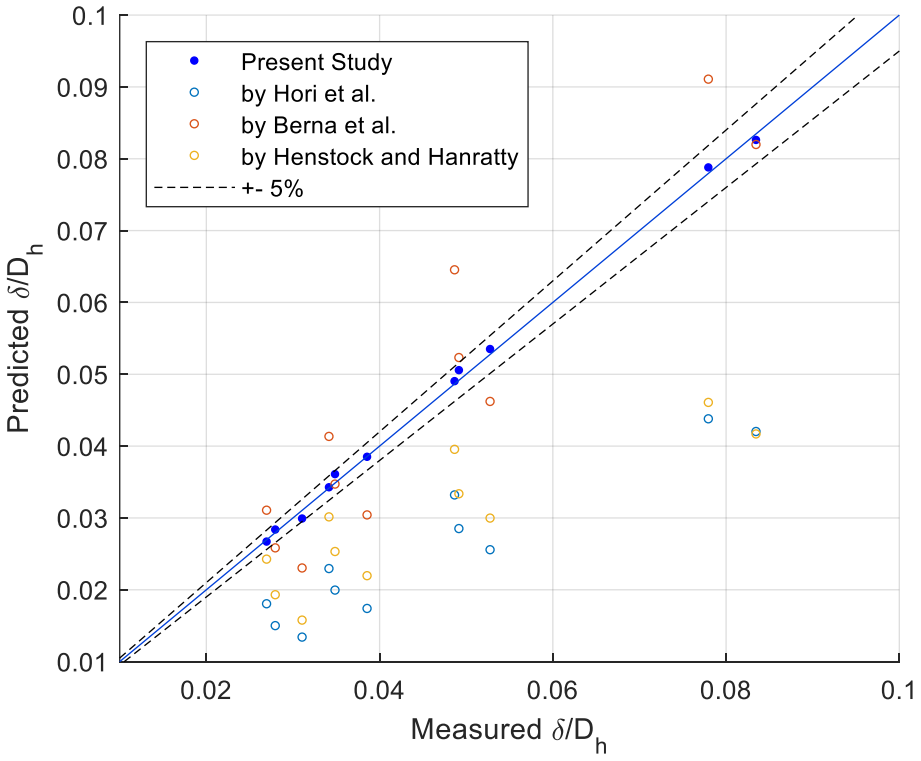

***Figure 6-23**: Comparison of the proposed correlation with other existing correlations [29][30][33].*

7. IR Thermography Results: SNB Wall Superheat, Heat Flux, and Heat Transfer Coefficient (HTC)

In this chapter, the measurements of the heat transfer properties and the SNB conditions in upward two-phase annular flow are presented. A unique periodic oscillation of the wall temperature, caused by the periodic passage of disturbance waves, is observed for the first time. A nucleate boiling time-ratio is introduced to identify the SNB conditions. A set of system-code-friendly correlations is developed for predicting the SNB heat transfer coefficient (HTC), wall superheat, and heat flux. A 1-D mechanistic heat transfer model is developed to simulate the instantaneous variation of the local heat transfer process from forced convective evaporation all the way to ONB, in upward two-phase annular flow.

This chapter shows how the phenomena at the microscale, such as nucleation cavity and the thinnest films, interact with the macroscale phenomena (order of centimeters), such as the disturbance waves and the related HTC oscillation. These multi-scale phenomena are both captured by semi-empirical correlations and mechanistic model.

7.1. Measured Thermohydraulic Boundary Conditions

The flow conditions and the corresponding local saturation temperature are important thermohydraulic boundary conditions to the local heat transfer process. As observed in experiments, the liquid film at annular flow is never truly steady due to the existence and traveling of disturbance waves. The measured flow conditions and the local saturation temperature, acquired after the annular flow reached quasi-steady state, are listed in the following Table 7-1. The saturation temperature was calculated from the interpolated test section pressure listed in Table 6-1. The listed uncertainty represents the total uncertainty (total propagated uncertainty if a quantity is not measured directly).

***Table 7-1**: Measured thermohydraulic boundary conditions at each test.*

Test #	***G* [kg·m^{-2}·s^{-1}]**	**x_e [-]**	**T_{sat} [^{o}C]**
1	772 ±47	0.016±0.001	102.33±0.43
2	1061±47	0.016±0.001	103.53±0.38
3	1352±46	0.015±0.001	102.44±0.11
4	760 ±48	0.030±0.002	103.76±0.17
5	1055±48	0.031±0.001	104.11±0.21
6	1345±46	0.030±0.001	105.16±0.14
7	751 ±49	0.052±0.003	105.18±0.20
8	1030±50	0.051±0.002	106.08±0.34
9	1336±49	0.050±0.002	108.09±0.46
10	737 ±50	0.074±0.005	106.21±0.30
11	1028±54	0.073±0.004	108.68±0.42
12	1318±54	0.070±0.003	110.22±0.84

7.2. Forced Convective Evaporation

Before boiling occurs, the heat transfer mechanism in annular flow is dominated by forced convective evaporation, which comprises forced convective heat transfer through the liquid film and evaporation at the liquid-steam interface. A typical wall superheat contour is plotted in Figure 7-1 at nominal G= 750 kg·m^{-2}·s^{-1}, x_e=0.030, and imposed heat flux of 620.50 ± 0.83 kW·m^{-2}, which is right below SNB. Periodic superheat oscillations are clearly observed from the contour, and behave like “cooling waves” sweeping over the heater surface. The chordal-average wall superheat, heat flux and HTC near the axial center location of the heater are plotted in Figure 7-2. The location of the chord is marked on the bottom contour in Figure 7-1.

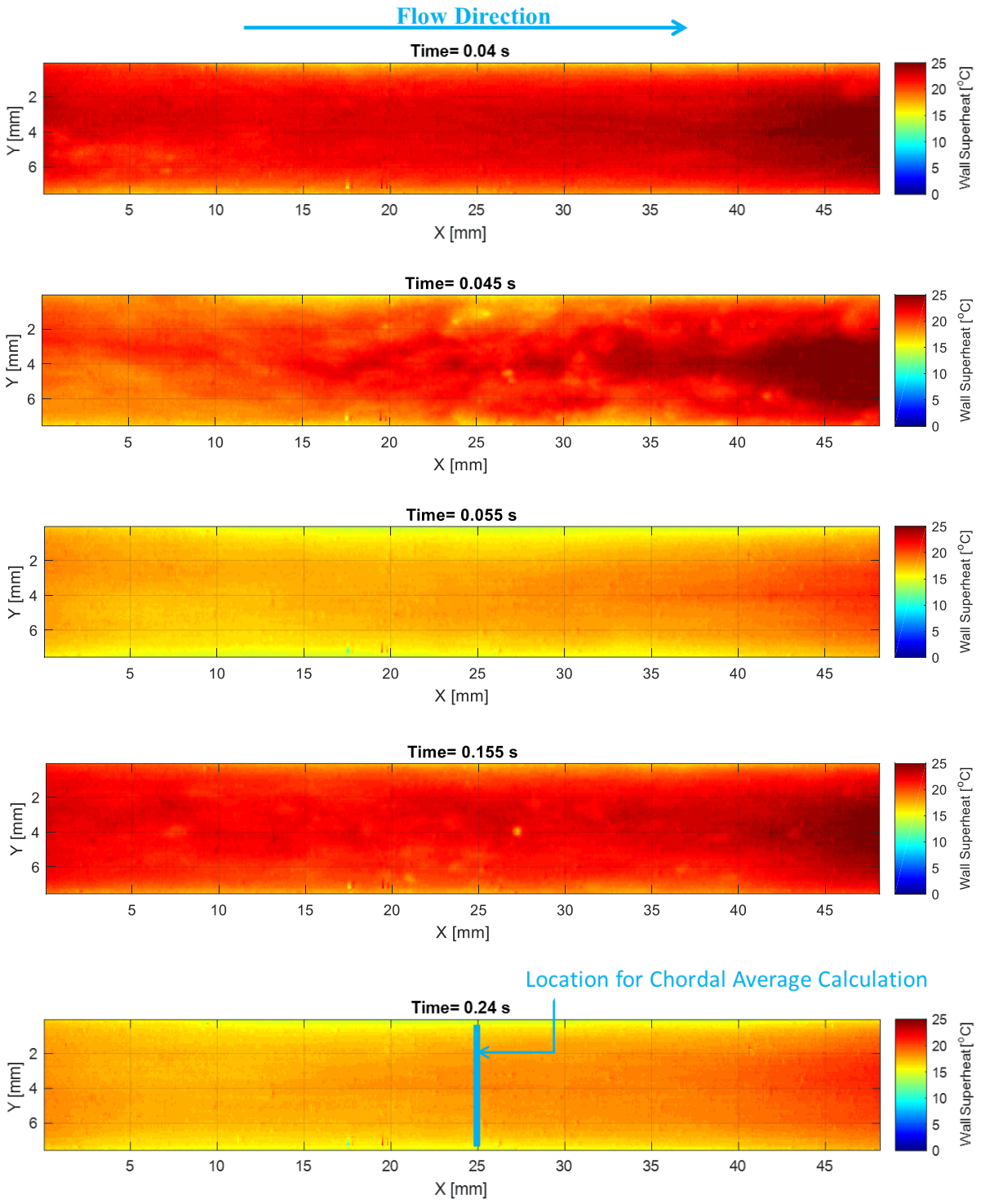

***Figure 7-1**: Typical wall superheat contour at $G=750\ kg \cdot m^{-2} \cdot s^{-1}$, $x_e=0.030$, imposed heat flux of $620.50 \pm 0.83\ kW \cdot m^{-2}$, and various time steps. Periodic cooling waves are observed. The light blue bar indicates the location at which the chordal average thermal properties are calculated.*

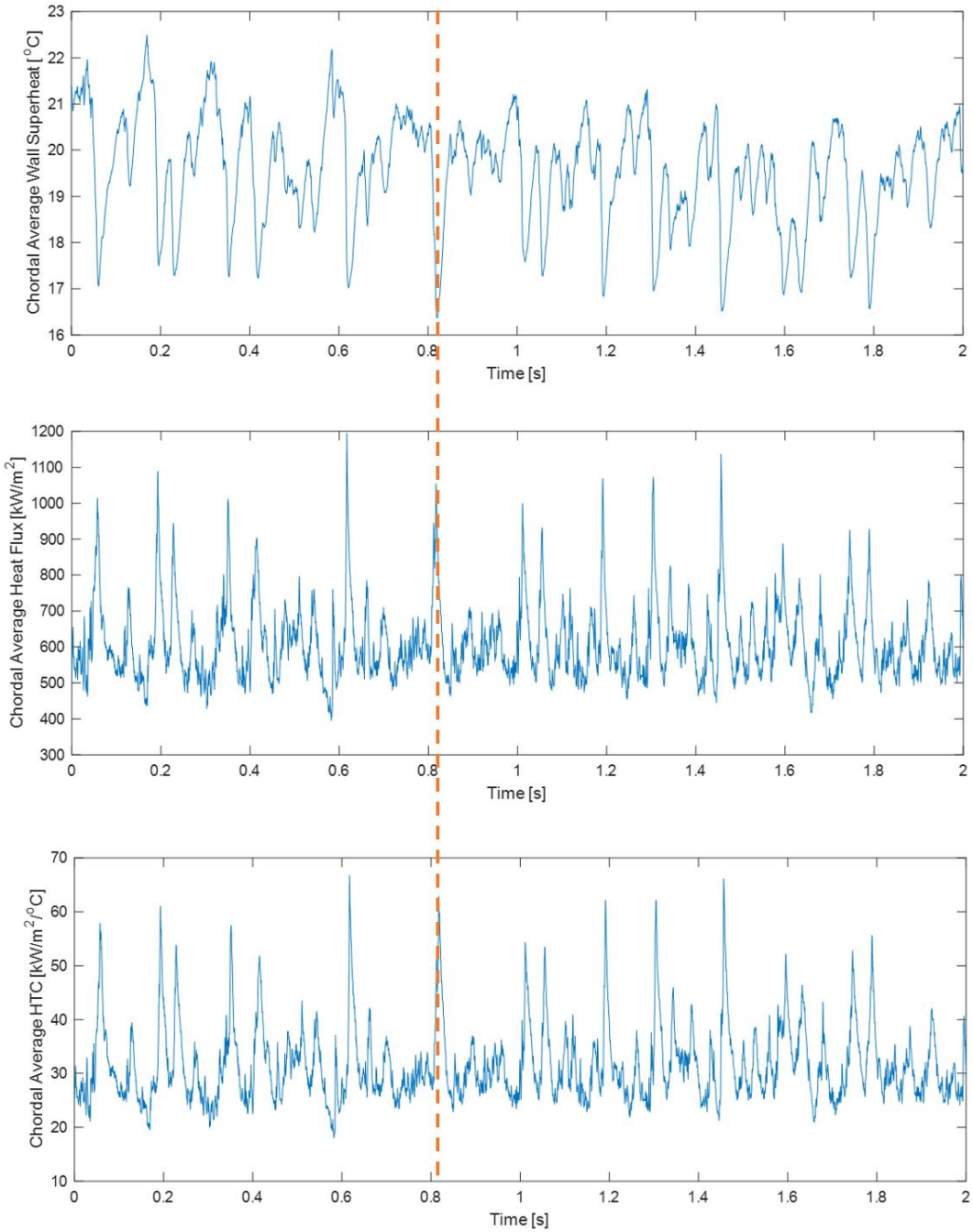

***Figure 7-2**: Time history of the chordal average wall superheat (top), heat flux (middle), and HTC (bottom). Periodic oscillations are evident.*

Unique periodic oscillations of the chordal-average thermal properties are observed, even though the annular flow is stable and the imposed heat flux is constant. Such thermal oscillations are attributed to the variation of the local heat transfer, which is caused by the periodic change of liquid film thickness with the passage of disturbance waves. Figure 7-2 clearly shows the time

coherence among the three thermal properties: when there is a spike in HTC, the heat flux also peaks, while the wall superheat sharply drops. The full list of the time histories of the chordal average thermal properties at each test condition after SNB is reported in Appendix F.

To corroborate the hypothesis on the relationship between disturbance waves and thermal properties' oscillations, each chordal average heat flux in Appendix F was analyzed by the same bandwidth criterion shown in Figure 6-11 to obtain the thermal oscillation frequency. The heat flux signal was used instead of temperature, because of its relatively large oscillating range and clear peaks, which enhanced the calculation accuracy. The cross-correlation of two chordal-average heat flux signals acquired at locations 45 mm away from each other in the flow direction was calculated to estimate the velocity of the "cooling wave", at each test condition. The disturbance wave velocity and frequency from film thickness signal and the "cooling wave" velocity and frequency from the heat flux signal are compared from Figure 7-3 to Figure 7-6.

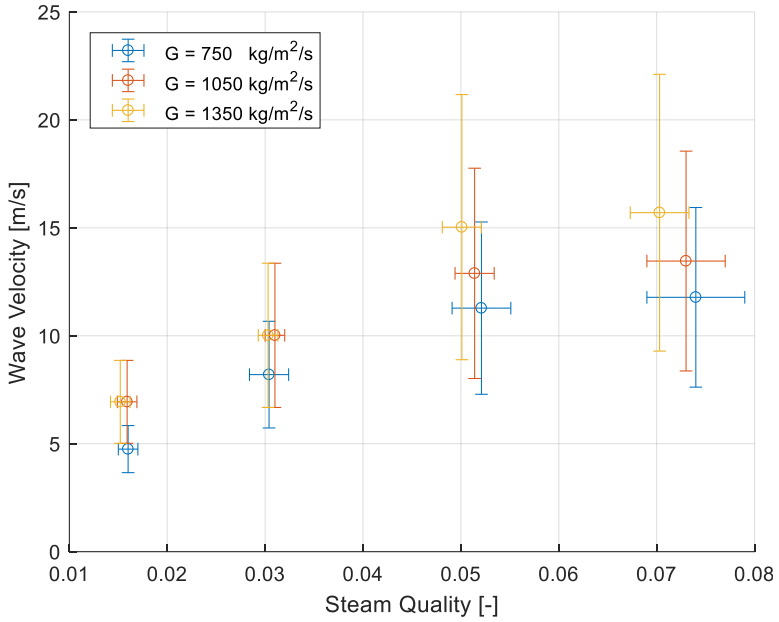

***Figure 7-3**: The measured "cooling wave" velocity from the heat flux signal versus steam quality at different mass fluxes. The trend is the same as the disturbance wave velocity in Figure 6-18.*

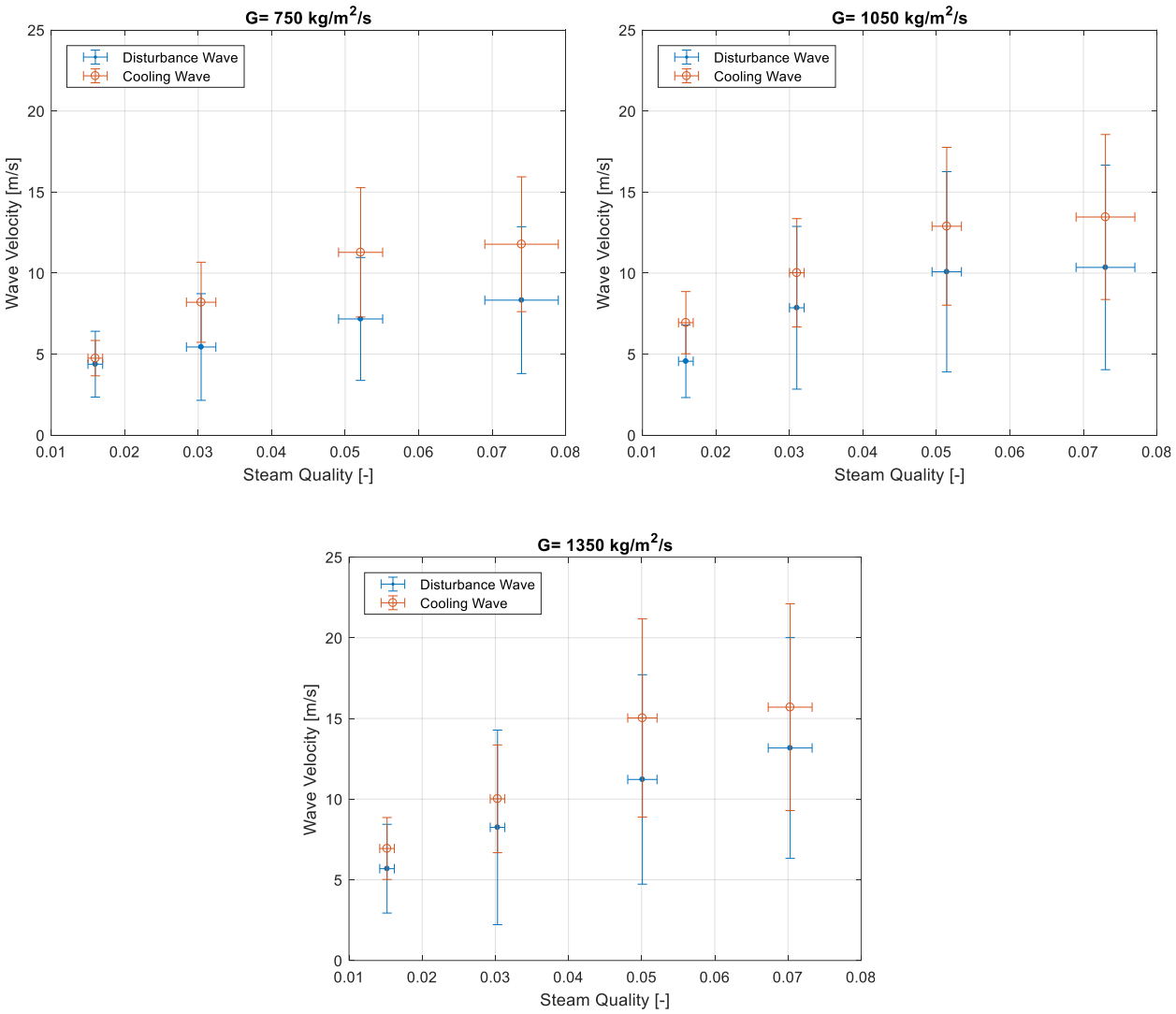

***Figure 7-4**: Comparison between the disturbance wave velocity and "cooling wave" velocity versus steam quality at different mass fluxes.*

As shown in Figure 7-3, the wave velocities calculated from the heat flux signal shows the same trend as the disturbance wave velocities in Figure 6-18. In addition, the "cooling wave" velocity agrees reasonably well with the disturbance wave velocity, as shown in Figure 7-4. The uncertainty of the "cooling wave" velocity, calculated from Poisson distribution, is fairly large. In addition, the thermal response to the passage of a disturbance wave is not instantaneous due to the delay induced by the non-negligible thermal inertia of the sapphire substrate, which further adds to the uncertainty in the velocity calculation. The mechanistic model presented in Section 7.4.2 below will analytically show such thermal inertia delay. The error bar for the disturbance wave velocity represents the velocity distribution from a spectrum of disturbance waves detected, which

has already been discussed in Section 6.3.3. The uncertainty of each individually calculated disturbance wave velocity is much less than the one for “cooling wave”.

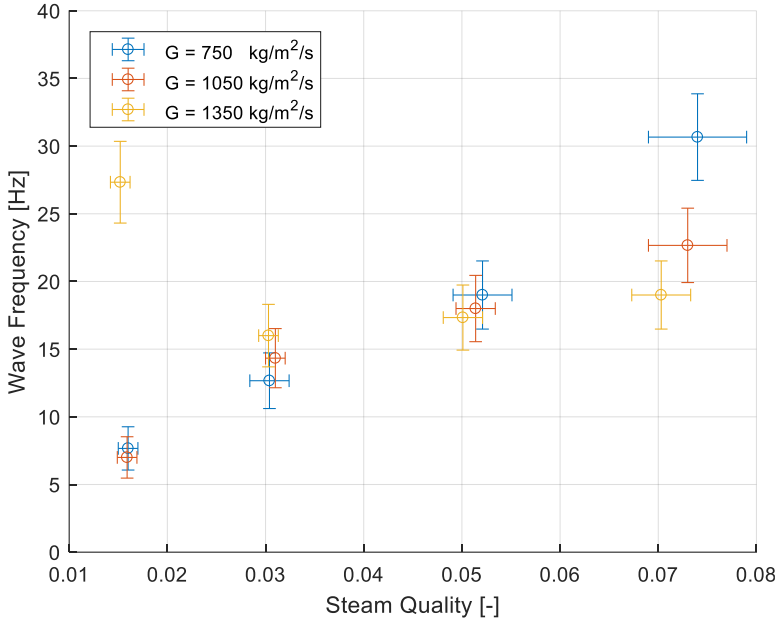

***Figure 7-5**: The measured “cooling wave” frequency from the heat flux signal versus steam quality at different mass fluxes. The trend is exactly the same as the disturbance wave frequency in **Figure 6-18**.*

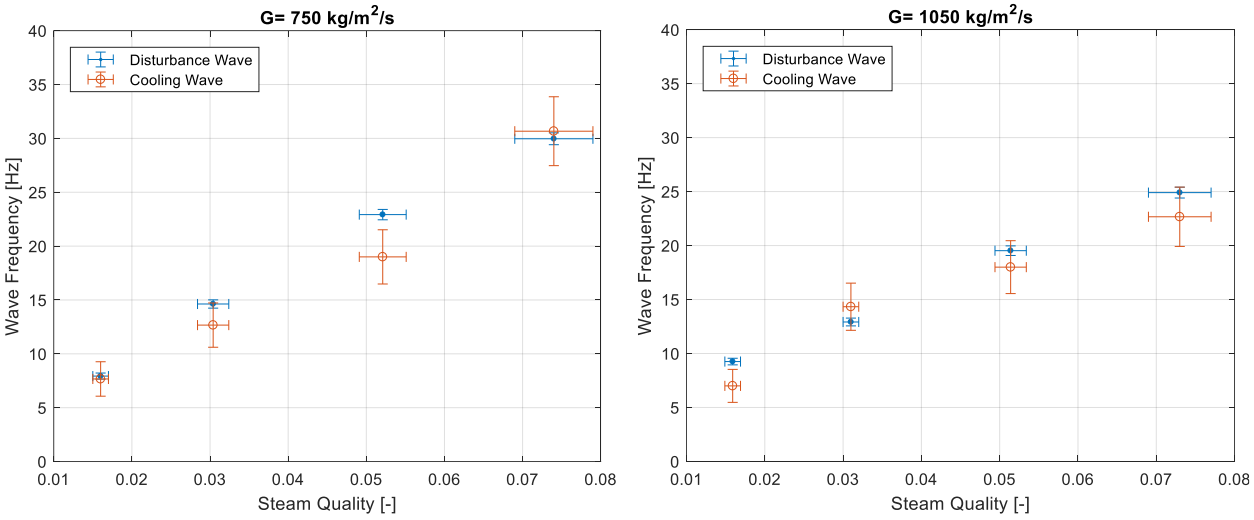

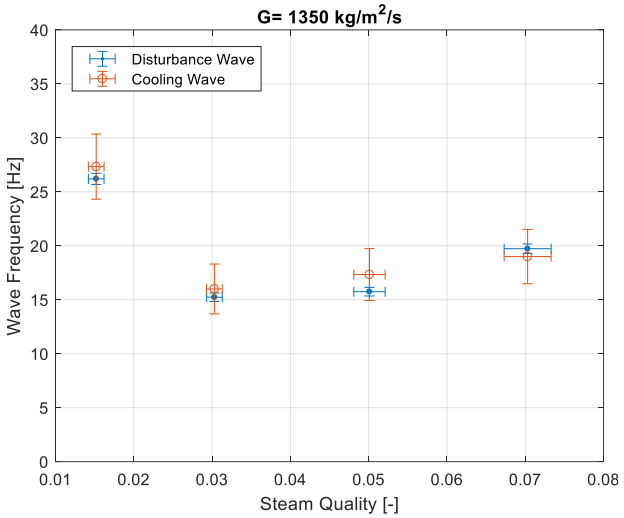

***Figure 7-6**: Comparison between the disturbance wave frequency and "cooling wave" frequency versus steam quality at different mass fluxes.*

As shown in Figure 7-5, the "cooling wave" frequencies calculated from the heat flux signal show the same trend as the disturbance wave frequencies in Figure 6-18. In addition, the "cooling wave" frequency agrees remarkably well with the disturbance wave frequency, as shown in Figure 7-6. The uncertainty of the "cooling wave" frequency, calculated from Poisson distribution, is clearly larger than disturbance wave frequency, due to a smaller sample. The good agreement in velocity and frequency between the "cooling wave" and the disturbance wave, confirms that the oscillations of the thermal properties, i.e., wall superheat, heat flux and HTC, are caused by the variation of the film thickness due to the passage of disturbance waves.

Moreover, the cross-correlation between the temperature signal and the film thickness signal was calculated and is illustrated in Figure 7-7 at nominal G= 1050 kg·m^{-2}·s^{-1}, x_e=0.016, and imposed heat flux of 493.22 ± 0.76 kW·m^{-2}. In the top plot of Figure 7-7, the original film thickness signal does not show clear correlation with the temperature signal. In the bottom plot of Figure 7-7, the cross-correlation shows a clear peak at 0.058 sec.

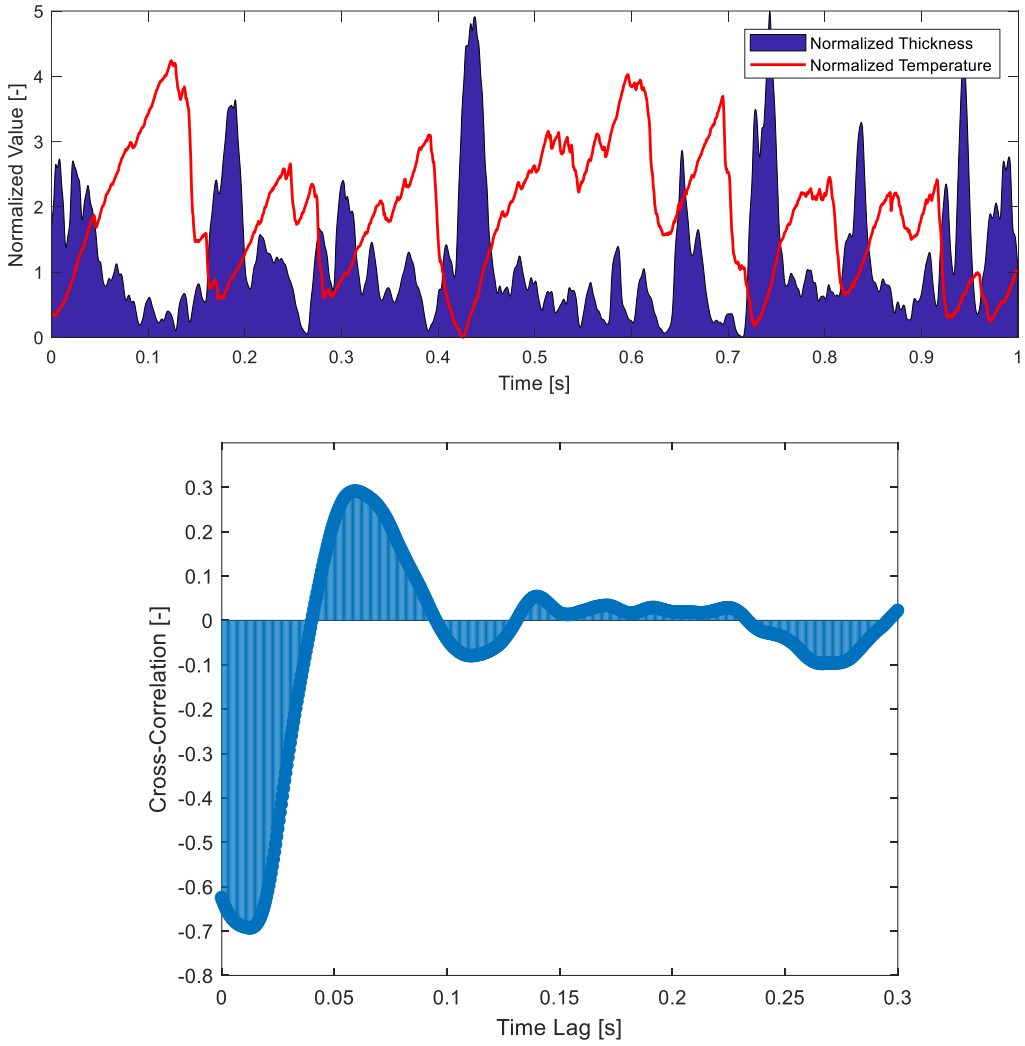

***Figure 7-7**: Cross-correlation between temperature signal and film thickness signal at nominal G= 1050 kg·m^{-2}·s^{-1}, x_e=0.016, and imposed heat flux of 493.22 ± 0.76 kW·m^{-2}. The top plot shows the normalized temperature and film thickness as originally measured. The bottom plot shows the cross-correlation value versus time lag.*

The film thickness signal is shifted backwards by this time lag and compared with the temperature signal in Figure 7-8. As shown, the peaks from the temperature signal generally line up with the ones from the shifted film thickness signal. Another comparison with shifted film thickness signal is shown in Figure 7-9, at nominal G= 750 kg·m^{-2}·s^{-1}, x_e=0.030, and imposed heat flux of 620.50± 0.83 kW·m^{-2}. Good agreement is achieved again. The resulted velocities calculated from the time delays, and the distance between the selected pixel of temperature measurement and the specific LFS, are 3.25 m.s^{-1} and 4.08 m.s^{-1}, respectively for the two conditions in Figure 7-8

and Figure 7-9. These two velocity values are well within the corresponding ranges plotted in Figure 7-4.

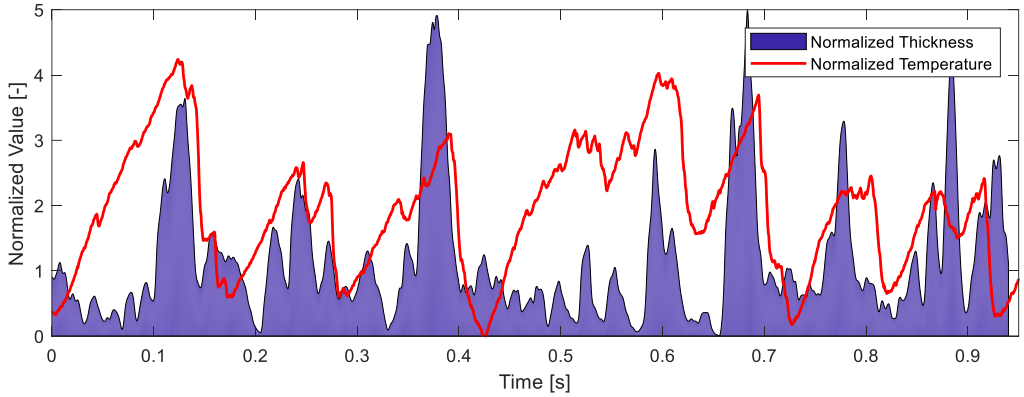

***Figure 7-8**: Comparison between temperature signal and shifted thickness signal according to the calculated time delay, at nominal G= 1050 kg·m^{-2}·s^{-1}, x_e=0.016, and imposed heat flux of 493.22 ± 0.76 kW·m^{-2}.*

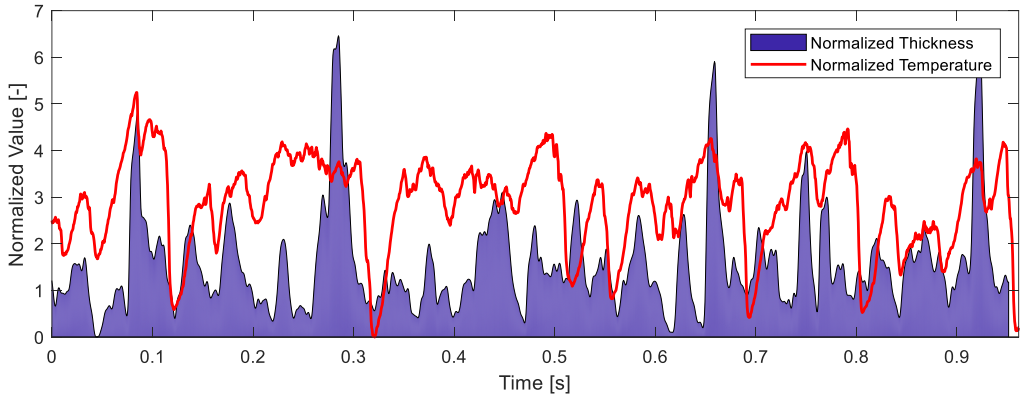

***Figure 7-9**: Comparison between temperature signal and shifted thickness signal according to the calculated time delay, at nominal G= 750 kg·m^{-2}·s^{-1}, x_e=0.030, and imposed heat flux of 620.50± 0.83 kW·m^{-2}.*

The small discrepancies between the times of the temperature peaks and the film thickness peaks could be attributed to three causes. First, the presence of a spectrum of different waves with different velocities. A second cause could be the aforementioned thermal response delay to a change of film thickness due to the thermal inertia of the substrate. Such thermal delay ideally makes the temperature peak appear at a later moment than film thickness peak. The third cause could be the change of the wave morphology from merging, splitting or dissipation as the wave propagates.

7.3. Suppression of Nucleate Boiling (SNB) in Annular Flow

7.3.1. SNB Detection

A major goal of the present study is to determine the local thermal conditions at which SNB occurs, including wall superheat, heat flux, and HTC. Precisely locating the nucleation sites is the first step toward the analysis of SNB. In pool boiling and subcooled flow boiling, the temperature footprint of the bubble is normally used to identify the nucleation site location as shown in Figure 5-5. However, in the presence of the disturbance waves, the bubble nucleation process is periodically disturbed, and the bubble footprint is distorted and stretched toward flow direction, as shown in Figure 7-10. Such "smearing" effect makes the detection of bubble nucleation events more challenging.

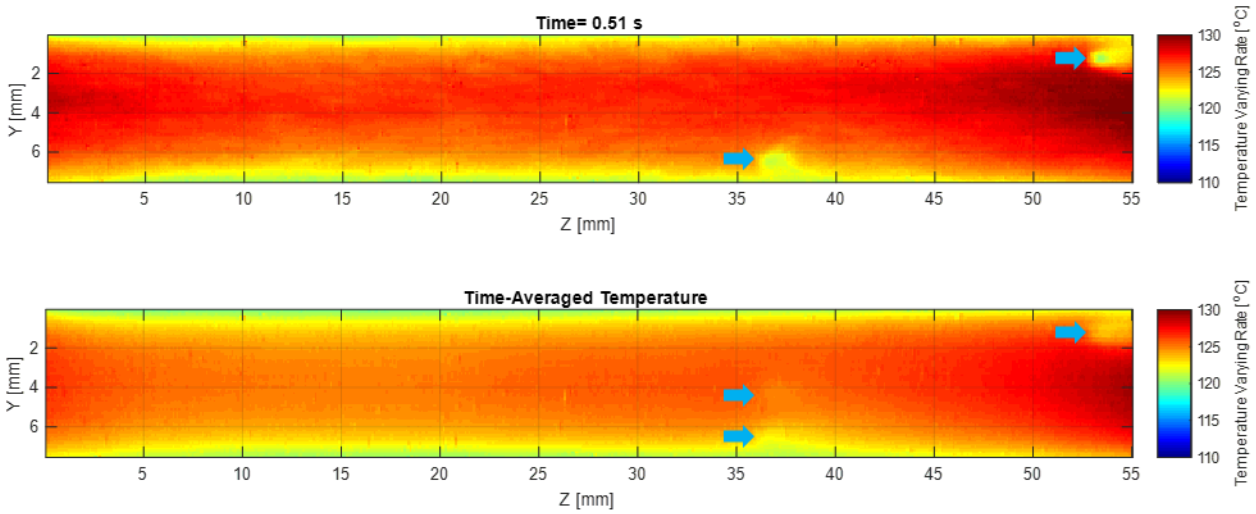

***Figure 7-10**: Instantaneous (top) and time-averaged (bottom) heating wall temperature contour. The nucleation sites are marked by the blue arrows. The bubble footprint is distorted and smeared by the disturbance wave. Note: flow direction left to right.*

In the experiments, the largest and fastest cooling rates were observed underneath a growing bubble, while the cooling/heating cycles induced by the passage of the disturbance waves were slower and of smaller amplitude. Therefore, the absolute value of the time derivative of local temperature is used to map the nucleation sites as shown in Figure 7-11 at nominal G= 1050 kg·m^{-2}·s^{-1}, x_e= 0.016 condition with imposed heat flux of 561.55± 1.22 kW·m^{-2}. There are three clear nucleation sites on the contour: two active and sustained sites (dark red), and a third less active site (light blue). The average cooling rate due to the disturbance waves is several times

smaller than the average bubble cooling rate. The approach is effective in capturing the nucleation sites, as well as determining the area thermally affected by bubble nucleation. At selected conditions, manual counting was performed to verify the accuracy of such method.

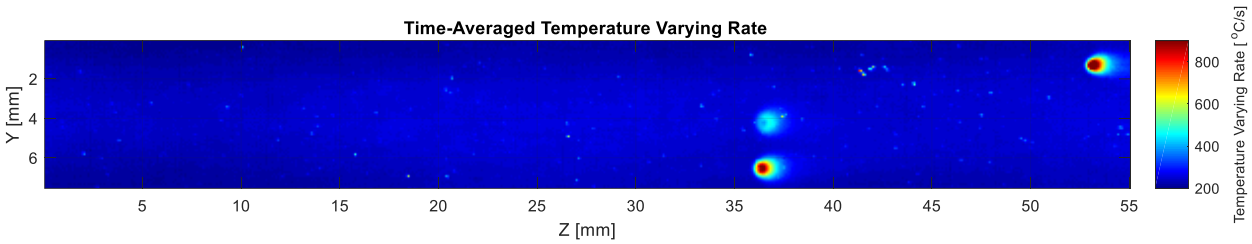

***Figure 7-11**: Mapping nucleation sites with the time-averaged absolute temperature varying rate. The two dark red dots represent active and sustained nucleation site, while the light blue one indicates a less active site. Note: flow direction left to right.*

After the nucleation sites are located, various approaches can be applied to capture the ONB/SNB conditions. The traditional method is to use the boiling curve, i.e., heat flux versus wall superheat plot, which is expected to exhibit an appreciable change in slope at ONB due to the enhanced HTC. An example of boiling curve is plotted in Figure 7-12 based on the average temperature around the active nucleation site next to Z= 35 mm in Figure 7-11. No appreciable change of the slope is observed on the boiling curve, although the IR video shows a clear transition from non-boiling to sustained boiling. The discrepancy may be attributed to the efficient convective evaporation that masks the heat transfer enhancement from nucleate boiling. Therefore, the boiling curve is not an appropriate approach to identifying SNB in annular flow.

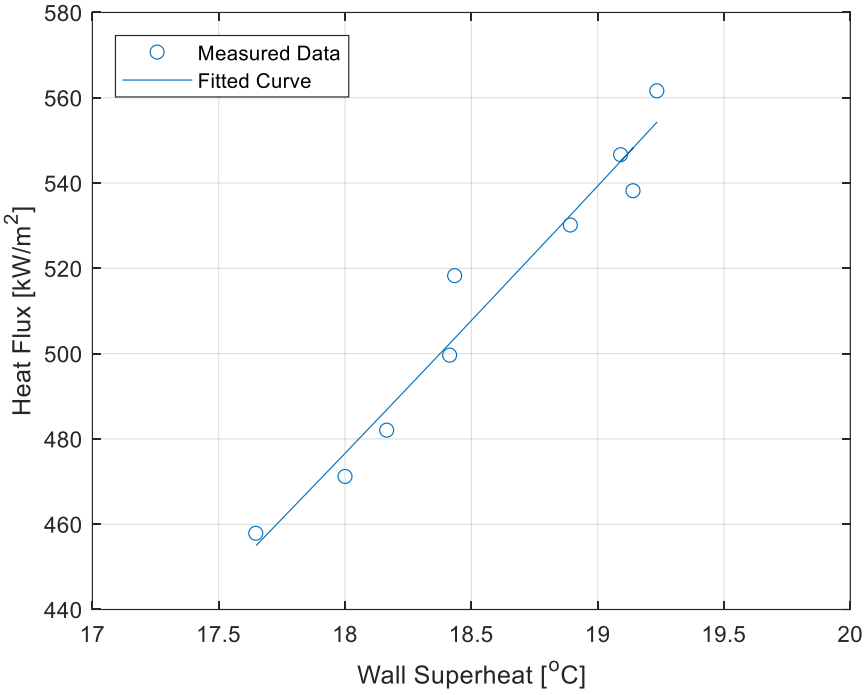

***Figure 7-12**: Boiling curve based on the average temperature around the active nucleation site next to Z= 35 mm in Figure 7-11, from non-boiling to sustained boiling condition. No significant slope change is observed.*

Another widely used approach is based on the direct visual observation of the boiling event, i.e., the observation of the first bubble for ONB or the last bubble for SNB. Such approach is fairly effective in pool and flow boiling conditions. However, in annular flow, the wall superheat oscillations due to the disturbance waves may cause intermittent ONB and SNB at a given location. As a result, a short-lived nucleating bubble can occasionally occur at relatively low heat flux, which adds uncertainty to the determination of a well-defined ONB/SNB condition.

Given the issues mentioned above, the first difficulty is to separate the temperature change due to nucleate boiling from the temperature oscillation caused by disturbance waves. To that end, the temperature difference between the nucleation site and the upstream neighboring area was considered, as shown in Figure 7-13. A threshold value of this temperature difference ($\Delta T = |T_{upstream}\text{-}T_{site}|$) is used to identify the existence of boiling. The threshold value is selected with occurrence probability of 99% of the temperature difference distribution at non-boiling conditions, as shown in Figure 7-14.

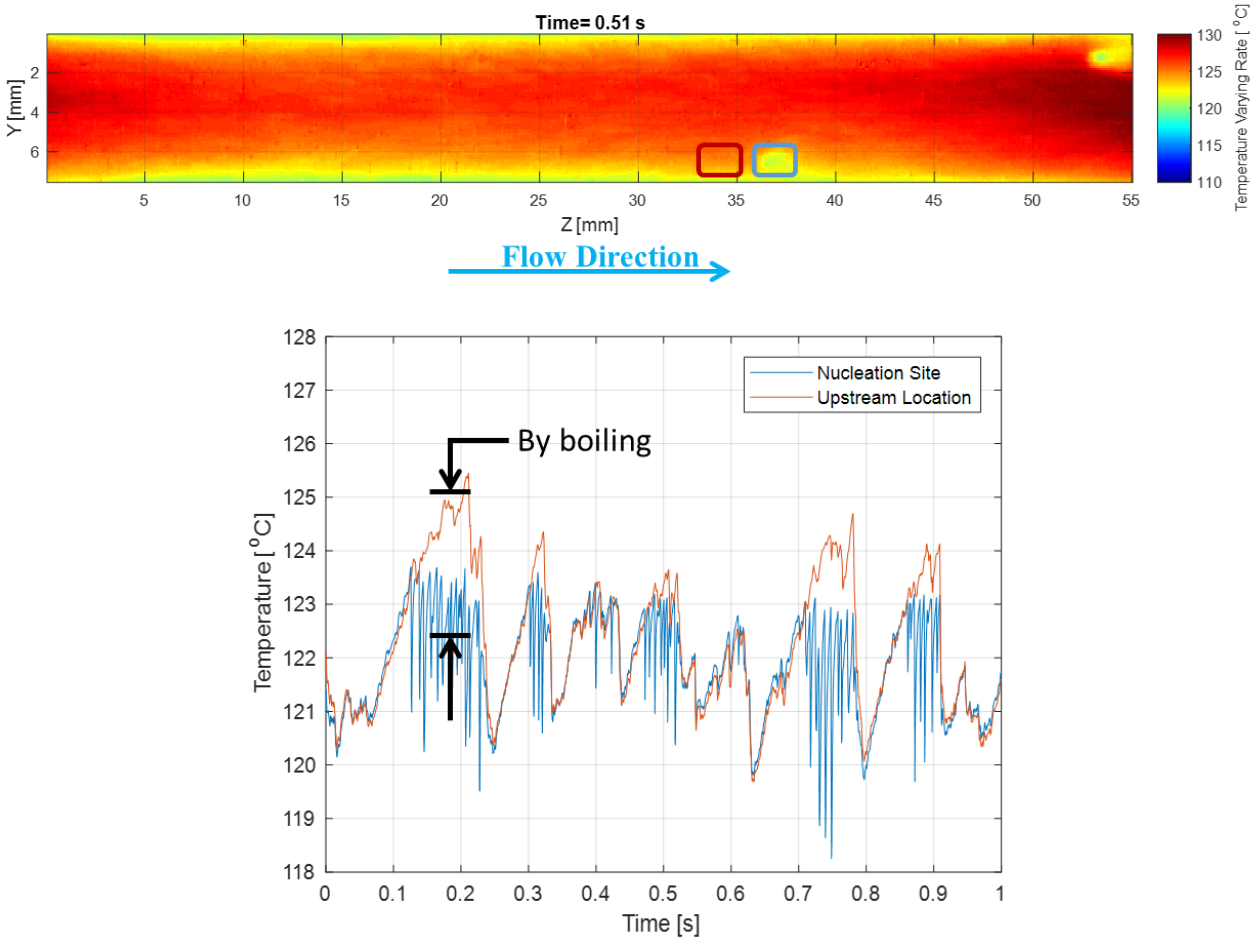

***Figure 7-13**: Comparison between the upstream temperature and the nucleation site temperature. The upstream and the nucleation site locations are marked on the top contour. The temperature difference (bottom plot) caused by boiling is obvious.*

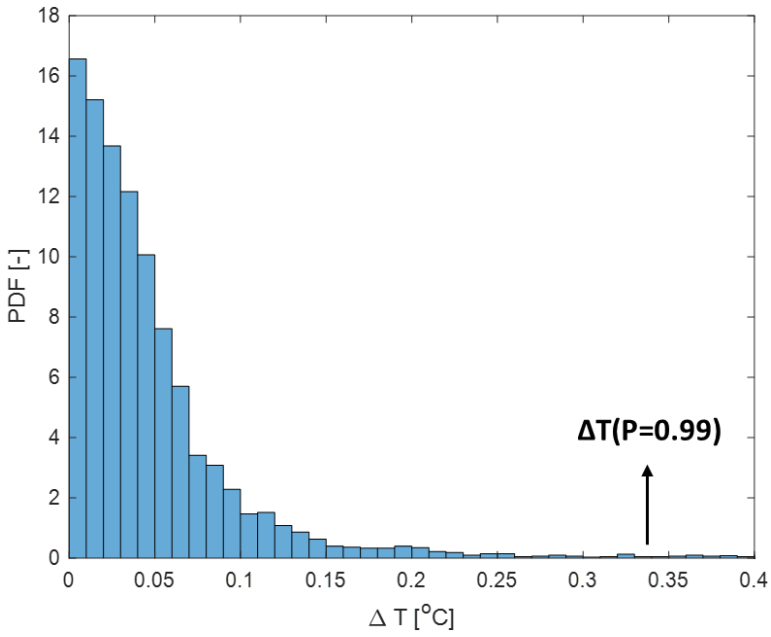

***Figure 7-14**: The determination of the threshold temperature difference at non-boiling condition. The 99% probability value is selected as the threshold.*

Once the nucleate boiling events are accurately detected, a new criterion to determine SNB was developed. A 'time fraction of boiling' is defined as the ratio of the cumulative time, during which nucleate boiling occurs, to the total recording time. At high values of such ratio, it can be postulated that boiling affects (and possibly even disrupts) the liquid film, potentially leading to dryout.

The time fraction of nucleate boiling was calculated and plotted at each heat flux, as shown in Figure 7-15, at nominal G= 1050 kg·m^{-2}·s^{-1}, x_e= 0.016. A threshold value of 0.5 was arbitrarily chosen to define the nominal SNB condition. The region above the threshold is defined as sustained nucleate boiling. The full dataset of time fraction of boiling is presented in Appendix G.

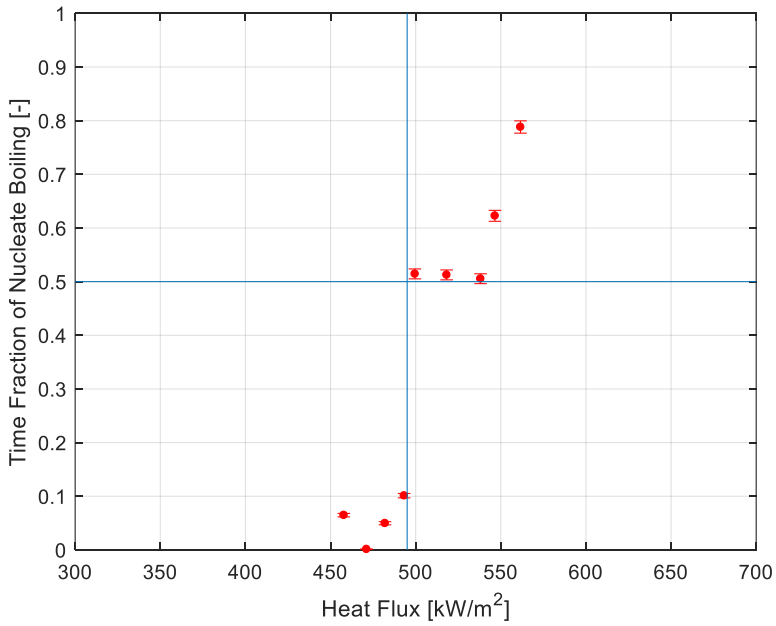

***Figure 7-15**: Determining SNB from the time fraction of nucleate boiling at nominal G= 1050 kg·m^{-2}·s^{-1}, x_e= 0.016 condition. Horizontal line represents 0.5 threshold, while the vertical line identifies the nominal SNB position.*

With a well-established SNB criterion, it is now possible to evaluate if there is any hysteresis between SNB and ONB conditions, i.e., if the time fraction plot in a test with decreasing heat flux is significantly different from that of a test with increasing heat flux. A specific test was conducted to answer this question, the result of which is plotted in Figure 7-16, showing that there is no hysteresis between SNB and ONB conditions. Note that the SNB and ONB heat fluxes are linearly interpolated from the two measured data points above and below the 0.5 threshold respectively.

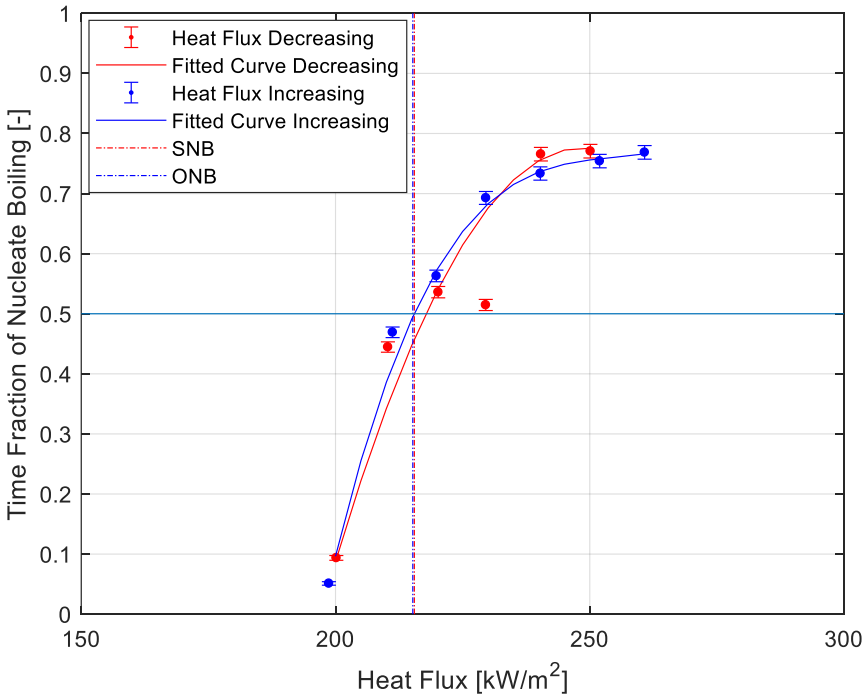

***Figure 7-16**: Comparison of time fraction plots from decreasing heat flux (red dots) and increasing heat flux (blue dots) at nominal G= 750 kg·m^{-2}·s^{-1}, x_e= 0.016 condition. The identified nominal SNB (red vertical line) and ONB (blue vertical line) heat fluxes are practically the same.*

7.3.2. SNB Thermal Parameters: Wall Superheat, Heat Flux, and HTC

With the identified SNB heat flux (q''), the SNB wall superheat (ΔT_{sat}) and HTC were also extracted from the IR thermography data. Since it is impossible to control the time fraction of nucleate boiling right at 0.5, the nominal SNB condition is linearly interpolated from the two test conditions with time fraction above and below the 0.5 threshold. The SNB thermal parameters are reported as the average value from the two test conditions. All the SNB thermal parameters are summarized in Table 7-2. The listed heat flux is the imposed heat flux, which has relatively small uncertainty. However, the uncertainties for wall superheat and HTC are relatively large. The large uncertainty on the wall superheat mainly comes from the disturbance wave induced temporal and spatial temperature oscillations. The averaging of the measured values from the two test conditions for identifying SNB also contributes to the uncertainty. Such large uncertainty propagates to the calculation of the HTC. The listed uncertainties represent the total propagated uncertainty, which are for quantities that are not measured directly.

***Table 7-2**: SNB thermal parameters at each test condition.*

Test #	***G***	x_e	q'' [kW·m^{-2}]	ΔT_{sat} [^{o}C]	***HTC*** [kW·m^{-2}·^{o}C^{-1}]
1	750	0.016	236.26 ±4.01	9.31 ±1.32	26.42±10.67
2	1050	0.016	496.39 ±3.20	19.42±2.08	26.38±8.36
3	1350	0.016	736.97 ±5.14	25.32±1.83	29.46±6.47
4	750	0.030	625.64 ±5.14	19.49±1.70	32.71±9.17
5	1050	0.030	824.30 ±6.37	22.32±1.68	37.38±8.82
6	1350	0.030	1034.93±3.92	26.26±1.83	39.84±8.06
7	750	0.050	816.16 ±5.09	20.66±1.34	39.93±8.12
8	1050	0.050	1096.16±2.97	25.46±1.64	43.43±8.38
9	1350	0.050	1276.24±4.05	28.53±1.96	45.18±8.42
10	750	0.070	1321.01±11.23	28.55±1.97	46.69±8.08
11	1050	0.070	1515.54±3.76	30.59±1.82	49.93±8.00
12	1350	0.070	1602.61±5.97	33.11±2.08	48.80±7.85

The extracted SNB wall superheat, heat flux and HTC are plotted against total mass flux at various steam qualities in Figure 7-17. Similar to the mean film thickness plot in Figure 6-5, all the SNB thermal parameters weakly depend on the mass flux, while they show strong dependency on steam quality. The SNB wall superheat at the nominal G= 750 kg·m^{-2}·s^{-1}, x_e= 0.016 condition is a little bit off the trend, mostly because such flow condition is still in the slug/churn flow to annular flow transition, and behaved as an outlier also in the mean film thickness plots. Particularly, the SNB thermal parameters slightly increase with increasing mass flux at constant steam quality, while they appreciably increase with increasing steam quality (that is, the opposite trend of the mean film thickness). Such dependency on mass flux and steam quality suggest a relationship between mean film thickness and the heat transfer.

At constant steam quality, increasing mass flux leads to both increasing gas velocity and increasing liquid film flow rate. The increasing gas velocity leads to higher entrainment and higher liquid velocity from higher interfacial drag, resulting in thinner film. Conversely, the higher mass flow rate in liquid film increases film thickness. These two effects compete with each other, so

that the dependency on mass flux is weakened. The experimental results indicate that the increase in liquid velocity overcomes the increase in film thickness at increasing mass flux and constant steam quality, so that SNB thermal parameters slightly increase with mass flux.

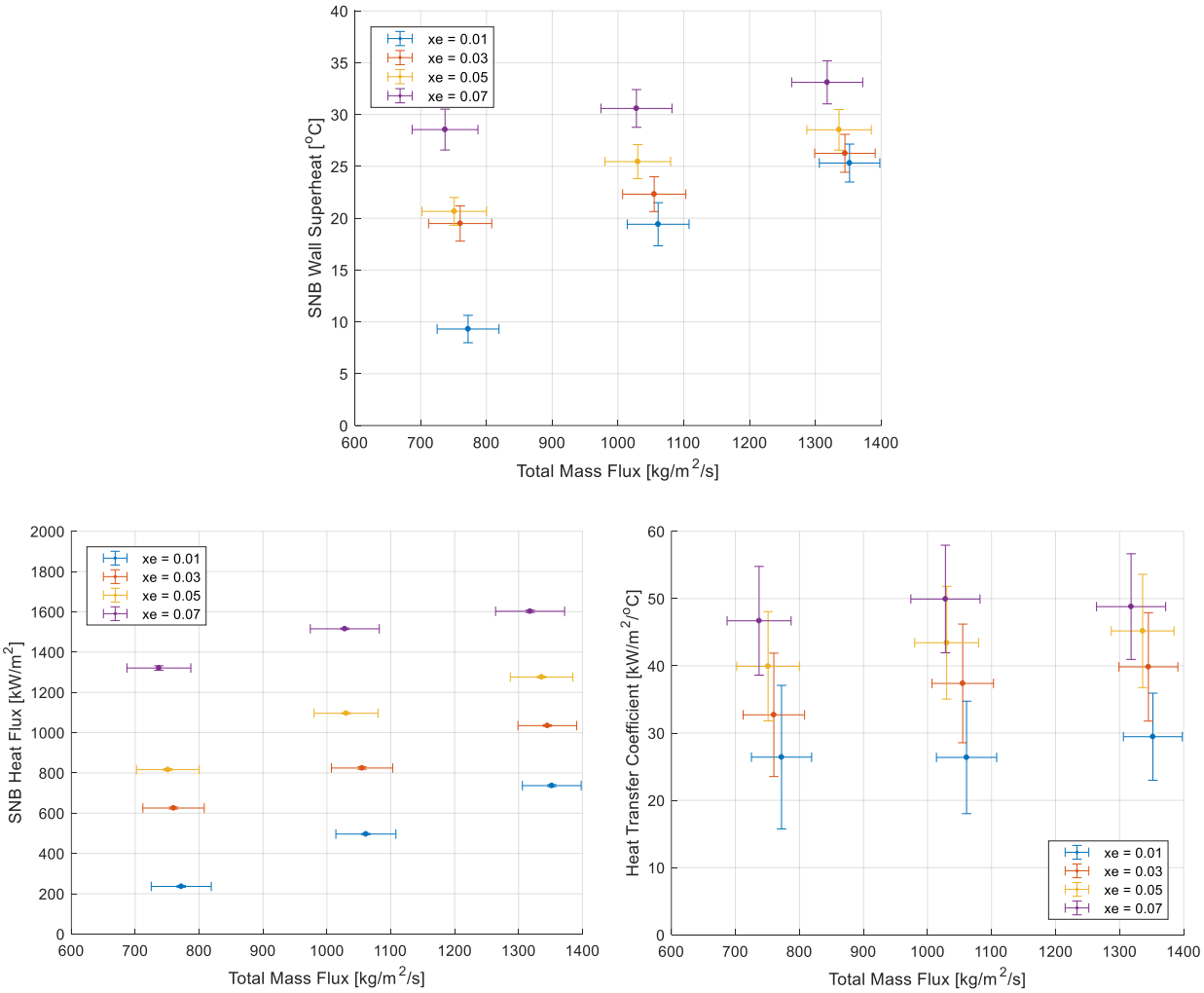

***Figure 7-17**: SNB wall superheat (top), heat flux (bottom left), and HTC (bottom right) against total mass flux at various steam qualities. The dependency on steam quality is strong while the dependency on mass flux is weak.*

Given the strong dependency on steam quality, the SNB thermal parameters are replotted against steam quality at various mass fluxes in Figure 7-18. At constant mass flux, the higher steam quality leads to higher liquid entrainment that thins down the film thickness, and thus promotes the heat transfer. Besides, the higher steam quality also leads to higher interfacial drag, and thus higher liquid film velocity, which results in higher HTC, and thus higher SNB heat flux and wall superheat.

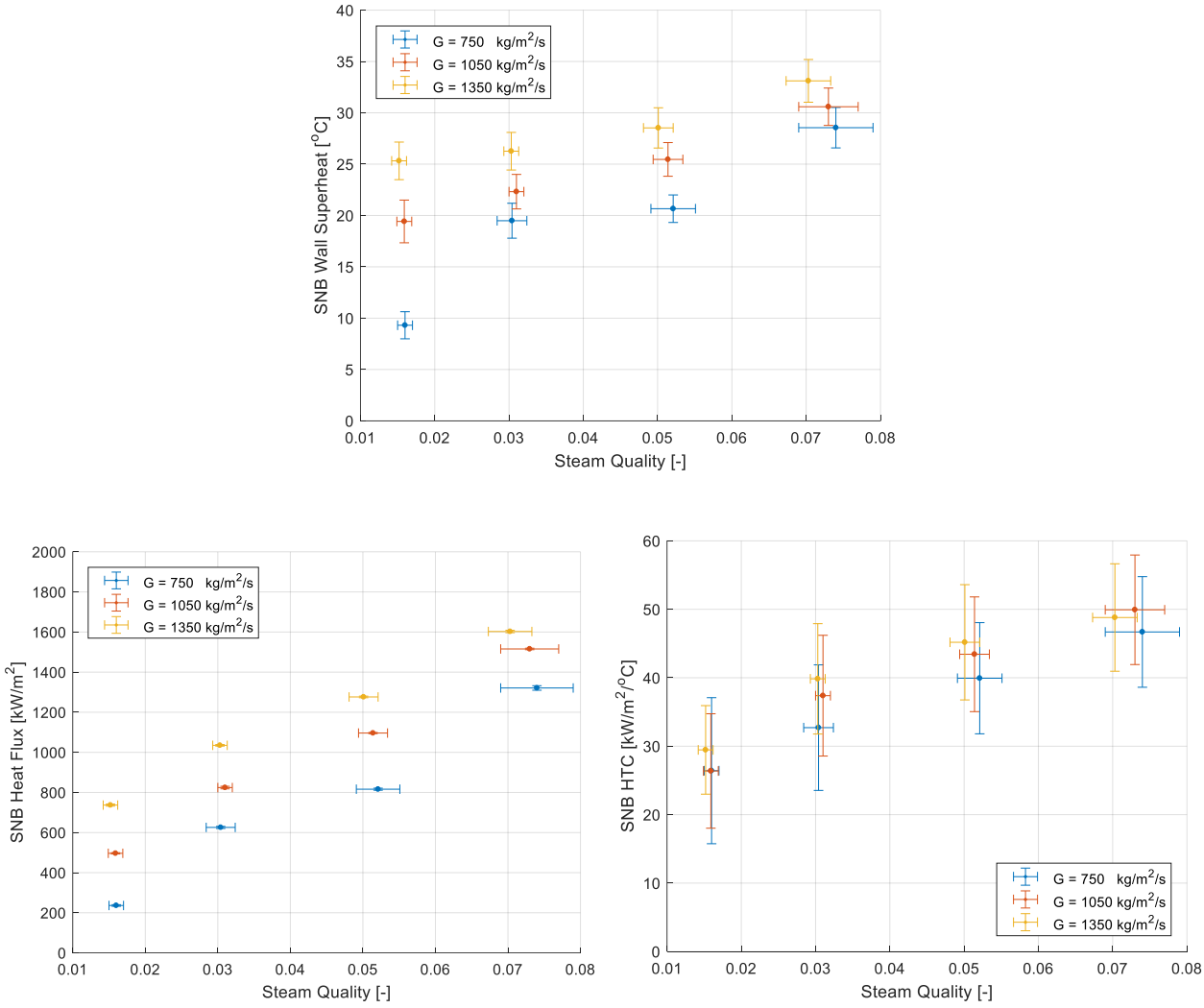

***Figure 7-18**: SNB wall superheat (top), heat flux (bottom left), and HTC (bottom right) against steam quality at various total mass fluxes.*

Another interesting finding is that SNB wall superheat and heat flux seem to have very similar dependencies on steam quality and heat flux. The SNB heat flux is plotted against SNB wall superheat in Figure 7-19. Surprisingly, all the data points from different mass fluxes and steam qualities collapse into one trend, except for the outlier at nominal G= 750 kg·m^{-2}·s^{-1}, x_e= 0.016. The remarkable observation indicates that SNB wall superheat and SNB heat flux share similar dependencies on the flow parameters, so that the dependency cancels out when one is plotted against the other.

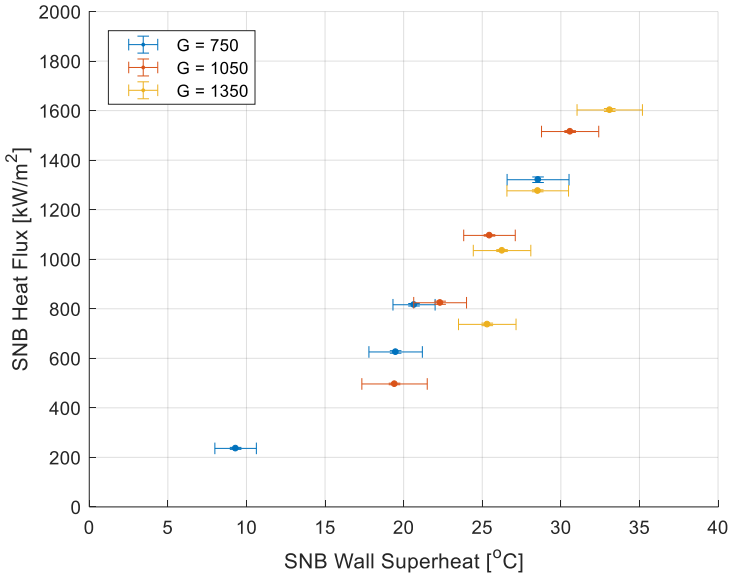

***Figure 7-19**: All the data points collapse into one trend on SNB heat flux versus SNB wall superheat plot.*

7.4. Modeling SNB Thermal Parameters

Mechanistic correlations and model were also developed to correlate the SNB thermal parameters with the flow and surface conditions for accurate prediction. A set of correlations were generated to predict the time average HTC, wall superheat and heat flux at SNB. A transient 1D mechanistic model was also developed to simulate the instantaneous variation of the local thermal parameters accounting for the effect of disturbance waves.

7.4.1. Semi-Empirical Correlations

SNB HTC

HTC is the entry point for analyzing the complicated local heat transfer at annular two-phase flow, since it links wall superheat, heat flux, and flow condition together. Unlike the single-phase HTC in a channel flow, the SNB HTC is a quantity that relates not only to the average flow (Reynolds number), but also to the morphology of the liquid film (film thickness). As observed in experiments, the liquid film at annular two-phase flow is never truly steady and uniform due to the existence and traveling of disturbance waves. However, since the correlation aims to predict the time averaged HTC but not the instantaneous variation, the time averaged liquid

film thickness is used for correlating the HTC. The correlation is built upon the correlation for liquid film thickness as introduced in Section 6.4.

The 2D thin film and a simplified steady-state fully developed condition for both flow and energy still apply here, as illustrated in Figure 6-21. Similar to single-phase boundary flow, the turbulent liquid film is also assumed to be divided in three regions, i.e., the laminar sub-layer adjacent to the channel wall, and buffer layer, and the turbulent sub-layer, now bounded by the liquid-steam interface, where turbulence damping occurs [2]. The present analysis only focuses on the two sub-layers (laminar and turbulent). The definition of Newtonian fluid shear and Fourier's law give the momentum transfer and the heat transfer in the laminar sub-layer respectively:

$$\tau = \mu_l \left(\frac{dv}{dy}\right) \tag{7-1}$$

$$q'' = -k_l \left(\frac{dT}{dy}\right) \tag{7-2}$$

$$\rightarrow \frac{q''}{\tau} = -\frac{k_l}{\mu_l} \left(\frac{dT}{dv}\right) \tag{7-3}$$

Applying Prandtl's approximation [74] that q''/τ is constant in the entire boundary layer, the approximate integration of q''/τ over the momentum laminar boundary layer gives:

$$\frac{q''_w}{\tau_w} = -(\frac{k_l}{\mu_l})(\frac{T_{ml} - T_w}{v_{ml}}) \tag{7-4}$$

where subscripts *w* and *ml* indicate the location at channel wall and the outer edge of momentum laminar boundary layer, respectively. Due to the difference between momentum and thermal boundary layer, the Prandtl number needs to be used to convert the temperature at the edge of the momentum laminar layer to the value at the edge of the thermal boundary layer (indicated with subscript *tl*):

$$T_{tl} - T_w \cong \frac{T_{ml} - T_w}{Pr^{1/3}} \tag{7-5}$$

According to the boundary layer theory, the velocity and temperature profile in the turbulent sub-layer is fairly flat. The temperature at the edge of the laminar layer (T_{tl}) can be

approximated by the bulk temperature (T_b). The velocity at the edge of the laminar layer (v_{ml}) can be approximated by the average film velocity ($\bar{v}_l$). Combining Eq. 7-4 and Eq. 7-5 gives:

$$h = \frac{q''_w}{(T_w - T_b)} = \left(\frac{k_l}{\mu_l}\right)\left(\frac{\tau_w}{\bar{v}_l}\right) Pr^{\frac{1}{3}} \tag{7-6}$$

The wall shear stress can be related to the average liquid film velocity with Darcy's friction factor:

$$\tau_w = f_l \frac{\rho_l \bar{v}_l^{\,2}}{8} \tag{7-7}$$

$$\tau_w = C_l Re_l^{-0.25} \frac{\rho_l \bar{v}_l^{\,2}}{8} \tag{7-8}$$

Eq. 7-6 is then rewritten as:

$$h = \frac{q''_w}{(T_w - T_b)} = (\frac{k_l}{\mu_l})(C_l Re_l^{-0.25} \frac{\rho_l \bar{v}_l}{8})\, Pr^{\frac{1}{3}} \tag{7-9}$$

Representing the actual average liquid film velocity in term of the superficial velocity with the geometry relation:

$$\bar{v}_l \cong \frac{D_h}{4\delta} v_{sl}(1 - E) \tag{6-8}$$

Substituting Eq. 6-8 into Eq. 7-9 gives the final form:

$$h = \left(\frac{4^{-0.75} k_l}{8 D_h} C_l\right) Re_{sl}^{0.75} \left(\frac{\delta}{D_h}\right)^{-0.75} (1 - E)^{0.75}\, Pr^{0.33} \tag{7-10}$$

Reorganizing the above equation, the functional form for the Nusselt number is achieved:

$$Nu_l \propto a_0 Re_{sl}^{a_1} \left(\frac{\delta}{D}\right)^{-a_2} (1 - E)^{a_3} Pr^{\frac{1}{3}}, a_i > 0 \tag{7-11}$$

The final expression with the set of coefficients that best fit to the data is shown below:

$$Nu_l = 0.96 Re_{sl}^{0.4} Pr^{0.33} \left(\frac{\delta}{D}\right)^{-0.65} (1 - E)^{0.15} \tag{7-12}$$

where $\frac{\delta}{D}$ is calculated by the proposed Eq. 6-18 in Section 6.4, and entrainment fraction is calculated by Al-Sarkhi et al. correlation [51].

$$\frac{\delta}{D} = 0.0146 Re_{sl}^{0.78} Re_{sg}^{-0.65} (1-E)^{0.1} \left(\frac{\rho_g}{\rho_l}\right)^{0.333} \left(\frac{\mu_l}{\mu_g}\right)^{0.667} \tag{6-18}$$

The comparison of the measured Nu_l and the predicted values by Eq. 7-12 is plotted in Figure 7-20, which shows a close agreement within ±5% discrepancy. Note that the data point at G= 750 kg·m^{-2}·s^{-1}, x_e= 0.016 is excluded from comparison as discussed previously.

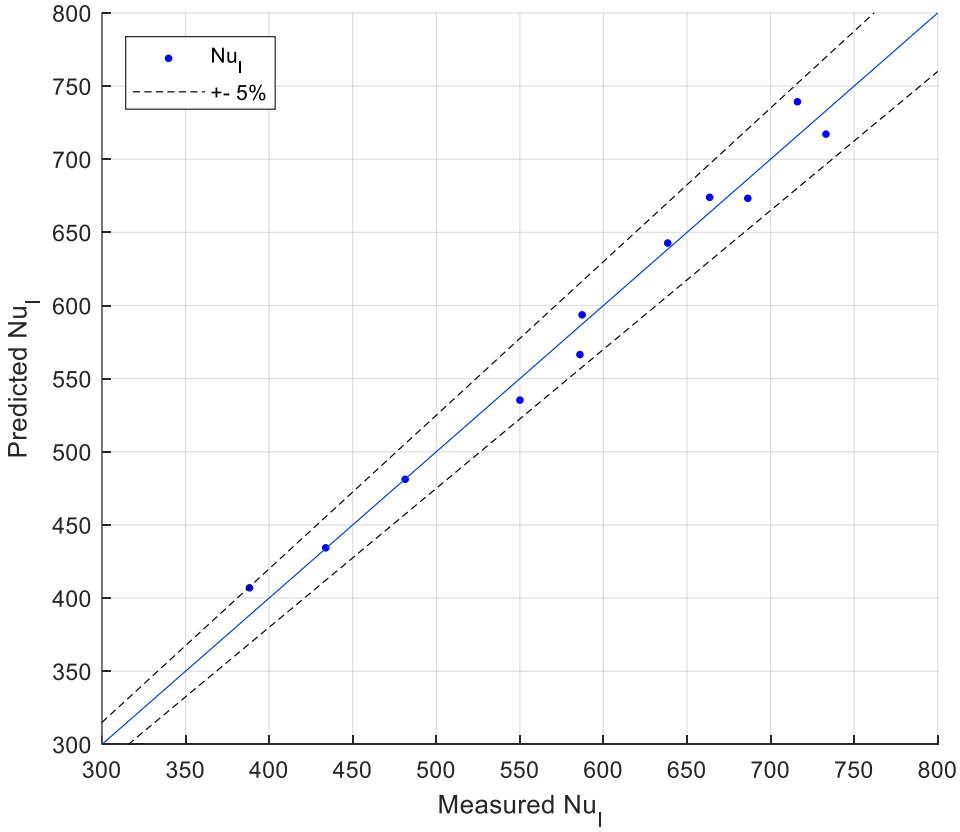

***Figure 7-20**: Comparison between measured and proposed correlation predicted Nusselt number Nu_l. Close agreement within ±5% discrepancy has been achieved.*

The proposed Eq. 7-12 is compared with other authors' correlations introduced in Section 2.2. As shown in Figure 7-21, Eq. 7-12 obviously gives the best prediction of the present experimental data, since the correlation is fitted to the data. Klimenko's correlation [12] systematically underpredicts our data, while Kandlinka's correlation [11] exhibits very significant

errors with slightly less bias than Klimenko's correlation. The author believes that the large uncertainty of the previous correlations comes from the lack of direct measurement of SNB conditions in those studies.

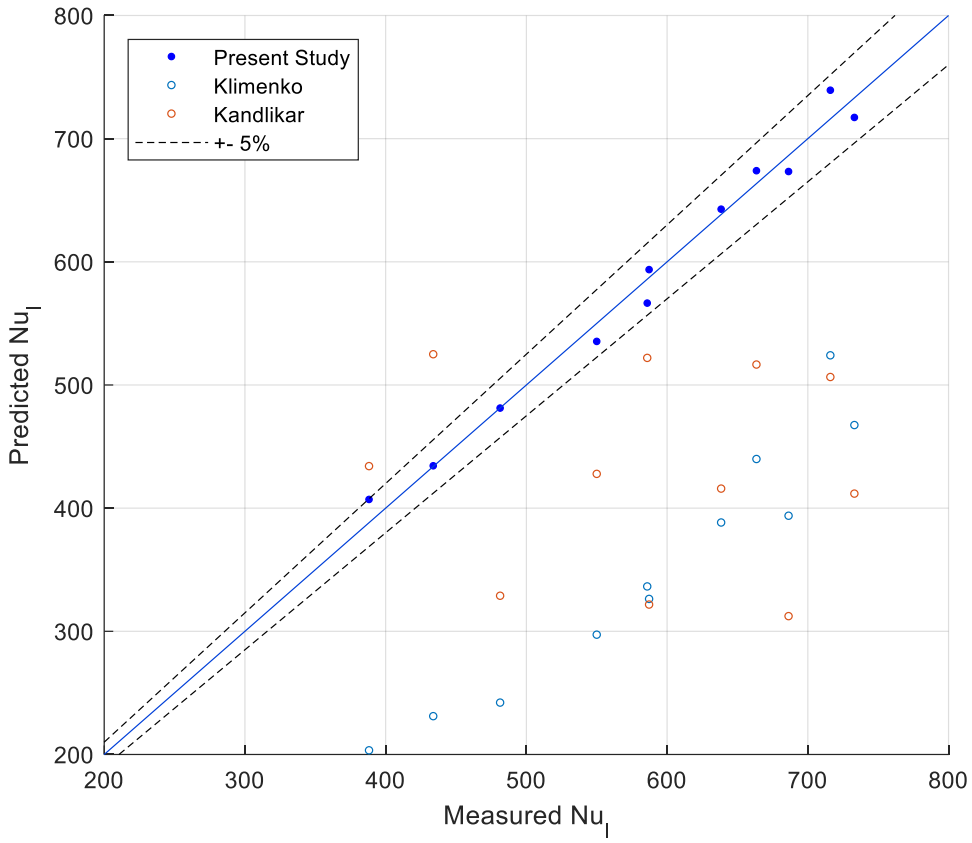

***Figure 7-21**: Comparison of the proposed correlation with the existing correlations [11][12].*

SNB Wall Superheat and Heat Flux

Once the SNB HTC is found, one can find the SNB heat flux from the Hsu's criterion for nucleation, i.e., the temperature required at the tip of a nucleated bubble equals the local saturation temperature required for mechanical equilibrium of a bubble, as calculated from the Young-Laplace equation. For a cavity radius of r_c on a hydrophilic surface, the local equilibrium temperature is:

$$T_{le} = T_{sat}(p_l + \frac{\sigma}{2r_c}) \tag{7-13}$$

The ITO-Sapphire heater was examined under an optical microscope. The most frequently observed surface cavities were in the length scale around 20 μm, as shown in Figure 7-22. The scale of such surface flaws is actually determined by the sapphire substrate, to which the ITO conforms; depending on the sapphire batch used, we observed cavities ranging from several microns to more than 20 μm.

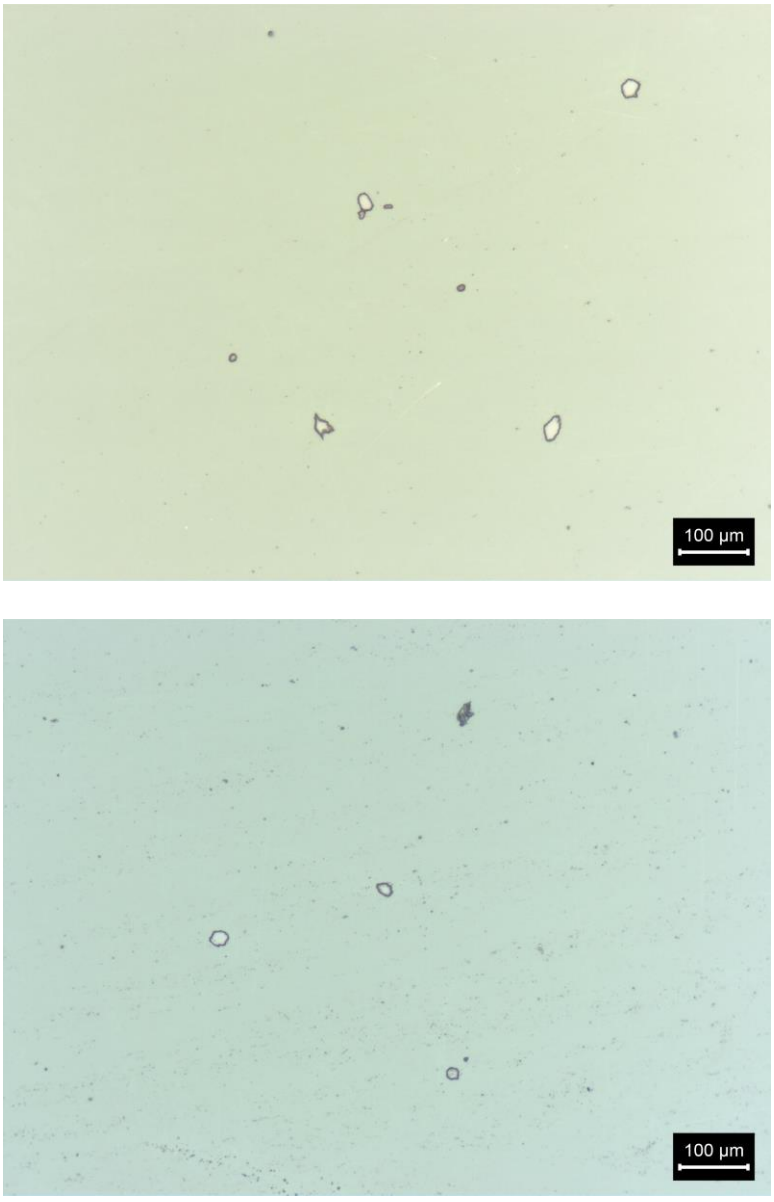

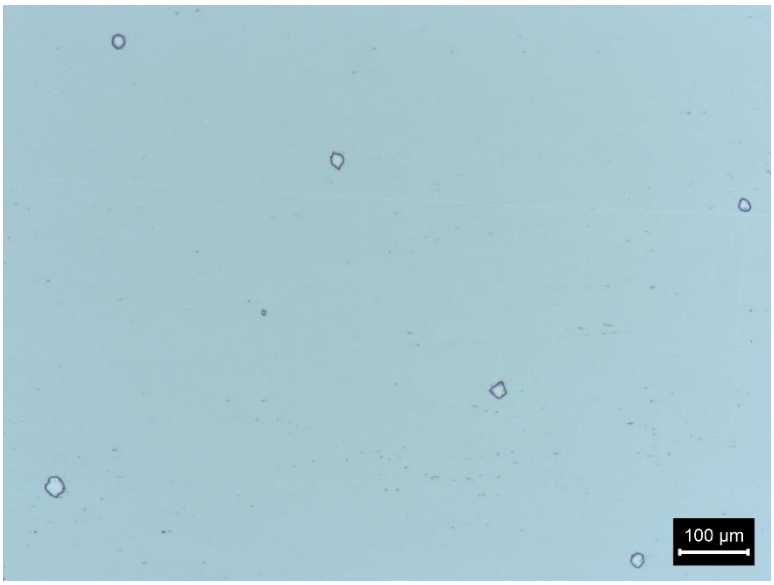

***Figure 7-22**: Typical flaws observed on the ITO-Sapphire heater from different locations: upstream (top), center (middle), and downstream (bottom). 20 µm is the most commonly observed size of the flaws.*

Among the flaws on the heater, only those with sufficient depth can trap gas/steam, thus become potential nucleation sites. On the image from optical microscope, it is impossible to measure the depth. However, one can still distinguish shallow flaws from deep ones. Most shallow flaws should have a very thin dark outline with a reflective bright center, assuming perfectly cylindrical pits do not exist on the heater. The thicker is the dark outline, the deeper is the flaw, since the sidewall reflects light off the microscope and appears like a thick and dark outline. Several potential nucleation sites are shown in Figure 7-23, which are also in the scale of 20 µm. Thus, the cavity radius of $r_c = 10\ \mu m$ is used in the calculation of present study.

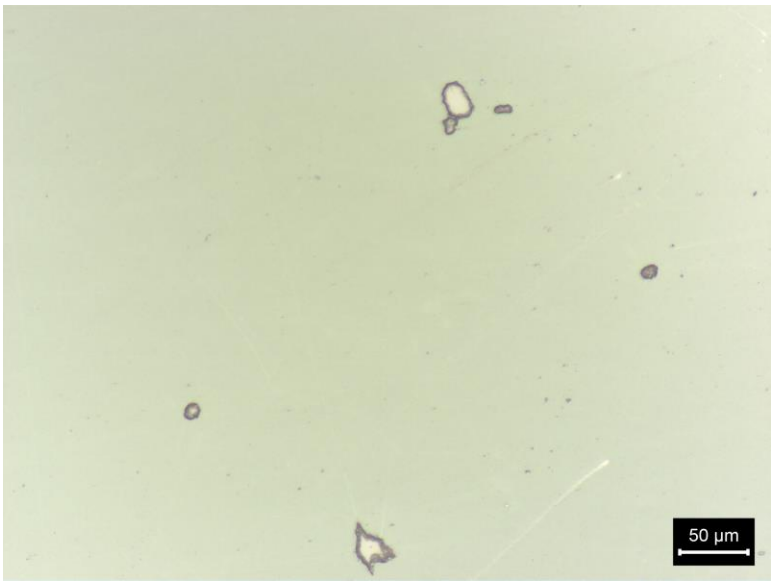
50 µm

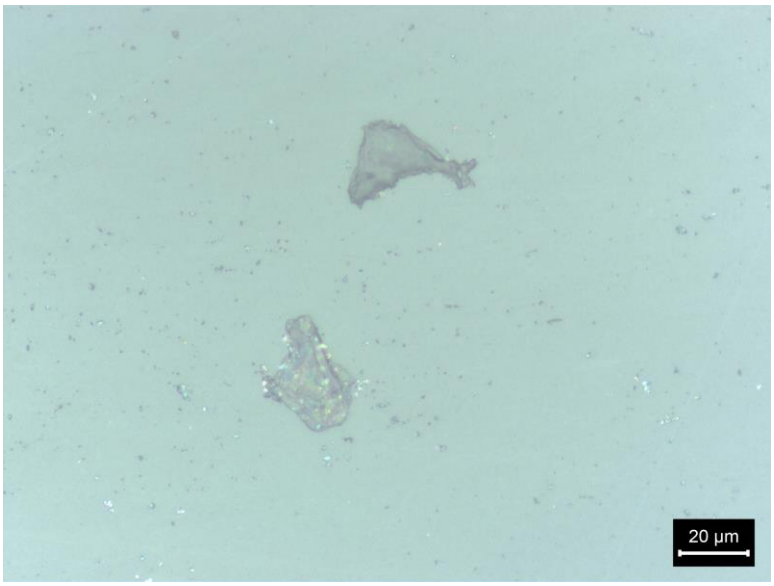
20 µm

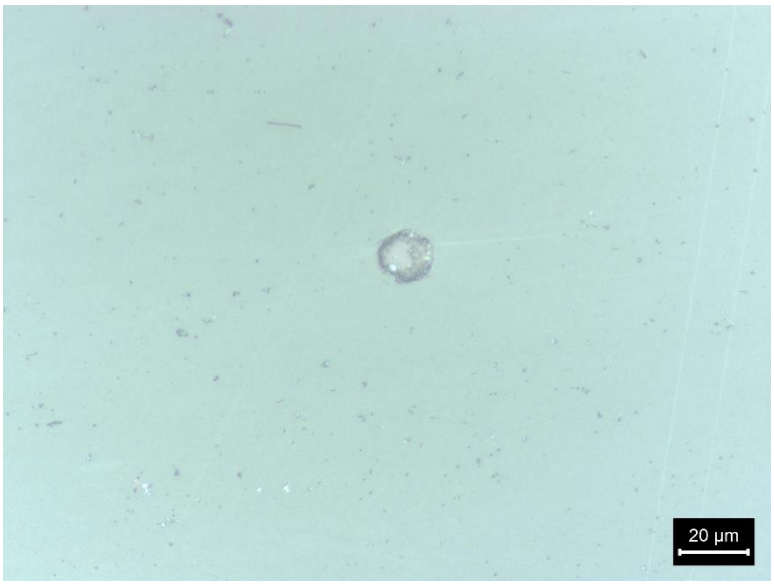

***Figure 7-23**: Examples of potential nucleation sites in the scale around 20 µm.*

For a cavity radius of 10 µm, the tip of the bubble embryo is well located within the laminar sublayer, thus the heat transfer is dominated by conduction.

$$q''_{SNB} = k_l \frac{T_w - T_{le}}{r_c} = k_l \frac{\Delta T_{sat} - \Delta T_{le_{sat}}}{r_c} \tag{7-14}$$

where $\Delta T_{sat} = T_w - T_{sat}$, $\Delta T_{le_{sat}} = T_{le} - T_{sat}$

Applying Newton's law of cooling, Eq. 7-14 becomes:

$$\Delta T_{sat} h = \frac{k_l}{r_c} (\Delta T_{sat} - \Delta T_{le_{sat}}) \tag{7-15}$$

$$\rightarrow \frac{\Delta T_{sat}}{\Delta T_{le_{sat}}} = \frac{1}{1 - Nu_{lc}} \tag{7-16}$$

where $Nu_{lc} = \frac{h r_c}{k_l}$

In a truly steady situation with a constant liquid film thickness, the above equation would give the heat flux for SNB/ ONB condition. However, at the actual annular flow conditions in the presence of the disturbance waves, the liquid film thickness oscillates periodically, which greatly disturbs the temperature profile and thus affects SNB/ONB. In order to support sustained boiling, a superheated layer defined on ($T_w - T_{le}$) needs to grow beyond the tip of the bubble. Considering

both Eq. 7-16 and postulating a dependence on the ratio of the film thickness to the cavity radius, the dimensionless superheat should be governed by the following equation:

$$\frac{\Delta T_{sat}}{\Delta T_{le_{sat}}} = a_0 Nu_{lc}^{a_1} \left(\frac{\delta}{r_c}\right)^{a_2} \tag{7-17}$$

Where $a_i > 0$. Fitting Eq. 7-17 to the experimental data gives:

$$Su_T = \frac{\Delta T_{sat}}{\Delta T_{le_{sat}}} = 3.4 Nu_{lc}^{2.2} \left(\frac{\delta}{r_c}\right)^{0.6} \tag{7-18}$$

Multiplying HTC to both sides of Eq. 7-18 gives the SNB heat flux:

$$Su_q = \frac{q''_{SNB} r_c}{k_l \Delta T_{le_{sat}}} = 3.4 Nu_{lc}^{3.2} \left(\frac{\delta}{r_c}\right)^{0.6} \tag{7-19}$$

The comparison of the measured SNB wall superheat and heat flux with the predicted values by Eq. 7-18 and Eq. 7-19 is plotted in Figure 7-24, which shows reasonably good agreement within ±15% discrepancy. The data point at G= 750 kg·m^{-2}·s^{-1}, x_e= 0.016 is excluded from comparison.

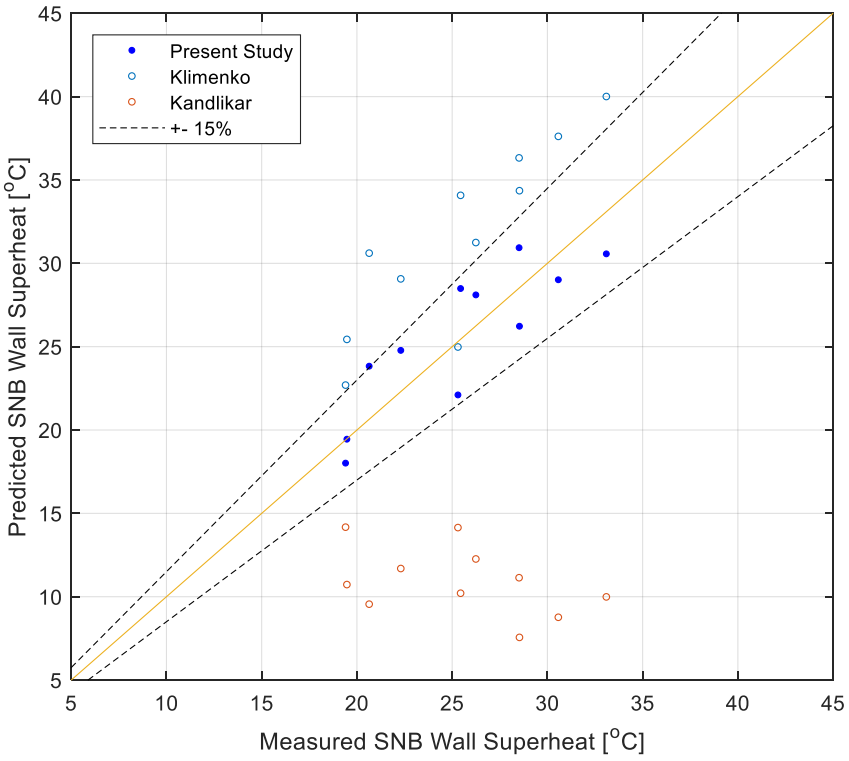

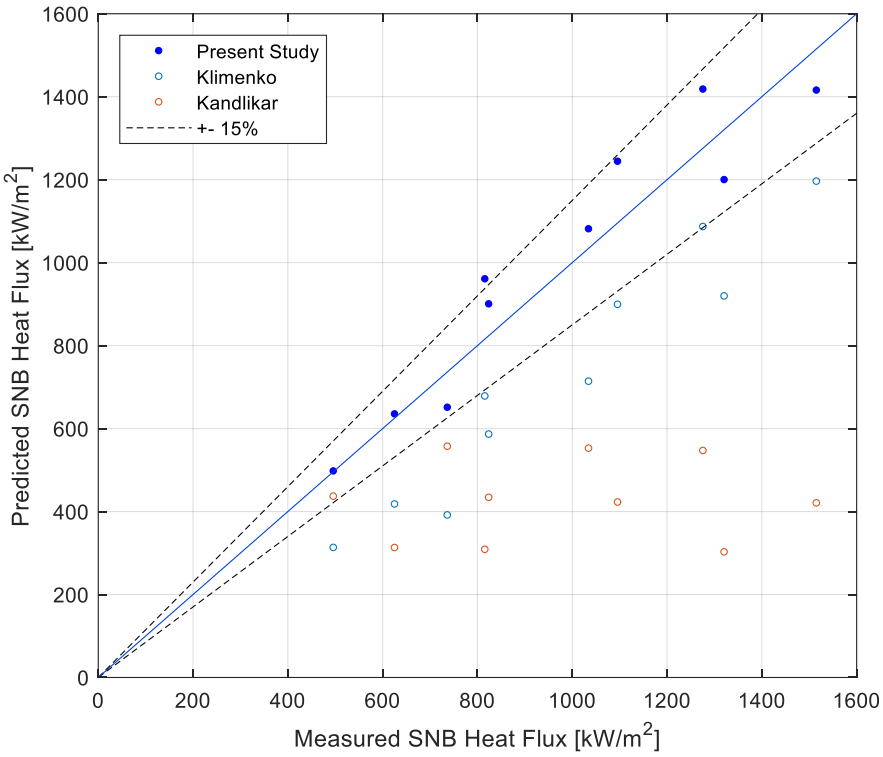

***Figure 7-24**: Comparison of the correlation proposed in present study other existing correlations [11][12] for SNB wall superheat (top) and heat flux (bottom). Reasonably good agreement within ±15% discrepancy has been achieved by the correlation proposed in present study.*

The proposed correlations (Eq. 7-18 and Eq. 7-19) are also compared with other authors' correlations introduced in Section 2.2. Thanks to the direct measurement of SNB conditions from the innovative diagnostics, Eq. 7-18 and Eq. 7-19 obviously give the best prediction of the present experimental data. Klimenko's correlation underpredicts the measured heat flux, while overpredicts the measured wall superheat. Kandlikar's correlation underpredicts both the measured heat flux and wall superheat.

The correlation predicted SNB heat flux versus SNB wall superheat is plotted in Figure 7-25, together with the measured data from Figure 7-19. The similarity of the dependency on dimensionless groups for Eq. 7-18 and Eq. 7-19 corroborates the earlier discussion on the collapsing trend in Figure 7-19.

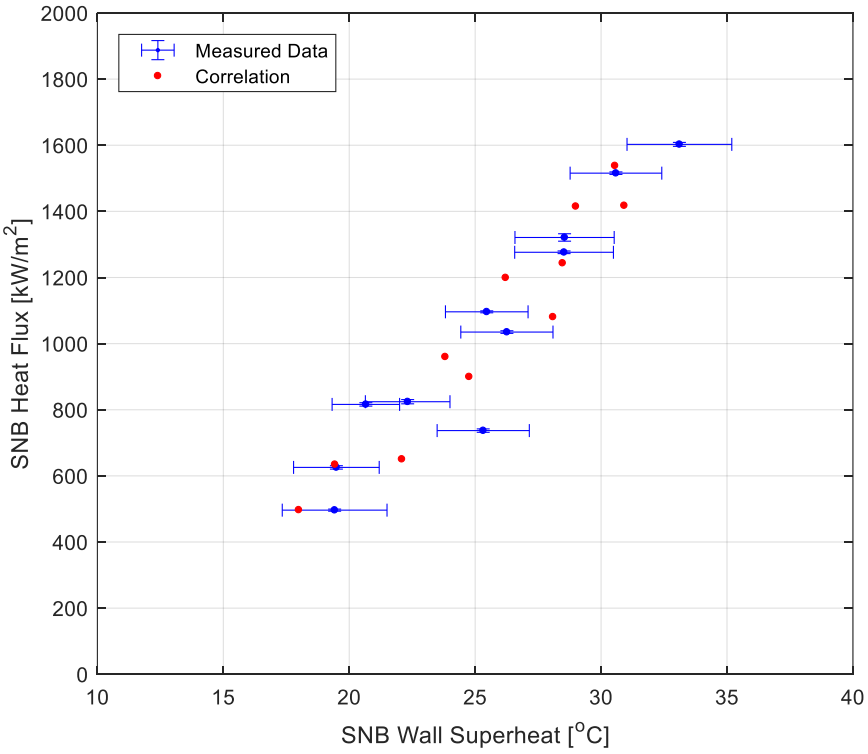

***Figure 7-25**: Comparison of the SNB heat flux versus SNB wall superheat between correlation prediction and measured data.*

7.4.2. Transient 1-D Mechanistic Model

As discussed in Section 7.2, periodic oscillations of the local thermal parameters exist, due to the variation of the heat transfer coefficient, which is caused by the periodic change of liquid film thickness induced by the passage of a wave. Although the semi-empirical correlations developed in the previous section have successfully predicted the time-averaged SNB parameters, they still cannot provide any information on the instantaneous variations of the local heat transfer parameters, which have been proved to affect the SNB/ONB process. To elucidate such intriguing time-dependent phenomena, a transient fluid flow and heat transfer model was developed to simulate the interaction between the disturbance wave and the local heat transfer.

Simulation of Temperature and Flow Profiles

Heat transfer in forced convective evaporation was approximated as a one-dimensional process, due to the large aspect ratio between the lateral scales of the heating area (9 mm by 94.5 mm), and the thickness of the heater and film (order of 1 mm). The situation is shown in

Figure 7-26. Since the ITO layer is very thin (700 nm), both its thermal resistance and thermal capacity are completely negligible. Therefore, the ITO was modeled as a planar heat source. The sapphire surface exposed to air was safely modeled as an adiabatic boundary due to the low free-convection HTC. The temperature of the water-vapor interface was fixed at the saturation value. When the film thickness changes due to the passage of a disturbance wave, the response time of the velocity profile is much faster than the period of the wave. Thus, the velocity field is assumed to attain its steady-state profile corresponding to the instantaneous liquid film thickness.

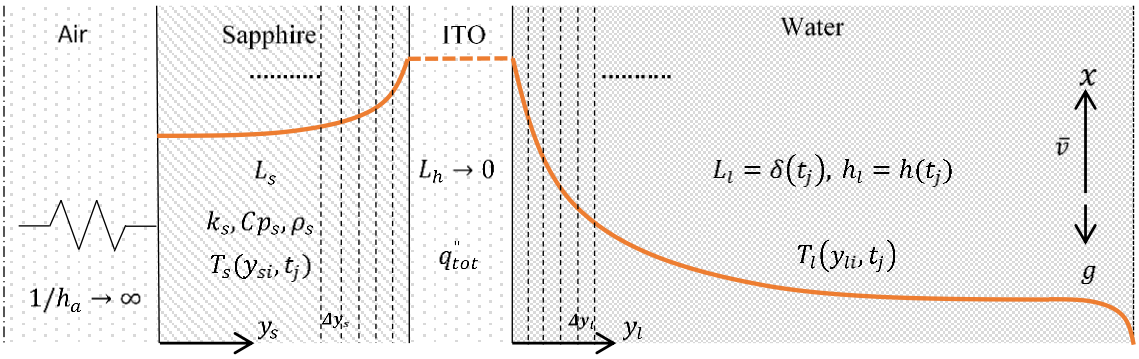

***Figure 7-26**: Sketch of the one dimensional heat transfer system consisting of sapphire substrate, ITO and water.*

Moreover, the measured time-averaged wall temperature changes very slowly along the flow direction, after a short initial thermal entry region of less than 20 mm, as shown in Figure 7-27 at the heat fluxes right below SNB. Note that the wall temperature at the upstream end of the heater is equal to the measured saturation temperature. The slow change in temperature after the entrance region suggests that the advection term in the energy equation can be neglected.

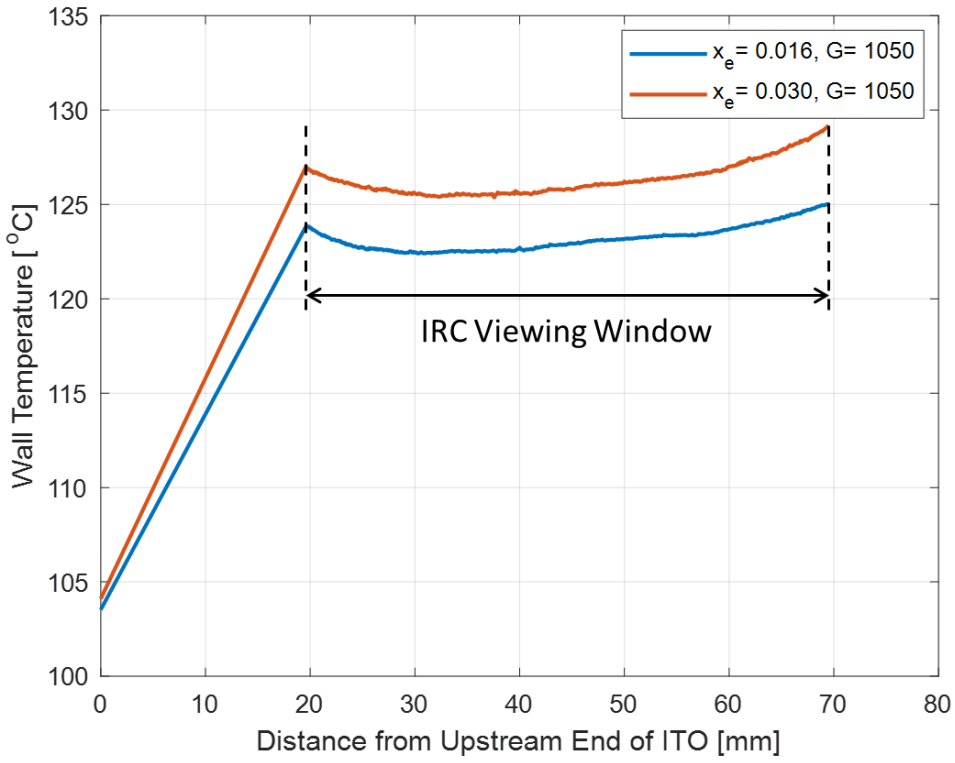

***Figure 7-27**: Time-averaged wall temperature along the flow direction, at two different flow conditions both under heat fluxes right below SNB. Mass flux G in the unit of kg·m^{-2}·s^{-1}. Note: the length of the ITO heater is 94.5 mm.*

Given the aforementioned simplifications, the fully developed momentum and energy equations, together with the appropriate boundary conditions are as follows:

- Momentum equation for water:

$$-g - \frac{1}{\rho_l}\frac{\partial \bar{p}}{\partial z} + \frac{\partial}{\partial y_l}\left(\left(\varepsilon_M(y_l) + \frac{\mu_l}{\rho_l}\right)\frac{\partial \bar{v}}{\partial y_l}\right) = 0 \tag{7-20}$$

$$\rightarrow \left(\varepsilon_M(y_l) + \frac{\mu_l}{\rho_l}\right)\frac{\partial v}{\partial y_l} = \tau_w\left(1 - \frac{y_l}{\delta(t)}\right) + \tau_i\frac{y_l}{\delta(t)} \tag{7-21}$$

where the interfacial friction factor is given by Henstock and Hanratty correlation [30]:

$$\frac{f_i}{f_s} = 1 + 1400F\left(1 - \exp\left(-\frac{(1+1400F)^{1.5}}{13.2G_0F}\right)\right) \tag{7-22}$$

$$\tau_i = f_i\frac{\rho_g v_{sg}^2}{2} \tag{7-23}$$

where

$$f_s = 0.046 Re_{sg}^{-0.2} \tag{7-24}$$

$$G_0 = \frac{D_h g \rho_l}{f_s \rho_g v_{sg}^2} \tag{7-25}$$

$$F = \frac{\left(\left(0.707 Re_{lf}^{0.5} \right)^{2.5} + \left(0.0379 Re_{lf}^{0.9} \right)^{2.5} \right)^{0.4}}{Re_{sg}^{0.9}} \left(\frac{\mu_l}{\mu_g} \right) \left(\frac{\rho_g}{\rho_l} \right)^{0.5} \tag{7-26}$$

$$Re_{lf} = \frac{\rho_l v_{sl} D_h (1 - E)}{\mu_l} \tag{7-27}$$

The entrainment rate in the above equation is calculated from Al-Sarkhi et al. correlation [51].

The momentum diffusivity ε_M from Fu and Klausner's paper [75] is modified to solve the turbulent velocity profile in the liquid thin film. The modification is inspired by PIV measurement of the velocity profile in liquid thin film flow found in reference [76].

$$\begin{cases} \varepsilon_M = 0.001 {y_l^+}^3 \dfrac{\mu_l}{\rho_l}, & y^+ \le 10 \\ \varepsilon_M = \left\{ 0.38 y_l \left[1 - exp\left(-\dfrac{y_l^+}{25} \right) \right] \right\}^2 \left| \dfrac{\partial v}{\partial y_l} \right| \left(1 - \dfrac{y_l}{\delta(t)} \right)^{1.3}, & y^+ > 10 \end{cases} \tag{7-28}$$

The transient heat equations are solved in both the heater substrate and the liquid thin film to capture the interaction between the heater and the flow:

- Heat equation for substrate:

$$\frac{\partial T_s}{\partial t} = \alpha_s \frac{\partial^2 T_s}{\partial y_s^2} \tag{7-29}$$

- Heat equation for water:

$$\frac{\partial T_l}{\partial t} = \frac{\partial}{\partial y_l} \left((\varepsilon_H(y_l) + \alpha_l) \frac{\partial T_l}{\partial y_l} \right) \tag{7-30}$$

where the modified turbulent Prandtl number (Pr_t) [75] is used to obtain ε_H from ε_M:

$$Pr_t = \frac{\varepsilon_M}{\varepsilon_H} = \begin{cases} 1.07, & y_l^+ < 10 \\ 1 + 0.855 - tanh(\, 0.2(y_l^+ - 7.5)\,), & y_l^+ \ge 10 \end{cases} \tag{7-31}$$

In addition to the main governing equations, several boundary and interfacial conditions are utilized to approximate the actual conditions. At the substrate-air boundary, adiabatic condition

is assumed due to low convective HTC. At the substrate-water interface, the energy conservation is imposed. At the heating wall, the no-slip flow condition is applied. At the water-steam interface, saturation temperature is imposed. The mathematical expressions of the boundary and interfacial conditions are summarized as:

$$k_s \frac{\partial T_s}{\partial y_s}\Big|_{y_s=0} = 0 \ \ \forall t \geq 0 \tag{7-32}$$

$$k_s \frac{\partial T_s}{\partial y_s}\Big|_{y_s=L_s} - k_l \frac{\partial T_l}{\partial y_l}\Big|_{y_l=0} = q''_{tot} \ \ \forall t \geq 0 \tag{7-33}$$

$$v|_{y_l=0} = 0 \ \ \forall t \geq 0 \tag{7-34}$$

$$T_l|_{y_l=\delta(t)} = T_{sat} \ \ \forall t \geq 0 \tag{7-35}$$

As shown in the above equations, the time-dependent liquid film thickness is an important input to the simulation. The experimentally measured liquid film thickness is applied as the input $\delta(t)$ to the model. The measured film thickness comes from the synchronized LFS and IRC recording at a specific experimental heat flux condition.

A finite difference method with both implicit time and space was used to discretize the governing equations of the model, so that a stable result was achieved at relatively large time step (0.5 ms) to accelerate the computation. In order to resolve the temperature profile within several microns from the heating wall, a small cell size was assigned: 1/3 μm at water side; 2/3 μm at substrate side. Dynamic mesh was used to maintain the cell size at varying liquid film thickness condition. The flow chart of the iteration process is illustrated in Figure 7-28. Total mass flux, steam quality, film thickness are the major inputs to the model at each time step, from which the entrainment rate is calculated, and thus the mean liquid film velocity is also known. The interfacial shear stress is calculated from Henstock's correlation. An order of magnitude estimation of the wall shear stress is also conducted with McAdams's and Blasius's correlations [3]. Then the velocity profile and momentum diffusivity profile are solved, and a new mean velocity is estimated. Finally, the mass conservation is checked via this new mean velocity. If the mass conservation is satisfied within accepted tolerance, the temperature profile is calculated and the model moves on to the next time step. Otherwise, the wall shear stress is adjusted according to the difference in mean velocity for another iteration of the model.

At rare situations when the liquid film thickness increases very sharply, the mass conservation cannot be satisfied even if wall shear stress decreases to zero, which indicates the overestimation of the interfacial hear stress. Such situation is similar to flowing over a tall obstruction (step), in which the form drag rises while the friction drag lowers down due to the existence of the local vortex on the windward or leeward of the obstruction, depending on the actual flow condition. The existence of the local vortex was analytically discussed by Hewitt [2], and an analytical analysis of the approximated periodic shear stress was discussed by Brooke-Benjamin [77]. The present code simulates such situation by numerically assigning the wall shear stress with the value in the previous time step assuming the wall shear stress changes slowly, while the interfacial shear stress is decreased iteratively until the mass conservation is satisfied. Nevertheless, the iteration process in Figure 7-28 is still executed successfully for the vast majority of the time steps.

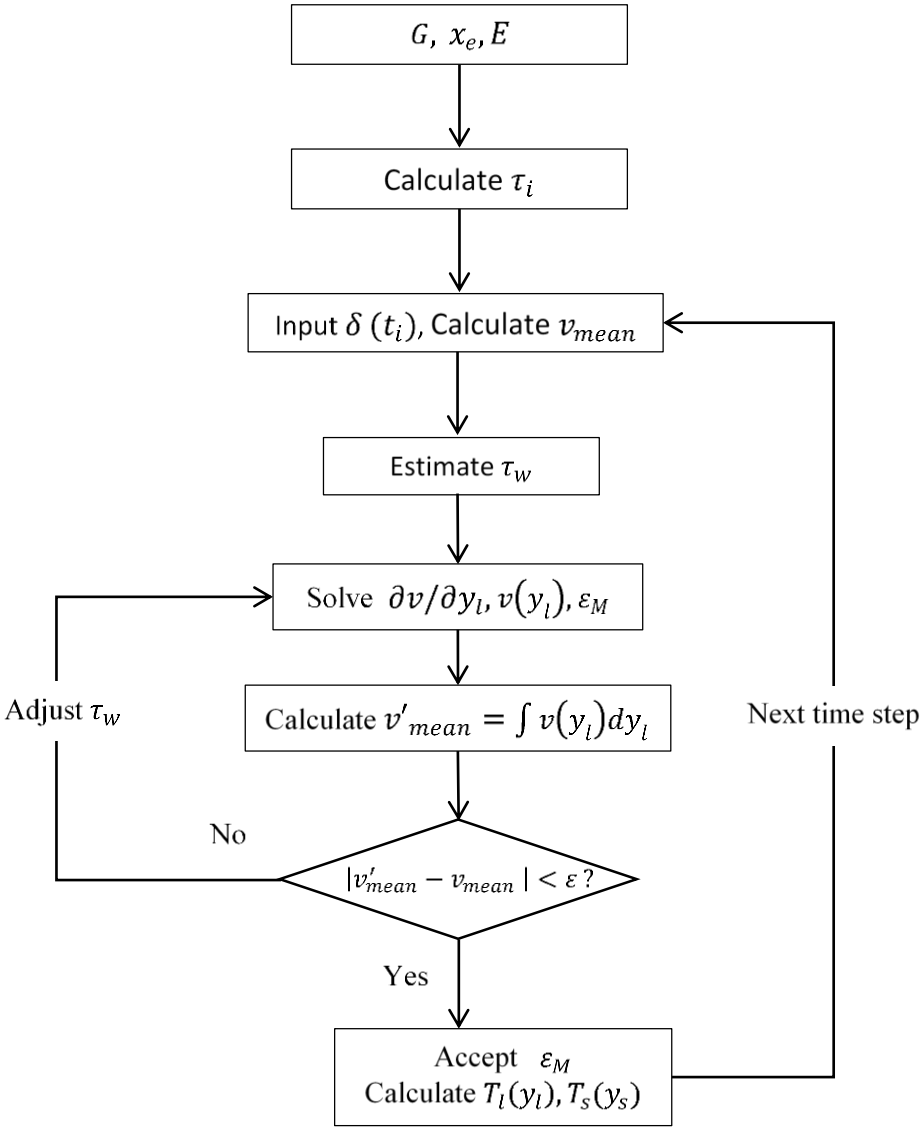

***Figure 7-28**: Flow chart for the iteration of the 1D model. The velocity iteration is the main focus of the chart since it is the crucial part of the calculation. The temperature calculation and time evolution are straightforward.*

The measured liquid film thickness was acquired at a sampling rate of 10k Hz (0.1 ms time interval). If 0.5 ms time step (2k Hz) was used for the simulation, four film thickness data points out of five had to be discarded. A conservative comparison was conducted at the highest mass flux and steam quality condition, to confirm if the reduced data points (2 kHz) was still able to provide the heating wall temperature accurately enough. As shown in Figure 7-29, the simulated wall superheats from film thickness at different sampling rates agree with each other very well. There

is only small deviation at several spiky peaks. Other simulations at lower mass flux and steam quality conditions should achieve even better agreement between 2 kHz input and 10 kHz input.

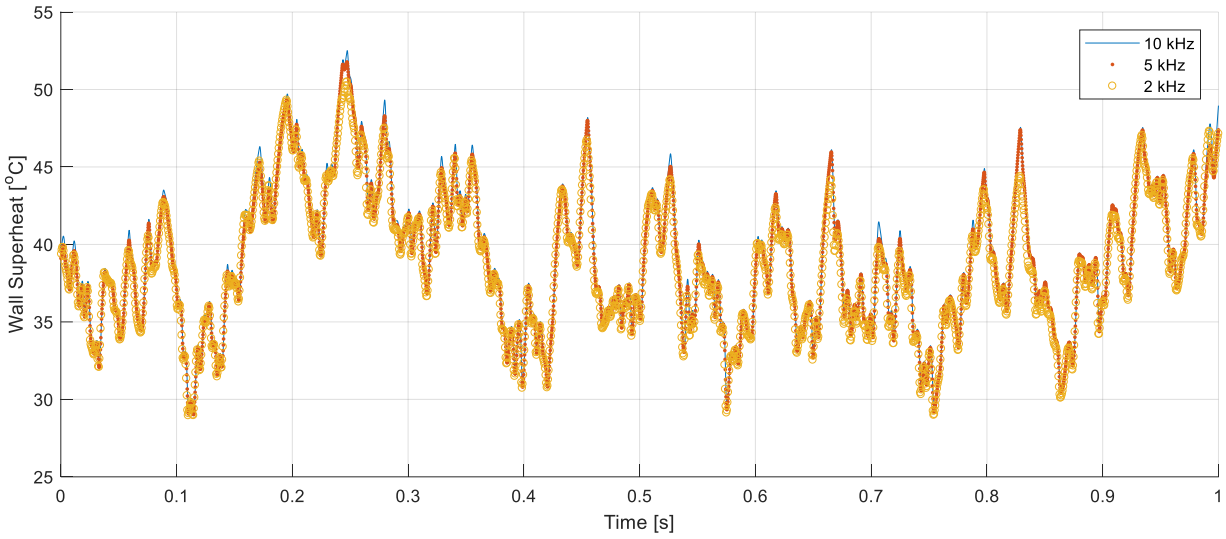

***Figure 7-29**: Comparison of the simulated wall superheat at nominal G= 1350 kg·m^{-2}·s^{-1}, x_e= 0.07 condition, with the film thickness input at different sampling rates. The result from 2 kHz input can accurately represents the result from 10 kHz input.*

The simulations were carried out at each combination of flow conditions, except for the nominal G= 750 kg·m^{-2}·s^{-1}, x_e= 0.016 condition for the usual reason. The heat flux right below SNB (i.e., 5 kW·m^{-2} lower than SNB) and the synchronized measured film thickness were used as the inputs to the simulation representing nominal SNB condition. A typical result of the simulated velocity and wall superheat profile in the liquid film at nominal G= 1050 kg·m^{-2}·s^{-1}, x_e= 0.016, with heat flux right below SNB is plotted in Figure 7-30.

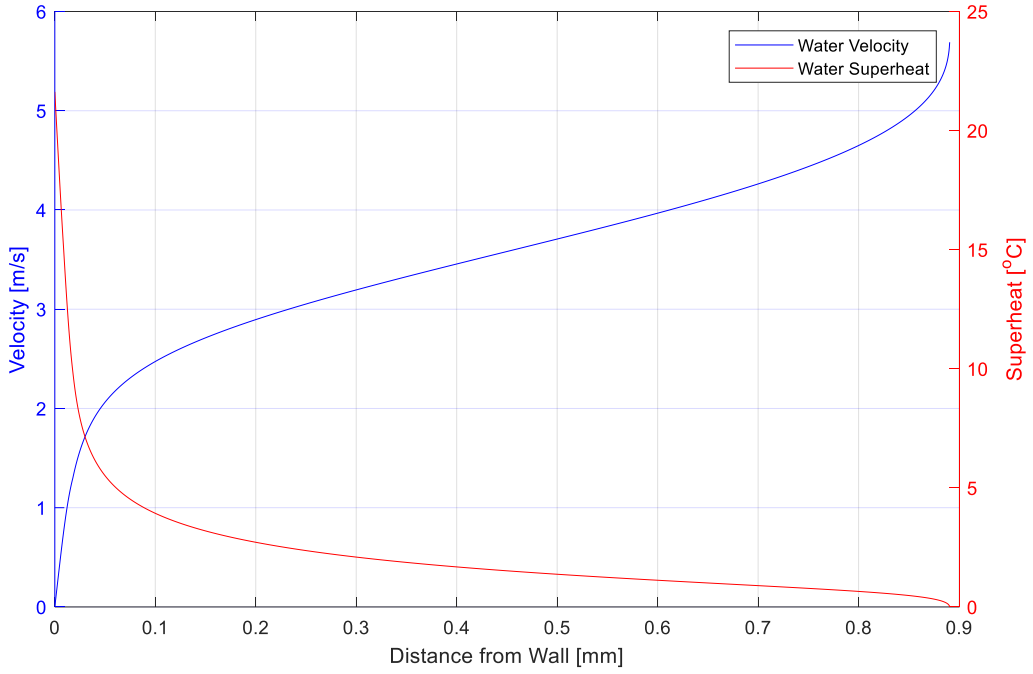

***Figure 7-30**: Typical velocity and superheat profile in the liquid film at nominal G= 1050 kg·m^{-2}·s^{-1}, x_e= 0.016, with heat flux right below SNB.*

As shown, three regions are clearly seen in the velocity and superheat profiles from the heating wall to the steam-water interface: near wall region, bulk region, and interface region. The first region is adjacent to the heating wall (about 0 mm to 0.05 mm on the plot), in which sharp and linear profiles of velocity and superheat are established. In the near wall region, the flow is mainly laminar and the heat transfer is dominated by conduction, which is the same situation of the near wall region in a single-phase turbulent flow condition. The second region is at the bulk or center part of the liquid film (about 0.05 mm to 0.85 mm on the plot), in which the trends of the velocity and superheat change much slower than in the near wall region due to effective turbulent mixing. However, different from the single-phase turbulent flow, the trends do not entirely flatten out, instead the velocity still gradually increases while the superheat gradually decreases. The lack of a plateau is mostly caused by the weakened turbulence in thin film condition, due to limited film thickness and the existence of the steam-water interface where turbulence is dampened. The unique region in thin film flow is near the steam-water interface (about 0.85 mm to 0.89 mm on the plot), in which the slopes of the velocity and superheat profiles sharpen again, similar to the near wall region. Such behavior is caused by the large interfacial shear stress, as well as the damping effect of the turbulence by surface tension at interface which tends to laminarize the flow.

In order to compare the simulated time history of wall superheat with the measured time history of wall superheat, the simulated value needs to be shifted backward in time. The time shift is due to the time lag of the disturbance wave transit from the ITO heater upstream to the LFS downstream, which was shown earlier in Figure 7-8 and Figure 7-9. The same time delay of the film thickness is used for shifting the simulated wall superheat, the result of which is shown in Figure 7-31 at various flow and heat flux conditions.

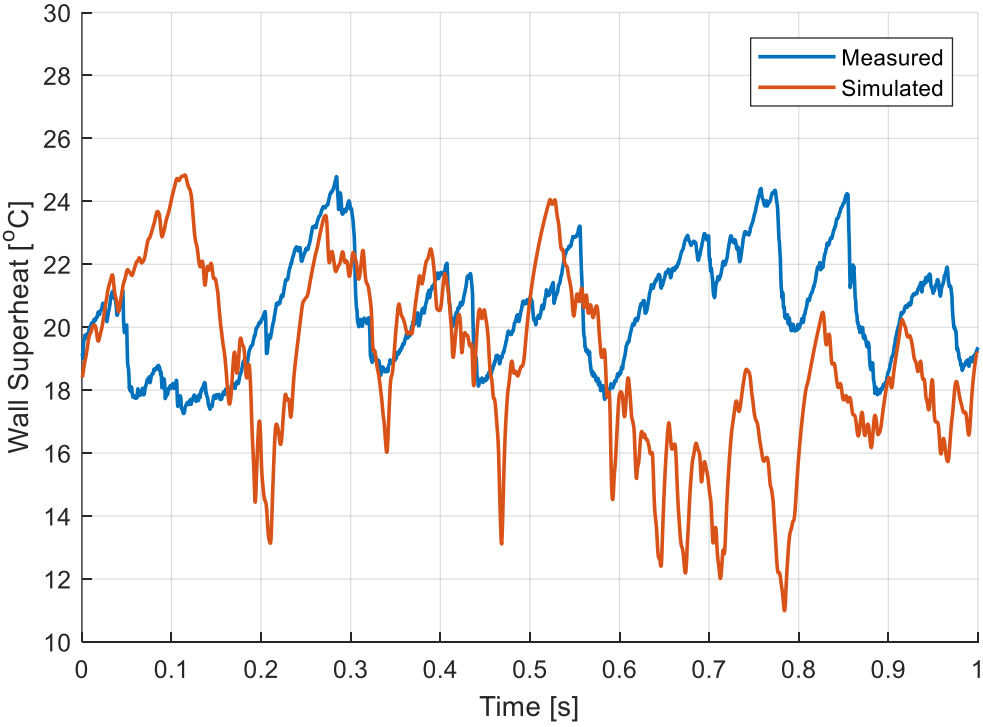

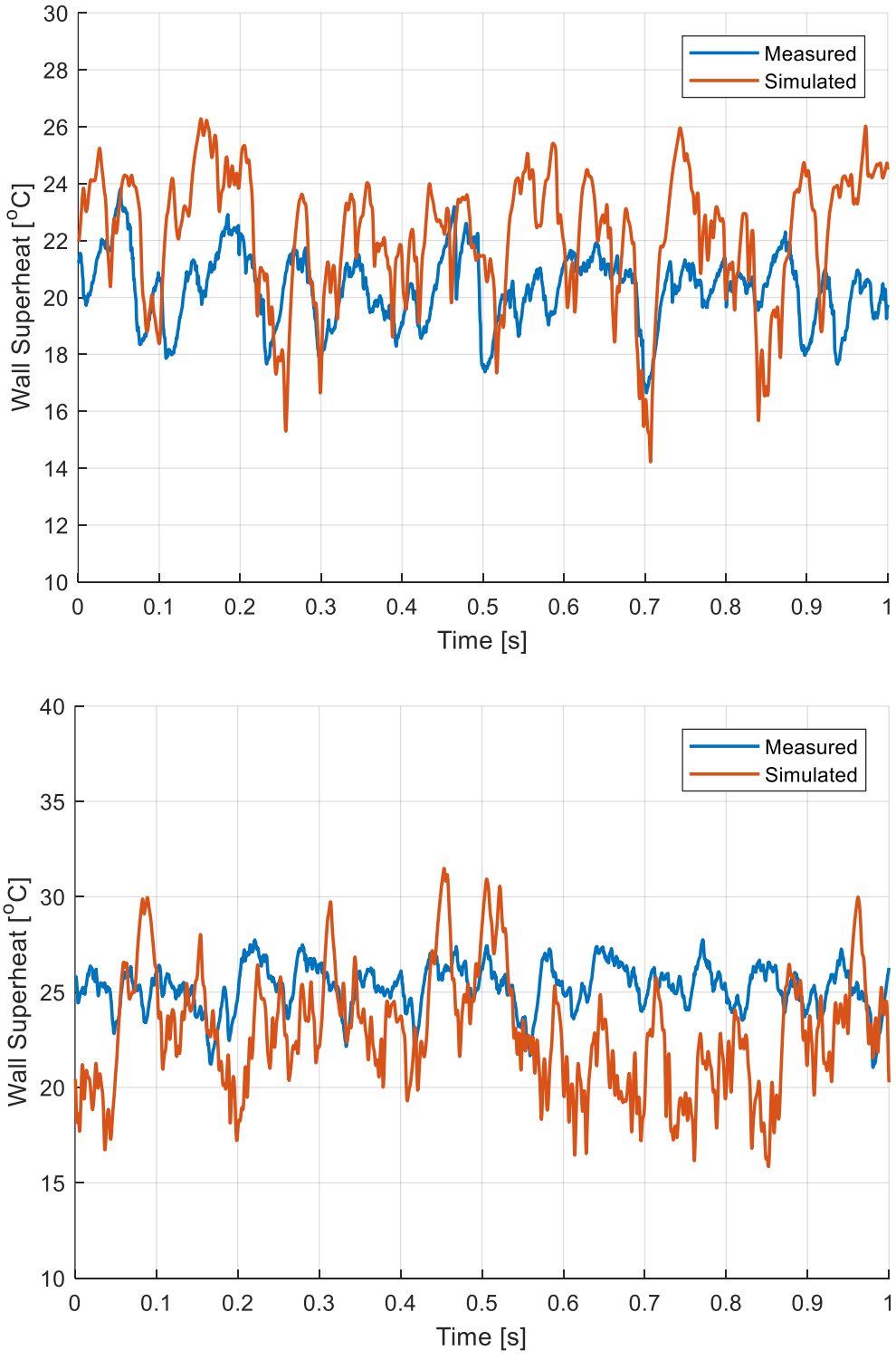

***Figure 7-31**: Comparison between measured and shifted simulated time history of the wall superheat at various flow and heat flux conditions: G= 1050 kg·m^{-2}·s^{-1}, xe=0.016, and imposed heat flux of 493.22 ± 0.76 kW·m^{-2} (top); G= 750 kg·m^{-2}·s^{-1}, xe=0.03, and imposed heat flux of 620.50 ± 0.83 kW·m^{-2} (middle);*

G= 1050 kg.m^{-2}.s^{-1}, xe=0.05, and imposed heat flux of 1272.33± 1.50 kW·m^{-2} (bottom).

As shown in Figure 7-31, the performance of the transient model is fairly good, given the number of assumptions and the complexity of the phenomena. The 1D transient mechanistic model predict the average wall superheat remarkably well, and it also seems to capture the oscillating characteristics, such as the peak positions, the oscillating amplitude, the transient ascending and descending slopes of the variation, etc. To the best of our knowledge, this is the first attempt to simulate such characteristics in annular flow over a broad range of steam quality, mass flux, and heat flux conditions. The discrepancies between the simulated results and the measured values mainly come from the non-collocated measurement of temperature and film thickness, and the noise of the film thickness measurement itself.

The mean wall superheat, wall superheat oscillation frequency and amplitude at each simulated nominal SNB condition are compared with the experimental SNB results in Figure 7-32. The 1D transient mechanistic model predicts the mean wall superheat and oscillation frequencies remarkably well. However, it systematically overestimates the wall superheat oscillation amplitude. The large error bars on the plot are not due to measurement uncertainties, but rather to the temporal and spatial temperature oscillations induced by the disturbance waves.

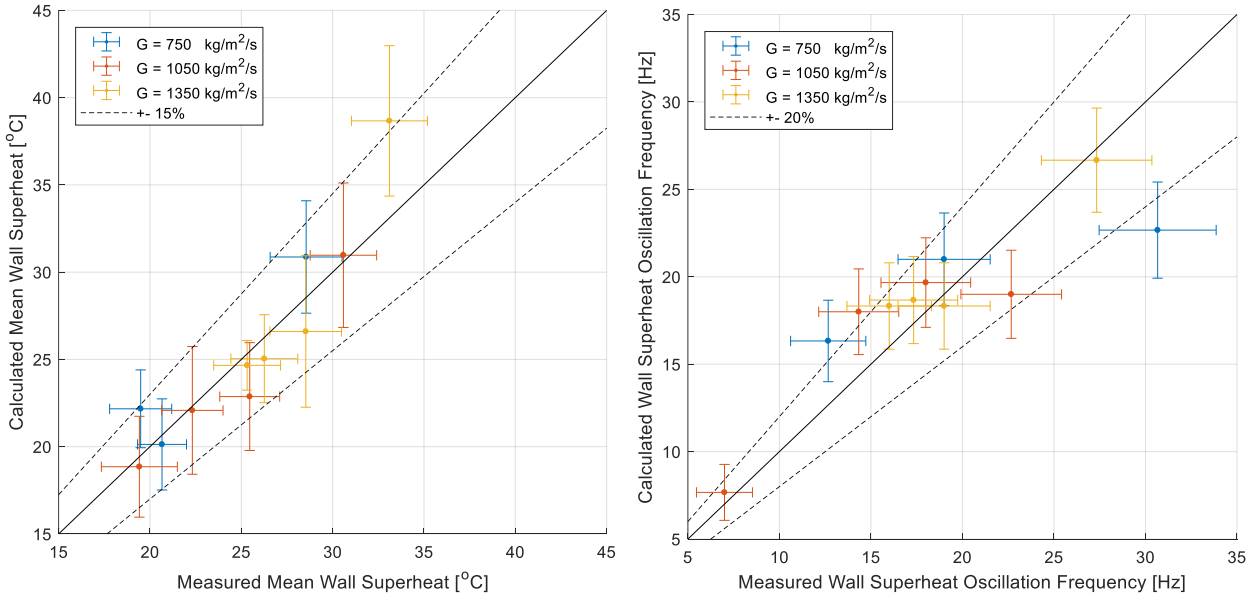

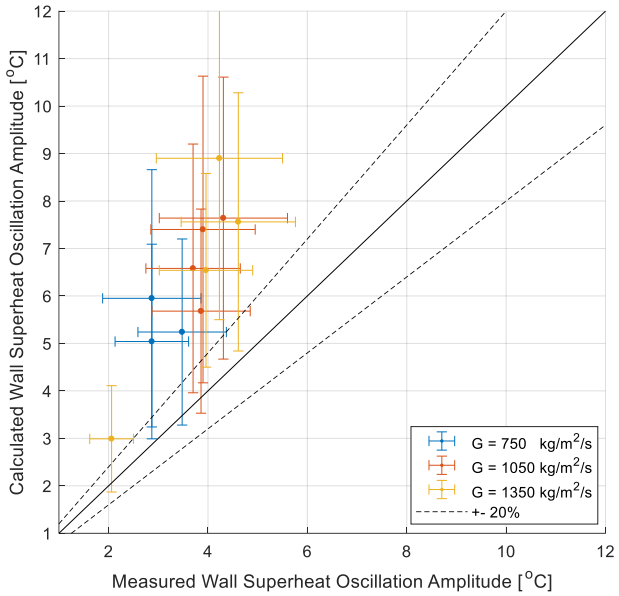

***Figure 7-32**: Comparison of mean wall superheat (top left), oscillation frequency (top right) and oscillation amplitude (bottom) between measurement and calculation from 1D transient mechanistic model*

The largest deviation of mean wall superheat occurs at the highest SNB heat flux condition, which is also at the highest mass flux and steam quality. Such deviation likely comes from the uncertainty on the predicted entrainment fraction. The overestimated entrainment fraction leads to the underestimated liquid film flow rate, thus results in higher wall superheat. If the entrainment fraction is reduced to 80% of the predicted value, the simulated time-averaged wall superheat is exactly the same as the measured value.

The good agreement in wall superheat in a wide range of flow and heat flux conditions (2 times difference in mass flux, 5 times difference in steam quality, and almost 10 times difference in heat flux) gives credence to the 1D transient model. The 1D transient model could also be used with a model for the instantaneous film thickness, should one be developed in the future.

SNB and ONB Condition

Once the temperature profile in the liquid film is predicted, a first-principle transient ONB model can be developed from the combination of Hsu's criterion [9] and the 1-D transient model for the forced convective evaporation. Hsu's criterion is discussed and illustrated in Section 2.2 Figure 2-2. Since our surface is hydrophilic (i.e., contact angle < 90^o), the Hsu's criterion can be expressed as:

$$T_l(r_c, t) \geq T_{sat}\left(p_g + \frac{2\sigma}{r_c}\right) \tag{7-36}$$

Combining Eq. 7-36 with the numerical solution of the temperature profile in water under the variation of the film thickness, the transient ONB conditions are predicted as shown in Figure 7-33. When the simulated wall temperature is higher than the value required by the ONB criterion, the time range is marked as grey, and signifies that bubble nucleation could occur. According to the transient ONB conditions, three ONB scenarios can be identified: a) ONB criterion is satisfied continuously; b) ONB criterion is satisfied intermittently; c) ONB criterion is never satisfied.

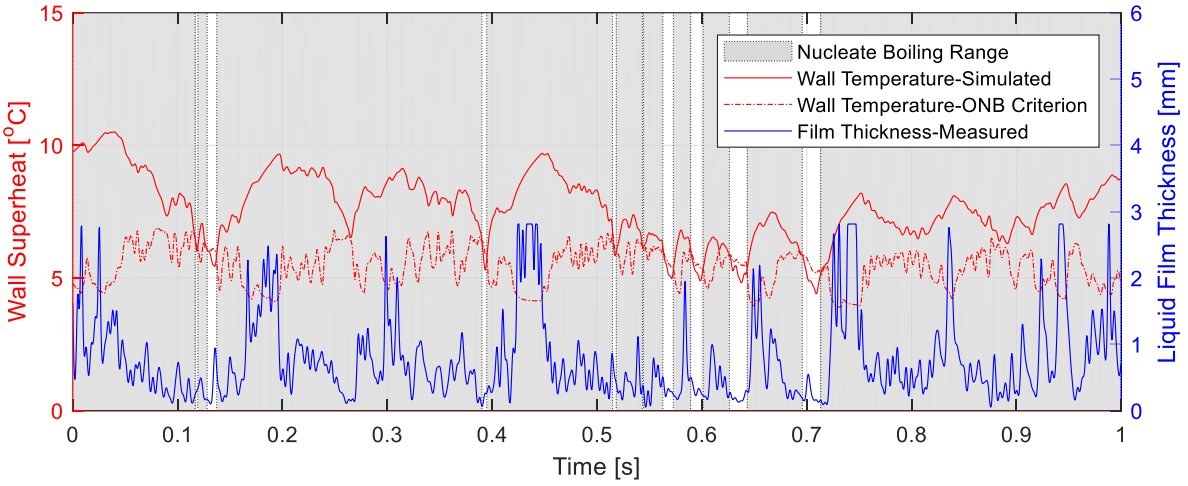

***Figure 7-33**: Sample of transient ONB identification in liquid film flow condition.*

As expected, the transient ONB approach highly underestimates the heat flux and wall superheat compared to the experimentally identified SNB condition. The difference is mainly due to the definition of SNB in the present study which is based on sustained boiling instead of the last bubble to disappear. As discussed in Section 7.4.1, the local equilibrium temperature $T_{le} = T_{sat}\left(p_g + \frac{2\sigma}{r_c}\right)$ needs to be met beyond the distance r_c required by the Hsu's model, in order to support continuous and experimentally appreciable sustained boiling events. Note that even if the ONB criterion is satisfied the entire time does not necessarily lead to a sustained boiling. The strong local force convective evaporation can prolong the wait time before boiling, while the extremely thin film and thus sharp shear stresses can detach a bubble from a nucleation site early. Both effects make the boiling event quite short-lived. The disturbing effect of turbulent flow on ONB was observed in previous experiments in transient subcooled flow boiling at MIT [78], suggesting another possible cause for underestimating the SNB heat flux and wall superheat: the

use of time-averaged (RANS) equations for heat and momentum transfer in the liquid film. Unlike large eddy simulation or direct numerical simulation, the RANS equations do not capture instantaneous turbulence features (such as vortex down sweeps) on the local heat transfer. Such deviation of simulated and measured SNB condition was not caused by the uncertainty of cavity size. Various cavity sizes down to 5 μm were tested in the transient model, and yet the simulated result still underestimated the SNB heat flux and wall superheat.

In conclusion, although the 1D transient model can predict wall superheat accurately, the ONB module of the code still needs to be modified for use in predicting SNB in annular flow. One approach is to modify the length scale in the Hsu's criterion. However, such modification is outside the scope of the present study.

7.5. Unsolved Issues

Despite the progress of the present study in measuring, analyzing and modeling various phenomena in annular two-phase flow heat transfer, there are still several unresolved issues. The two most interesting issues are the impact of surface contamination on SNB, and thermal non-equilibrium effects.

7.5.1. The Impact of Contamination on SNB

In the present study, a careful cleaning procedure of the ITO heater was carried out before starting the experiments each day successively with DI water, Acetone, Ethanol, Isopropanol, and DI water again. The purpose of this cleaning was to remove the possible deposition of dirt or chemicals from previous test and keep the heater in pristine conditions, so that the fundamental mechanisms of SNB could be clearly identified. The test matrix in Table 3-4 was conducted under the clean heater surface condition.

In the actual nuclear reactor conditions, contamination (e.g. CRUD) inevitably deposits on the surface of the fuel rod after operating for a long time, which deviates from the clean surface condition of present study. In the present experimental investigation, due to the large imposed voltage on the ITO, electrochemically induced contamination would also gradually grow on the ITO surface if it was not cleaned after many days of boiling test. Some experimental observations on aged heaters suggested that the contamination of the heating surface may have a significant

impact on the SNB, since longer-lived bubbles were observed in tests with decreasing heat fluxes descending tests.

An aged heater operated after long hours of boiling, on which whitish scale was clearly visible, was used for demonstration tests at two different flow conditions. The same experimental procedure and data post-processing method were applied. The time fraction of nucleate boiling versus heat flux plots are shown in Figure 7-34.

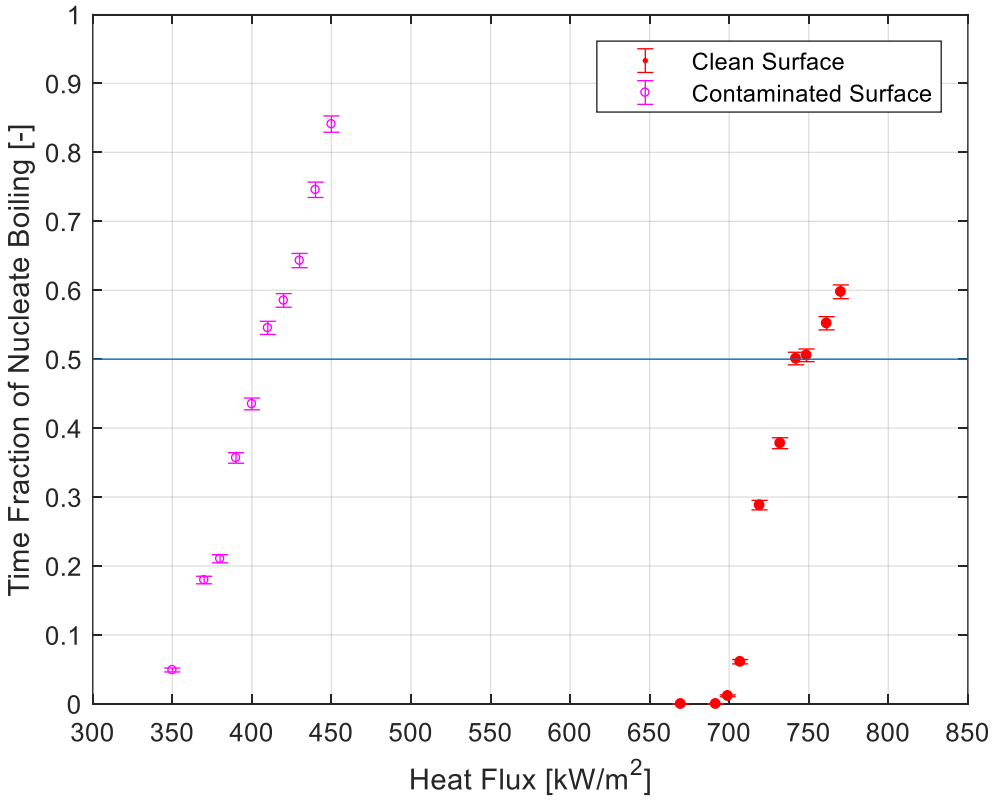

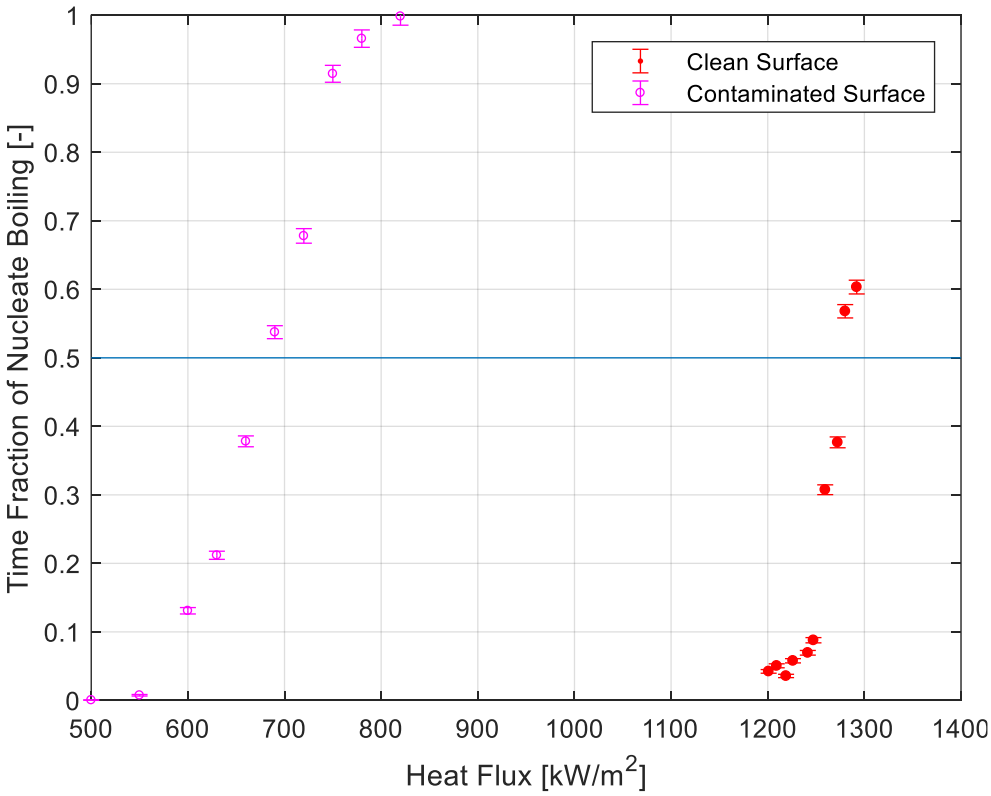

***Figure 7-34**: Comparison of time fraction of nucleate boiling at two different flow conditions: nominal G=1350 kg·m^{-2}·s^{-1}, x_e= 0.016 (top), and nominal G=1350 kg·m^{-2}·s^{-1}, x_e= 0.05 (bottom). The difference between clean and contaminated surfaces is obvious.*

As clearly shown in the plots, the contaminated heater surface lowers down the SNB heat fluxes to barely half the values measured from a clean heater surface. Such effect is observed at both high and low steam quality conditions. Interestingly, the contaminated heater surface provides more nucleation sites than the clean surface as shown in Figure 7-35. On the clean surface (top contour), there are about 4 to 5 active nucleation sites at the imposed heat flux of 1280 kW·m^{-2}. However, on the contaminated surface (bottom contour), there are more than 10 active nucleation sites at the imposed heat flux of barely 820 kW·m^{-2}. Except for the difference in nucleation site density, there is also an obvious difference in the temperature-varying rate of the nucleation site. On the clean surface, the time-averaged temperature varying rate at the center of the site is more than 800 ^{o}C.s^{-1}, while the value is less than 400 ^{o}C.s^{-1} on the contaminated surface.

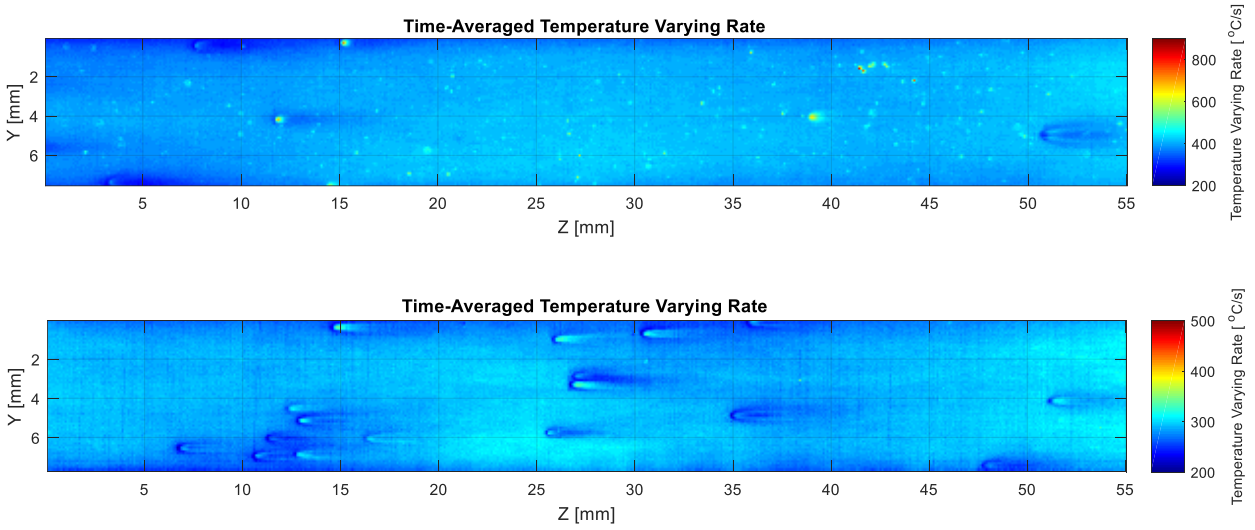

***Figure 7-35**: Comparison of the time-averaged temperature varying rate (the nucleation site map) on clean surface and contaminated surface at the same nominal flow condition. The differences in the varying rate at the center of the nucleation sites and the density of the nucleation site are obvious.*

The two demonstration tests have already shown the large effect of the contamination on the SNB thermal conditions. However, the mechanism by which contamination affects the heat transfer process is still not clear. We assume it is due to creation of additional surface defects, which serve as nucleation sites. In addition, the impact of the deposited contaminant to the liquid film is also important but unknown, especially when the film thickness becomes very thin and thus comparable with the size of such defects. Further investigation is recommended in the future.

7.5.2. The Thermal Non-equilibrium Effect

In almost all the heat transfer experiments of annular flow, thermal equilibrium is assumed at the test section inlet, if the test section is preceded by an adiabatic section. However, according to the present study, this assumption may not be valid, especially in two-phase flow with high steam quality and mass flux, because of the pressure drop along the flow.

At each experimental flow condition, the ITO temperature was recorded at non-heated situation (ITO power was off), after quasi-steady state flow condition was achieved. In such situation, the flow from the inlet of the entrance channel to the outlet of the test section is adiabatic. Thus, if thermal equilibrium was reached, the measured ITO temperature should be equal to the saturation temperature corresponding to the local pressure. In other words, the non-equilibrium

superheat, defined as $\Delta T_{sat_{neq}} = T_{ITO}\text{-}T_{sat}(p_l)$, should be zero, or at least within the small measuring uncertainty. However, the measured non-equilibrium superheat is not close to zero, but rather large, as shown in Figure 7-36.

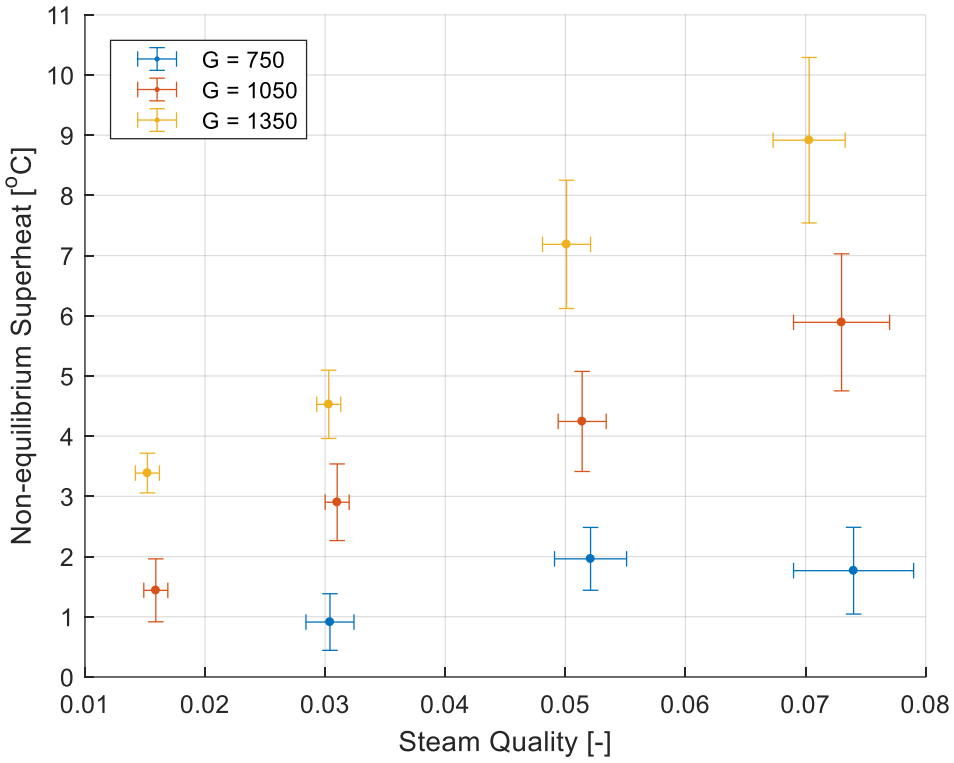

***Figure 7-36**: Measured non-equilibrium superheat on ITO versus steam quality at various mass fluxes, under adiabatic condition.*

As shown in Figure 7-36, the measured non-equilibrium superheat is clearly above 1 °C with the highest value reaching 10 °C. The trend of non-equilibrium superheat increases with the increasing steam quality at constant mass flux, as well as increasing mass flux and constant steam quality. The result indicates that a dynamic heat transfer process is happening in the liquid film even as the adiabatic condition exists at the channel wall. Since a direct measurement of the temperature profile within the liquid film is not available in the present study, a plausible dynamic process with the associated heat and mass transfer mechanisms is proposed for future evaluation:

a) The annular two-phase flow with high steam quality and mass flux leads to high pressure drop, and thus continuously dropping local saturation temperature along the flow.

b) The pressure drop leads to flashing at the liquid-steam interface, where the new and lower saturation temperature is present instantaneously.
c) Heat transfer then occurs within the liquid film to the liquid-steam interface, thus creating a significant temperature gradient between the wall (i.e., the ITO) and the liquid-steam interface.
d) Since such heat transfer process is gradually slower down from the turbulent bulk flow to the wall (especially in the laminar sublayer near the wall), the local wall temperature is higher than the local saturation temperature, creating this non-equilibrium effect.

In addition to the above proposed dynamic heat transfer mechanism, Joule-Thomson cooling effect could also play a role in such process [79]. In the present investigated flow conditions, the non-equilibrium superheat does not seem to affect much the prediction of the wall superheat at heating condition. Although the 1D transient model assumes an instantaneous response of temperature profile to the change of flow, excellent agreement is still achieved between the measured and simulated wall superheat. The non-equilibrium effect is most probably restricted to a very narrow region adjacent to the channel wall, and the bulk of the film is not affected.

Nevertheless, it is clearly seen from Figure 7-36 that the non-equilibrium superheat increases quickly with the increasing flow parameters. At higher mass flux and steam quality condition, the pressure gradient along the flow is larger and the advection is faster. Turbulent mixing is not guaranteed to still effectively homogenize the bulk of the liquid film. Such high flow parameters inevitably and unfortunately exist in the BWR condition close to the exit of the fuel bundle (mass flux and steam quality both higher than present study) or in a postulated accident condition (steam quality could be much higher than present study). Understanding how such thermal non-equilibrium effect could influence heat transfer at reactor conditions is left to future work.

8. Conclusions and Future Works

8.1. Summary and Conclusions

An apparatus was constructed for establishing and investigating heat transfer in steam-water annular flow at atmospheric pressure. An innovative diagnostic technique combining synchronized infrared (IR) thermography and an electrical conductance-based liquid film thickness sensor (LFS) was used in the present study to directly measure the flow and thermal parameters of the SNB phenomena. The LFS achieved a 10000 Hz acquisition rate and 1.25 mm spatial resolution. The IR thermography achieved 2000 Hz frame rate and 0.1 mm spatial resolution. The SNB conditions were investigated in large ranges of the control parameters: mass flux from 700 to 1400 $kg \cdot m^{-2} \cdot s^{-1}$ (two-fold change), steam quality from 0.016 to 0.08 (five-fold change), and heat flux from 100 to 2000 $kW \cdot m^{-2}$ (twenty-fold change). The system pressure was held close to atmospheric pressure. At each set of conditions, the local distributions of 2D wall superheat, 2D heat flux, and quasi-2D liquid film thickness were measured, from which the SNB heat flux and wall superheat were extracted. The hydrodynamic properties of the disturbance waves, such as wave velocity, frequency and amplitude, were also post-processed from a Skewed Gaussian decomposition algorithm.

A first of a kind 1D mechanistic model was developed for accurately capturing the unique transient effect of disturbance wave on SNB conditions and local heat transfer. A complete set of semi-empirical correlations was proposed for predicting the time-averaged film thickness and SNB thermal conditions. Good agreement is achieved between the semi-empirical correlations and the experimental results.

The main findings and conclusions are summarized under two main topics: the hydrodynamics of liquid film and the heat transfer in annular flow.

8.1.1. Hydrodynamics of Liquid Film

The time-averaged liquid film thickness shows a concave profile in transversal direction (in cross section plain), while a flat profile in longitudinal direction (along the flow). The existence of disturbance waves was clearly observed from the measured time history of the liquid film thickness.

The statistical distribution of the film thickness shows a peak at medium thickness, and a skewed distribution toward the large thickness. The mean film thickness represents the base of the film as dictated by the conservation of mass. The plus deviation of the film thickness represents the average height of the surface waves above the base film, including both the ripples and the disturbance waves. The minus deviation of the film thickness represents the accelerated flow to satisfy mass conservation after surface waves leave. The mean, plus deviation, and minus deviation of the film thickness are found to be strongly dependent on steam quality while weakly dependent on mass flux. All three parameters monotonically decrease with the increasing steam quality at constant mass flux.

Disturbance waves were identified by a new robust bandwidth recognition criterion from the film thickness time history. Thus, the wave frequency and wave amplitude were extracted. An in-house Skewed Gaussian decomposition algorithm was developed for calculating the velocity of each individual disturbance wave. The disturbance wave velocity, frequency, and amplitude depend on both steam quality and mass flux, although the dependency is more pronounced on steam quality. Specifically, the disturbance wave velocity increases with the increasing steam quality at constant mass flux, as well as increasing mass flux at constant steam quality. The disturbance wave amplitude generally decreases with increasing steam quality, while the trends at different mass fluxes converge as steam quality increases. The disturbance wave frequency also generally increases with increasing steam quality at constant mass flux, except for the abnormal data points at nominal G= 1350 $kg \cdot m^{-2} \cdot s^{-1}$.

A mechanism-based semi-empirical correlation was developed to predict mean liquid film thickness. Close agreement within ±5% discrepancy was achieved between the prediction from this correlation and the measurements. Other authors' correlations result in large deviations from the measured value. Such large deviation may come from much larger superficial liquid Reynolds number in present study compared to other authors' databases.

8.1.2. Heat Transfer in Annular Flow

Under convective evaporation heat transfer regime in annular flow, periodic superheat oscillations were clearly seen from the IR thermography data, behaving like "cooling waves" sweeping over the heater surface. Periodic oscillations of the chordal-average thermal properties

(wall superheat, heat flux, HTC) were observed, even though the annular flow was stable, and the imposed heat flux was constant. The wave velocity and frequency of these "cooling waves" were calculated. The agreement of the wave velocity and frequency between "cooling waves" and disturbance waves suggests that the oscillation of thermal properties is caused by the periodic change of liquid film thickness with the passages of disturbance waves. The conclusion was confirmed time cross-correlation of the wall superheat signal and the timely shifted film thickness signal

A novel mapping method based on the time-averaged temperature varying rate was developed to locate the nucleation site positions under the impact of the disturbance waves. Based on the nucleation site map, a criterion using the time fraction of nucleate boiling was developed to determine SNB, since the traditional bubble footprint method and boiling curve inflection method failed due to the temperature oscillations caused by the disturbance waves. The hysteresis between SNB and ONB conditions was observed to not exist, at least at the conditions in our experiments. The extracted SNB/ONB thermal parameters, i.e., wall superheat, heat flux and HTC, weakly depend on total mass flux, while they show strong dependency on steam quality. All the SNB/ONB thermal parameters, i.e., wall superheat , heat flux and HTC, increase with increasing steam quality at constant mass flux, as well as increasing mass flux at constant steam quality. The SNB/ONB wall superheat and heat flux in annular flow are found to be much larger than the values typically seen in ONB for single-phase liquid flow. Specifically, the SNB/ONB wall superheat ranges from 19 ^{o}C to 33 ^{o}C, while the SNB/ONB heat flux ranges from 496 kW$\cdot$m^{-2} to 1602 kW$\cdot$m^{-2}.

A mechanism-based semi-empirical correlation was developed for the SNB HTC in annular flow, using the semi-empirical correlation for film thickness developed in the present study. Close agreement within ±5% discrepancy is achieved between the prediction from my proposed correlation and the measurement. Other authors' correlations result in large deviations from the measured value. Such prediction deviation comes from the lack of direct measurement of SNB conditions in previous researches. In addition to the semi-empirical correlations for HTC, two semi-empirical correlations for SNB wall superheat and heat flux were also developed. Good agreement is achieved between the predicted SNB wall superheat and heat flux within ±15% discrepancy.

A transient 1D mechanistic model was developed for predicting the instantaneous velocity and temperature profile in the liquid film. The oscillating wall superheat caused by disturbance wave and the interfacial velocity were correctly reproduced. The simulated wall superheat oscillation using the measured film thickness as input, agrees reasonably well with the measured wall superheat. For the first time, the oscillating wall superheat in annular flow is simulated, over a broad range of steam quality, mass flux, and heat flux conditions. With the locally simulated temperature profile, the transient 1D mechanistic model also has the capability to predict transient SNB conditions. However, since the definition of SNB in present study is based on sustained boiling instead of the last bubble, the traditional Hsu's ONB criterion is no longer applicable. The SNB module of the transient 1D model still needs to be improved with a modified or new ONB criterion.

Except for the results summarized above, the present study also discovers two new findings that are intriguing but not yet fully explained. One finding is about the impact of contamination on SNB heat flux. The SNB heat flux on contaminated surface is almost 50% lower than the value observed on a clean surface, at the same nominal flow condition. The nucleation site density is also found to be higher on the contaminated surface. The other finding is the existence of thermal non-equilibrium within the film under adiabatic condition. The non-equilibrium wall superheat increases quickly with the increasing flow parameters.

8.2. List of Contributions

1) Designed and built the first steam-water annular flow loop in NSE, MIT for the direct measurement of the local thermohydraulic parameters of the annular flow associated phenomena.

2) Developed a first of a kind multi-physics diagnostics that simultaneously interrogates the flow dynamics of the thin film in annular flow and the heating wall parameters from synchronized LFS and IR thermography. The new type of surface mounted LFS developed in collaboration with ETH Zurich can non-intrusively measure film thickness from 2.5 μm to 2.5 mm (a measuring span over 3 orders of magnitudes), at a temporal resolution of 10000 Hz and spatial resolution of 1.25 mm.

3) Generated a large database of quasi-2D liquid film thickness in steam-water annular flow with steam quality and mass flux close to the BWR operating condition, but at atmospheric pressure. Statistical profile of the liquid film thickness was obtained.

4) A new bandwidth criterion was developed for recognizing the disturbance waves from the time history of the film thickness, which is robust against artificial bias and the noise from ripples on disturbance waves. Disturbance wave frequency and amplitude were successfully extracted from the bandwidth recognition criterion.

5) A unique in-house Skewed Gaussian decomposition algorithm was developed for calculating the traveling velocity of each individual disturbance wave. A statistical profile of the wave velocity was achieved at each individual flow condition. Together with the disturbance wave frequency and amplitude, a large database was generated for complete description of the disturbance wave characteristics in steam-water annular flow with steam quality and mass flux close to the BWR operating condition.

6) A mechanism-based semi-empirical correlation was developed for predicting the mean film thickness obtained at present study, which agrees with the present data within ±5%,

7) Disturbance wave induced oscillations of the thermal parameters (i.e., wall superheat, local heat flux, local HTC) was observed for the first time under forced convective evaporation heat transfer regime in steady-state annular flow, even though the imposed heat flux was constant. The propagating velocity and frequency of the “cooling wave”-like thermal oscillations were extracted for the first time. The coherence between such “cooling waves” and the disturbance waves was corroborated from the good agreement of the wave parameters.

8) A new SNB detection method was developed incorporating a nucleation site mapping method based on average temperature-variation rate, and a time fraction of nucleate boiling tracking approach. Such SNB detection method successfully identifies the nucleation site locations even in the presence of disturbance wave induced thermal oscillations.

9) First of a kind direct measurement of SNB thermal parameters was achieved, from which a database was generated including transient 2D SNB wall superheat, SNB heat flux, and

SNB HTC. Such database gives a close look into the SNB phenomena, based on which models and CFD simulations can be developed.

10) A set of mechanism-based semi-empirical correlations for predicting time-averaged SNB thermal parameters was developed. The correlation for SNB HTC agrees with the present data within ±5%, while ±15% agreement was found for SNB wall superheat and heat flux.

11) A first of a kind transient 1D mechanistic model was developed for predicting the transient temperature and velocity profile in the oscillating liquid film, with good agreement in the instantaneous and time-averaged temperature compared to measurements.

8.3. Recommended Future Works

Parameter Range More Representative of BWR Situation

The present experimental tests were conducted at pressure close to atmospheric condition using water as coolant. The notable mismatch between current work and the BWR-5 situation is the operating pressure, which indirectly produces the distortion in the density and viscosity ratios as shown in Table 3-1. The distortion in such parameters leads to non-negligible impact on the liquid film characteristics and the SNB thermal conditions. At higher operating pressure, lower liquid-gas density ratio, lower liquid-gas viscosity ratio, lower surface tension and higher saturation temperature are expected. Lower liquid-gas density ratio leads to the expansion of liquid phase and the contraction of gas phase, which potentially results in larger mean film thickness. The lower liquid-gas viscosity ratio leads to lower interfacial shear stress, which may result in lower disturbance wave and less liquid droplet entrainment, thus larger mean film thickness. Lower surface tension leads to lower local saturation temperature required by nucleation criterion, which potentially leads to lower SNB wall superheat and heat flux. Future tests should be carried out to extend the experimental results to a range of parameters more representative of actual BWR situation. Two approaches are proposed here. One approach is to keep using water as coolant, while raise the operating pressure of the test facility to BWR condition (~7 MPa). Such approach is straightforward and capable of matching every parameter exactly the same as the BWR condition. However, the associated difficulties in building and operating the pressurized loop are phenomenal, not even mentioning the cost. The durability of the ITO heater and the LFS at such high pressure and temperature condition are also questionable. The other practical approach is to

scale down the operating pressure and temperature using a fluid that satisfies the similarity criteria. One successful example is the flow boiling experiments conducted in the famous DEBORA loop at CEA [80]. Freon 12 was used as the experimental fluid, which matches the scaling factors remarkable well with actual PWR condition, such as density ratio, boiling number and Weber number. Lower cost and operating difficulty thus benefit from much lower operating pressure (~6 times lower) and heat flux (~10 times lower) compared to using water as coolant.

Integrated LFS+ITO Heater

The present measurement of the LFS and IR thermometry is synchronized but not collocated. In practice the film thickness signal can be shifted by a time delay calculated from the cross correlation, and thus compared with the temperature signal or used for simulation. However, as discussed in the earlier chapters, there are two effects that cannot be quantified from this simple time shift. First, the change of the morphology of the disturbance wave, for example due to wave merging, from the ITO heater to the LFS. Second, the unknown but likely non-negligible time delay between the arrival of the disturbance wave and the response of the "cooling wave", due to the thermal inertia of the wall. Although the 1D transient model can simulate the time delay due to the thermal mass, the result still needs to be validated against the synchronized-collocated measurement. In addition, the use of stand-alone two test sections could still potentially trip up the film, even though great care was taken to align them. To solve the above mentioned issues, an integrated LFS+ITO heater (as shown in Figure 5-11 and Figure 5-12) is needed to achieve synchronized and collocated measurements.

Full 2D LFS

In the present study, a prototype LFS with quasi-2D measurement was applied. Although rich data were obtained, the prototype LFS still missed the full 2D structure of the liquid film or disturbance waves, such as the lateral coherence structure of the wave, the merging of the waves along flow, due to its relatively low resolution. A full 2D LFS, i.e., with multiple arrays of transversal units deploying along the flow direction, will provide us more in-depth information of the liquid thin film in annular flow.

Measuring the Steam Core Properties

All the measuring techniques in the present study stops at the steam-water interface, except for the two RTDs at the inlet and outlet of the test assembly. As an important component of annular flow, the behavior of the steam core plays an important role in determining the boundary conditions for the liquid film where heat transfer occurs. Lacking direct measurements for the steam core flow in present study, many assumptions and correlation predictions were used whenever the steam core flow properties were required, which introduced uncertainties to the analysis, e.g. likely underestimation of interfacial velocity at the highest steam quality and mass flux due to the uncertainty on the entrainment fraction. Incorporation of experimental techniques for the steam core, to measure steam velocity and entrainment fraction, would augment the value of the innovative diagnostics presented here. The wire-mesh sensor can be used for velocity.

Modeling the Transient Liquid Film

A semi-empirical correlation was developed for predicting the time-averaged liquid film thickness, which leads to the good prediction of time-averaged SNB thermal parameters. However, without a prediction of the transient liquid film thickness, the transient 1D mechanistic model cannot be generally used, unless that information is supplied by direct measurements. Therefore it is desirable to develop a model for the pdf of film thickness, and the disturbance wave characteristics (velocity, frequency, amplitude).

Enhancing the IR Thermography

After years of continuous development in our group, the IR thermography technique is relatively mature in both the experimental operation and the radiation-conduction post-processing. The application of the IR thermometry in the present study was fairly straightforward. However, when applied to interrogation of fast transient processes on a relatively large spatial scale, several shortcomings emerge. One major shortcoming is the insufficient sampling rate at 2000 Hz, which introduces uncertainty in calculating the “cooling wave” velocity. In general, higher frequency is preferred for a better interrogation of the “cooling wave” properties. The other obvious drawback comes from the halo effect. Although good quality image was achieved here, the small bias of temperature profile close to the end of the heater was amplified as the imposed heat flux grew. If pixel-by-pixel calibration can be achieved, the halo effect can be entirely eliminated. The pixel-by-pixel calibration requires not only the mathematical algorithm, but also the additional mechanical structure to fix the relative position between the test section and the IR camera

Fabricating Artificial Nucleation Sites

The location of nucleation sites is typically random and unexpected. Although the heater can be examined before the test and potential nucleation sites identified, the in-depth geometry of the potential site is almost impossible to know. Fabricating well-defined artificial nucleation sites that are guaranteed to trap steam and fulfill the ONB criterion at reasonable wall superheat is an approach that should be explored in the future. A pre-requisite of this approach would be the improved smoothness of the ITO heater.

First Principle Transient Interfacial Shear Stress Model

As shown in the derivation of the transient 1D mechanistic model in Section 7.4.2, the predicted interfacial shear stress is one of the most important input that highly affects the velocity profile. The transient 1D model presented here uses an interfacial shear stress correlation that was developed for predicting the time-averaged shear stress. A numerical approach is used to compensate the appreciable change of interfacial shear stress at the windward or leeward of a tall disturbance wave. In fact, all the existing interfacial shear stress correlations were developed based on time-averaged quantities. Although correlations can be fed with instantaneous local conditions, such as film thickness or steam velocity, the accuracy of the correlations in transient conditions is questionable. Thus, a first principle transient interfacial shear stress model needs to be developed, based on transient measurement of the interfacial shear stress. Such model will enhance the prediction accuracy of the transient velocity and temperature profile in the liquid film.

Modifying the Transient Mechanistic Model for Transient SNB Prediction

Although the transient 1D mechanistic model successfully predicts the wall superheat and interfacial velocity, the SNB portion of the model is still preliminary. Compared to classical definition of ONB, the definition of SNB/ONB for annular flow in the present study is different, which makes the classical Hsu's ONB criterion not applicable to the SNB prediction. The transient mechanistic model needs to be equipped with a new length scale or even a modified criterion to simulate the sustained boiling in the presence of the periodic "cooling waves" in annular flow. In addition to modifying the ONB criterion, extending the model from 1D to 2D by including the advection term may help the prediction accuracy when the flow parameters (mass flux and quality) are even higher than the ranges investigated here.

Investigating the Two Unsolved Issues

As discussed in the previous sections, two findings need to be investigated. One is the impact of the surface contamination on SNB conditions (certainly for the nuclear fuel cladding application). The other is the impact of the thermal non-equilibrium in the film, which is expected to be more and more important as the flow parameters grow beyond the ranges investigated in this study (e.g. at typical BWR outlet conditions and postulated accident conditions).

More Objective SNB/ONB Criterion

As introduced in Section 7.3.1, the nominal SNB/ONB condition in annular flow is determined from the time fraction of boiling, for which an arbitrary critical value of 0.5 is used. Such criterion is intended to be universal and easy to apply. However, the time fraction of boiling is still phenomenological, and the physical meaning behind the critical value of 0.5 is not clear. With the help of heat partitioning approach, a more objective SNB/ONB criterion can be developed from evaluating the partitioned heat transfer of convective evaporation and nucleate boiling separately. For example, the ratio of the convective evaporation heat flux over the nucleate boiling heat flux can potentially be an SNB/ONB criterion.

Verify the Fully-Developed Annular Flow

In the present work, the length of the entrance channel is estimated to be sufficient to reach fully-developed annular flow condition using Ishii-Mishima's criterion [48]. However, other people's work also suggests longer entrance length to confidently reach fully-developed annular flow condition[81]. In order to clear such confusion, new tests are required to experimentally verify the developing conditions for present flow geometry. Thanks to the modular design, the length of the entrance channel can be easily changed by adding or removing the modules. The measured mean liquid film thickness can be a good indicating parameter for the developing condition of the annular flow.

References

[1] J. G. Collier and J. R. Thome, *Convective Boiling and Condensation (Third Edition)*, Oxford University Press, (1994).

[2] G. F. Hewitt, *Annular Two-Phase Flow (First Edition)*, Pergamon Press (1970)

[3] N. E. Todreas and M. S. Kazimi, *Nuclear Systems – Volume 1*, Taylor and Francis (2012).

[4] G. B. Wallis, *One Dimensional Two-Phase Flow,* Mcgraw-Hill (1969).

[5] Y. Taitel, D. Barnea, A. E. Dukler, "Modelling Flow Pattern Transitions for Steady Upward Gas-Liquid Flow in Vertical Tubes", *AIChE Journal*, Vol. 26, pp. 345-354(1980).

[6] D. Barnea, "A Unified Model for Predicting Flow-Pattern Transitions for the Whole Range of Pipe Inclinations", *Int. J. Multiphase Flow,* Vol. 13, pp.1-12 (1987).

[7] A. M. Ansari, et al., "A Comprehensive Mechanistic Model for Upward Two-Phase Flow in Wellbores", *SPEPF Journal*, Vol. 297, pp. 217-226 (1994).

[8] L. S. Tong and Y. S. Tang, *Boiling Heat Transfer and Two-Phase Flow (Second Edition)*, Taylor and Francis, 1997.

[9] Y.Y. Hsu, "On the size range of active nucleation cavities on a heating surface", *J. Heat Transfer*, Vol. 14, pp. 67–8 2(1971).

[10] S. G. Kandlikar, "An Improved Correlation for Predicting Two-Phase Flow Boiling Heat Transfer Coefficient in Horizontal and Vertical Tubes", *ASME/AIChE national heat transfer conference*, 24 July, 1983, Seattle, WA.

[11] S. G. Kandlikar, "A General Correlation for Saturated Two-Phase Flow Boiling Heat Transfer inside Horizontal and Vertical Tubes", *Journal of Heat Transfer*, Vol. 112, pp. 219-228(1990).

[12] V. V. Klimenko, "A Generalized Correlation for Two-Phase Forced Flow Heat Transfer", *Int. J. Heat Mass Transfer*, Vol. 31, pp. 541-552(1988);

[13] J. R. Barbosa Jr., G. F. Hewitt, S. M. Richardson, "Forced Convective Boiling of Steam–Water in A Vertical Annulus at High Qualities", *Experimental Thermal and Fluid Science*, Vol. 26, pp. 65-75(2002).

[14] I. D. Johnson, "Method and apparatus for measuring water in crude oil", U.S. Patent No. 4644263A, issued February 17, 1987.

[15] H.-M. Prasser, A. Bottger, J. Zschau, "A new electrode-mesh tomograph for gas-liquid flows", *Flow Measurement and Instrumentation*, Vol. 9, pp. 111-119 (1998).

[16] H.-M. Prasser, E. Krepper, D. Lucas, “Evolution of the two-phase flow in a vertical tube—decomposition of gas fraction profiles according to bubble size classes using wire-mesh sensor”, *Int. J. Therm. Sci*, Vol. 41, pp.17-28 (2002).

[17] H.-M. Prasser, M. Misawa, I. Tiscanu, “Comparison between wire-mesh sensor and ultra-fast X-ray tomograph for an air- water flow in a vertical pipe”, *Flow Measurement and Instrumentation*, Vol. 16, pp. 73-83 (2005).

[18] D. Schubring, et al., “Planar laser-induced fluorescence (PLIF) measurements of liquid film thickness in annular flow. Part I: Methods and data”, *Int. J. Multiphase Flow*, Vol. 36, pp. 815-824(2010).

[19] L.-M. Pan, et al., “Experimental study and modeling of disturbance wave height of vertical annular flow”, *Int. J. Heat and Mass Transfer*, Vol. 89, pp. 165-175(2015).

[20] A. Navabi, “Amazing water refraction”, *YouTube*, Published on Feb. 6, 2015, https://www.youtube.com/watch?v=tVtg_YJ0Bbo

[21] M. Damsohn and H. M. Prasser, “High-Speed Liquid Film Sensor with High Spatial Resolution”, *Meas. Sci. Technol.*, vol. 20(2009).

[22] M. Damsohn and H.-M. Prasser, “Droplet Deposition Measurement with High-Speed Camera and Novel High-Speed Liquid Film Sensor with High Spatial Resolution”, *Nucleare Science and Design*, vol. 241, pp. 2494-2499(2011).

[23] M. Damsohn and H. M. Prasser, “Dynamic Film Thickness between Bubbles and Wall in a Narrow Channel”, *Exp. Fluid*, vol. 51, pp.821-833(2011).

[24] F. P. D’Aleo, H. M. Prasser, “Design, Calibration and Testing of A Thin Film Temperature Gauge Array for Temperature and Heat Flux Measurements in Fluid Mixing Experiments”, *Flow Measurement and Instrumentation*, vol. 24, pp.29-35(2012).

[25] D. F. Tatterson, J. C. Dallman, and T. J. Hanratty, “Drop size in annular gas-liquid flows”, *AIChE Journal*, Vol. 23, pp. 68-76 (1977).

[26] S. V. Paras and A. J. Karabelas, “Properties of the liquid layer in horizontal annular flow”, *Int. J. Multiphase Flow*, Vol. 17, pp. 439-454 (1991).

[27] D. Schubring and T.A. Shedd, “Wave behavior in horizontal annular air-water flow”, *Int. J. Multiphase Flow* , Vol. 34, pp. 636-646 (2008).

[28] M. B. Alamu, “Investigation of periodic structures in gas-liquid flow”, PhD Thesis, University of Nottingham, 2010.

[29] K. Hori, et al., “Study of Ripple Region in Annular Two-Phase Flow (3rd Report, Effect of Liquid Viscosity on Gas-Liquid Interfacial Character and Friction Factor)”, Transactions of Japan Society of Mechanical Engineers, 1978.

[30] W. Henstock and T. Hanratty, “The Interfacial Drag and the Height of the Wall Layer in Annular Flows”, *American Institute of Chemical Engineers Journal*, vol. 22, pp. 990-1000 (1976).

[31] T. Fukano and T. Furukawa, “Prediction of the Effects of Liquid Viscosity on Interfacial Shear Stress and Frictional Pressure Drop in Vertical Upward Gas-Liquid Annular Flow”, *Int. J. Multiphase Flow*, vol. 24, pp. 587–603 (1998).

[32] R. MacGillivray, “Gravity and Gas Density Effects on Annular Flow Average Film Thickness and Frictional Pressure Drop”, Master’s thesis, University of Saskatchewan, 2004.

[33] C. Berna, et al., “Review of Droplet Entrainment in Annular Flow: Interfacial Waves and Onset of Entrainment”, *Progress in Nuclear Energy*, vol. 74, pp. 14-43(2014).

[34] J. J. Ginoux, ed., “Two-Phase Flows and Heat Transfer with Applications to Nuclear Reactor Design Problems”, McGraw-Hill, 1978.

[35] P. Sawant, et al., “Properties of Disturbance Waves in Vertical Annular Two-Phase Flow”, *Nuclear Engineering and Design*, vol. 238, pp. 3528- 3541(2008).

[36] Y. Zhao, et al., “Disturbance Wave Development in Two-Phase Gas-Liquid Upwards Vertical Annular Flow”, *Int. J. Multiphase Flow*, vol. 55, pp. 111- 129(2013).

[37] H. Han, Z. Zhu, and K. Gabriel, “A Study on the Effect of Gas Flow Rate on the Wave Characteristics in Two-Phase Gas-Liquid Annular Flow”, *Nuclear Engineering and Design*, vol. 236, pp. 2580- 2588(2006).

[38] P. B. Whalley, “Boiling, Condensation, and Gas-Liquid Flow”, Clarendon Press, 1987.

[39] J. Shi and G. Kocamustafaogullari, “Interfacial Measurements in Horizontal Stratified Flow Patterns”, *Nuclear Engineering and Design*, vol. 149, pp. 81-96(1994).

[40] M. Ishii and M. A. Grolmes, “Inception criteria for droplet entrainment in two-phase concurrent film flow”, *AIChE Journal*, Vol. 21, pp. 308-318 (1975).

[41] N. S. Hall-Taylor, G. F. Hewitt and P.M.C. Lacey, “The motion and frequency of large disturbance waves in annular two-phase flow of airewater mixtures”, *Chem. Eng. Sci.*, Vol. 18, 537-552 (1963).

[42] D. E. Woodmansee, T. J. Hanratty, "Mechanism for the removal of droplets from a liquid surface by a parallel air flow", *Chem. Eng. Sci.*, Vol. 24, 299-307 (1969).

[43] C. R. Arnold and G. F. Hewitt, "Further developments in the photography of two phase gaseliquid flow", *J. Photogr. Sci.*, Vol. 15, pp. 97-114 (1967).

[44] I. I. Paleev and B. S. Filippovich, "Phenomena of liquid transfer in two-phase dispersed annular flow", *Int. J. Heat Mass Transfer*, Vol. 9, pp. 1089-1093 (1966).

[45] G. B. Wallis, "Phenomena of liquid transfer in two-phase dispersed annular flow", *Int. J. Heat Mass Transfer*, Vol. 11, pp. 783-785 (1968).

[46] K. L. Magrini, et al., "Liquid entrainment in annular gas-liquid flow in inclined pipes", *SPE Journal*, June 2012, pp. 617-630.

[47] R. V. A. Olimans, B. F. M. Pots and N. Trompe, "Modelling of annular dispersed two-phase flow in vertical pipes", *Int. J. Multiphase Flow*, Vol. 12, pp. 711-732(1986).

[48] M. Ishii and K. Mishima, "Droplet entrainment correlation in annular two-phase flow", *Int. J. Heat Mass Transfer*, Vol. 32, pp. 1835-1846 (1989).

[49] L. Pan and T. Hanratty, "Correlation of entrainment for annular flow in vertical pipes", *Int. J. Multiphase Flow*, Vol. 28, pp. 363-384(2002).

[50] P. Sawant, M. Ishii and M. Mori, "Prediction of amount of entrained droplets in vertical annular two-phase flow", *International Journal of Heat and Fluid Flow*, Vol. 30, pp. 715-728 (2009).

[51] A. Al-Sarkhi, C. Sarica, B. Qureshi, "Modeling of droplet entrainment in co-current annular two-phase flow-A new approach", *Int. J. Multiphase Flow*, Vol. 39, pp.21-28(2012).

[52] L. Gilman and E. Baglietto, "A self-consistent, physics-based boiling heat transfer modeling framework for use in computational fluid dynamics", *Int. J. Multiphase Flow*, Vol. 95, pp. 35-53(2017).

[53] B. Phillips, Personal communication, June, 2015.

[54] E. C. Forrest, "Study of Turbulent Single-Phase Heat Transfer and Onset of Nucleate Boiling in High Aspect Ratio Mini-Channels to Support the MITR LEU Conversion", PhD Thesis, Massachusetts Institute of Technology, 2014.

[55] McMaster-Carr Supply Company, "Conductive adhesive for electronics", Retrieved Mar. 02 2018, https://www.mcmaster.com/#7661a11/=1bsug9s.

[56] McMaster-Carr Supply Company, “Polysulfone Rod”, Retrieved Mar. 02 2018,, https://www.mcmaster.com/#8676k53/=1cca5uc.

[57] McMaster-Carr Supply Company, “High-temperature soft silicone o-ring”, Retrieved Mar. 02 2018, https://www.mcmaster.com/#1173n018/=1bsujdu.

[58] Azom Materials, “Macro (machinable glass ceamic)-applications”, Retrieved Mar. 02 2018, https://www.azom.com/properties.aspx?ArticleID=1441.

[59] Peter C. Jordan, *Chemical Kinetics and Transport*, Springer, 1979.

[60] R. A. Robinson and R. H. Stokes, *Electrolyte Solutions-Second Revised Edition*, London, Butterworths, 1970.

[61] B. Phillips, Personal communication, July, 2015.

[62] J. R. Howell, M. P. Menguc, R. Siegel, *Thermal Radiation Heat Transfer, 6th Edition*, CRC Press, 2015.

[63] G.R. Fowles, *Introduction to Modern Optics*, Holt, Rinehart and Winston, 1975.

[64] G.-Y. Su, et al., “Transient boiling of water under exponentially escalating heat inputs. Part I: Pool boiling”, *Int. J. Heat Mass Transfer*, Vol. 96, pp. 667-684 (2016).

[65] M. Bucci, et al., “A mechanistic IR calibration technique for boiling heat transfer investigations”, *Int. J. Multiphase Flow*, Vol. 83, pp. 115-127(2016).

[66] K. J. Chu and A. E. Dukler, “Statistical characteristics of thin, wavy films: Part II. Studies of the substrate and its wave structure”, *AIChE Journal*, Vol. 20, pp. 695-706(1974).

[67] K. J. Chu and A. E. Dukler, “Statistical characteristics of thin, wavy films: Part III. Structure of the large waves and their resistance to gas flow”, *AIChE Journal*, Vol. 21, pp. 583-593(1975).

[68] T. H. Lyu and I. Mudawar, “Statistical investigation of the relationship between interfacial waviness and sensible heat transfer to a falling liquid film”, *Int. J. Heat Mass Transfer*, Vol. 34, pp. 1451-1464 (1991).

[69] Mother Ji’s Public Service Reading, “Diary of dung beetles”, Retrieved Mar. 02 2018, http://blog.sina.com.cn/s/blog_8dbd6dd10102vor7.html.

[70] Y. Zhao, et al., “Disturbance wave development in two-phase gas–liquid upwards vertical annular flow”, *Int. J. Multiphase Flow*, Vol. 55, pp.111-129(2013).

[71] I. Rychlik, P. Johannesson, and M. R. Leadbetter, "Modelling and Statistical Analysis of ocean-wave data using transformed gaussian processes", *Marine Structures*, Vol. 10, pp. 13-47(1997).

[72] M. Damsohn, "Liquid films and droplet deposition in a BWR fuel element", PhD Thesis, ETH Zurich, 2011.

[73] A. Pewsay, "Problems of inference for Azzalini's skewnormal distribution", *Journal of Applied Statistics*, Vol. 27, pp. 859-870 (2000).

[74] J. H. Lienhard IV and J. H. Lienhard V, *A Heat Transfer Textbook, Fourth Edition*, Phlogiston Press, Cambridge, Massachusetts, 2017.

[75] F. Fu and J. F. Klausner, "A separated flow model for predicting two-phase pressure drop and evaporative heat transfer for vertical annular flow", *Int. J. Heat and Fluid Flow*, Vol. 18, pp. 541-549 (1997).

[76] A. C. Ashwood, et al. , "A multiphase, micro-scale PIV measurement technique for liquid film velocity measurements in annular two-phase flow", *Int. J. Multiphase Flow*, Vol. 68, pp. 27-39(2015).

[77] T. Brooke-Benjamin, "Shearing flow over a wavy boundary", *Journal of Fluid Mechanics*, Vol. 6, pp. 161-205 (1959).

[78] G.-Y., Su, "Transient boiling of water under exponentially escalating heat inputs. Part II: Flow", *Int. J. Heat Mass Transfer*, Vol. 96, pp. 685-698 (2016).

[79] E. M. Al-Safran and J. P. Brill, *Applied Multiphase Flow in Pipes and Flow Assurance - Oil and Gas Production*, Society of Petroleum Engineers (2017).

[80] J. Garnier, E. Manon, and G. Cubizolles, "Local measurements on flow boiling of refrigerant 12 in a vertical tube", *Multiphase Science and Technology*, Vol. 13, pp. 1-111 (2001).

[81] A. Wolf, S. Jayanti, and G. F. Hewitt, "Flow development in vertical annular flow", *Chemical Engineering Science*, Vol. 56, pp. 3221-3235 (2001).

[82] MathWorks, "Practical introduction to ditital filter design", Retrieved Mar. 02 2018, https://www.mathworks.com/help/signal/examples/practical-introduction-to-digital-filter-design.html.

[83] MathWorks, "Kaiser", Retrieved Mar. 02 2018, https://www.mathworks.com/help/signal/ref/kaiser.html?requestedDomain=www.mathworks.com.

Appendix A: Kaiser Window FIR Filter

The linear time invariant (LTI) theory states that any LTI system can be characterized entirely by a single function called the system's impulse response *h(t)*. The output of the system *y(t)* is simply the convolution of the input *x(t)* to the system with the system's impulse response. The same result is true of discrete-time linear shift-invariant systems in which signals are discrete-time samples, and convolution is defined on sequences.

$$y[n] = \sum_{k=-\infty}^{\infty} x[k]h[n-k] \tag{A-1}$$

$$y(t) = \int_{-\infty}^{\infty} h(\tau)x(t-\tau)d\tau = x(t) * h(t) \tag{A-2}$$

The impulse response is an especially important property of any LTI system, and can be used to describe an LTI system and predict the system output for any input. The impulse response for an LTI system is the output, *y(t)=h(t)*, when the input is the unit impulse signal, *x(t)=σ(t)* . The unit impulse signal is simply a signal that produces a signal of 1 at time = 0, and is zero everywhere else. The sigma function *σ(t)* is a specific integral of the Dirac delta function.

$$\delta(t) = \begin{cases} \infty, & if\ t = 0 \\ 0, & if\ t \neq 0 \end{cases} \tag{A-3}$$

$$\sigma(t) = \int_{0-}^{0+} \delta(t)dt = \begin{cases} 1, & if\ t = 0 \\ 0, & if\ t \neq 0 \end{cases} \tag{A-4}$$

An ideal lowpass filter keeps all the frequency components of an input signal below a specified cutoff frequency value f_c (or ω_c), while discarding all the other components higher than f_c. However, the ideal lowpass filter requires infinitely long impulse response, similar to perfect Taylor expansion or Fourier series. FIR approximates the ideal impulse response with truncated finite length. As a result, the filtered signal accompanies with ripples in both the passband ($f < f_c$) and the stopband ($f > f_c$). In addition, a finite width transition region exists in between the passband and the stopband. Furthermore, the signal components in the stopband can only be suppressed, but not totally discarded. The comparison between ideal filter and FIR filter is shown below. [82]

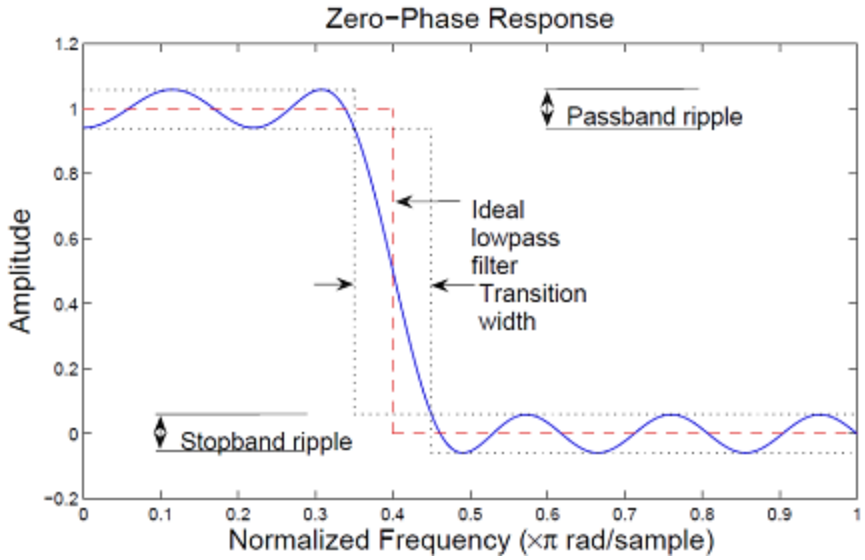

***Figure A-0-1**: Characteristics of FIR low pass filter (blue curve) in comparison with an ideal low pass filter (red dash line). Passband ripple, stopband ripple and a transition region exist for the output signal of FIR low pass filter.[82]*

In order to achieve a computationally realizable approximation of the ideal impulse response, a truncation has to be done for the convolution in Eq. A-1. One idea is to apply a window (window function $\omega(n)$), i.e., a specific range, to the impulse response. Within the window, the impulse response is activated with the weight of the window function, while it is forced to be zero outside of the window range. The order of the filter is defined as the finite window function number *N*, while *N+1* is the length of the window.

$$\omega[n] = \begin{cases} \omega[n], & n = 0,1,\dots,N \\ 0, & otherwise \end{cases} \tag{A-5}$$

$$Thus, h[n] = \begin{cases} h[n]\omega[n], & n = 0,1,\dots,N \\ 0, & otherwise \end{cases} \tag{A-6}$$

As a result, the approximate output of the LTI system (ideal filter) becomes:

$$y[n] = \sum_{k=-\infty}^{\infty} x[k]h[n-k] \cong \sum_{k=n-N}^{n} x[k]h[n-k]\omega[n-k] \tag{A-7}$$

Note, the k in the above function relates to the filter order, while n represents the discrete samples.

The window function applied for the Kaiser Window algorithm is [83]:

$$\omega[n] = \frac{I_0\left(\beta\sqrt{1-\left(\frac{n-\frac{N}{2}}{\frac{N}{2}}\right)^2}\right)}{I_0(\beta)}, 0 \le n \le N \tag{A-8}$$

$$\beta = \begin{cases} 0.1102(\alpha - 8.7), \alpha > 50 \\ 0.5842(\alpha - 21)^{0.4} + 0.07886(\alpha - 21), 50 \ge \alpha \ge 21 \\ 0, \alpha < 21 \end{cases} \tag{A-9}$$

$$N = \frac{\alpha - 8}{2.285|\omega_p - \omega_s|} + 1 \tag{A-10}$$

where I_0 is the zeroth-order modified Bessel function of the first kind; α is the expected ripple height in decibel; ω_p and ω_s are passband and stopband angular frequency respectively.

Appendix B: Time-Averaged Liquid Film Thickness Profile

Time-averaged liquid film thickness measurement from the transversal unit and the longitudinal unit at all test conditions are summarized in the following figure. As discussed in Section 6.2, the time-averaged liquid film thickness exhibits a concave shape profile in the transversal direction, i.e., thinner towards the center of the channel and thicker towards the corners of the channel, for all tests conducted. Such profile becomes thinner and more conformal to the channel geometry (square shape), as mass flux and steam quality increase.

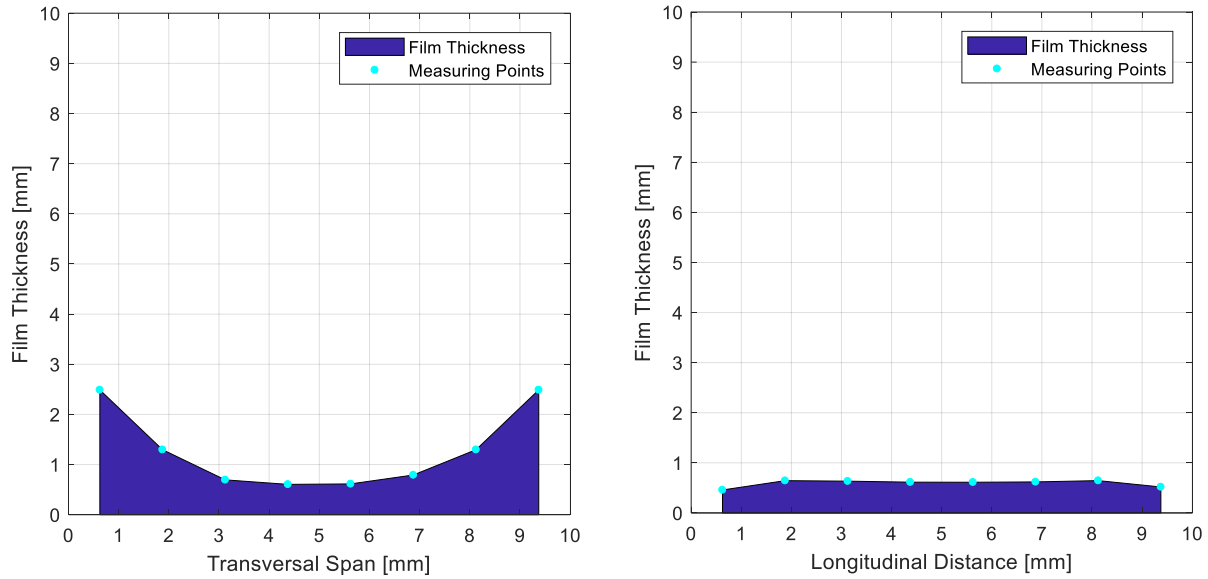

$G=750\ kg \cdot m^{-2} \cdot s^{-1}$, $x_e = 0.016$

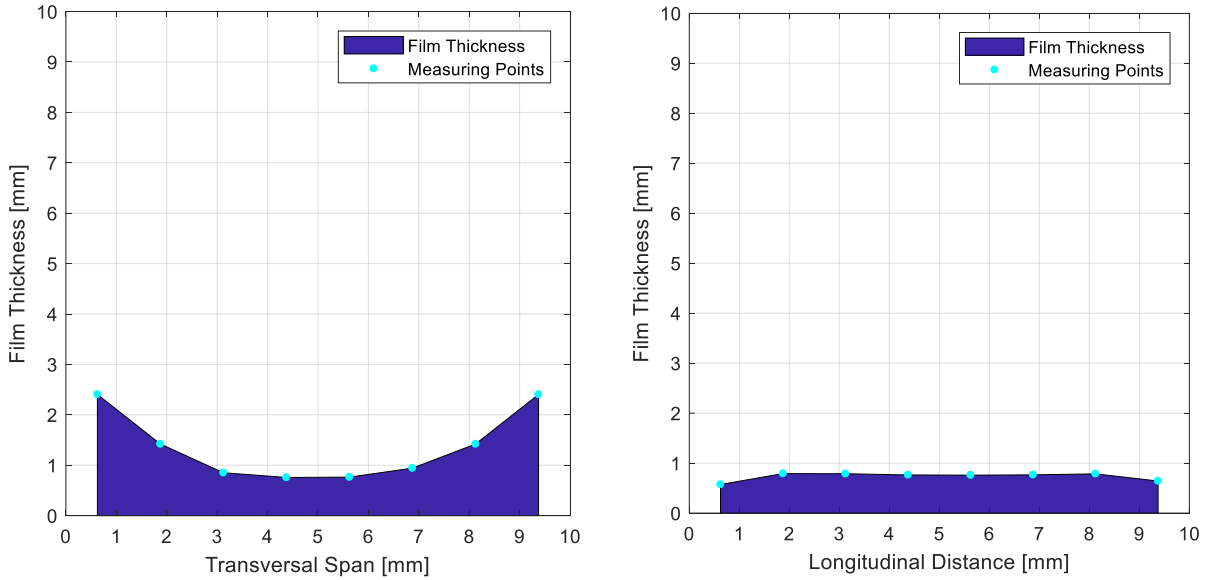

$G=1050\ kg \cdot m^{-2} \cdot s^{-1}$, $x_e = 0.016$

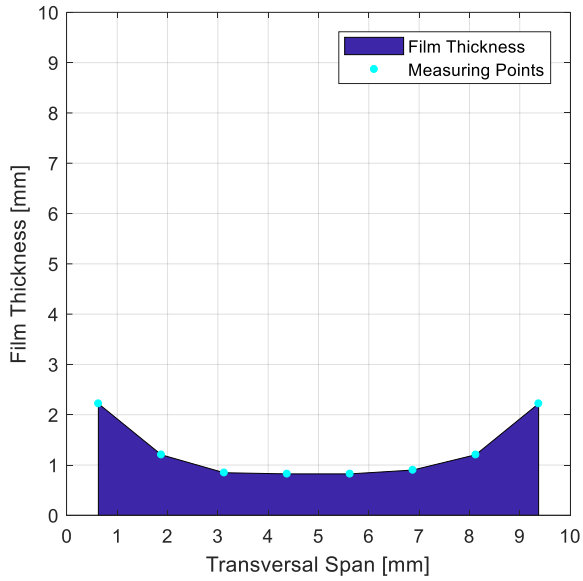

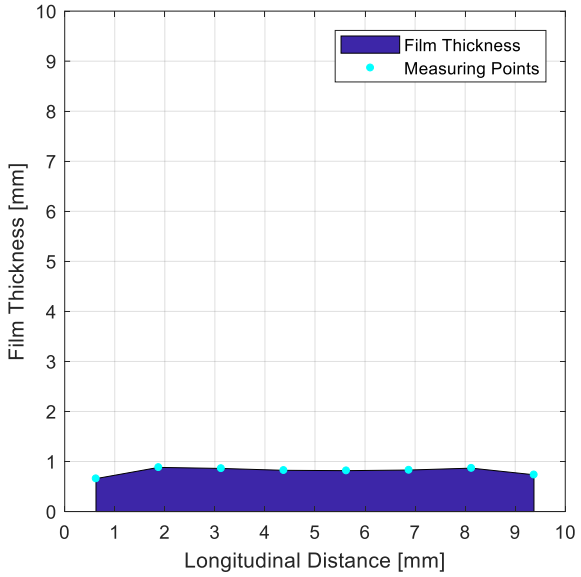

$G=1350\ kg \cdot m^{-2} \cdot s^{-1}$, $x_e = 0.016$

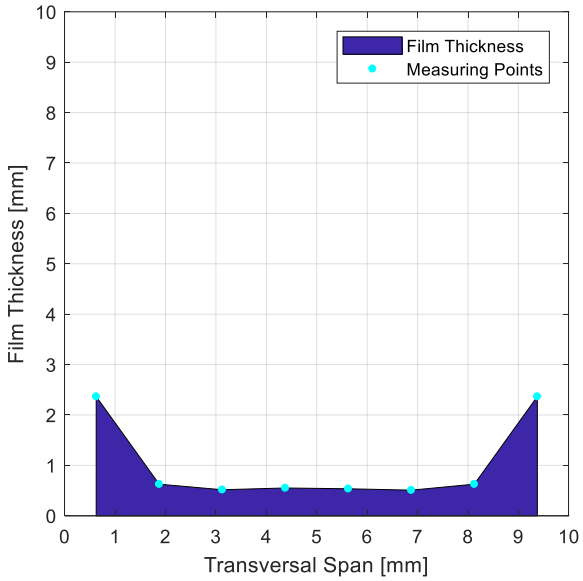

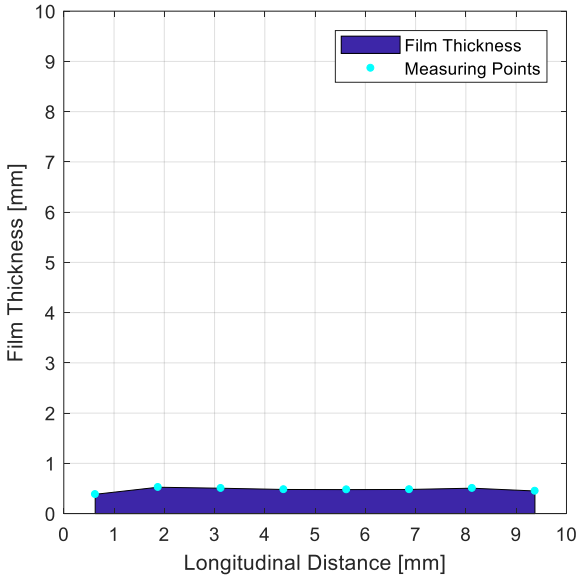

$G=750\ kg \cdot m^{-2} \cdot s^{-1}$, $x_e = 0.03$

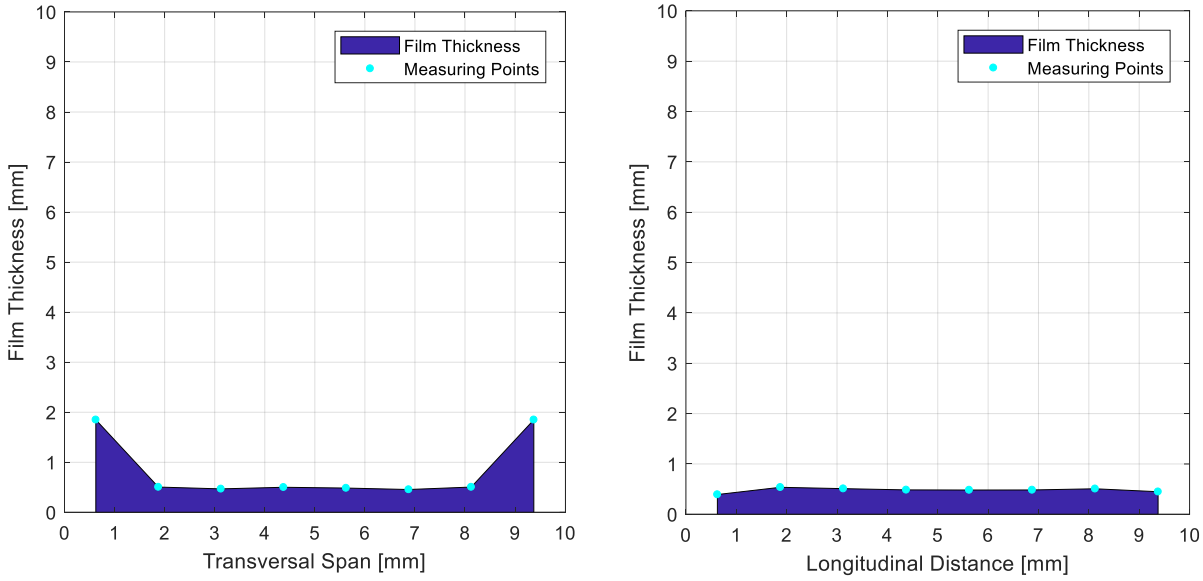

$G=1050\ kg \cdot m^{-2} \cdot s^{-1}$, $x_e = 0.03$

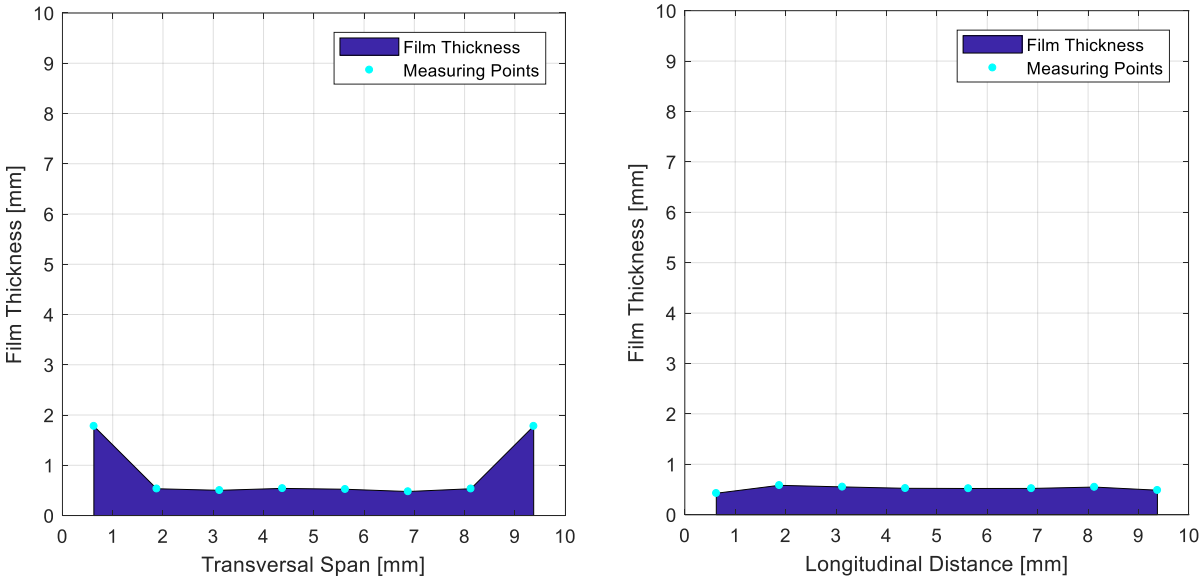

$G=1350\ kg \cdot m^{-2} \cdot s^{-1}$, $x_e = 0.03$

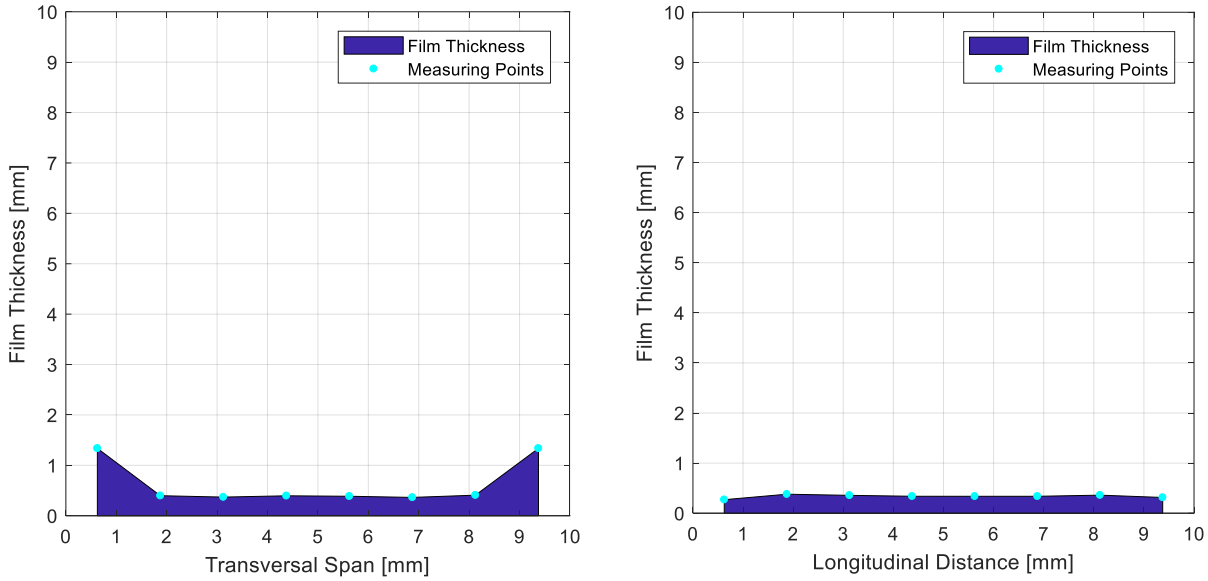

$G=750\ kg \cdot m^{-2} \cdot s^{-1}$, $x_e= 0.05$

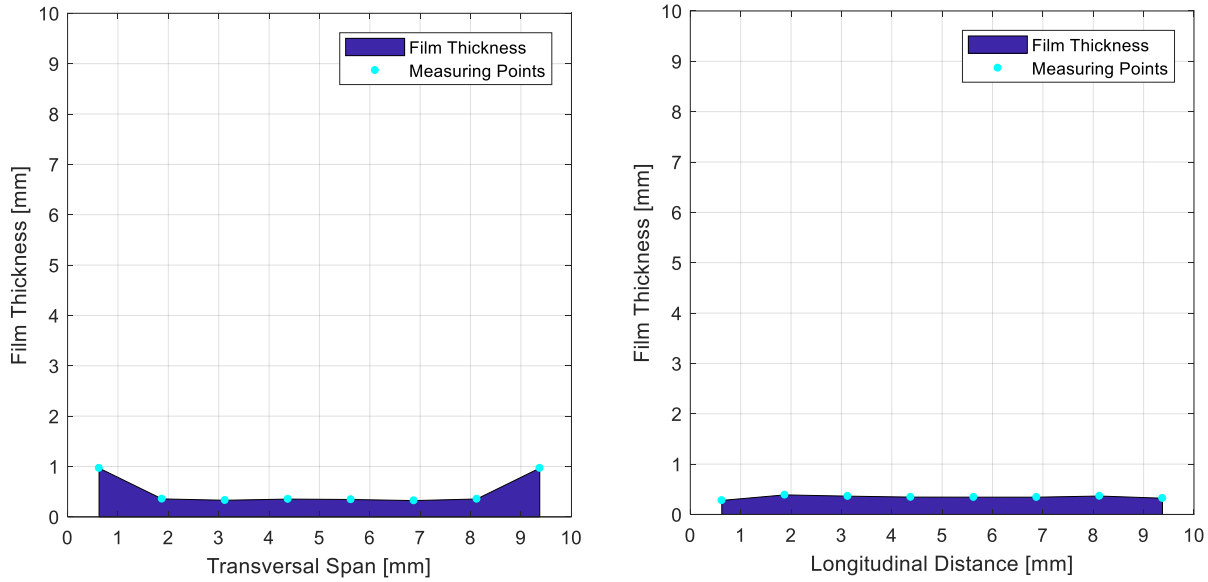

$G=1050\ kg \cdot m^{-2} \cdot s^{-1}$, $x_e= 0.05$

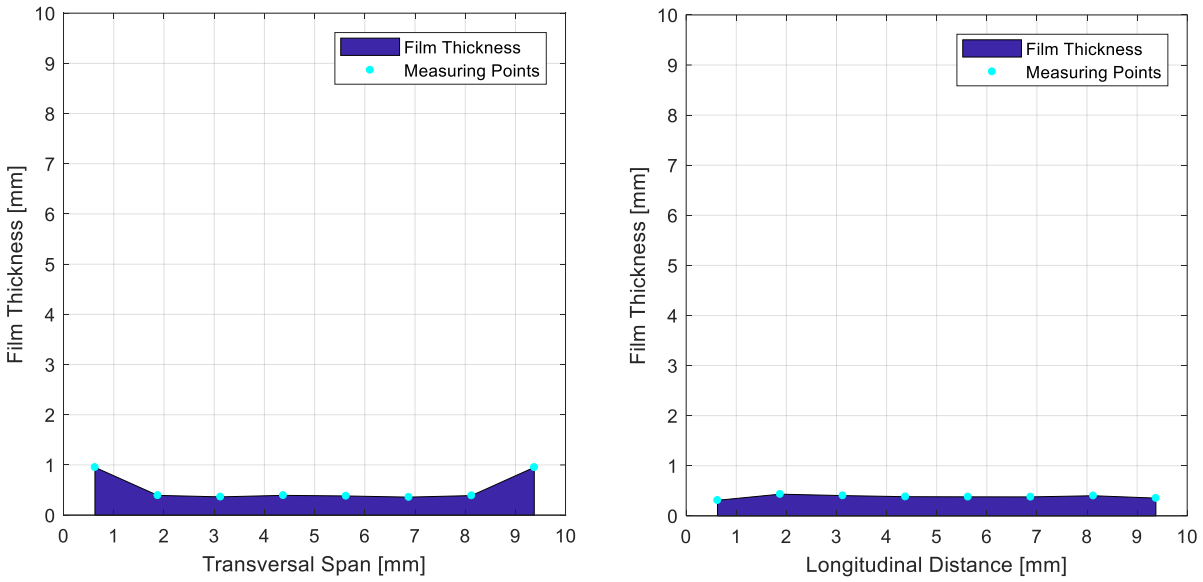

$G=1350\ kg \cdot m^{-2} \cdot s^{-1}$, $x_e = 0.05$

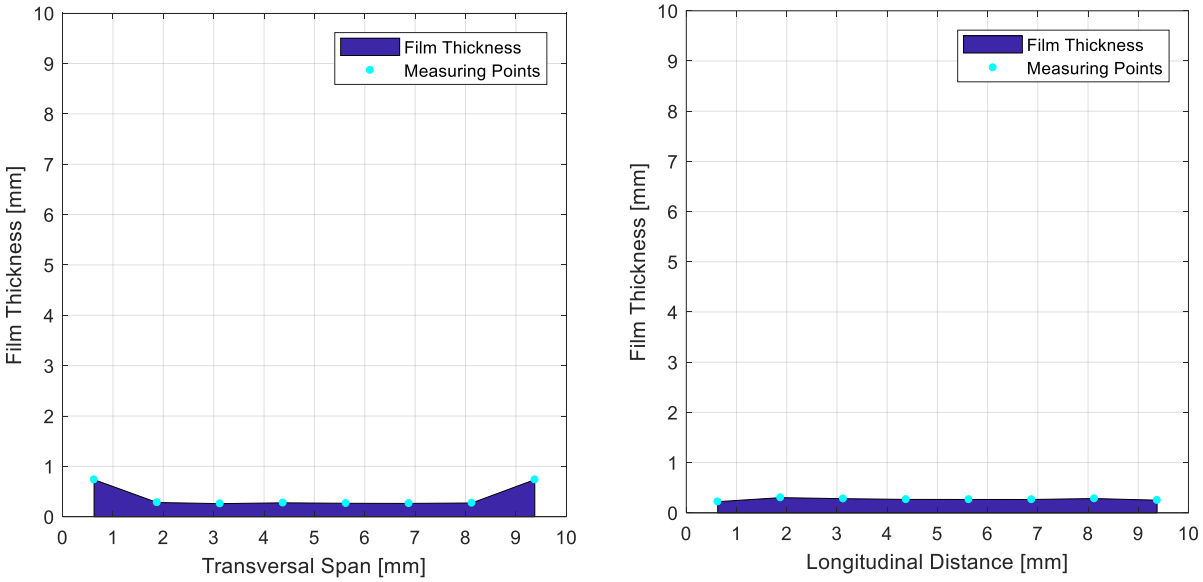

$G=750\ kg \cdot m^{-2} \cdot s^{-1}$, $x_e = 0.07$

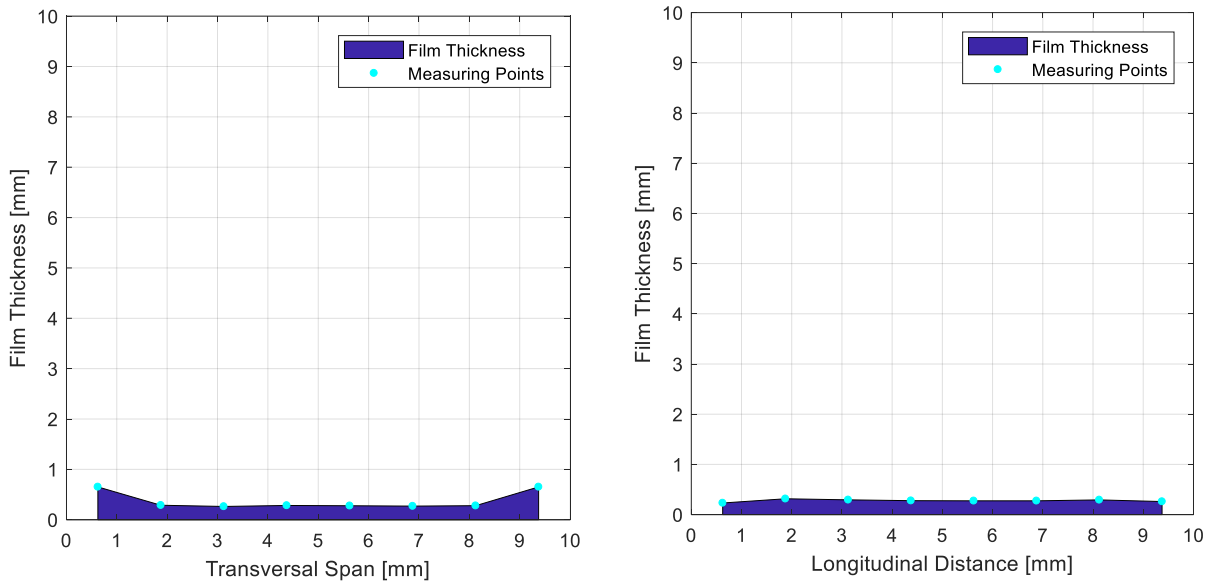

$G=1050\ kg \cdot m^{-2} \cdot s^{-1}$, $x_e = 0.07$

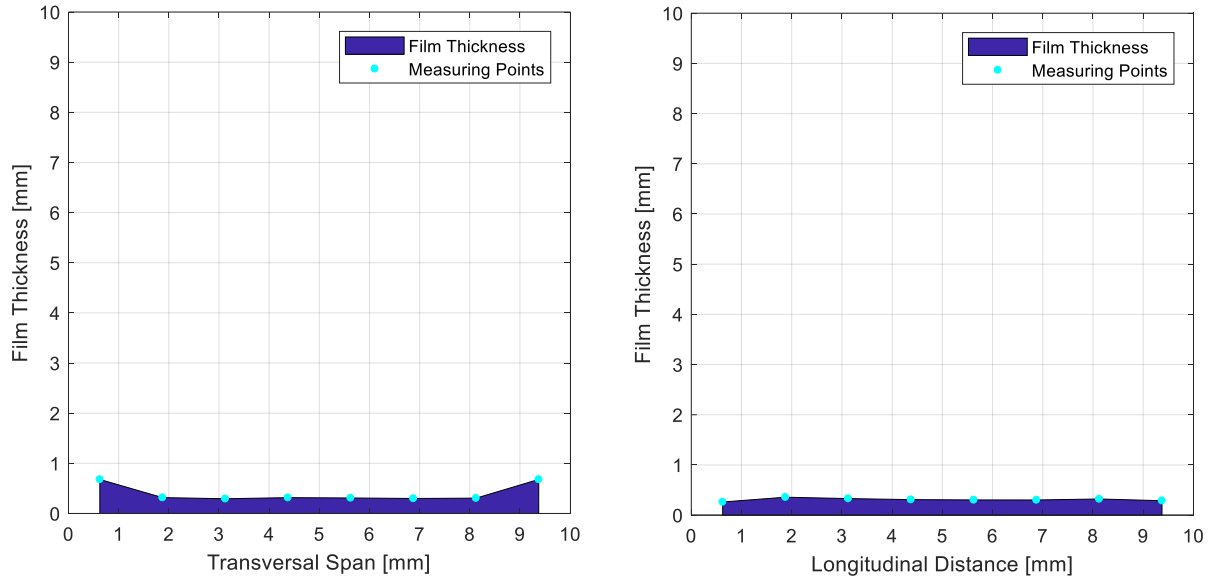

$G=1350\ kg \cdot m^{-2} \cdot s^{-1}$, $x_e = 0.07$

***Figure B-0-1**: Time-averaged liquid film thickness measurement from the transversal unit (left column) and the longitudinal unit (right column).*

Appendix C: Typical Time History and PDF of A Single Sensor from Longitudinal Unit

The typical time history of a single sensor element from the longitudinal unit, which is located at the center of the channel wall (equivalent to 5 mm transversal location in Figure 6-3), and the PDF of the whole 100 s measurement at all test conditions are summarized in the figure below. As discussed in Section 6.2, the typical time history shows periodic appearance of tall disturbance waves. The PDF shows a clear peak at medium thickness, and a skewed distribution toward the large thickness. The single bar spike at 2.8 mm indicates the heights of some large disturbance waves exceed the measuring range of the LFS.

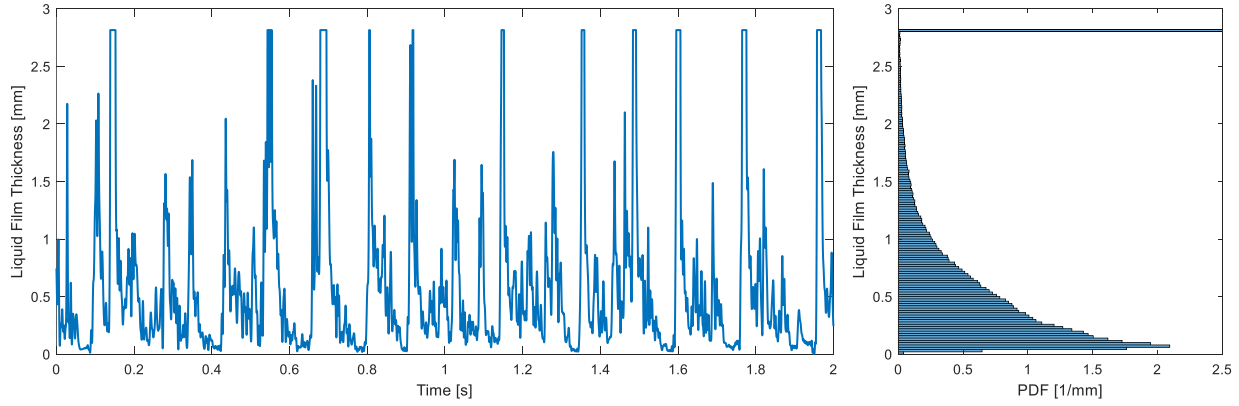

G=750 kg·m^{-2}·s^{-1}, x_e= 0.016

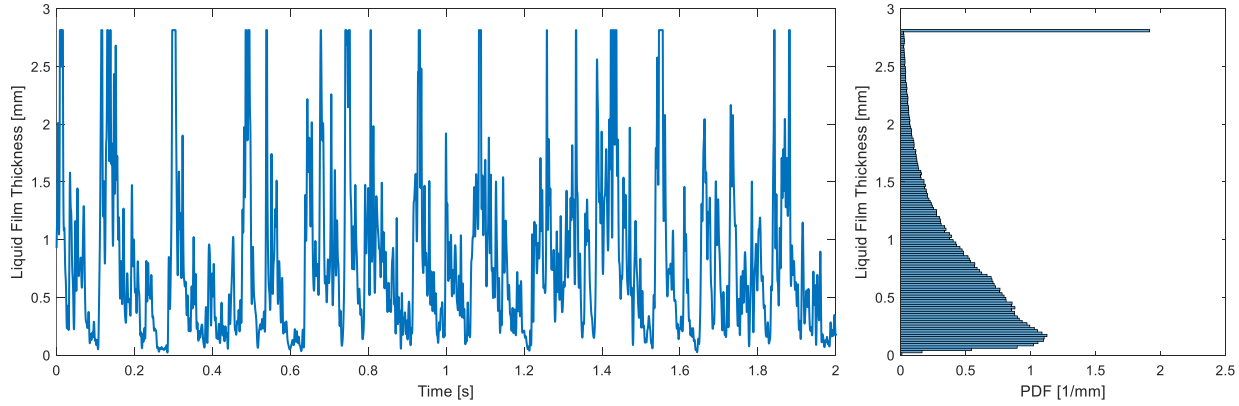

G=1050 kg·m^{-2}·s^{-1}, x_e= 0.016

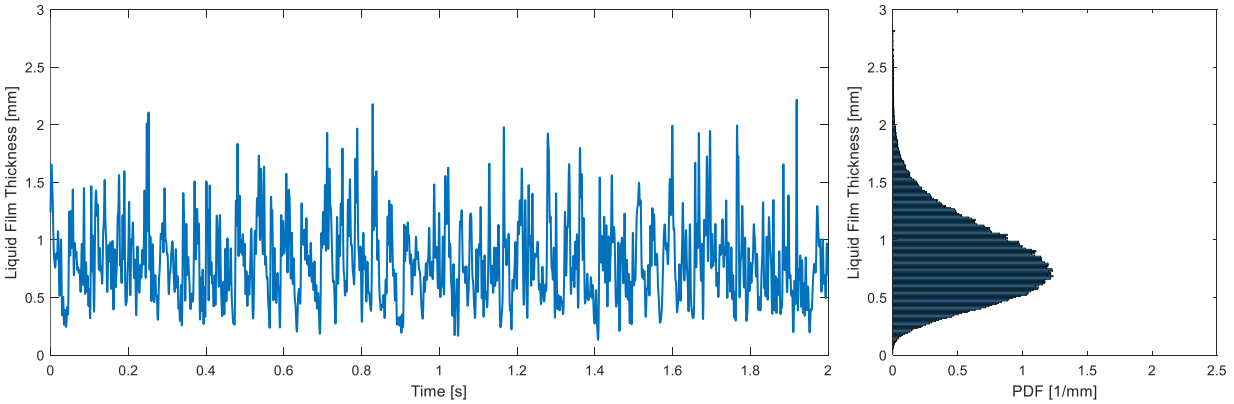

$G=1350\ kg \cdot m^{-2} \cdot s^{-1}$, $x_e= 0.016$

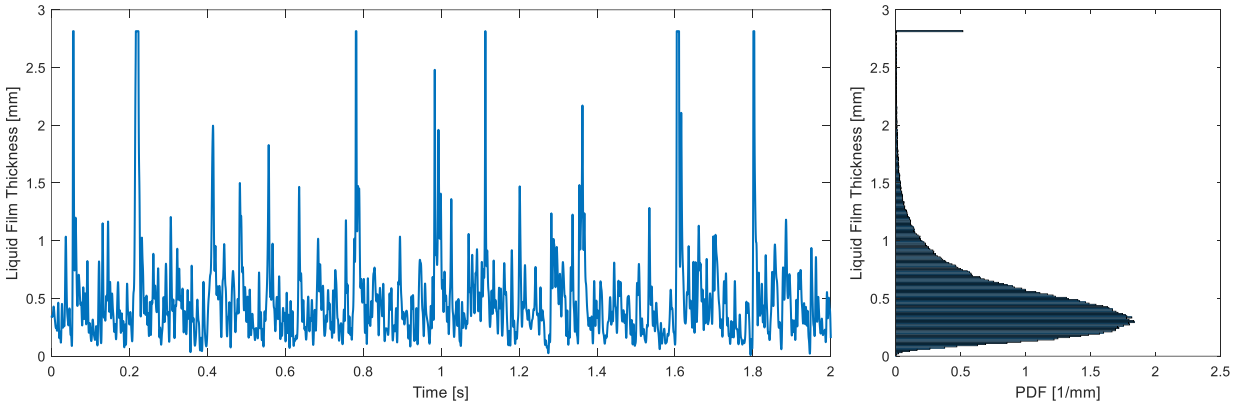

$G=750\ kg \cdot m^{-2} \cdot s^{-1}$, $x_e= 0.03$

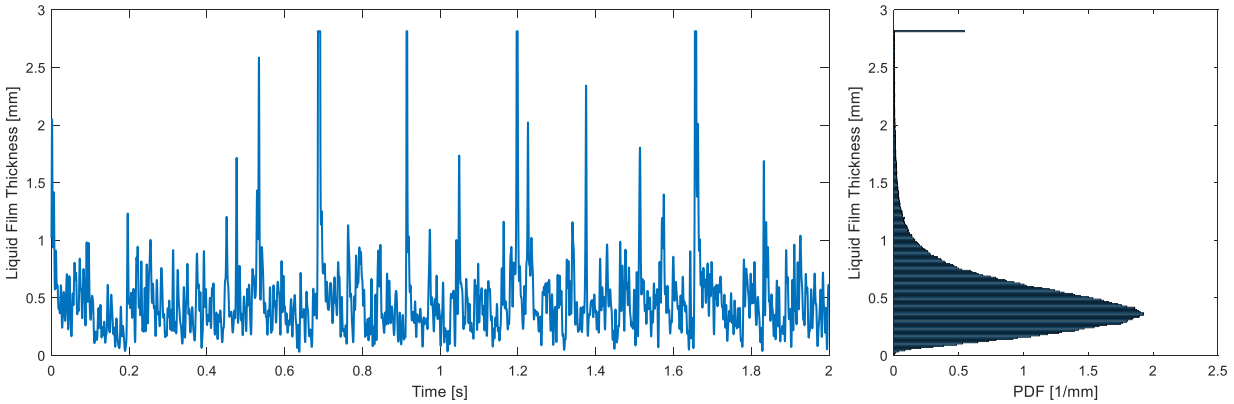

$G=1050\ kg \cdot m^{-2} \cdot s^{-1}$, $x_e= 0.03$

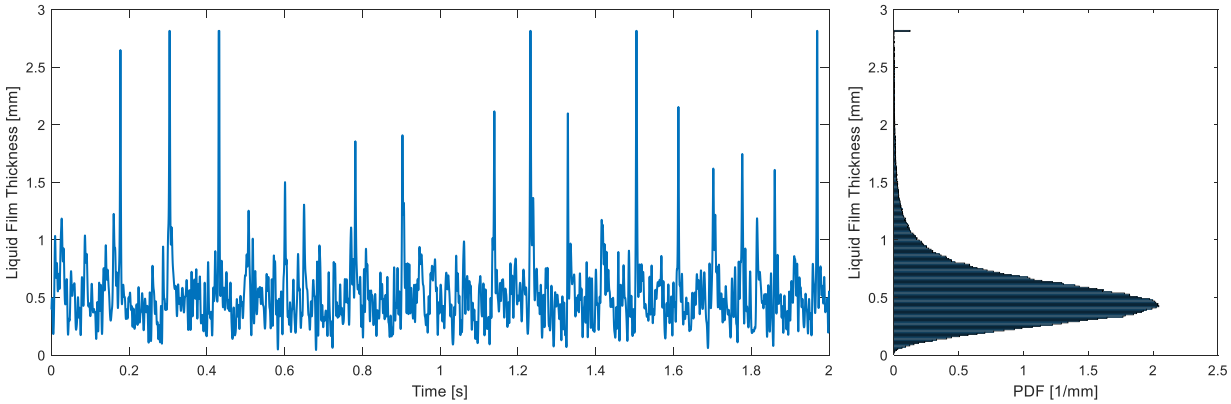

$G=1350\ kg \cdot m^{-2} \cdot s^{-1}$, $x_e= 0.03$

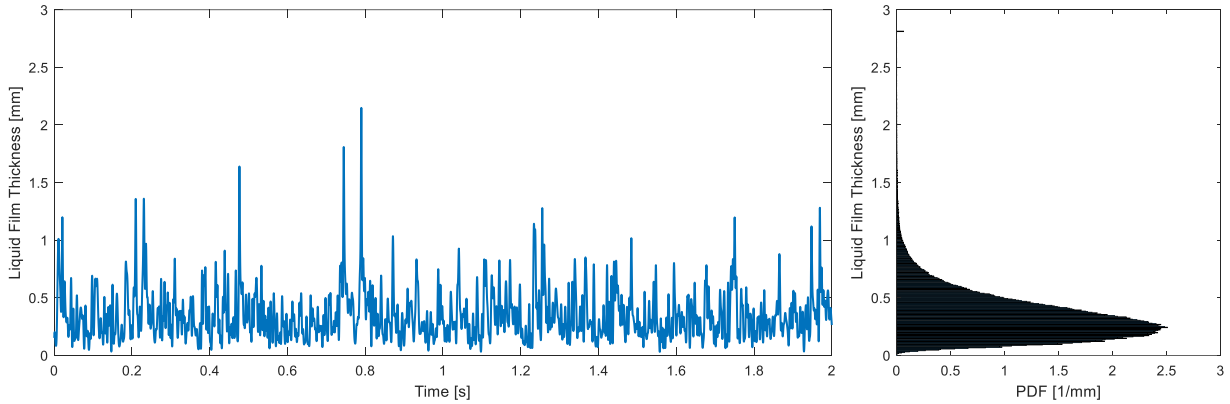

$G=750\ kg \cdot m^{-2} \cdot s^{-1}$, $x_e= 0.05$

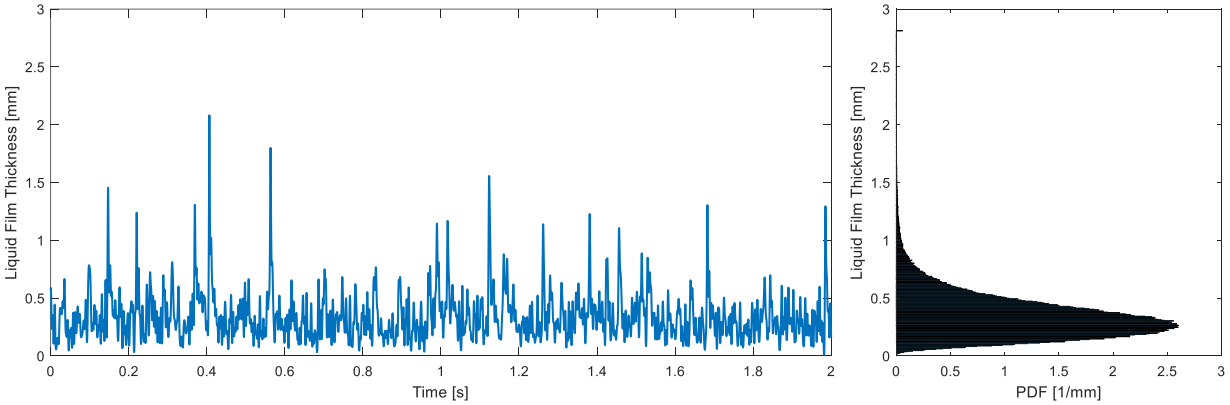

$G=1050\ kg \cdot m^{-2} \cdot s^{-1}$, $x_e= 0.05$

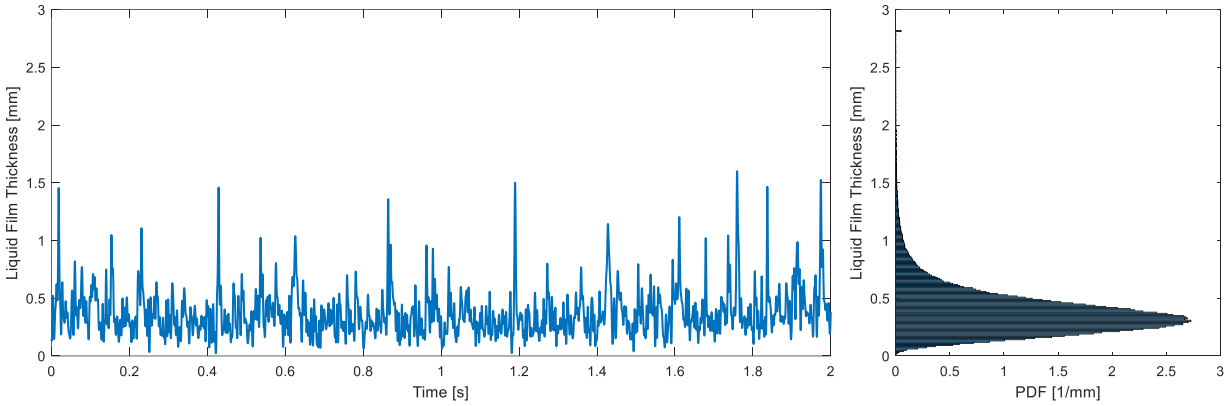

$G=1350\ kg \cdot m^{-2} \cdot s^{-1}$, $x_e= 0.05$

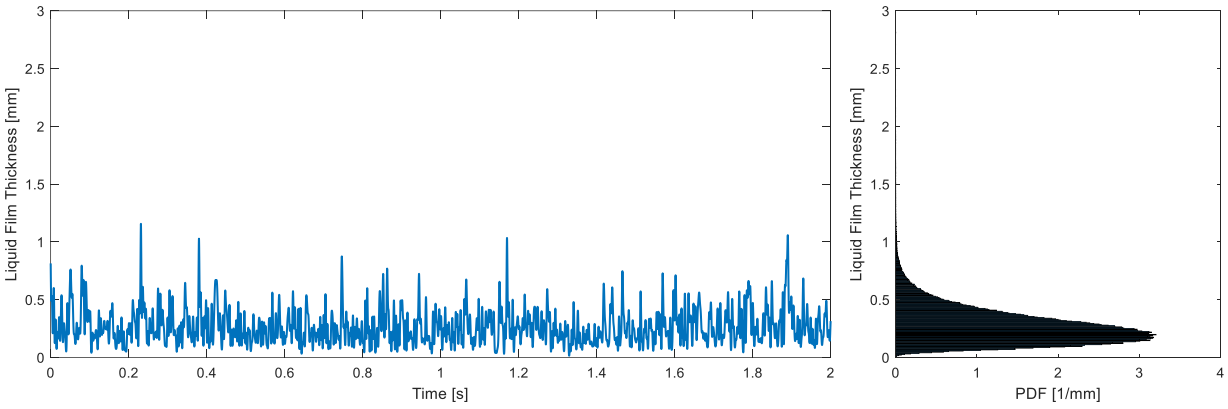

$G=750\ kg \cdot m^{-2} \cdot s^{-1}$, $x_e= 0.07$

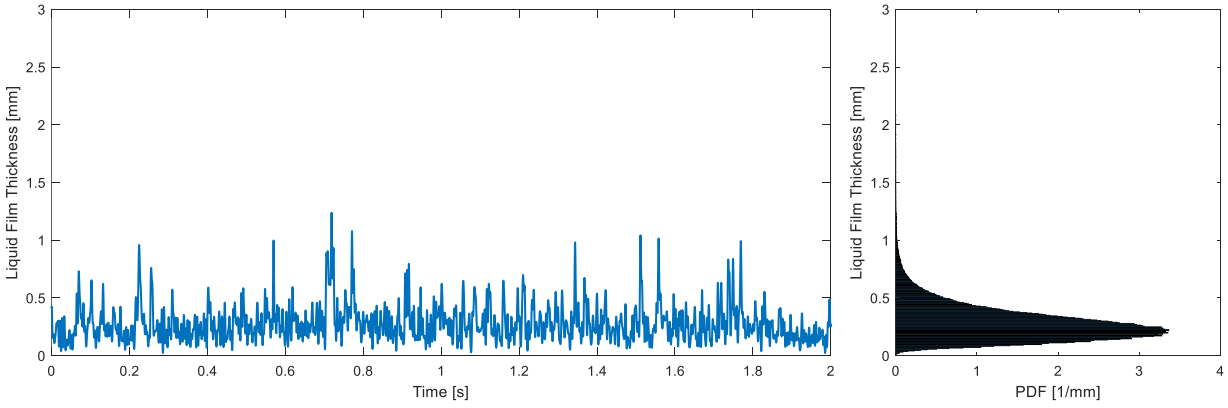

$G=1050\ kg \cdot m^{-2} \cdot s^{-1}$, $x_e= 0.07$

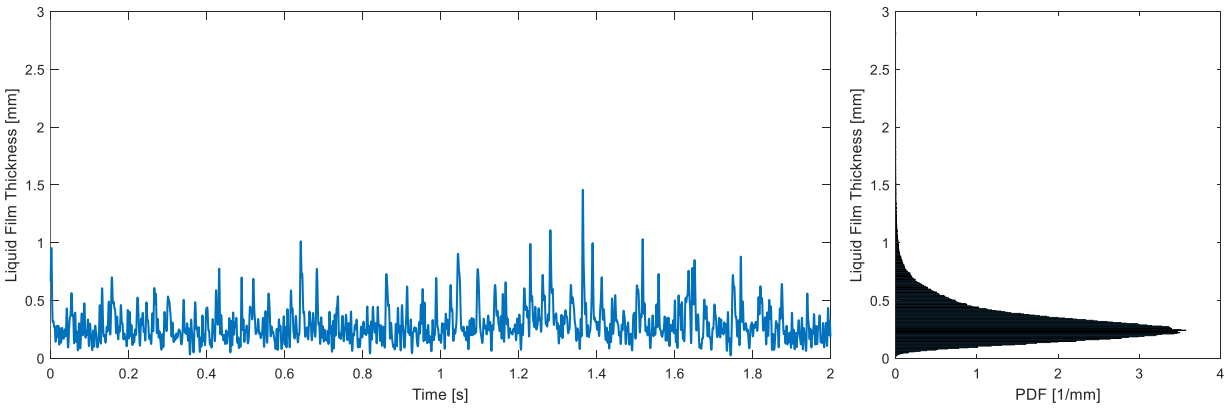

$G=1350\ kg \cdot m^{-2} \cdot s^{-1}$, $x_e= 0.07$

***Figure C-0-1**: Time history (left) and PDF (right) of the liquid film thickness measured at a single sensor element from the longitudinal unit at all test conditions.*

Appendix D: Validation of the Skewed Gaussian Decomposition Algorithm using LFS and HSV

Experimental tests were conducted to corroborate the validity of the Skewed Gaussian decomposition algorithm using synchronized LFS and HSV. The experimental setup is shown in Figure D-0-1. Water was injected in the gap between the flat nozzle and the LFS, which was then forced to flow over the LFS by the drag from the blowing nitrogen gas. The thickness and the oscillation of the liquid film were recorded by the synchronized LFS and HSV. In order to the image the side view of the liquid film, a 90^{o} mirror was used together with the HSV.

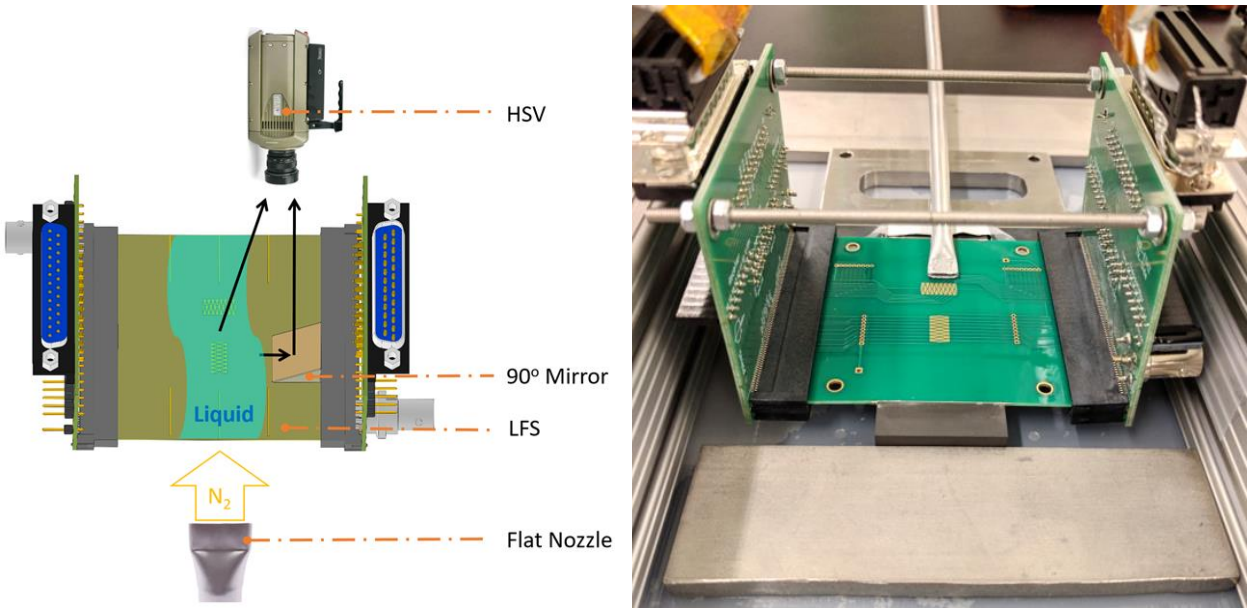

***Figure D-0-1**: The design (left) and the real picture (right) of the validation test setup for Skewed Gaussian decomposition algorithm*

Given the insufficient developing distance between the nozzle and the LFS, it was impossible to generate disturbance wave solely relying on gas accumulating water. A more reasonable approach was to introduce periodic mechanical disturbance during the injection, which successfully generated well defined disturbance wave as shown in Figure D-0-2.

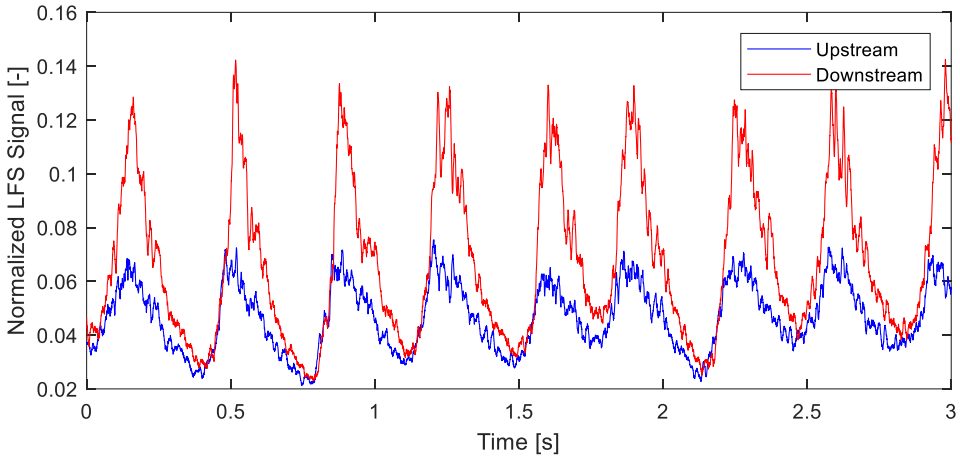

***Figure D-0-2**: Typical normalized LFS signal measured from upstream and downstream sensors. Strong correlation between the signals are observed.*

Due to the limited size of the mirror (~1.5 cm width) and the long wave length of the generated disturbance wave (~10 to 20 cm), it was impossible to directly track the whole disturbance wave from HSV image. A post-processing method based on bipolarized image was applied to extract the thickness information from multiple locations equivalent to the LFS layout, as shown in Figure D-0-3. The HSV image was first zoomed-in to the LFS area, and then bipolarized. The instantaneous film thickness (wave height) was thus measured from the vertical length across the dark area at various locations. The measured normalized film thickness (wave height) from LFS and HSV are fairly consistent with each other as shown in Figure D-0-4.

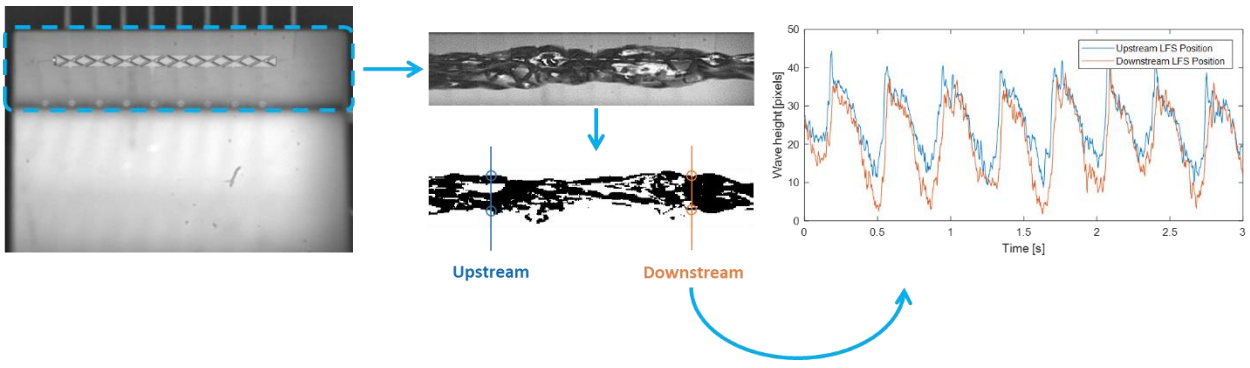

***Figure D-0-3**: Illustration of extracting film thickness from HSV image.*

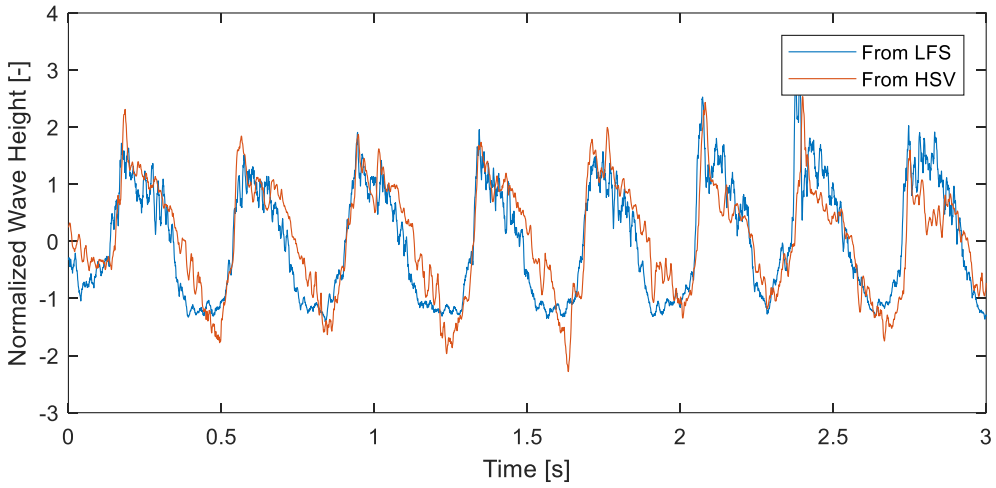

Upstream location

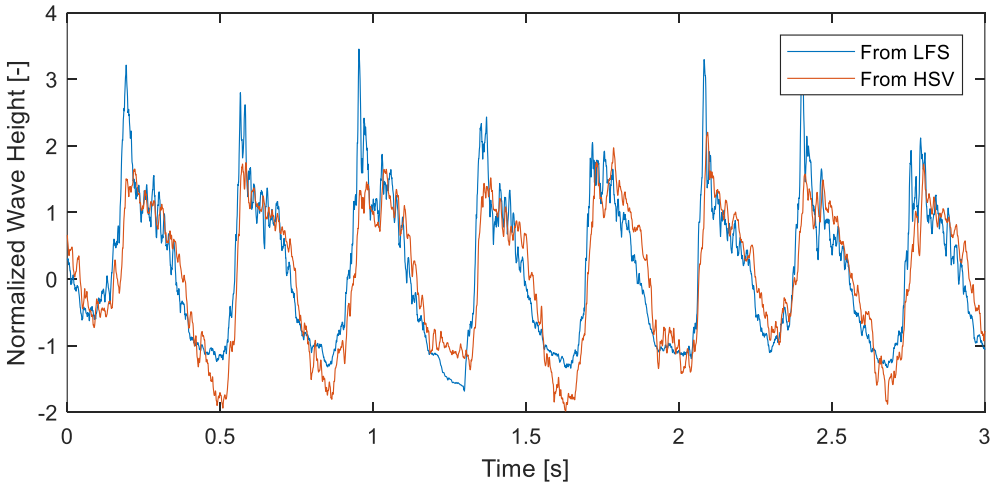

Downstream location

***Figure D-0-4**: The comparison of normalized wave height from LFS and HSV measurements shows good consistency.*

The signals from LFS and HSV were both post-processed by Skewed Gaussian decomposition algorithm for disturbance wave velocity. The velocities extracted from HSV agree reasonably well with the values calculated from LFS, with only a few points off, as shown in Figure D-0-5.

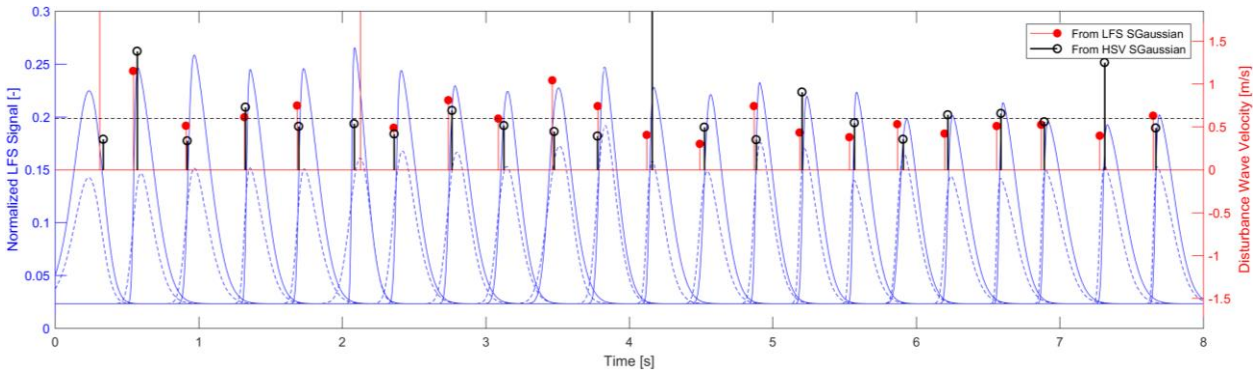

***Figure D-0-5**: The comparison of extracted wave velocities from LFS and HSV using Skewed Gaussian decomposition algorithm.*

Another separate simple method (edge-tracking) was also applied to check the order of magnitude of the velocity extracted from HSV signal other than Skewed Gaussian decomposition. The HSV signals measured at upstream and downstream locations were first strongly smoothed. Then the average time delay of each wave was simply calculated from the time difference at the windward side of the wave between the two signals at half wave height. The results are summarized in the following table, which shows reasonably good agreement among different approaches. The validity of the Skewed Gaussian algorithm is thus corroborated.

***Table D-0-1**: Comparison of the mean and standard deviation of the wave velocity calculated from different measured signals and post-processing methods.*

Method	**Mean Velocity [m·s^{-1}]**	**STD Velocity [m·s^{-1}]**
LFS_Skew Gaussian	0.598	0.279
HSV_Skew Gaussian	0.597	0.221
HSV_Edge Tracking	0.646	0.256

Appendix E: Statistical Profiles of Disturbance Wave Velocity and Amplitude.

The statistical profiles of the disturbance wave velocity and amplitude at all test conditions are summarized in the figure below. Since the horizontal axis for the disturbance wave velocity is in logarithmic scale, the probability is used instead of PDF for an easier understanding of the statistical profile. As discussed in Section 6.3.3, there is general only one mode (i.e., only one maximum in the PDF) for the wave velocity and wave amplitude respectively. However, at low steam quality condition, a second mode could appear at the largest wave amplitude, due to the upper limit of the LFS measurement. As a result, all the disturbance waves with amplitude larger than the LFS limit are concentrated into the last two bins at the largest amplitude end.

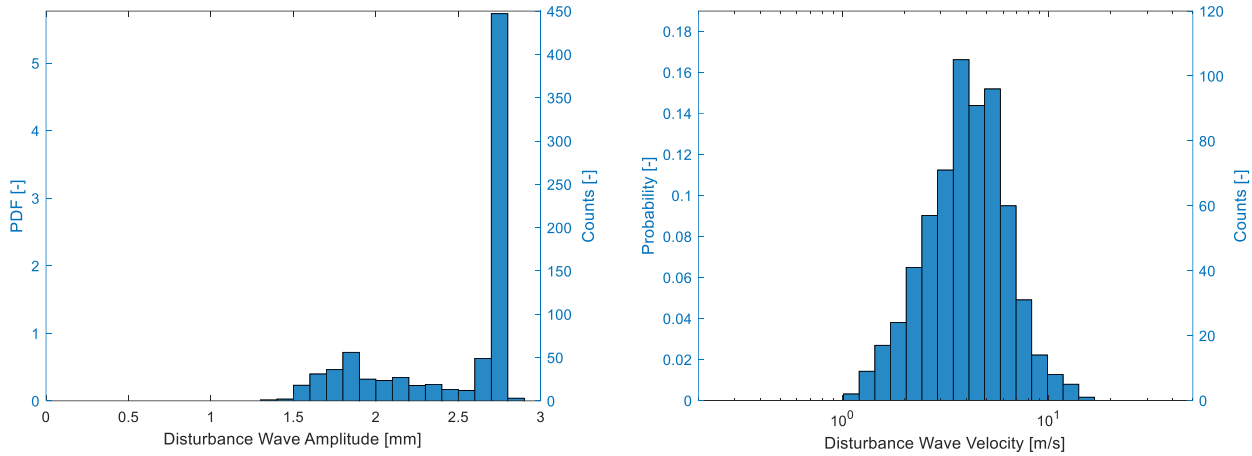

G=750 kg·m^{-2}·s^{-1}, x_e= 0.016

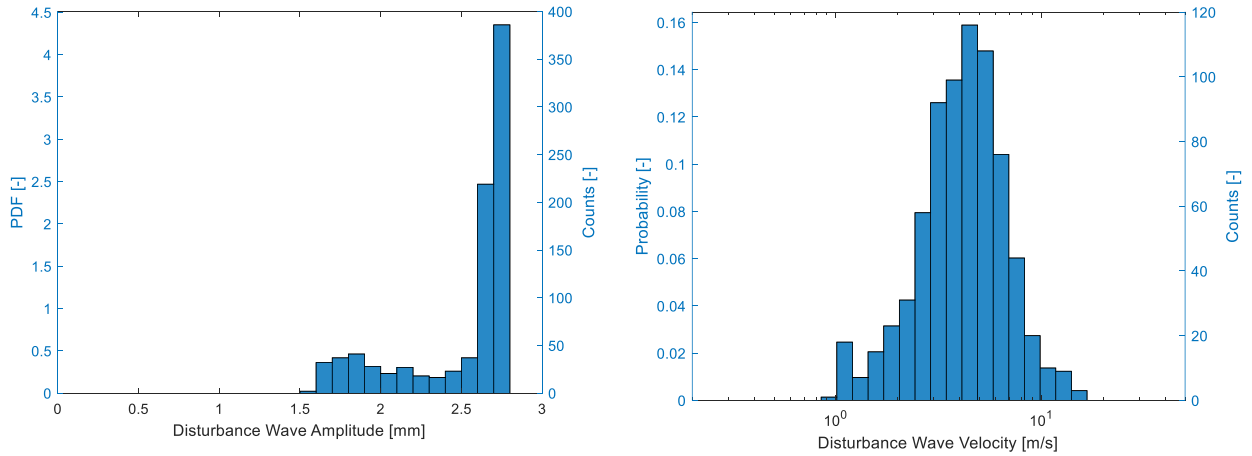

G=1050 kg·m^{-2}·s^{-1}, x_e= 0.016

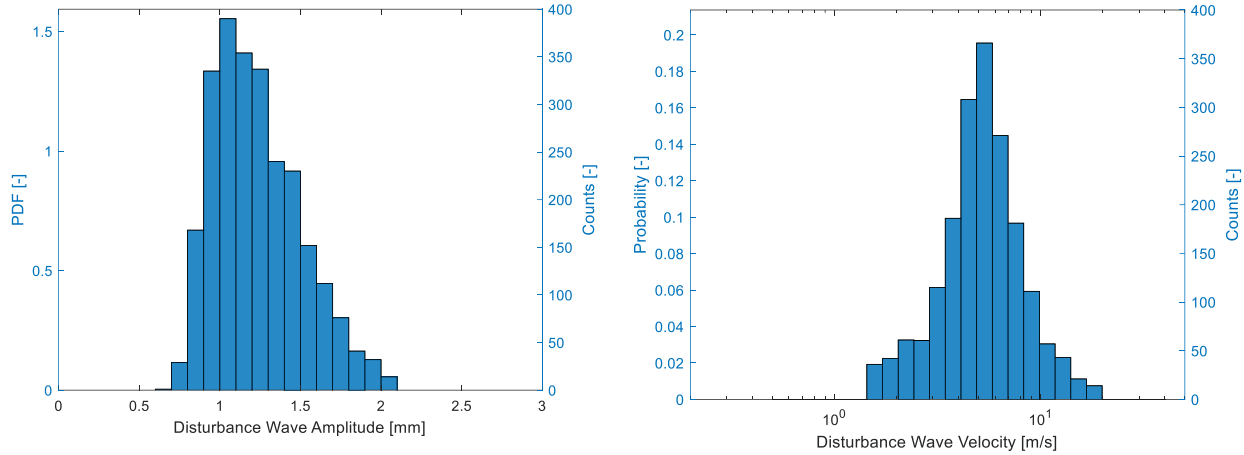

$G=1350\ kg \cdot m^{-2} \cdot s^{-1}$, $x_e = 0.016$

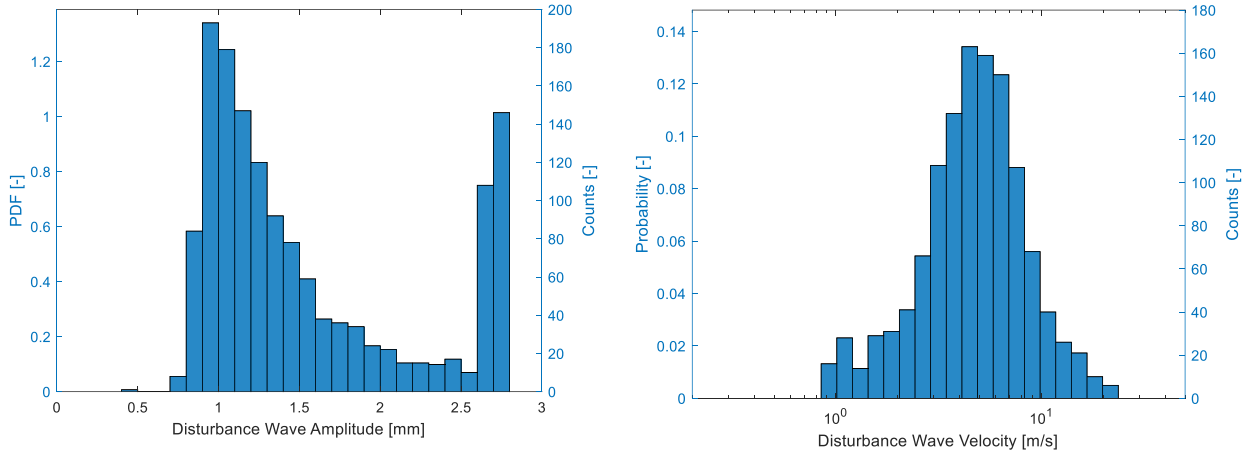

$G=750\ kg \cdot m^{-2} \cdot s^{-1}$, $x_e = 0.03$

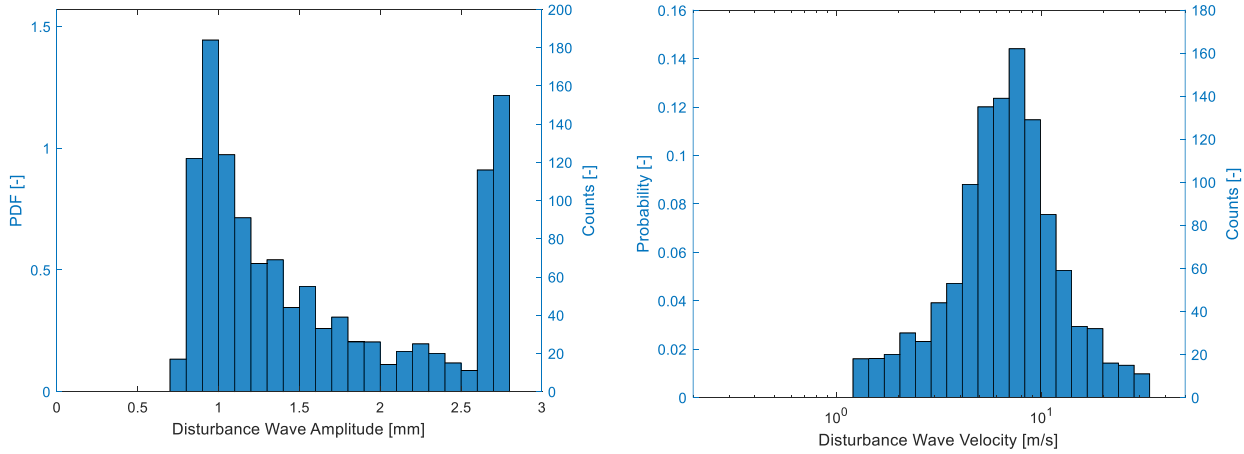

$G=1050\ kg \cdot m^{-2} \cdot s^{-1}$, $x_e = 0.03$

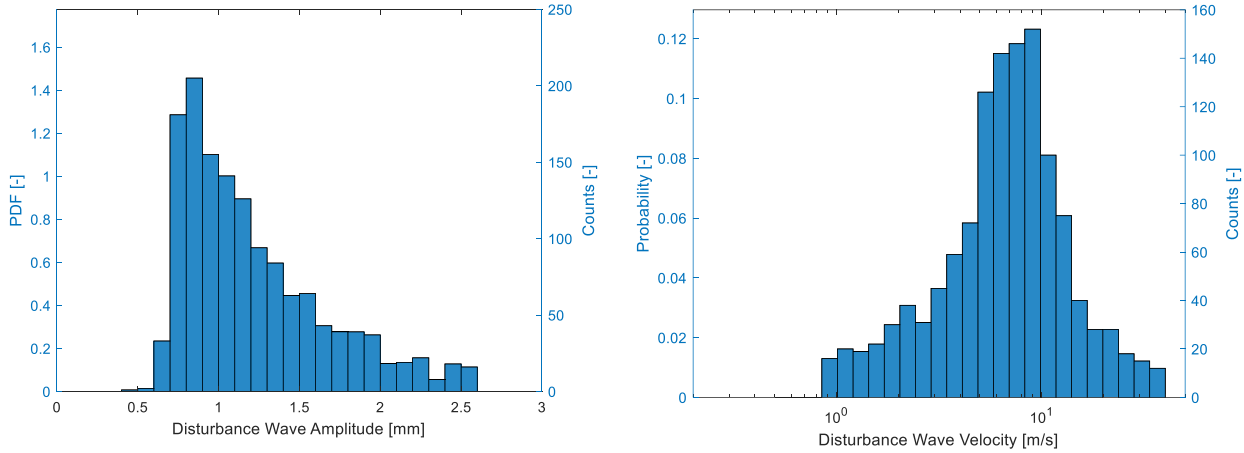

$G=1350\ kg \cdot m^{-2} \cdot s^{-1}$, $x_e = 0.03$

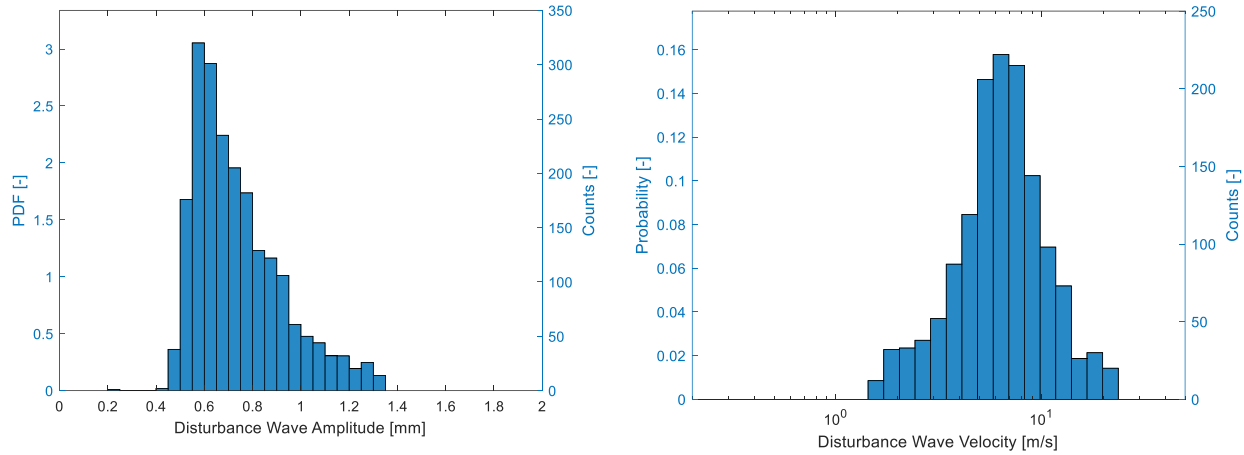

$G=750\ kg \cdot m^{-2} \cdot s^{-1}$, $x_e = 0.05$

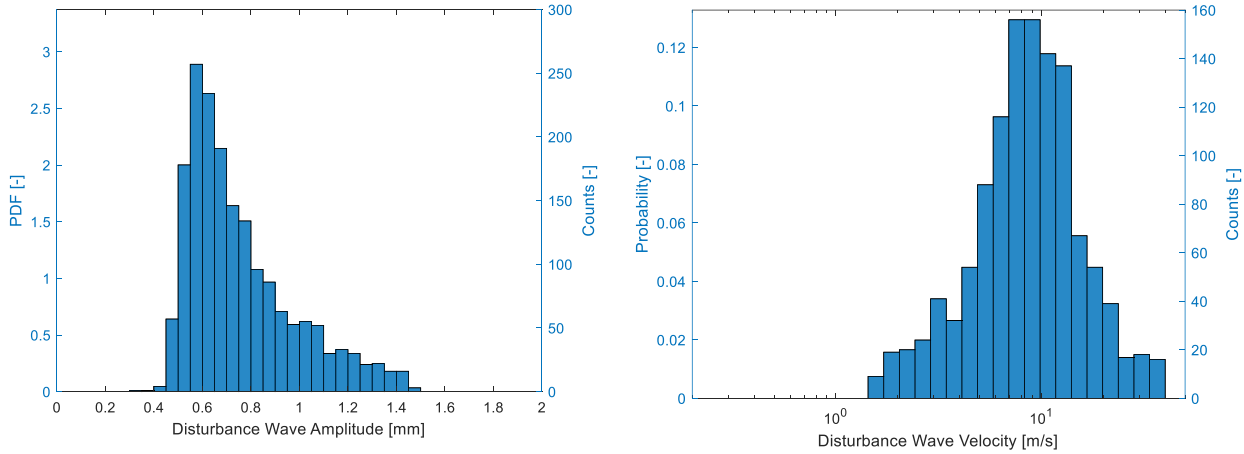

$G=1050\ kg \cdot m^{-2} \cdot s^{-1}$, $x_e = 0.05$

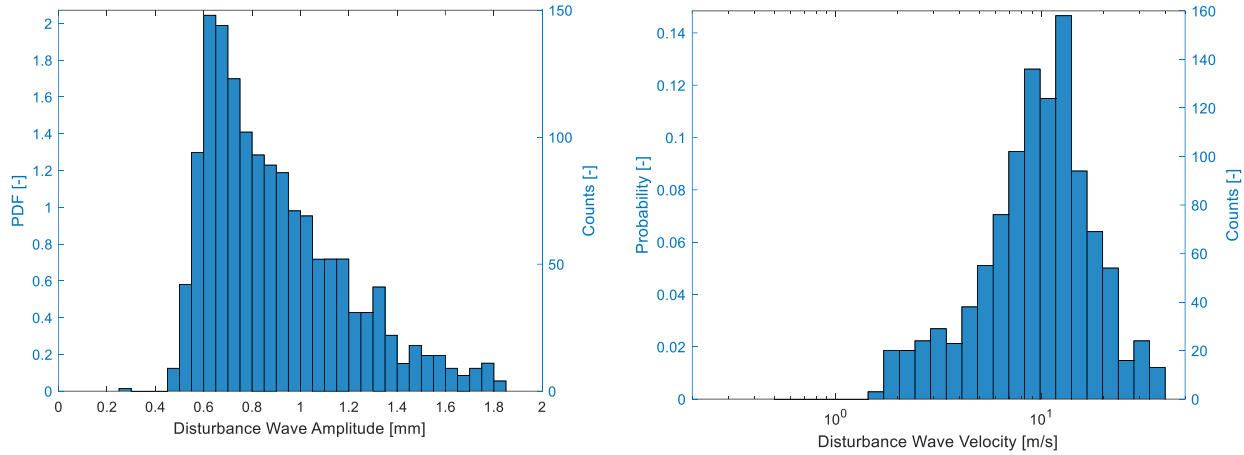

$G=1350\ kg \cdot m^{-2} \cdot s^{-1}$, $x_e = 0.05$

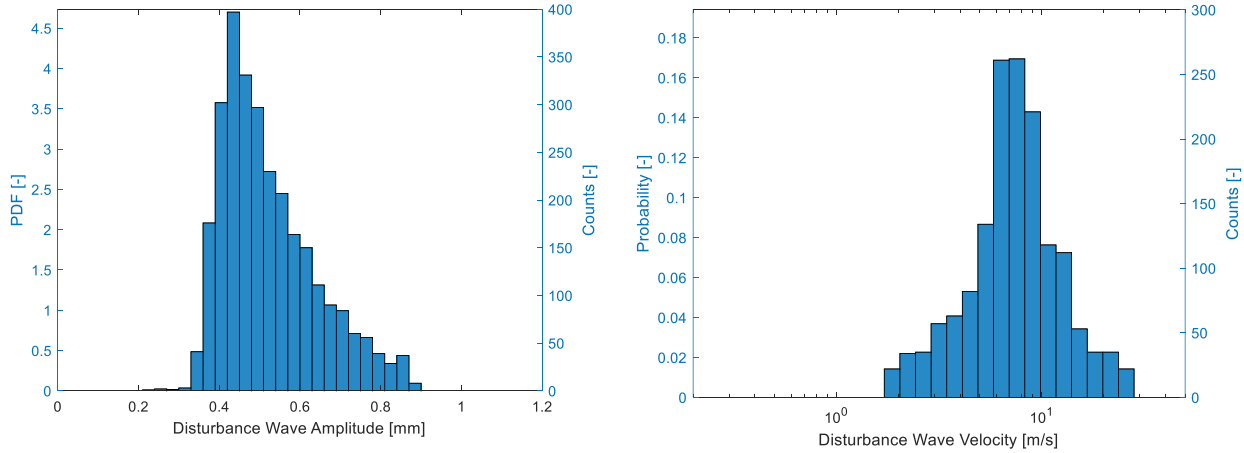

$G=750\ kg \cdot m^{-2} \cdot s^{-1}$, $x_e = 0.07$

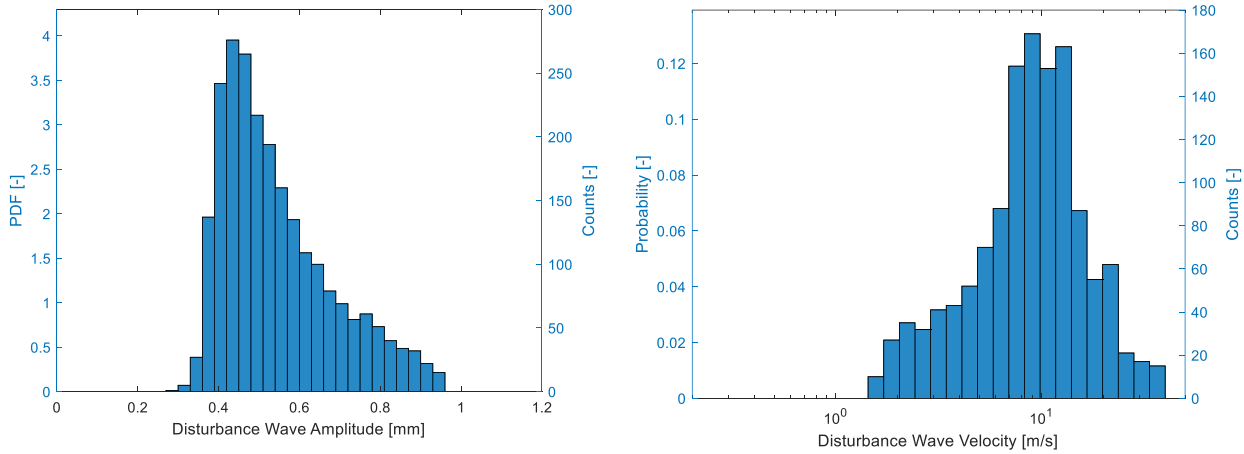

$G=1050\ kg \cdot m^{-2} \cdot s^{-1}$, $x_e = 0.07$

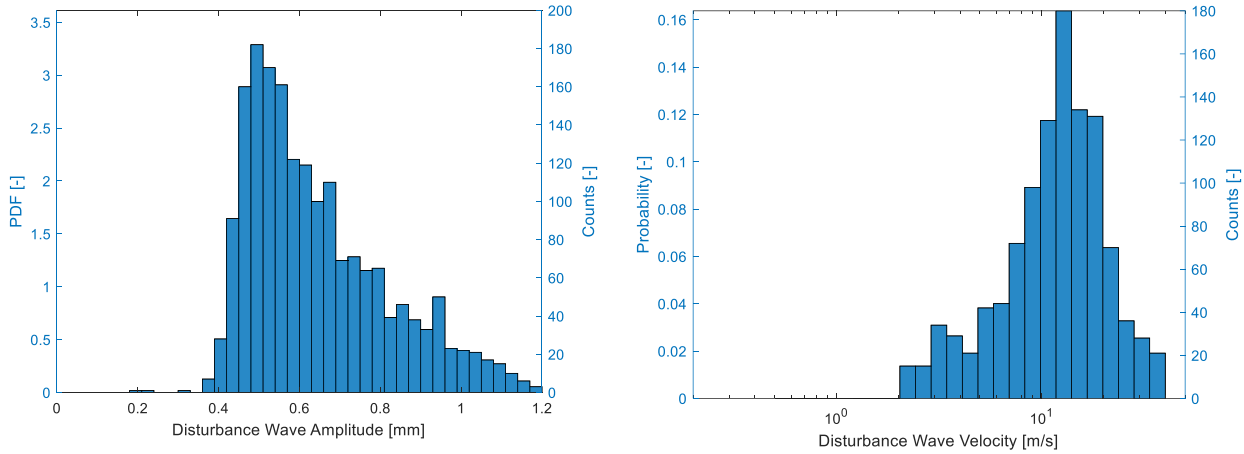

$G=1350\ kg \cdot m^{-2} \cdot s^{-1}$, $x_e = 0.07$

***Figure E-0-1**: The probability profiles of the disturbance wave velocity and amplitude at each test condition.*

Appendix F: Time History of the Chordal Average Thermal Parameters.

The time histories of the chordal average thermal parameters, i.e., wall superheat, heat flux and HTC, at each test condition below SNB are shown in Figure F-0-1. As discussed in Section 7.2, such thermal oscillations are attributed to the variation of the local heat transfer, which is caused by the periodic change of liquid film thickness with the passage of disturbance waves. Clear time coherence is observed among the three thermal properties: when there is a spike in HTC, the heat flux also peaks, while the wall superheat sharply drops.

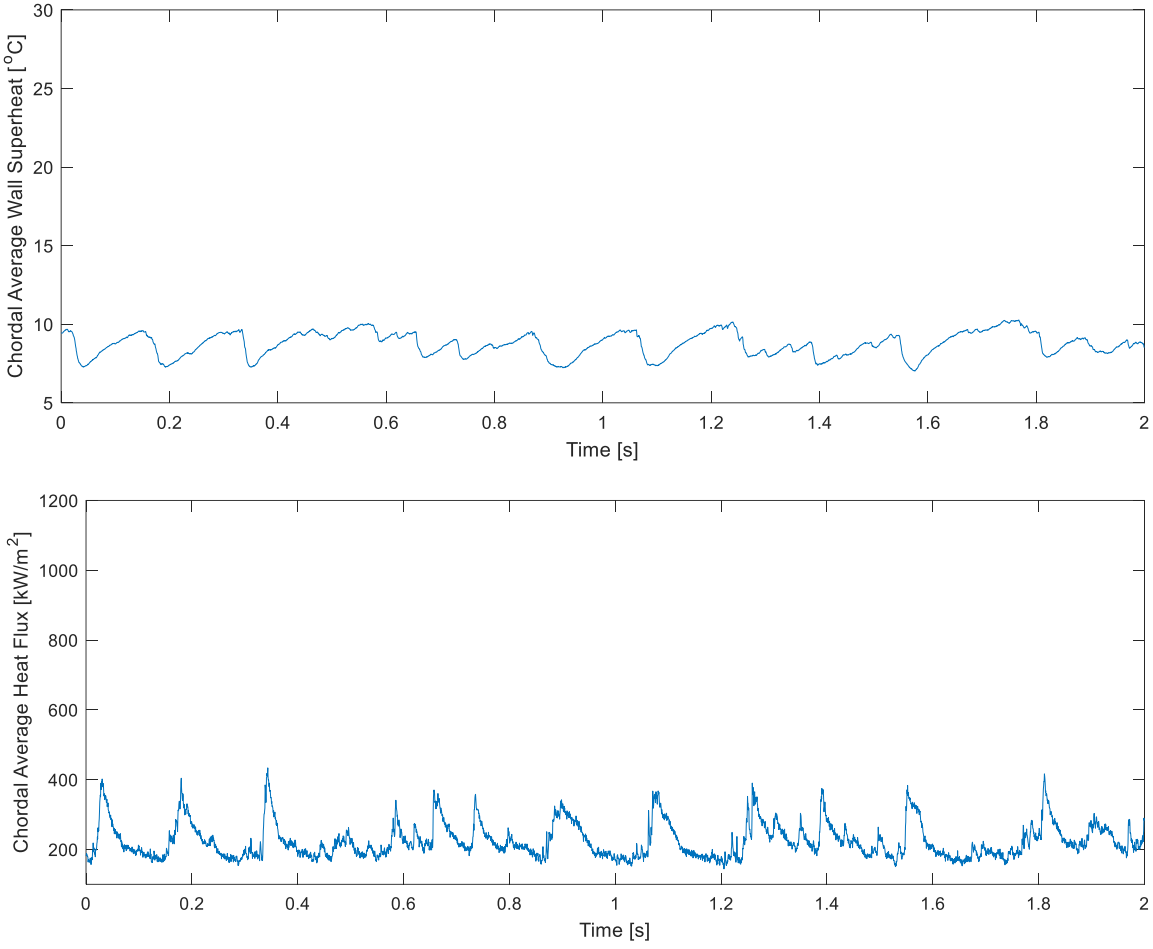

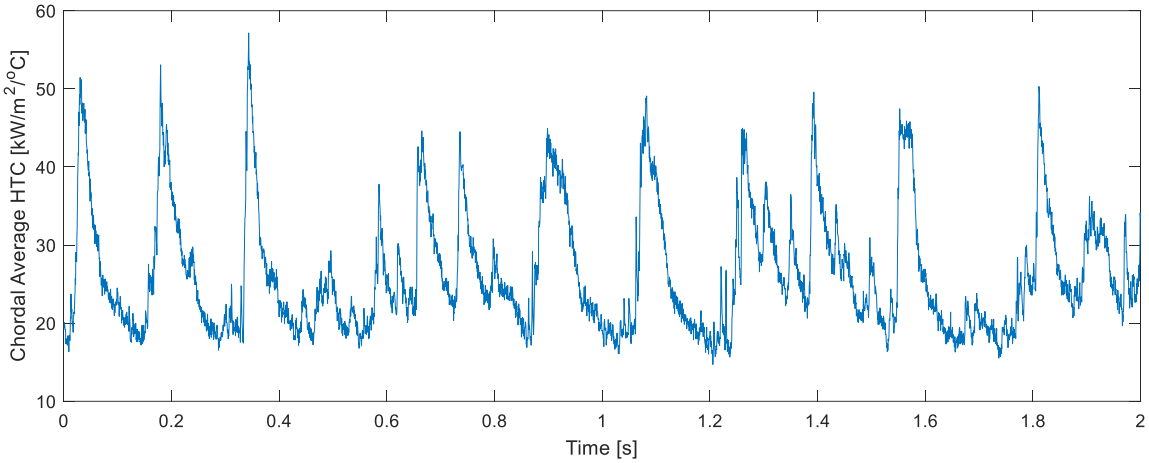

$G=750\ kg \cdot m^{-2} \cdot s^{-1}$, $x_e = 0.016$

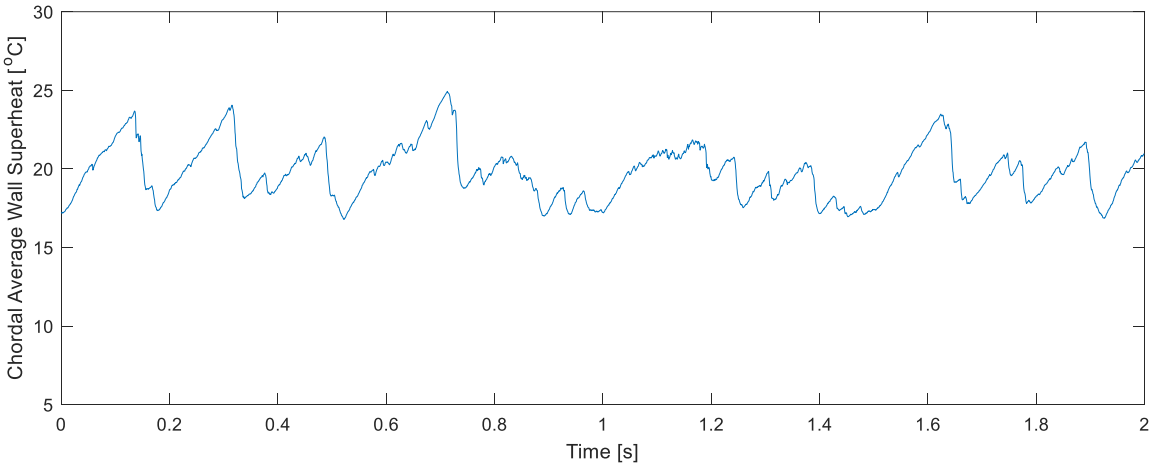

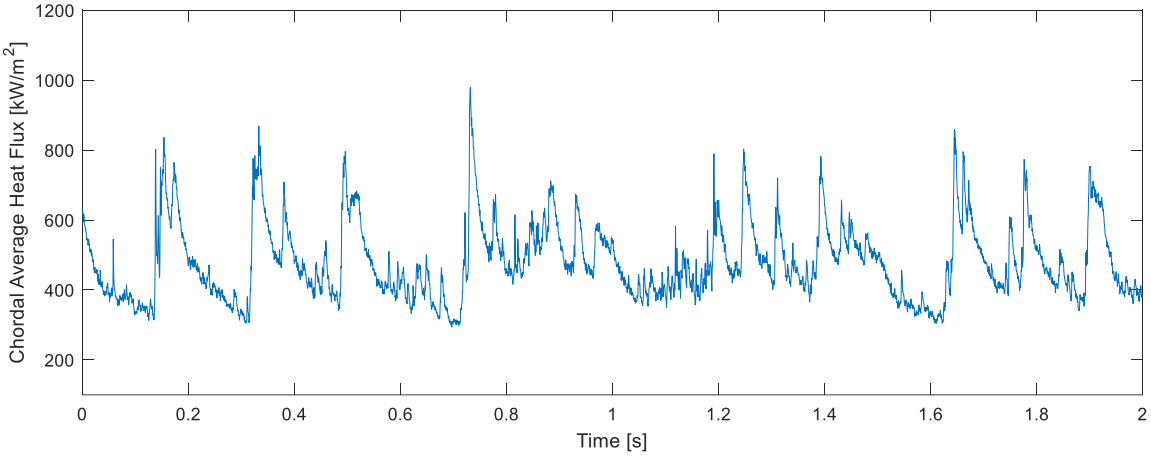

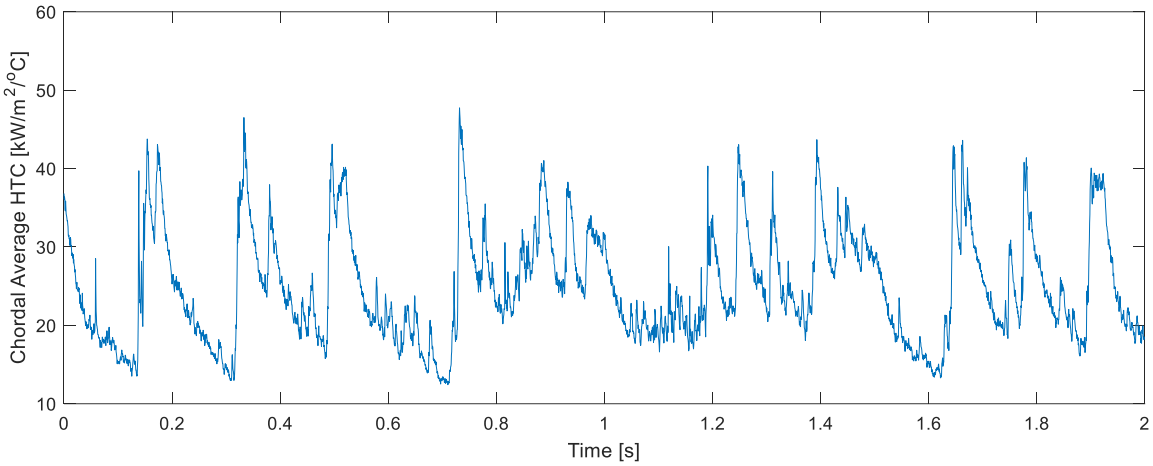

$G=1050\ kg \cdot m^{-2} \cdot s^{-1}$, $x_e = 0.016$

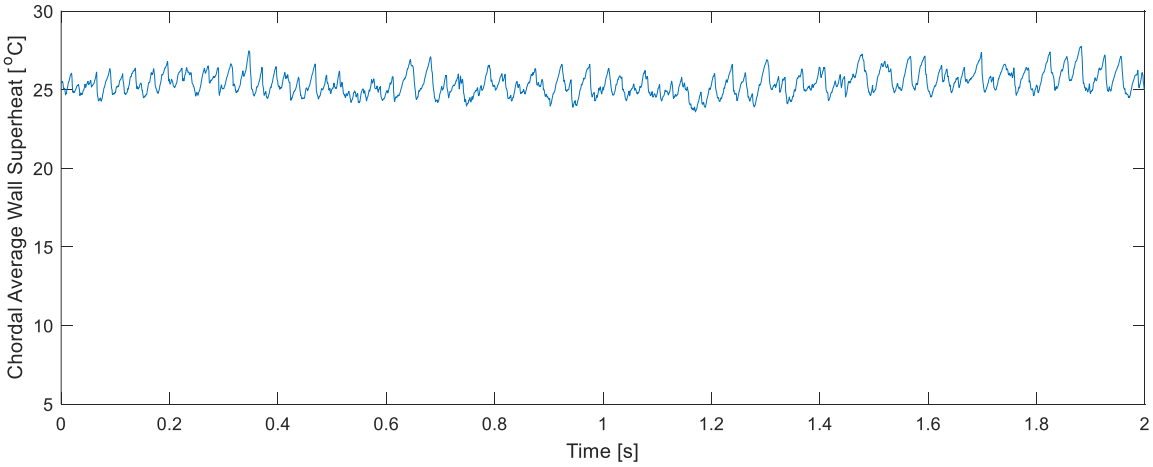

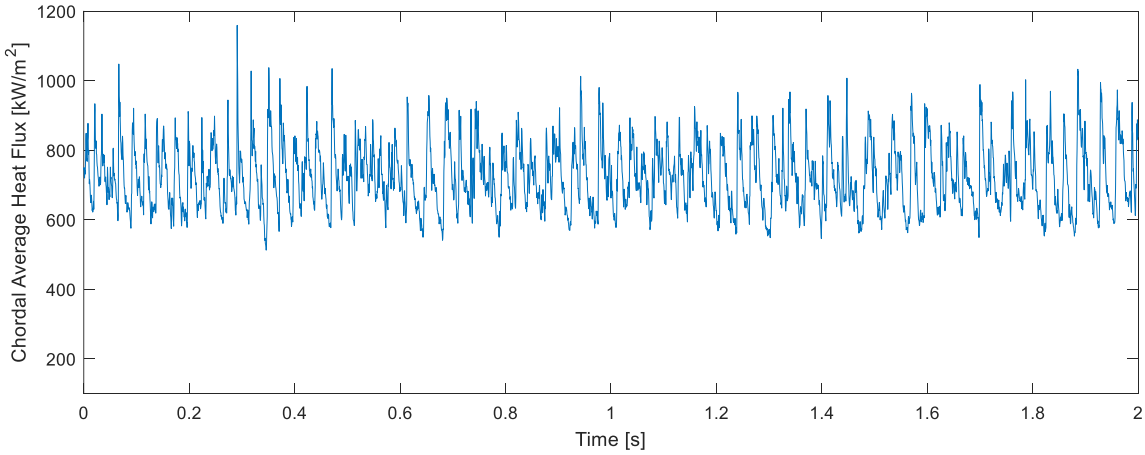

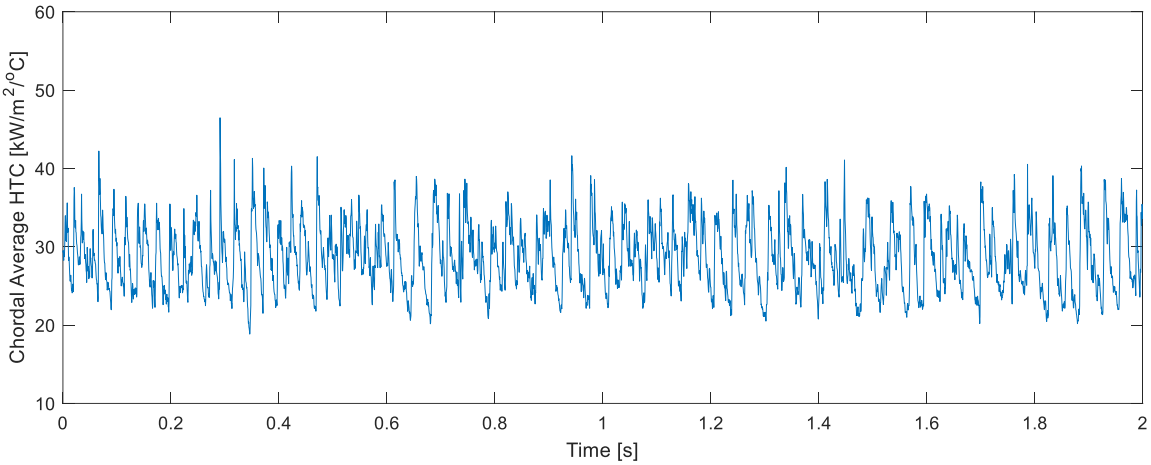

$G=1350\ kg \cdot m^{-2} \cdot s^{-1}$, $x_e = 0.016$

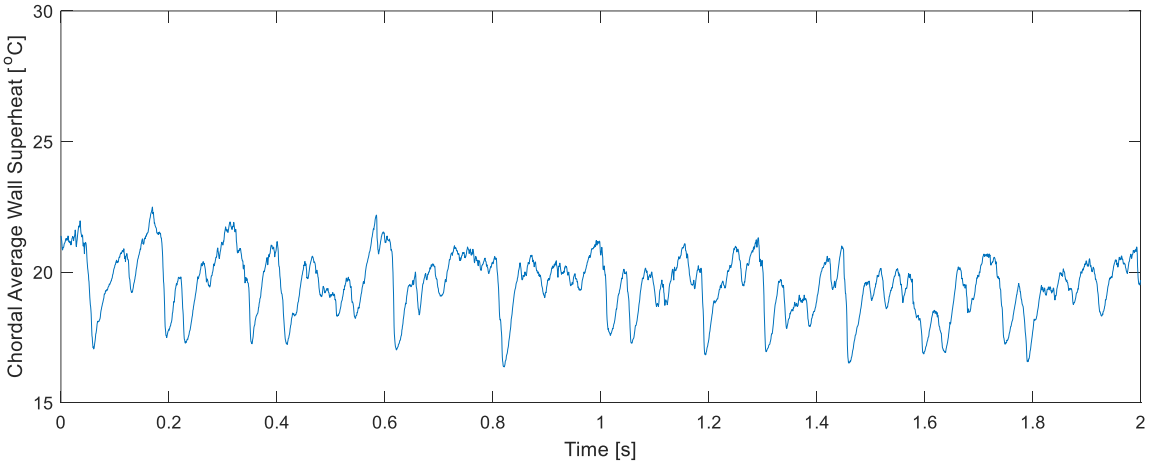

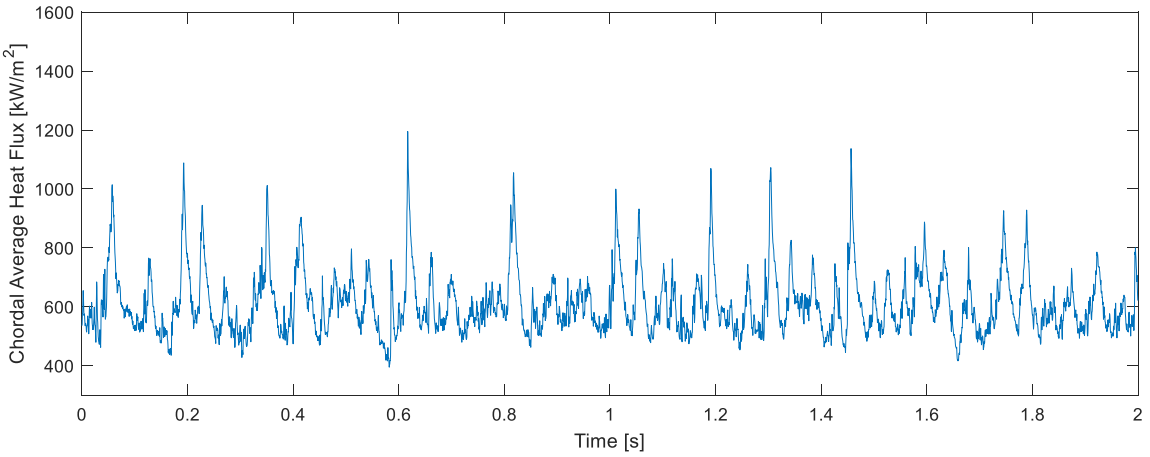

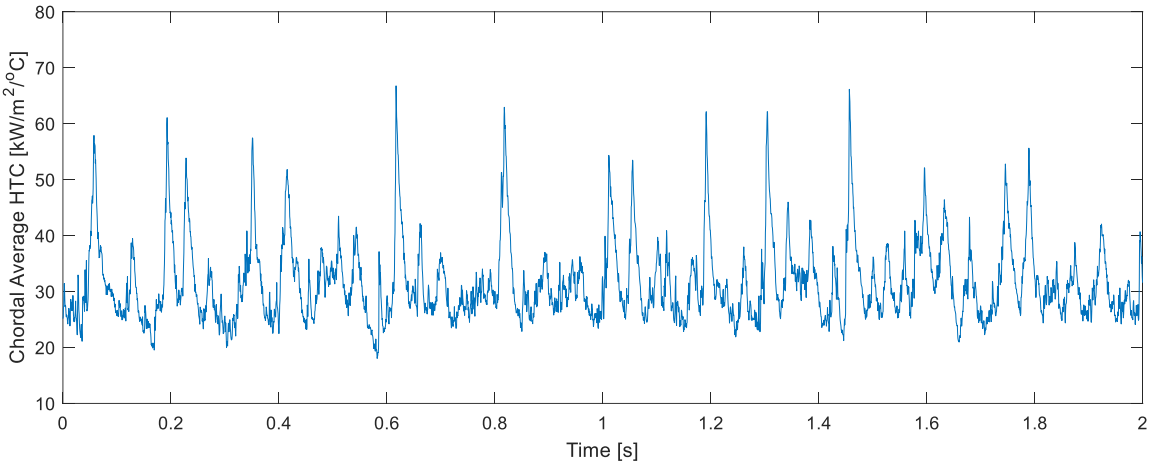

$G=750\ kg \cdot m^{-2} \cdot s^{-1}$, $x_e = 0.03$

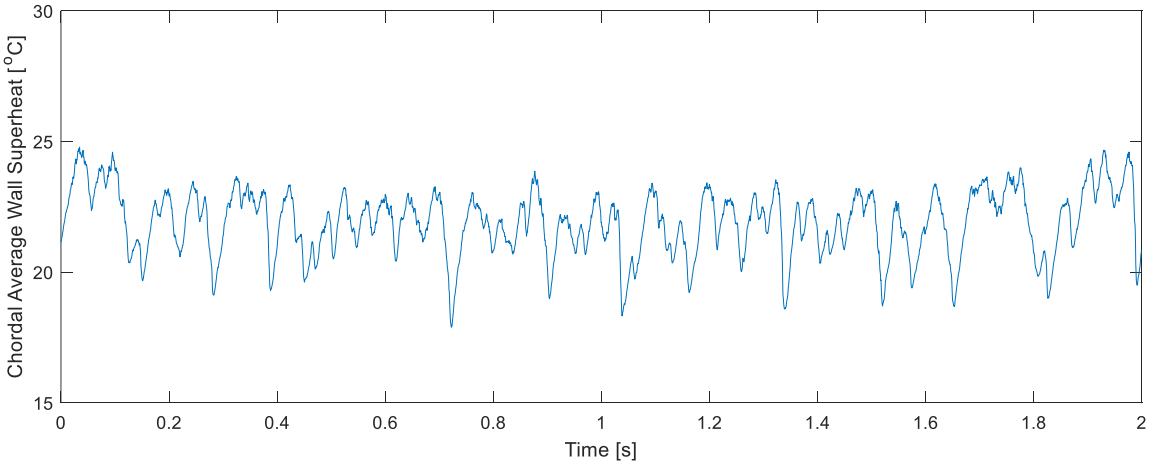

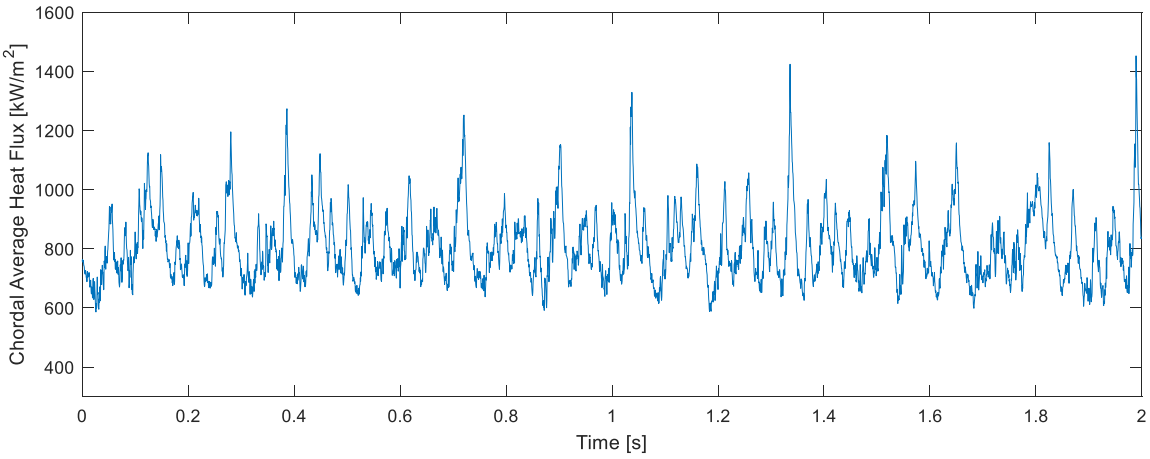

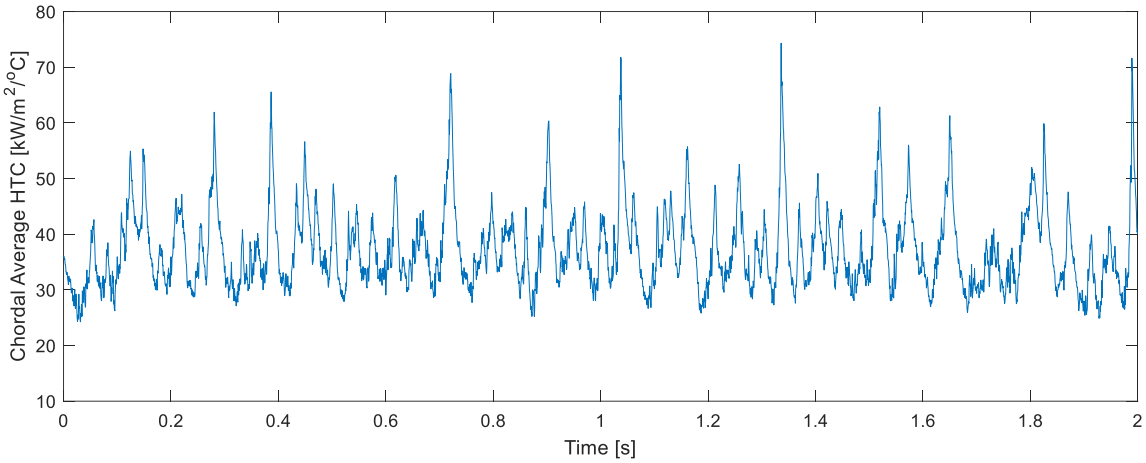

$G=1050\ kg{\cdot}m^{-2}{\cdot}s^{-1}$, $x_e= 0.03$

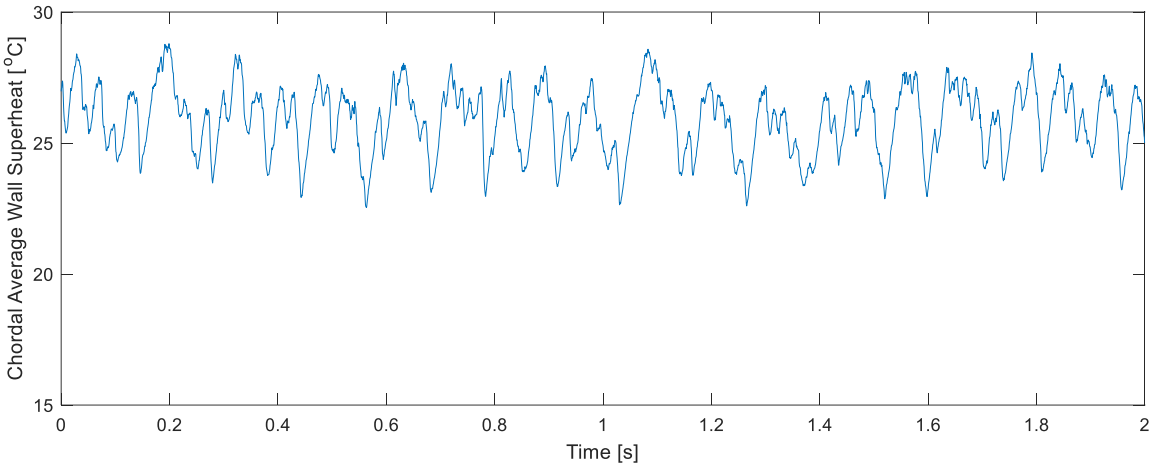

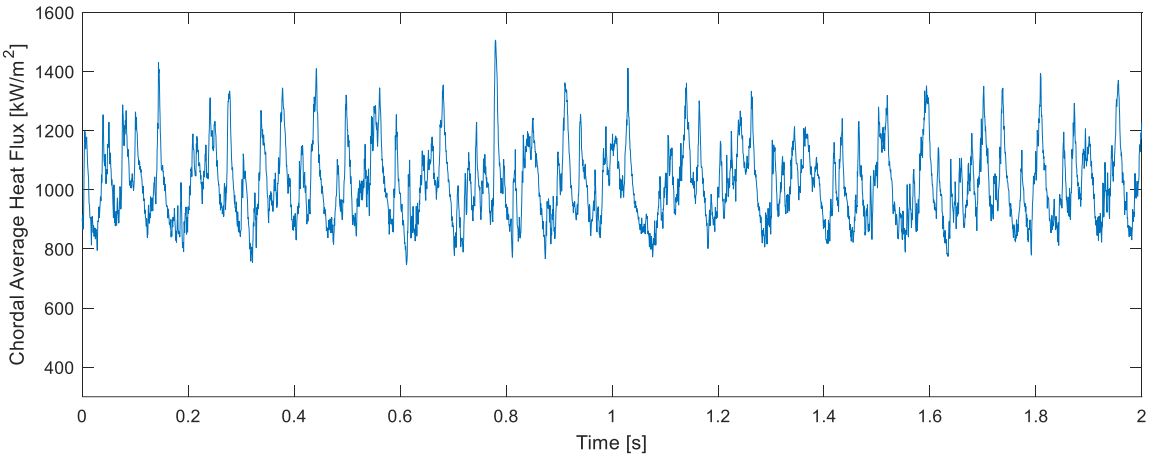

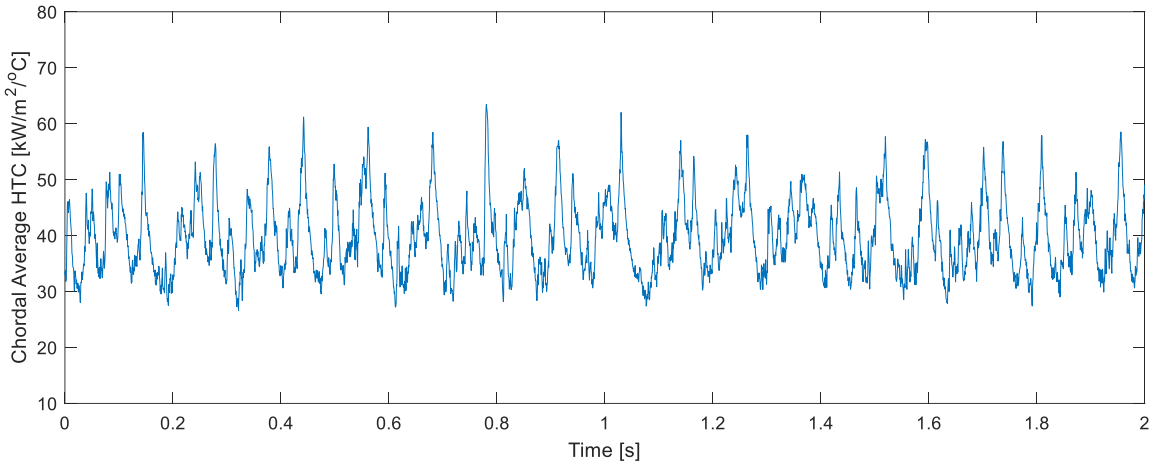

$G=1350\ kg{\cdot}m^{-2}{\cdot}s^{-1}$, $x_e= 0.03$

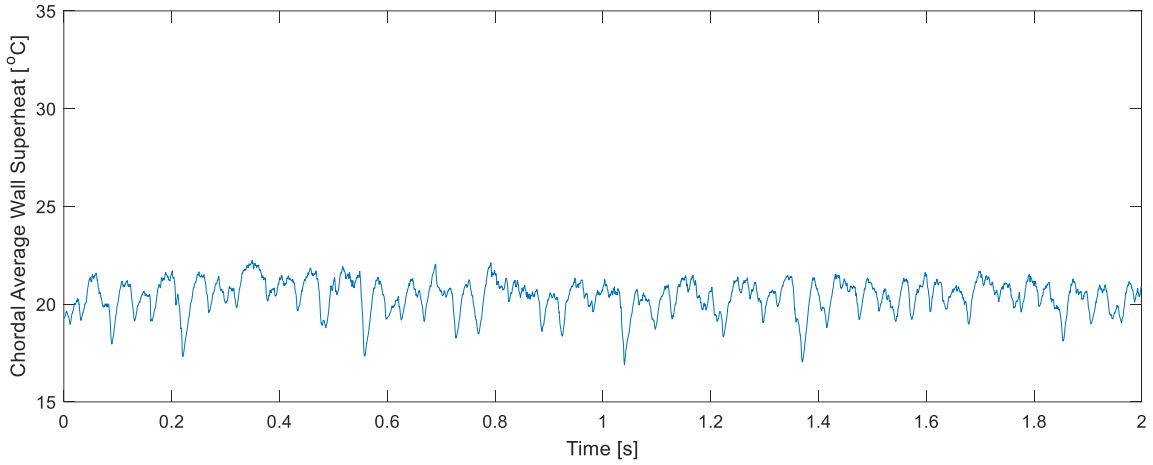

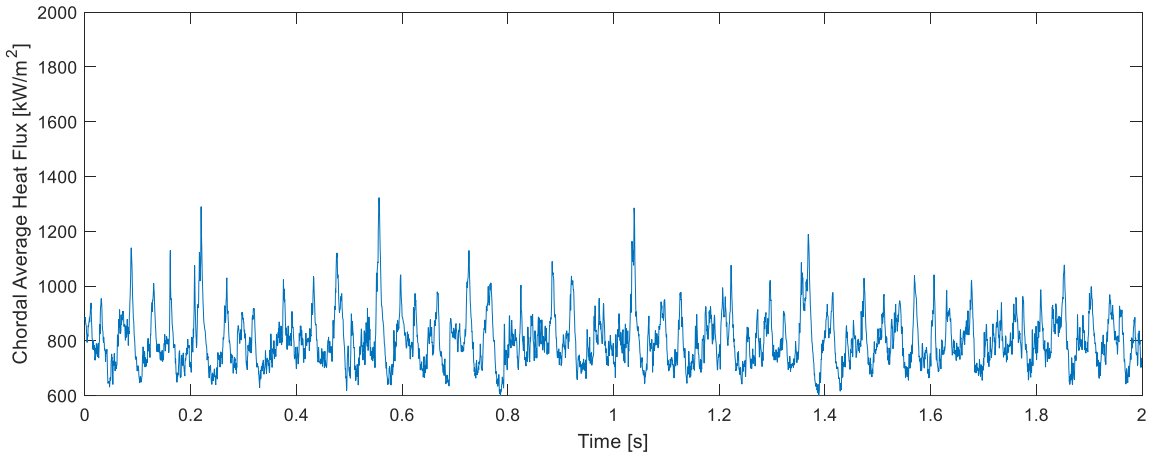

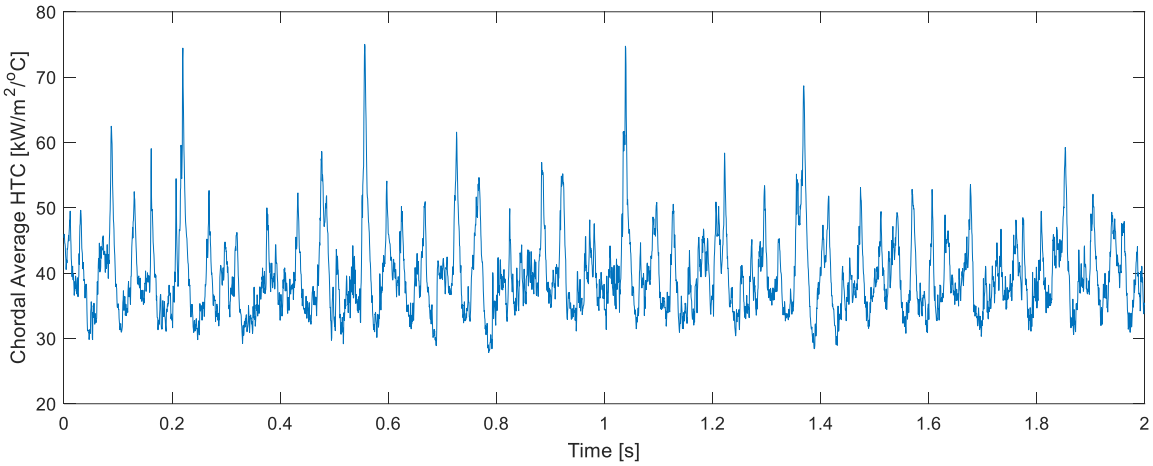

$G=750\ kg \cdot m^{-2} \cdot s^{-1}$, $x_e = 0.05$

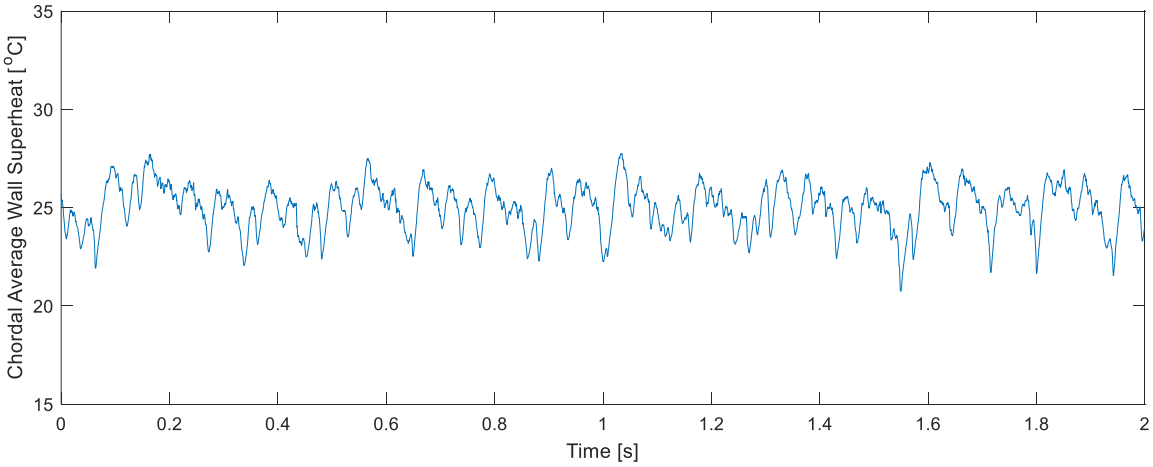

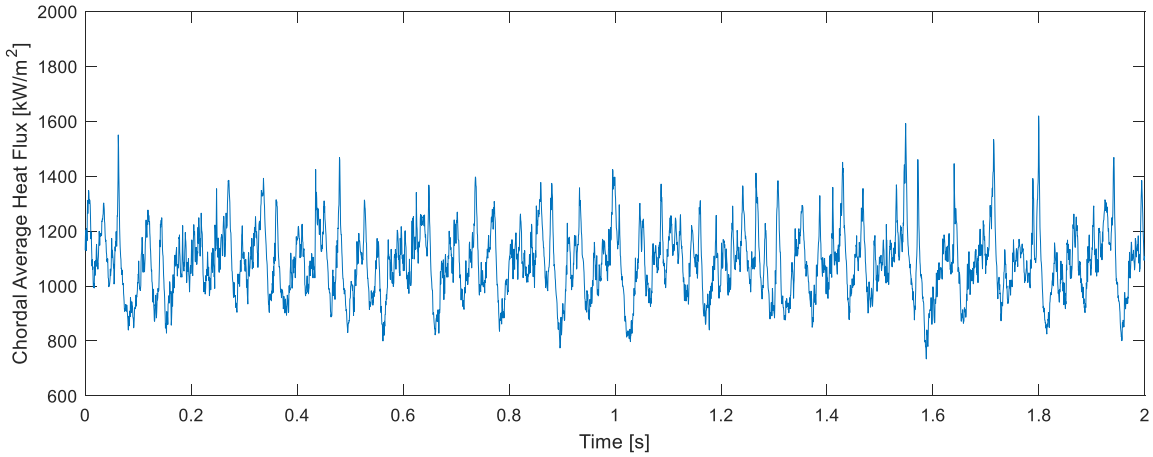

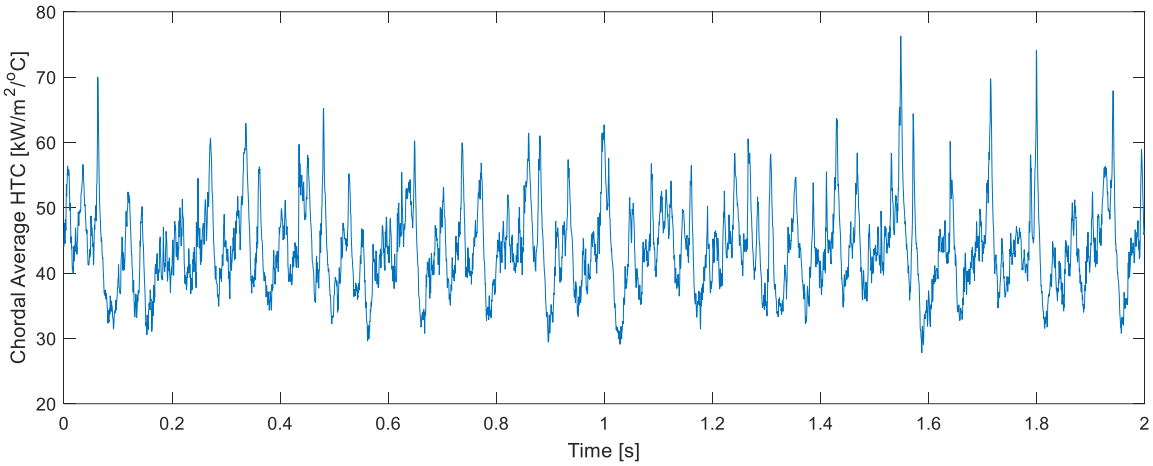

$G=1050\ kg{\cdot}m^{-2}{\cdot}s^{-1}$, $x_e= 0.05$

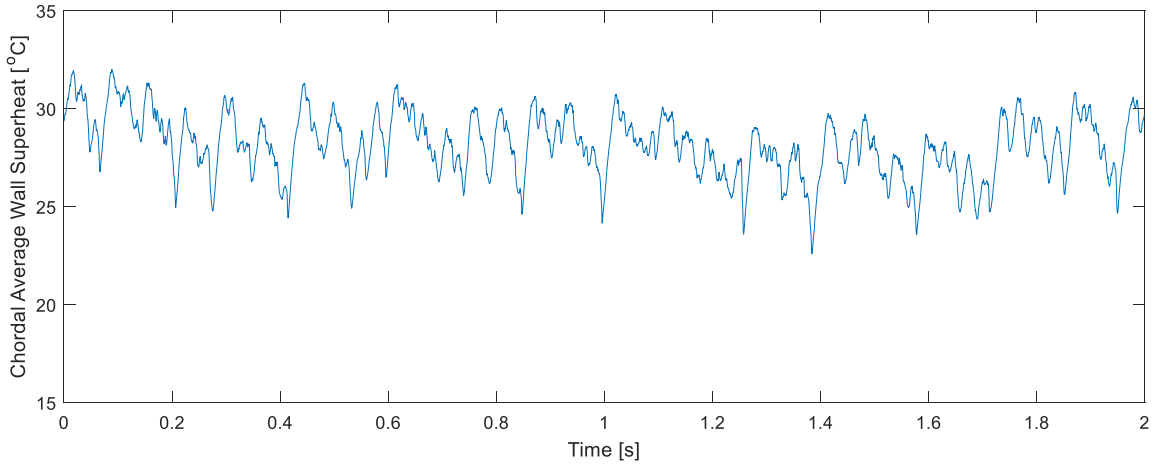

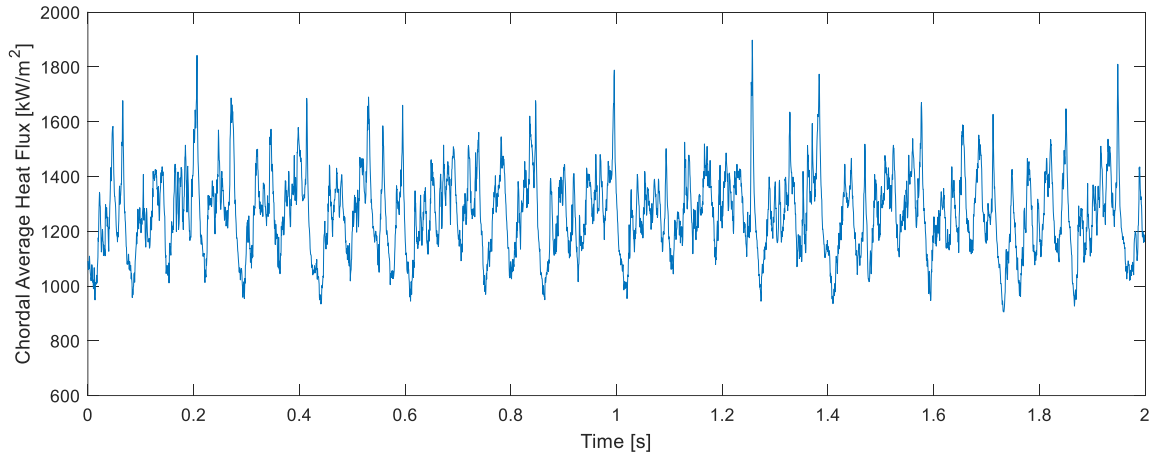

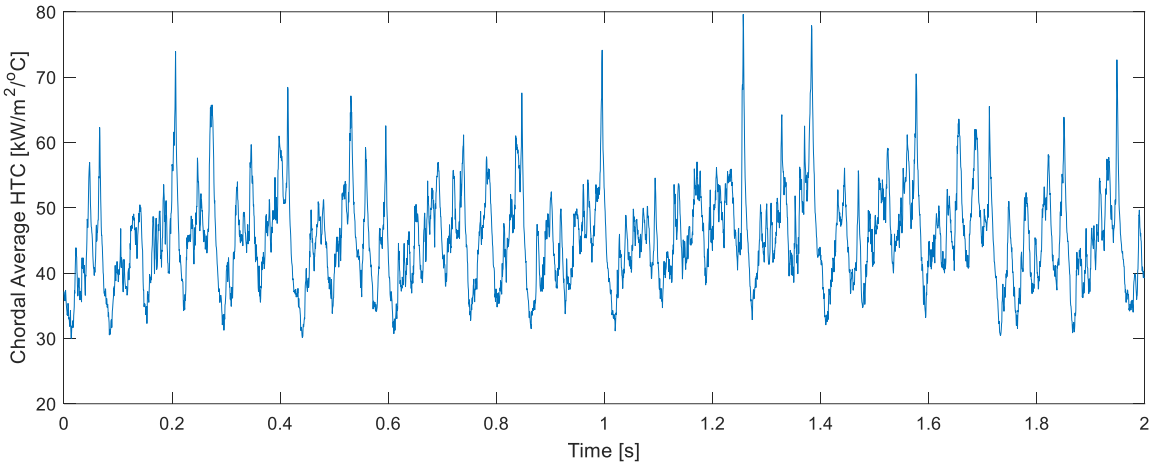

$G=1350\ kg{\cdot}m^{-2}{\cdot}s^{-1}$, $x_e= 0.05$

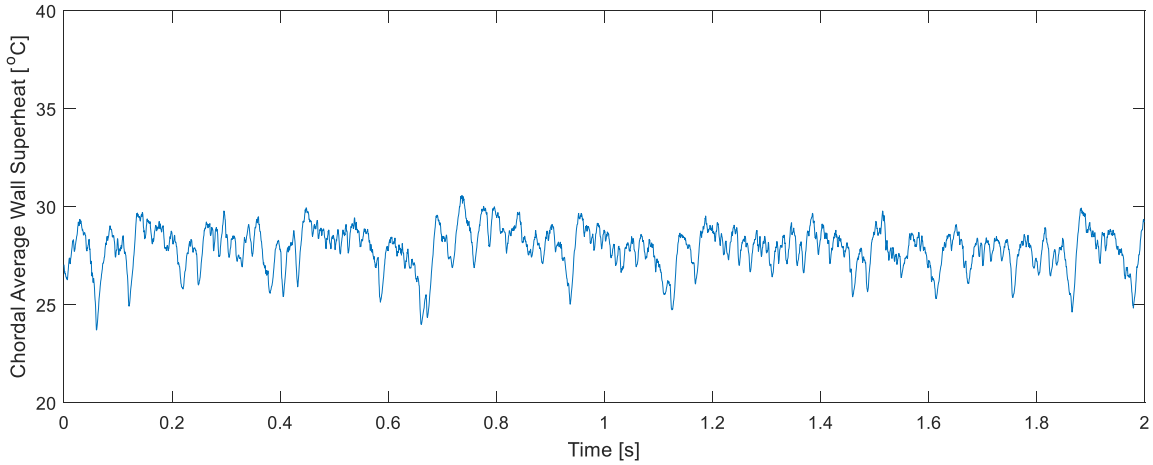

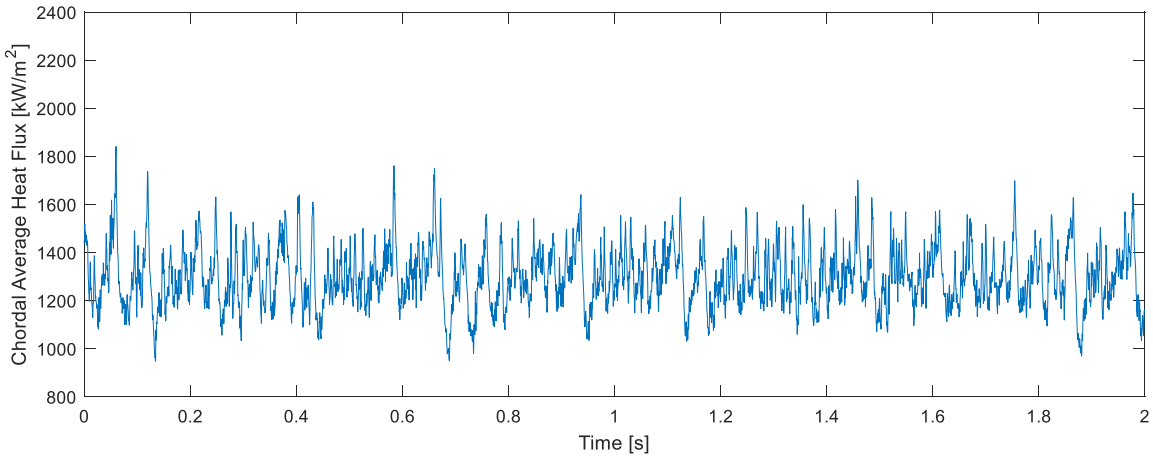

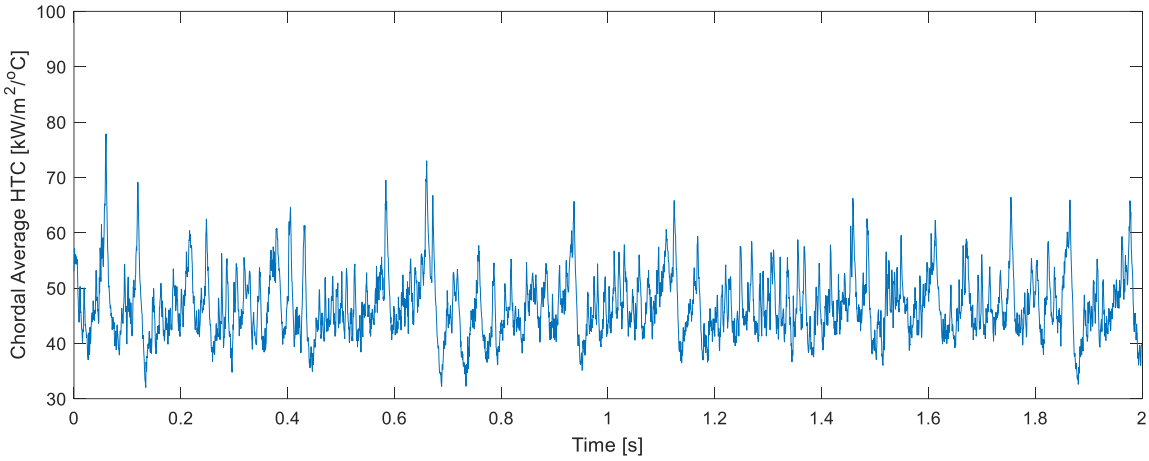

$G=750\ kg \cdot m^{-2} \cdot s^{-1}$, $x_e = 0.07$

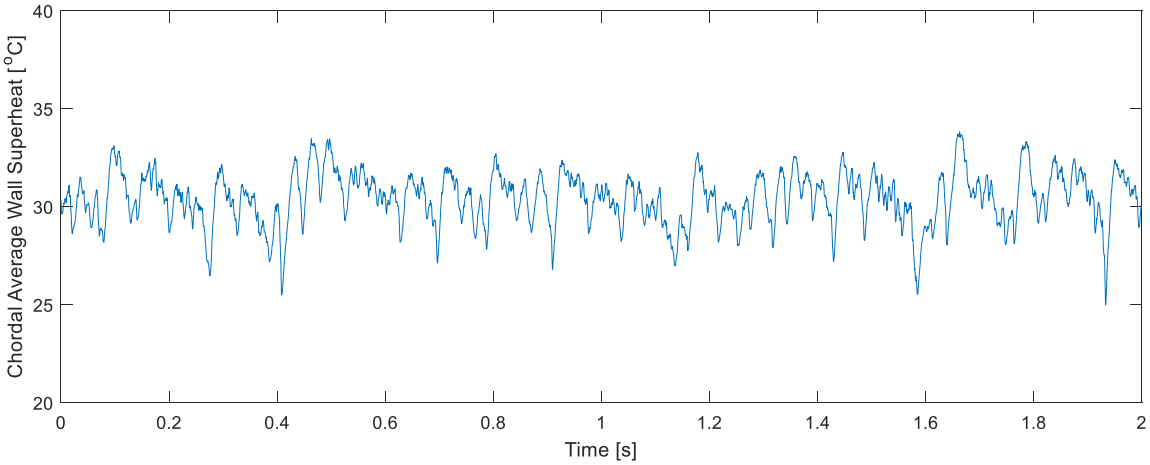

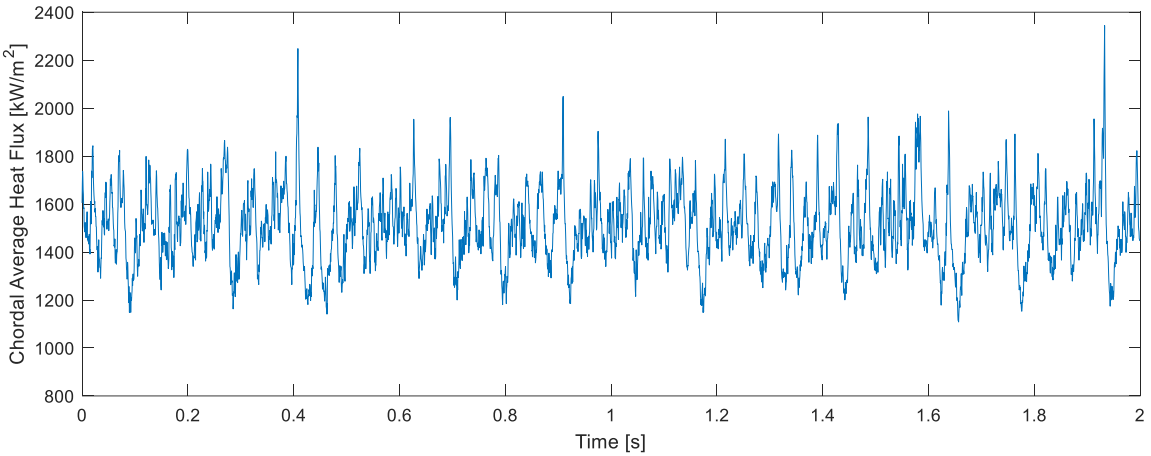

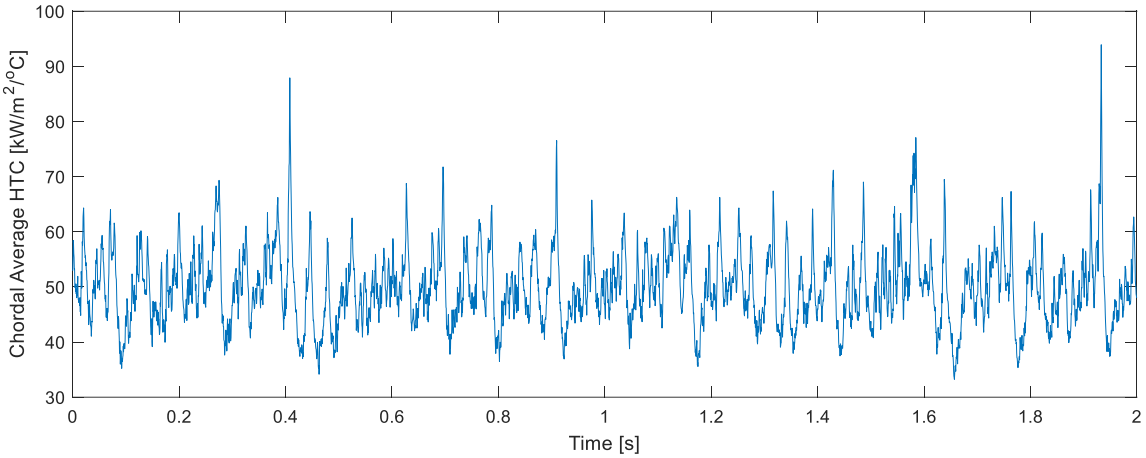

$G=1050\ kg{\cdot}m^{-2}{\cdot}s^{-1}$, $x_e= 0.07$

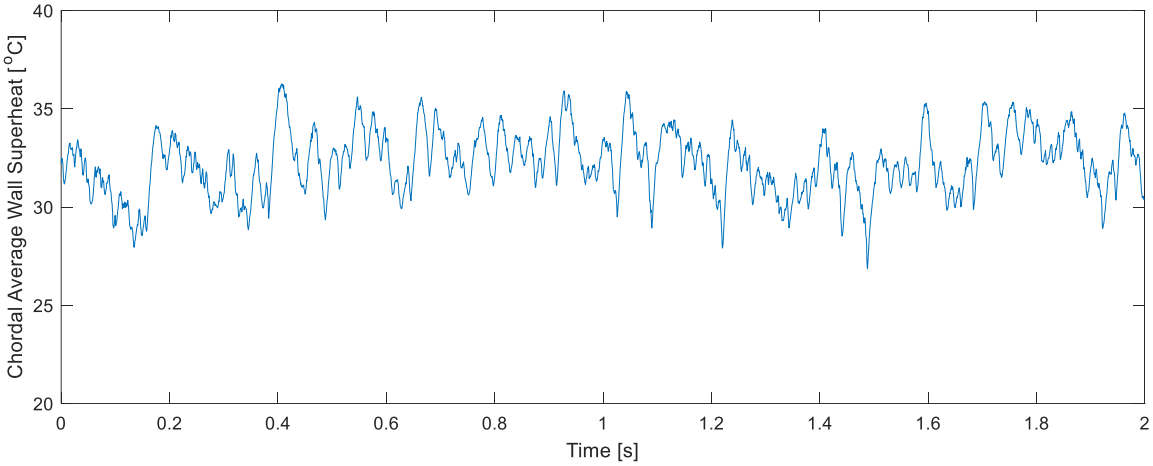

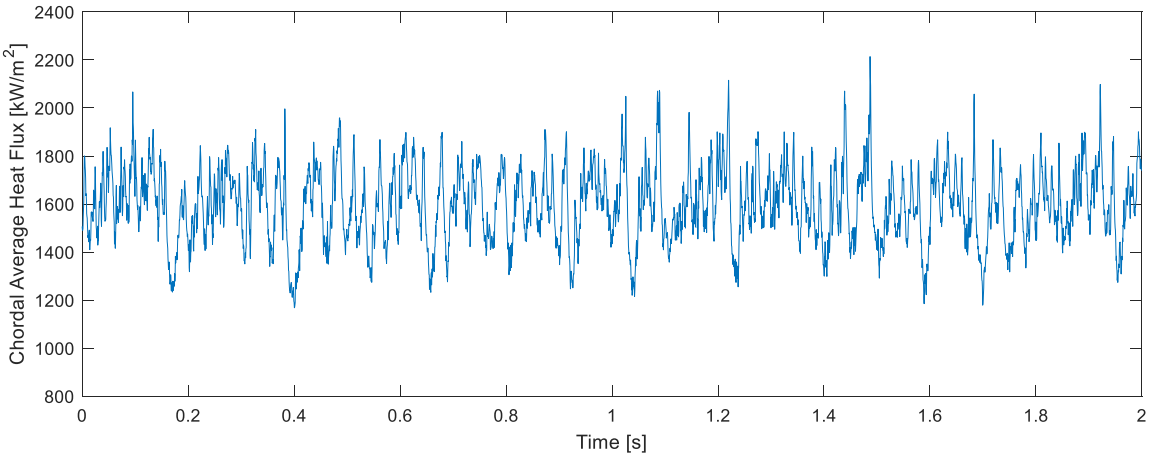

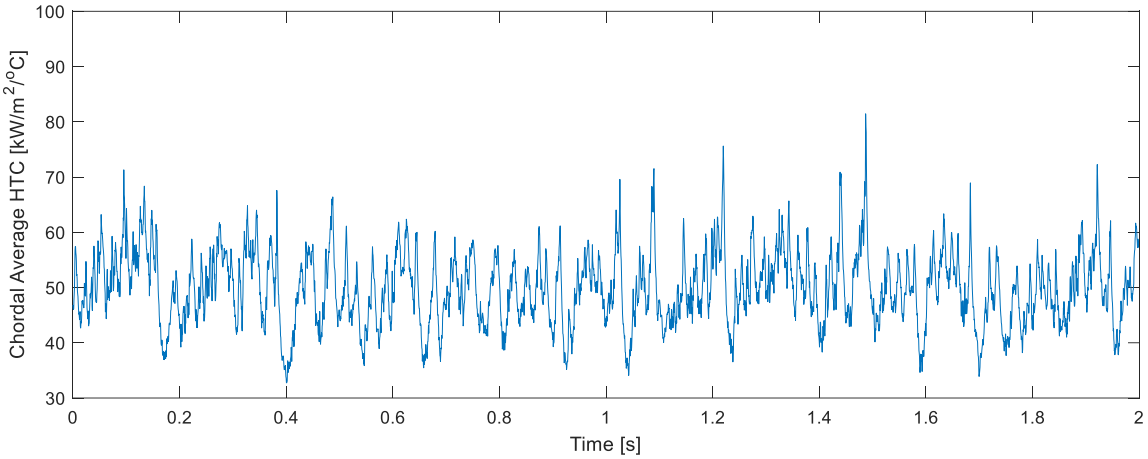

$G=1350\ kg{\cdot}m^{-2}{\cdot}s^{-1}$, $x_e= 0.07$

Figure F-0-1*: Time histories of the chordal average thermal parameters, i.e., wall superheat, heat flux and HTC, at each test condition below SNB.*

Appendix G: Time Fraction of Nucleate Boiling at each Test Condition.

The time fraction of nucleate boiling at each test condition is plotted against imposed heat flux, as shown in the figures below. As discussed in Section 7.3.1 a threshold value of 0.5 was arbitrarily chosen to define the nominal SNB condition. The region above the threshold is defined as sustained nucleate boiling.

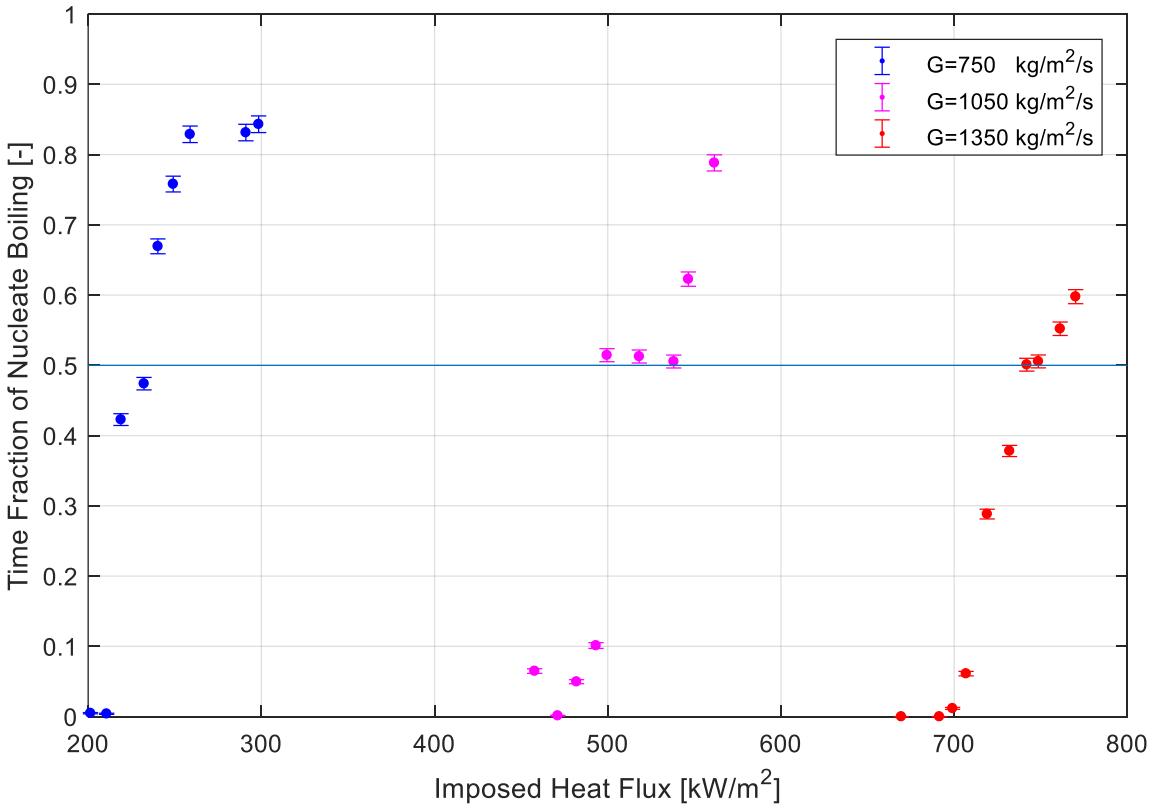

$x_e = 0.016$

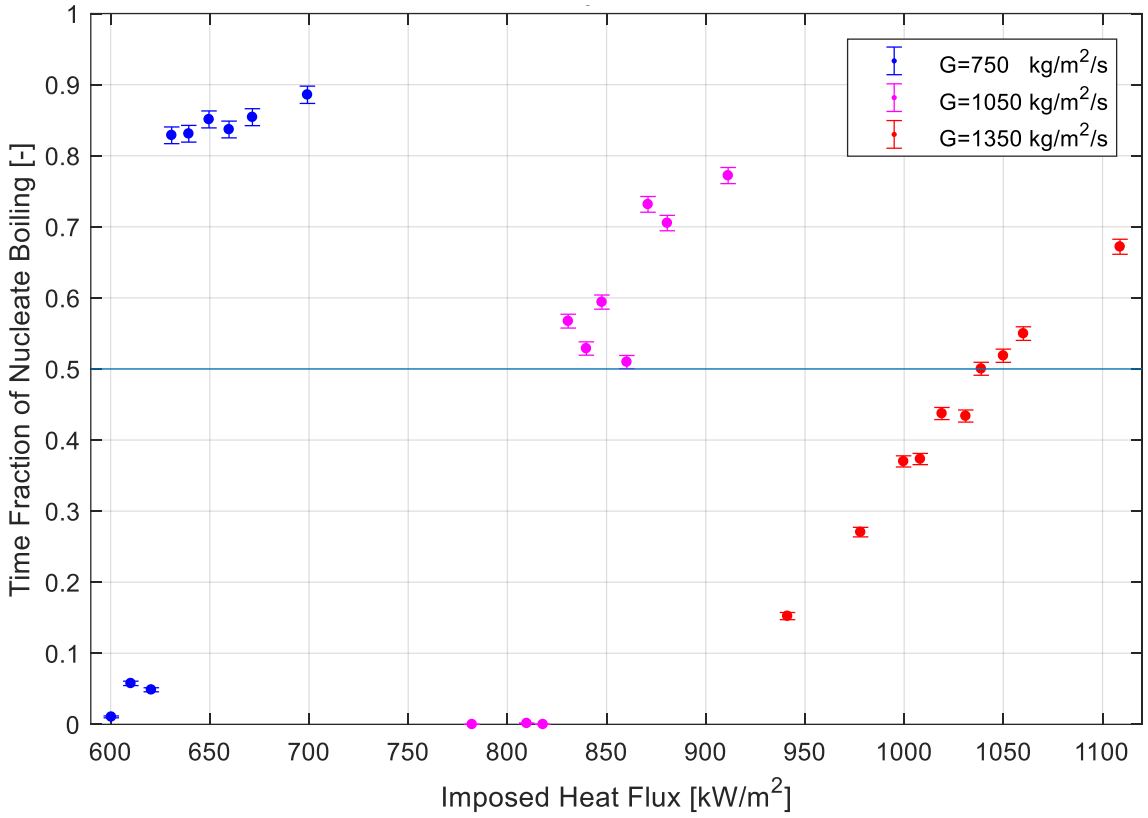
G=750 kg/m2/s
G=1050 kg/m2/s
G=1350 kg/m2/s
Time Fraction of Nucleate Boiling [-]
Imposed Heat Flux [kW/m2]
0
0.1
0.2
0.3
0.4
0.5
0.6
0.7
0.8
0.9
1
600
650
700
750
800
850
900
950
1000
1050
1100

$x_e = 0.03$

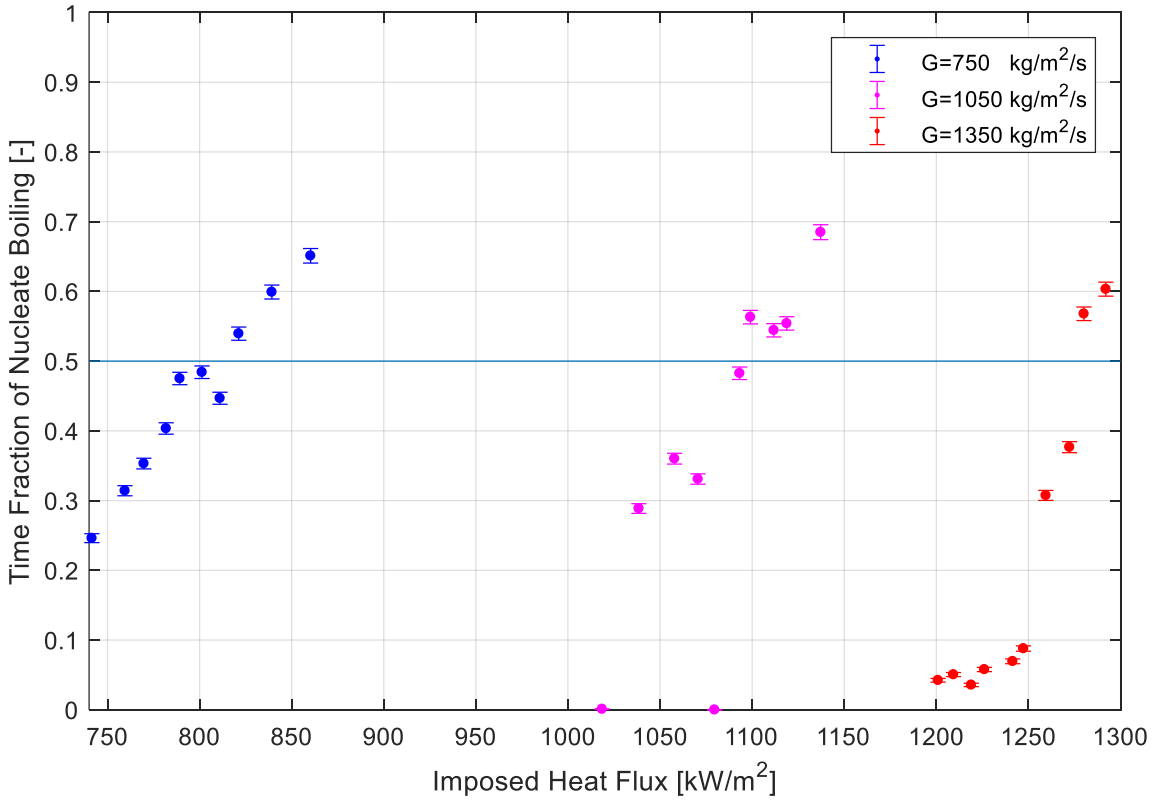
G=750 kg/m2/s
G=1050 kg/m2/s
G=1350 kg/m2/s
Time Fraction of Nucleate Boiling [-]
Imposed Heat Flux [kW/m2]
0
0.1
0.2
0.3
0.4
0.5
0.6
0.7
0.8
0.9
1
750
800
850
900
950
1000
1050
1100
1150
1200
1250
1300

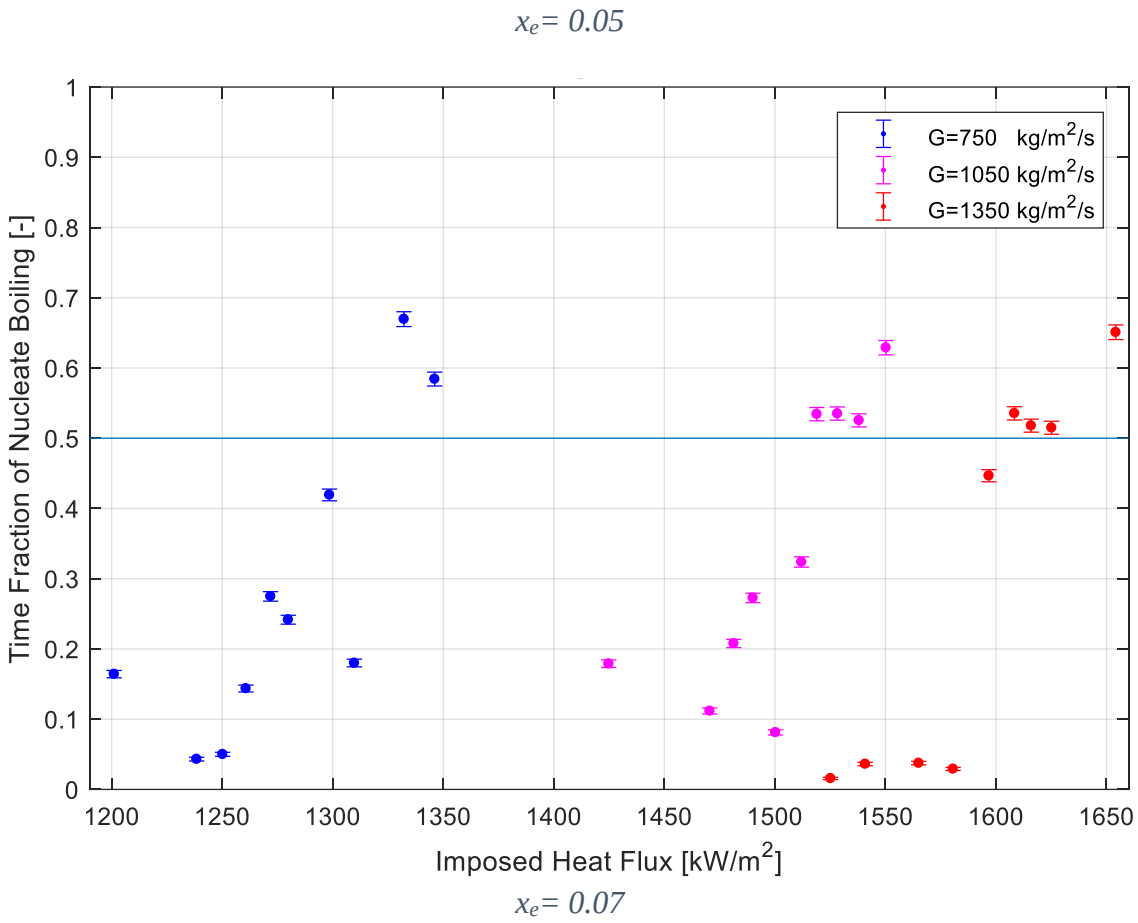

***Figure G-0-1**: Time fraction of nucleate boiling versus imposed heat flux at each test condition for detecting nominal SNB condition.*

Appendix H: Analysis and Summary of Uncertainties

In this chapter, the uncertainties of the directly measured quantities are summarized. Some instrumentation uncertainties already introduced separately in earlier chapters are still included, for a better reference to the readers. The propagated uncertainties of the major indirectly measured quantities are also analyzed.

H.1. Uncertainties of Directly Measured Quantities

H.1.1 Volumetric Flow Rate and Mass flux

The volumetric flow rate was directly measured from the Omega FV-102-SS vortex flow meter, with measuring range 0.756×10^{-4} to 7.56×10^{-4} $m^3.s^{-1}$. The flow meter was calibrated in the lab by a previous PhD student [54]. The uncertainties in slope and intercept of fitted calibration curve were 3.58×10^{-4} $m^3.s^{-1}.A^{-1}$ and 4.28×10^{-6} $m^3.s^{-1}$ respectively. From volumetric flow rate to the mass flux, the conversion equation is shown below:

$$G = \frac{Q_{mes} * \rho_l(T_{mes})}{A_{TS}} \tag{8-1}$$

The mass flux value is practically seen as a direct measurement, since the uncertainty of the measured volumetric flow rate overwhelms the other two involved quantities. The local temperature measurement (T_{mes}) from RTD holds high accuracy, which contributes negligible uncertainty to the fluid density ρ_l. The test section was precisely machined with a fabrication uncertainty of less than 50 μm at the cross-section side length of 10 mm. The resulted uncertainty of the cross-section area A_{TS} to the mass flux is also negligible. The maximum overall uncertainties in the present test range was 6% of the reading at 750 $kg{\cdot}m^{-2}{\cdot}s^{-1}$.

H.1.2. Temperature Measurement of the Flow Loop

The Omega PR-11-3-100-1/8-6-E four-wire RTDs, with measuring rage -200 ºC to 600 ºC, were deployed at various key locations to monitor the flow loop temperature, such as the inlet of the tube-bundle boiling, the inlet of entrance channel, the outlet of the test section. The manufacturer's stated accuracy is 0.15 ºC.

H.1.3. Pressure Measurement

The absolute pressure at various location of the loop was measured by Omega PX329-050A5V pressure transducers, with measuring range 0 to 3.4 bar. The manufacturer stated uncertainty was 0.25% of full scale, equivalent to 0.0085 bar.

H.1.4. Tube Bundle Boiler Voltage and Current

The voltage drop across the tube bundle was directly measured by the Agilent data acquisition system (DAS). The measuring uncertainty of the DAS is 0.005% of the reading. Two wire taps were spot welded to each pole of the boiler for measuring the imposed voltage. The taps were located as close to the root of the tube-bundle as possible to minimize the potential drop along the conductor plate.

Due to the large circulating current in the order of 1000 A, a non-contact transducer based on Hall effect was applied to measure the current circulating though the tube bundle, which was installed around the positive busbar of the DCP outlet. The applied LEM HAZ 6000 current transducer has a measuring range of 6000A, with a manufacturer stated uncertainty of 60 A.

H.1.5. ITO Heater Voltage and Current

The voltage drop across the ITO heater was also directly measured by the Agilent DAS. The measuring uncertainty of the DAS is 0.005% of the reading. Two voltage taps made of copper were directly installed at the back of the graphite electrodes for achieving voltage. The ultrafine graphite electrodes were epoxied to ITO heater via silver epoxy. The electrical resistance through the silver epoxy and graphite electrodes was negligible due to the low resistivity, small thickness, and large contact area (estimated 0.000046 Ω for silver epoxy and 0.0095 Ω for graphite electrodes), and so is the voltage drop.

The current circulating through the ITO was measured by a shunt resistor. The manufacturer stated uncertainty for the current is 0.005 A.

H.2. Uncertainties of Indirectly Measured Quantities

The propagated uncertainty of the indirectly measured quantities follows the propagation equation below, assuming the indirectly measured quantity is a function of various directly

measured quantities, i.e., $y = f(x_1, x_2, \dots, x_n)$. The directly measured quantities are further assumed to be independent of each other, so the covariance is zero.

$$\sigma_y = \sqrt{\sum_{i=1}^{n} \left(\frac{\partial y}{\partial x_i}\right)^2 \sigma_{x_i}^2} \tag{8-2}$$

H.2.1. Equilibrium Steam Quality

The equilibrium steam quality is calculated from the equation below:

$$x_e = \frac{(\dot{q}_{tot} - \dot{q}_{loss})/\dot{m} - Cp_l(T_{sat} - T_{boiler_{in}})}{h_{lg}} \tag{8-3}$$

The water heat capacity Cp_l, specific latent heat h_{lg}, and T_{sat} are all based on the locally measured saturation pressure. The uncertainty comes from the pressure probe and interpolation from the length, which is negligible compared to the one from mass flux. The subcooled boiler inlet temperature $T_{boiler_{in}}$ was measured by the RTD, the uncertainty of which is also negligible.

The heat loss $\dot{q}_{loss}$ of the whole test assembly (from tube-bundle boiler inlet to test section outlet) was examined at around 100 ^{o}C single-phase flow under slightly pressurized condition. The measured heat loss was around 0.1 kW at about 800 kg·m^{-2}·s^{-1} mass flux. Compared to the normal operating boiler power of larger than 10 kW, the heat loss is about 1% and thus negligible.

Therefore, the dominant uncertainty was from the mass flow rate measurement. The case-by-case calculated uncertainty of the equilibrium steam quality is report in Table 6-1. The maximum overall uncertainty is 7% of the calculated value.

H.2.2. Imposed Heat Flux on ITO Heater

The imposed ITO heat flux is simply calculated by voltage multiplying current divided by active area. The uncertainties of current and voltage is reported in earlier sections. The uncertainty in the active area comes from the slightly jagged edge of the ITO from manufacturing, as well as the unique wrap around design. Conservative uncertainties are given to the width and length at 0.1 mm and 0.5 mm respectively.

The largest relative uncertainty happened at the lowest imposed heat flux condition at lowest steam quality and mass flux, which is estimated to be 1.7%. The case-by-case calculated uncertainties of the imposed ITO heat flux at SNB is reported in Table 7-2. The uncertainties of the imposed ITO heat flux at other operating conditions are reflected as the error bars on the related plots.

H.2.3. Temperature Measurement from IR Thermography

The direct measurement from the IR camera is the photon flux equivalent digital counts. A radiation-conduction model is used to convert the counts to temperature. The determination of the coefficients for the radiation-conduction model relies on the calibration curve as shown in Figure 5-3. The accuracy of the calibration curve depends on the uncertainty of the temperature measurement from the RTD, which is 0.15 ^{o}C. According to our earlier publication [65], the overall uncertainty of the IR thermography output is also of the order of 0.1 ^{o}C, which indicates that the uncertainty of the radiation-conduction model itself is much smaller than RTD. The overall output uncertainty of the radiation-conduction model is dominated by the RTD measurement.

The major uncertainty of the IR thermography measurement comes from the spatial and temporal oscillation of the wall temperature caused by passage of disturbance waves, as well as the spatial halo effect (even after correction) as shown in Figure 5-8 The uncertianty reflected as the standard deviation when calculating the spatially and temporally averaged temperature. Such spatial and temporal uncertainty overwhelms the uncertainties from the RTD measurement and IR thermography. The maximum overall uncertainty of the heating wall temperature is 2 ^{o}C. The case-by-case calculated uncertainties of the wall superheat from IR thermography at SNB is reported in Table 7-2. The uncertainties of the wall superheat at other operating conditions are reflected as the error bars on the related plots.

H.2.4. HTC Measurement from IR Thermography

The HTC is determined by the wall superheat and heat flux. As discussed before, the uncertainty of temperature measurement is ± 0.15 ^{o}C, while the maximum uncertainty of the imposed heat flux is 1.7% of the recorded value. The maximum propagated uncertainty to HTC is 6% of the calculated value.

However, similar to the uncertainty on the heated wall temperature, the dominant uncertainty on HTC comes from the spatial and temporal oscillation caused by the passage of disturbance waves. Such spatial and temporal uncertainty, reflected as the standard deviation of the distribution, overwhelms the uncertainty propagated from the temperature and heat flux measurement. The maximum overall uncertainty of the HTC is as large as 10 $kW \cdot m^{-2}.^{o}C^{-1}$ that is equivalent to 40% of the calculated value. The case-by-case calculated uncertainties of the HTC from IR thermography at SNB is reported in Table 7-2. The uncertainties of the HTC at other operating conditions are reflected as the error bars on the related plots.

H.2.5. Film Thickness Measurement from LFS

The direct measurement from the LFS is the electrical current equivalent digital counts. The conversion from the digital counts to the film thickness requires a calibration curve, which is shown in Figure 5-16. The calibration curve is achieved experimentally from the calibration apparatus shown in Figure 5-14. The precision of the calibration apparatus is 2.5 μm. The calibration uncertainty including the electrical noise is 13 μm.

Due to the existence of the disturbance waves, the film thickness oscillates over time, which is the other major source of the uncertainty. As discussed in section 6.2, the mean film thickness, the plus deviation and the minus deviation represent different physical phenomena. Thus, the mean value of each quantity was evaluated in chopped up time segments. The overall maximum uncertainty on the mean film thickness is 5%.

H.2.6. Disturbance Wave Properties from Skewed Gaussian Decomposition Algorithm

The wave velocity is calculated by taking the ratio between the distance of the sensors and the time delay of the two measured signals. The conservative uncertainty on the distance between the two selected sensor pairs is 0.05 mm. The uncertainty on the time delay is the time interval of the sampling, i.e., 0.1 ms. The maximum propagated uncertainty on the velocity is 0.7 $m.s^{-1}$, equivalent to 6% of the calculated value. Since different disturbance waves travels in different speeds, the standard deviation associated with the mean velocity can be 10 times as large as the propagated uncertainty. Thus, the standard deviation is used as the uncertainty when reporting the mean velocity of the disturbance wave.

The frequency of the disturbance wave is calculated by taking the ratio between the wave counts and the total time duration. A Poisson distribution is assumed for the wave counts, and thus the uncertainty on the counts is just the square root of the counts. The maximum uncertainty on the frequency is 3.5% of the calculated value.

The uncertainty on the amplitude of the disturbance wave is basically just the uncertainty of the film thickness measurement, i.e., 13 μm. Since different disturbance waves have different amplitudes, the standard deviation associated with the mean amplitude is much larger than the propagated uncertainty. Thus, the standard deviation is used as the uncertainty when reporting the mean amplitude of the disturbance wave.

H.3. Summary of the Uncertainties

The uncertainties discussed in the chapter is summarized in the table below:

Table H-0-1*: Summary of the estimated uncertainties.*

Parameter	**Uncertainty**
Mass Flux	< ±6%
Temperature from RTD	± 0.15 ^{o}C
Pressure	± 0.0085 bar
Tube Bundle Boiler/ITO Heater Voltage	± 0.005%
Tube Bundle Boiler Current	± 60 A
ITO Heater Current	± 0.005 A
Equilibrium Steam Quality	< ± 7%
Imposed ITO Heat Flux	< ± 1.7%
Temperature from IR Thermography	± 0.15 ^{o}C, < ± 2 ^{o}C with waves
HTC from IR Thermography	< ± 6%, < ± 40% with waves
Film Thickness	± 13 μm

Disturbance Wave Velocity	< ± 6% for single wave
Disturbance Wave Frequency	< ± 3.5%
Disturbance Wave Amplitude	± 13 μm